

TABLE OF CONTENTS

<u>Section</u>	<u>Title</u>	<u>Page</u>
3.0	MODEL VERIFICATION AND VALIDATION APPROACH	3-1
3.1	General Approach	3-1
3.2	Vertical Flow Drift Flux Model Benchmarking	3-2
3.2.1	Introduction	3-2
3.2.2	NOTRUMP Drift Flux Model and Flooding	3-4
3.2.3	NOTRUMP Vertical Pipe Model	3-4
3.2.4	NOTRUMP Vertical CCFL Results	3-5
3.2.5	Conclusion	3-6
3.2.6	References	3-6
3.3	Levelizing Drift Flux Model Benchmarking	3-24
3.3.1	Introduction	3-24
3.3.2	NOTRUMP Horizontal Stratified Model and Flow Transition	3-25
3.3.3	NOTRUMP Horizontal Pipe Model	3-26
3.3.4	NOTRUMP Horizontal Flow Results; Leveling Drift Flux	3-26
3.3.5	Conclusion	3-27
3.3.6	References	3-27
3.4	Implicit Treatment of Gravitational Head	3-47
3.5	Net Volumetric Flow-Based Momentum Equation	3-63
3.5.1	AP600 Plant Transient	3-63
3.5.2	Demonstration Problem	3-64
3.6	Implicit Bubble Rise Model	3-82
3.7	Main Coolant Pump Model	3-91
3.8	Fluid Node Stacking Logic	3-97
3.8.1	Single-Phase Oscillating Manometer Problem	3-98
3.8.2	Two-Phase Constant-Pressure Boil-Off Problem	3-100

9610280145 961018
PDR ADOCK 05200003
A PDR

LIST OF TABLES

<u>Table</u>	<u>Title</u>	<u>Page</u>
3.2-1	Vertical Countercurrent Flow Limit Model Cases Analyzed	3-7
3.3-1	Horizontal Countercurrent Flow Limit Model (Levelizing) Cases Analyzed	3-28
3.8-1	Summary of the Stack Draining and Filling Events for the First 1.5 Seconds of the Single-Phase Oscillating Manometer Simulation	3-103

LIST OF FIGURES

<u>Figure</u>	<u>Title</u>	<u>Page</u>
3.2-1	Vapor Flux Zero Liquid Flux as Function of the Scale Ratio D^*	3-8
3.2-2	NOTRUMP Model for Vertical Pipe	3-9
3.2-3	3-in. Pipe, $W_l = 0.0587$ lbs/sec., $W_v = 0.2435$ lbs/sec. (20 psia)	3-10
3.2-4	3-in. Pipe, $W_l = 0.0587$ lbs/sec., $W_v = 0.2435$ lbs/sec. (20 psia)	3-11
3.2-5	3-in. Pipe, $W_l = 0.0587$ lbs/sec., $W_v = 0.2435$ lbs/sec. (20 psia)	3-12
3.2-6	3-in. Pipe, $W_l = 0.0587$ lbs/sec., $W_v = 0.2435$ lbs/sec. (20 psia)	3-13
3.2-7	3-in. Pipe, $W_l = 0.2937$ lbs/sec., $W_v = 0.2435$ lbs/sec. (20 psia)	3-14
3.2-8	3-in. Pipe, $W_l = 0.2937$ lbs/sec., $W_v = 0.2435$ lbs/sec. (20 psia)	3-15
3.2-9	3-in. Pipe, $W_l = 0.2937$ lbs/sec., $W_v = 0.2435$ lbs/sec. (20 psia)	3-16
3.2-10	3-in. Pipe, $W_l = 0.2937$ lbs/sec., $W_v = 0.2435$ lbs/sec. (20 psia)	3-17
3.2-11	$j_v^{1/2}, j_l^{1/2}$ Predictions Compared with Data Flooding Limits (0.75-in. pipe, 20 psia)	3-18
3.2-12	$j_v^{1/2}, j_l^{1/2}$ Predictions Compared with Data Flooding Limits (0.75-in. pipe, 1000 psia)	3-19
3.2-13	$j_v^{1/2}, j_l^{1/2}$ Predictions Compared with Data Flooding Limits (3-in. pipe, 20 psia)	3-20
3.2-14	$j_v^{1/2}, j_l^{1/2}$ Predictions Compared with Data Flooding Limits (3-in. pipe, 1000 psia)	3-21
3.2-15	$j_v^{1/2}, j_l^{1/2}$ Predictions Compared with Data Flooding Limits (2-ft. pipe, 20 psia)	3-22
3.2-16	$j_v^{1/2}, j_l^{1/2}$ Predictions Compared with Data Flooding Limits (2-ft. pipe, 1000 psia)	3-23
3.3-1	NOTRUMP Model for Horizontal Pipe	3-29
3.3-2	20 psia, $W_l = 10$ lbs/sec., $W_v = 40$ lbs/sec.	3-30
3.3-3	20 psia, $W_l = 10$ lbs/sec., $W_v = 40$ lbs/sec.	3-31
3.3-4	20 psia, $W_l = 10$ lbs/sec., $W_v = 40$ lbs/sec.	3-32
3.3-5	20 psia, $W_l = 10$ lbs/sec., $W_v = 40$ lbs/sec.	3-33
3.3-6	20 psia, $W_l = 10$ lbs/sec., $W_v = 40$ lbs/sec.	3-34
3.3-7	20 psia, $W_l = 150$ lbs/sec., $W_v = 40$ lbs/sec.	3-35
3.3-8	20 psia, $W_l = 150$ lbs/sec., $W_v = 40$ lbs/sec.	3-36
3.3-9	20 psia, $W_l = 150$ lbs/sec., $W_v = 40$ lbs/sec.	3-37
3.3-10	20 psia, $W_l = 150$ lbs/sec., $W_v = 40$ lbs/sec.	3-38
3.3-11	20 psia, $W_l = 150$ lbs/sec., $W_v = 40$ lbs/sec.	3-39
3.3-12	1000 psia, $W_l = 150$ lbs/sec., $W_v = 400$ lbs/sec.	3-40
3.3-13	1000 psia, $W_l = 150$ lbs/sec., $W_v = 400$ lbs/sec.	3-41
3.3-14	1000 psia, $W_l = 150$ lbs/sec., $W_v = 400$ lbs/sec.	3-42
3.3-15	1000 psia, $W_l = 150$ lbs/sec., $W_v = 400$ lbs/sec.	3-43
3.3-16	1000 psia, $W_l = 150$ lbs/sec., $W_v = 400$ lbs/sec.	3-44
3.3-17	$j_v^{1/2}, j_l^{1/2}$ Predictions Compared with Data Flooding Limits (20 psia)	3-45
3.3-18	$j_v^{1/2}, j_l^{1/2}$ Predictions Compared with Data Flooding Limits (1000 psia)	3-46
3.4-1	Noding Diagram for NOTRUMP Manometer Simulation	3-50
3.4-2	Explicit Gravitational Head - Manometer Water Levels	3-51
3.4-3	Implicit Gravitational Head - Manometer Water Levels	3-52

LIST OF FIGURES (Continued)

<u>Figure</u>	<u>Title</u>	<u>Page</u>
3.4-4	Explicit Gravitational Head - Flowlinks 3 and 4 Total Pressure Drop with Stack Water Level	3-53
3.4-5	Implicit Gravitational Head - Flowlinks 3 and 4 Total Pressure Drop with Stack Water Level	3-54
3.4-6	Explicit Gravitational Head - Flowlinks 3 and 4 Total Pressure Drop with Stack Water Level (Expanded Time Scale 0 to 0.35 Seconds)	3-55
3.4-7	Implicit Gravitational Head - Flowlinks 3 and 4 Total Pressure Drop with Stack Water Level (Expanded Time Scale 0 to 0.35 Seconds)	3-56
3.4-8	Explicit Gravitational Head - Flowlinks 3 and 4 Total Pressure Drop with Stack Water Level (Expanded Time Scale 0.3 to 0.35 Seconds)	3-57
3.4-9	Implicit Gravitational Head - Flowlinks 3 and 4 Total Pressure Drop with Stack Water Level (Expanded Time Scale 0.3 and 0.35 Seconds)	3-58
3.4-10	Explicit Gravitational Head - Difference Between Total Pressure Drop in Flowlinks 4 and 3 (Expanded Time Scale 0.3 to 0.35 Seconds)	3-59
3.4-11	Implicit Gravitational Head with Subcooled Mixture Regions - Fluid Nodes 3 and 4 Pressure (Expanded Time Scale 0 to 0.6 Seconds)	3-60
3.4-12	Implicit Gravitational Head with Saturated Mixture Regions - Fluid Nodes 3 and 4 Pressure (Expanded Time Scale 0 to 0.6 Seconds)	3-61
3.4-13	Implicit Gravitational Head with Subcooled Mixture Regions - Fluid Nodes 3 and 4 Pressure (Reduced Time Step Size; Expanded Time Scale 0. to 0.6 Seconds)	3-62
3.5-1	Reactor Coolant System Pressure	3-65
3.5-2	Comparison of Liquid Mass Flow Rates for Hot Leg 1	3-66
3.5-3	Comparison of Liquid Mass Flow Rates for Hot Leg 2	3-67
3.5-4	Comparison of Liquid Mass Flow Rates for Cold Leg 1	3-68
3.5-5	Comparison of Liquid Mass Flow Rates for Cold Leg 2	3-69
3.5-6	Comparison of Liquid Mass Flow Rates for Cold Leg 3	3-70
3.5-7	Comparison of Liquid Mass Flow Rates for Cold Leg 4	3-71
3.5-8	Comparison of Vapor Mass Flow Rates for Hot Leg 1	3-72
3.5-9	Comparison of Vapor Mass Flow Rates for Hot Leg 2	3-73
3.5-10	Comparison of Vapor Mass Flow Rates for Cold Leg 1	3-74
3.5-11	Comparison of Vapor Mass Flow Rates for Cold Leg 2	3-75
3.5-12	Comparison of Vapor Mass Flow Rates for Cold Leg 3	3-76
3.5-13	Comparison of Vapor Mass Flow Rates for Cold Leg 4	3-77
3.5-14	NOTRUMP Model for Demonstration Problem	3-78
3.5-15	Void Fraction	3-79
3.5-16	Mass Flow Rate Into System	3-80
3.5-17	Velocity	3-81

LIST OF FIGURES (Continued)

<u>Figure</u>	<u>Title</u>	<u>Page</u>
3.6-1	NOTRUMP Model for Boil-Off Problem	3-83
3.6-2	Mixture Levels	3-84
3.6-3	Void Fractions	3-85
3.6-4	Void Fractions	3-86
3.6-5	Bubble Rise per Step and Step Initial Mixture Bubble Mass (Explicit Bubble Rise)	3-87
3.6-6	Bubble Rise per Step and Step Initial Mixture Bubble Mass (Implicit Bubble Rise)	3-88
3.6-7	Node Pressures with Implicit Bubble Rise	3-89
3.6-8	Link 2 Flow Rate with Implicit Bubble Rise	3-90
3.7-1	Plant Noding Diagram	3-92
3.7-2	Pressurizer Pressure	3-93
3.7-3	Mass Flow into Cold Leg 2	3-94
3.7-4	Mass Flow into Cold Leg 1	3-95
3.7-5	Mass Flow into Cold Leg 4	3-96
3.7-6	Mass Flow into Cold Leg 3	3-97
3.8-1	Single-Phase Oscillating Manometer Case: Stack Mixture Level	3-104
3.8-2	Single-Phase Oscillating Manometer Case: Stack Node Mixture Region Masses with Stack Mixture Level	3-105
3.8-3	Single-Phase Oscillating Manometer Case: Stack Node Vapor Region Masses with Stack Mixture Level	3-106
3.8-4	Single-Phase Oscillating Manometer Case: Stack Node Mixture Region Specific Enthalpies with Stack Mixture Level	3-107
3.8-5	Single-Phase Oscillating Manometer Case: Stack Node Vapor Region Specific Enthalpies with Stack Mixture Level	3-108
3.8-6	Single-Phase Oscillating Manometer Case: Stack Node 3 Vapor Region Specific Enthalpy with Stack Mixture Level (with Expanded Time Scale 0.2 to 0.3 Seconds)	3-109
3.8-7	Single-Phase Oscillating Manometer Case: Stack Flowlink Liquid Mass Flow Rates with Stack Mixture Level	3-110
3.8-8	Single-Phase Oscillating Manometer Case: Stack Flowlink Vapor Mass Flow Rates with Stack Mixture Level	3-111
3.8-9	Single-Phase Oscillating Manometer Case: Stack Node Pressures with Stack Mixture Level	3-112
3.8-10	Two-Phase Constant-Pressure Boil-Off Case: Stack Mixture Level	3-113
3.8-11	Two-Phase Constant-Pressure Boil-Off Case: Stack Mixture Region Volumes with Stack Mixture Level	3-114

LIST OF FIGURES (Continued)

<u>Figure</u>	<u>Title</u>	<u>Page</u>
3.8-12	Two-Phase Constant-Pressure Boil-Off Case: Stack Node Vapor Region Volumes with Stack Mixture Level	3-115
3.8-13	Two-Phase Constant-Pressure Boil-Off Case: Stack Node Mixture Region Specific Enthalpies with Stack Mixture Level	3-116
3.8-14	Two-Phase Constant-Pressure Boil-Off Case: Stack Node Vapor Region Specific Enthalpies with Stack Mixture Level	3-117
3.8-15	Two-Phase Constant-Pressure Boil-Off Case: Stack Node Vapor Region Qualities with Stack Mixture Level	3-118
3.8-16	Two-Phase Constant-Pressure Boil-Off Case: Stack Node Vapor Region Qualities with Stack Mixture Level	3-119
3.8-17	Two-Phase Constant-Pressure Boil-Off Case: Stack Flowlink Liquid Mass Flow Rate with Stack Mixture Level	3-120
3.8-18	Two-Phase Constant-Pressure Boil-Off Case: Stack Flowlink Liquid Mass Flow Rate with Stack Mixture Level (with Expanded y-axis Scale)	3-121
3.8-19	Two-Phase Constant-Pressure Boil-Off Case: Stack Flowlink Vapor Mass Flow Rate with Stack Mixture Level	3-122
3.8-20	Two-Phase Constant-Pressure Boil-Off Case: Stack Node Pressures with Stack Node Pressure with Stack Mixture Level	3-123

3.0 MODEL VERIFICATION AND VALIDATION APPROACH

3.1 General Approach

Each of the model changes described in Section 2.0 has been verified and validated for use in AP600 plant analyses. Once the coding changes were written, reviewed, and tested, one or more of three methods of verification and validation were applied. The three methods include: 1) performance of simple test cases, 2) simulation of separate effects tests, and 3) simulation of integral facility tests.

This section describes test cases that were performed. Simulation of separate effects tests are described in a different section for each separate effects test facility, and the simulation of integral facility tests are described in a different section for each integral facility.

The discussion for each test described in this section includes the test purpose, the NOTRUMP model used, and a summary of the test results.

3.2 Vertical Flow Drift Flux Model Benchmarking

3.2.1 Introduction

The countercurrent flow limit (CCFL) in two-phase flow in vertical tubes has been found to be represented by the following equation:

$$j_v^{1/2} + m \left(\sqrt{\frac{\rho_l}{\rho_v}} \right)^{1/2} (-j_l)^{1/2} = C J^{1/2} \quad (3.2-1)$$

where j_v and j_l are vapor and liquid volumetric flux (positive upward), J is a characteristic velocity, and m and C are empirical constants.

The original form of the equation, due to Wallis, was written in dimensionless form as:

$$\begin{aligned} j_v^{*1/2} + m j_l^{*1/2} &= C \\ j_v^* &= \frac{j_v}{J} = \frac{j_v}{\sqrt{\frac{\Delta\rho g D}{\rho_v}}} \\ j_l^* &= \frac{\sqrt{\rho_l/\rho_v} j_l}{J} = \frac{j_l}{\sqrt{\frac{\Delta\rho g D}{\rho_l}}} \\ J &= \sqrt{\frac{\Delta\rho g D}{\rho_v}} \end{aligned} \quad (3.2-2)$$

The characteristic velocity, J , is assumed to be a function of the tube diameter, D . As the tube diameter increases, the liquid volumetric flux that can flow downward against a given upward flux of vapor increases. This type of behavior is usually called " J^* scaling." The constant C ranges from 0.7 to 1.0, and the constant m from 0.8 to 1.0 [Reference 3.2-1].

Subsequent tests at larger scales found that the appropriate length scale for large tubes was not the tube diameter but the Taylor instability wave length:

$$\lambda = \sqrt{\frac{\sigma}{\Delta\rho g}} \quad (3.2-3)$$

When the diameter length scale is replaced by the Taylor length scale, the following characteristic velocity results:

$$K = \left[\frac{\sigma\Delta\rho g}{\rho_v^2} \right]^{1/4} \quad (3.2-4)$$

This characteristic velocity is typically called the Kutateladze number, and the CCFL behavior under these conditions is called "K" scaling." The nondimensional fluxes, obtained by replacing J with K in Equation 3.2-2, are described as k^* . In this case, the liquid downward flux for a given vapor flux remains unchanged as tube diameter increases.

Figure 3.2-1 taken from Reference 3.2-1 plots the vapor flux at zero liquid flux as a function of the scale ratio D^* where $D^* = D/\lambda$. The y-axis scale on this figure is equivalent to C^2 in Equation 3.2-2, with J replaced by K and $j_l = 0$. Various tests indicate that the constant C^2 asymptotically approaches a value of 3 ($C = 1.7$), at which point the value of C does not change with geometric scale, indicating that K^* scaling applies. The transition from J^* to K^* scaling takes place when the ratio between tube diameter and Taylor length $D^* = D/\lambda$ is greater than about 30. For steam water mixtures ranging from 15 to 1000 psia, K^* scaling should apply at tube diameters greater than about 2 to 3 in. in diameter.

The constant C changes with tube geometry at large scale. However, wide variations in geometry do not strongly affect the value of C . For flooding through holes in a plate, for example, tests by Bankoff [Reference 3.2-2] show that the asymptotic value of C approaches a value of 2.

The constant m is primarily a function of end conditions and varies from 0.65 to 0.8 [Reference 3.2-1].

In summary, the CCFL data at small scales (pipe diameter less than 2 in.) can be adequately represented by the following equation:

$$j_v^{1/2} + (0.8 \rightarrow 1.0) \sqrt{\frac{\rho_l}{\rho_v}} j_l^{1/2} = (0.7 \rightarrow 1.0) J^{1/2} \quad (3.2-5)$$

For large pipes, the data can be represented by the following equation:

$$j_v^{1/2} + (0.7 \rightarrow 1.0) \sqrt{\frac{\rho_l}{\rho_v} j_l^{1/2}} = (1.5 \rightarrow 2.0) K^{1/2} \quad (3.2-6)$$

There are no CCFL data at high pressure; however, it can be assumed that the effects of pressure are captured in the equations above through the surface tension and the phase densities. When plotted on the $(j_v)^{1/2}$ and $(j_l)^{1/2}$ plane, the above equations are straight lines and define the boundary between permitted countercurrent flow and forbidden countercurrent flow. A two-phase flow computer model, be it drift flux or two fluid, should not predict countercurrent flow in the forbidden region.

3.2.2 NOTRUMP Drift Flux Model and Flooding

As described in previous submittals, NOTRUMP uses a drift flux model to calculate two-phase flow conditions. The code uses two constitutive models used to describe the relative velocity:

[] a,c

The flooding process described in the introduction can be expected to occur in all vertical pipe segments, such as the steam generator tubes, or across orifice plates, such as the core plate. "Flooding" also occurs in the core, of course, but this is manifested differently, by the rise and fall of the mixture level with changing steam flow. A falling mixture level with upward steam flow represents a countercurrent condition, a rising level represents a concurrent condition, and a stationary level represents a "flooded" condition. Predictions of mixture level movement within various tests is therefore sufficient to establish whether the drift flux model is applied correctly in the core; these comparisons are identified in Reference 3.2-4, Section 3-1-2. The description below will examine whether the CCFL for vertical tubes in the rest of the reactor coolant system (RCS) is predicted properly.

3.2.3 NOTRUMP Vertical Pipe Model

To evaluate the NOTRUMP drift flux model under countercurrent conditions, a model was developed, as shown in Figure 3.2-2. [] a,c

[] a,c

At the start of the NOTRUMP calculation, there is zero vapor flow, and liquid at a fixed flow rate is injected into the top of the pipe. The pressure in all nodes is approximately that of the boundary node

and constant. At 80 seconds, the vapor flow is increased linearly (see Figure 3.2-3; positive flow denotes upward flow) and flows up the pipe into the boundary fluid node. As the vapor flow increases, the liquid downward flow, which in this case is initially at a relatively low value (Figure 3.2-4 shows the liquid flow in the middle of the pipe), begins to decrease and at some point reverses and flows upward. As the liquid flow out of the bottom of the pipe begins to decrease, the vapor fraction, which was initially at 0.994 (see Figure 3.2-5), begins to decrease as the pipe fills up. Eventually, the liquid is expelled from the top of the pipe (see Figure 3.2-6), and the vapor fraction approaches 1.0.

Figures 3.2-7 to 3.2-10 show a similar set of plots for a case in which the initial downward liquid flow is substantially higher. In this case, the vapor fraction is initially lower (see Figure 3.2-9). There are more flow oscillations in this case. The liquid downward flow and hydrostatic head are sufficient to cause concurrent downward flow and drag vapor out of the bottom of the pipe (periods of negative flow prior to 100 sec. in Figure 3.2-7). The catch tank volume then pressurizes and pushes vapor back up into the pipe. Except for the oscillations, the general behavior and end point of this high flow case is similar to the low flow case.

Several calculations were performed at different pressures, diameters, and liquid flow rates (see Table 3.2-1). The results of these calculations were then plotted along with the data lines as described below.

3.2.4 NOTRUMP Vertical CCFL Results

The calculated values of $j_v^{1/2}$ and $j_l^{1/2}$ for flowlink 4 are arranged in pairs. All pairs in countercurrent flow are then saved, the square root is taken, and the resulting pairs are plotted as points as shown in Figures 3.2-11 to 3.2-16, along with the data boundaries described by Equations 3.2-5 and 3.2-6. A specific NOTRUMP run can usually be traced by the line of points starting near zero j_v . The left-most vertical line is a low liquid flow rate test. The line remains vertical as j_v is increased, indicating countercurrent flow with little interaction between liquid and vapor. As the flooding point is approached, the line veers to the left as j_l is reduced, and a second vertical line forms on the y axis at $j_l = 0$ after the flooding point is exceeded.

The results show that NOTRUMP generally predicts CCFL at a lower vapor flux than indicated by the data. The EPRI model does not exhibit a strong scaling trend as the tube diameter becomes small (Reference 3.2-3 indicates that only orifice plates with a small range of hole diameters were used to verify the CCFL predictions). In all cases, the NOTRUMP prediction is within or below the data range. In addition, the presence of flow oscillations does not affect the code's ability to represent CCFL correctly.

3.2.5 Conclusion

These comparisons show that CCFL is correctly predicted by the NOTRUMP drift flux model. The results also suggest that NOTRUMP will tend to predict more holdup of liquid in small and large diameter pipes than indicated by the data.

3.2.6 References

- 3.2-1 Bankoff, S. G. and S. C. Lee, "A Critical Review of the Flooding Literature," NUREG/CR-3060 (July 1983).
- 3.2-2 Bankoff, S. G., "Countercurrent Air/Water and Steam/Water Flow Above a Perforated Plate," NUREG/CR-1808 (November 1980).
- 3.2-3 Chexal, B. and G. Lellouche, "A Full Range Drift-Flux Correlation for Vertical Flows," EPRI NP-3989SR, Revision 1 (September 1986).
- 3.2-4 Lee, N., et. al., "Westinghouse Small-Break ECCS Evaluation Model Using the NOTRUMP Code," WCAP-10054-P-A (August 1985).

TABLE 3.2-1

VERTICAL COUNTERCURRENT FLOW LIMIT MODEL CASES ANALYZED

Pressure Psia	Case	Pipe ID		
		0.75 in. (0.0625 ft.)	3.0 in. (0.25 ft.)	2.0 ft.
1000 Vapor Flow Rate ($V_g = 10$ ft./sec.)	Liquid Flow Rate (V_l) ft./sec.	Vapor Mass Flow Rate, W_v (0.069 lbm/sec.)	Vapor Mass Flow Rate, W_v (1.101 lbm/sec.)	Vapor Mass Flow Rate, W_v (70.45 lbm/sec.)
		Liquid Mass Flow Rate, W_L (lbm/sec.)	Liquid Mass Flow Rate, W_L (lbm/sec.)	Liquid Mass Flow Rate, W_L (lbm/sec.)
	1) 0.02	2.842E-03	0.0455	2.91
	2) 0.10	0.0142	0.2274	14.55
	3) 0.25	0.0355	0.5684	36.376
4) 0.50	0.0710	1.1368	72.75	
20 Vapor Flow Rate ($V_g = 100$ ft./sec.)	Case	Pipe ID		
		0.75 in. (0.0625 ft.)	3.0 in. (0.25 ft.)	2.0 ft.
	Liquid Flow Rate (V_l) ft./sec.	Vapor Flow Rate, W_v (0.0152 lbm/sec.)	Vapor Flow Rate, W_v (0.2435 lbm/sec.)	Vapor Flow Rate, W_v (15.582 lbm/sec.)
		Liquid Mass Flow Rate, W_L (lbm/sec.)	Liquid Mass Flow Rate, W_L (lbm/sec.)	Liquid Mass Flow Rate, W_L (lbm/sec.)
	1) 0.02	3.671E-03	0.0587	3.7592
2) 0.10	0.0183	0.2937	18.796	
3) 0.25	0.0459	0.7343	46.990	
4) 0.50	0.0918	1.4685	93.981	

Notes:

Liquid was injected at a constant flow rate throughout the transient
(from time 0 to end of transient)

Vapor was injected at the following rate:

0 - 80 sec. ----- no vapor flow
80 - 300 sec. ----- 0.0 - full flow rate
300 - end of transient ----- full flow rate

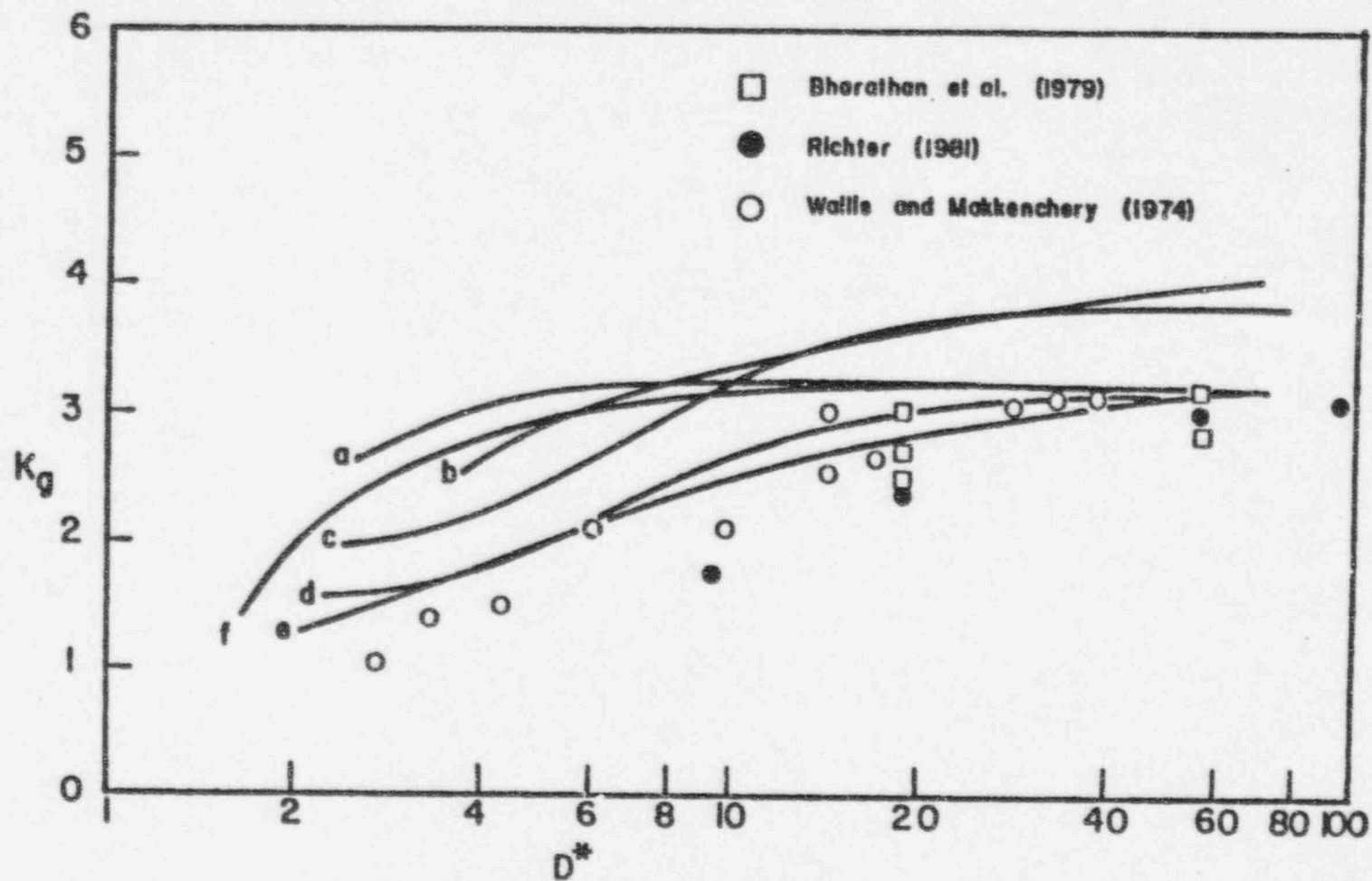
Figure 3.2-1 Vapor Flux at Zero Liquid Flux as Function of the Scale Ratio D^* 

Figure 25. Comparison of predictive models with data for zero penetration:
 (a) Pushkina and Sorokin (1969); (b) Bharathan et al. (1979);
 (c) Eichhorn (1980), $\beta=45^\circ$; (d) Eichhorn (1980), $\beta=60^\circ$;
 (e) Richter (1981); (f) Yao and Sun (1981).

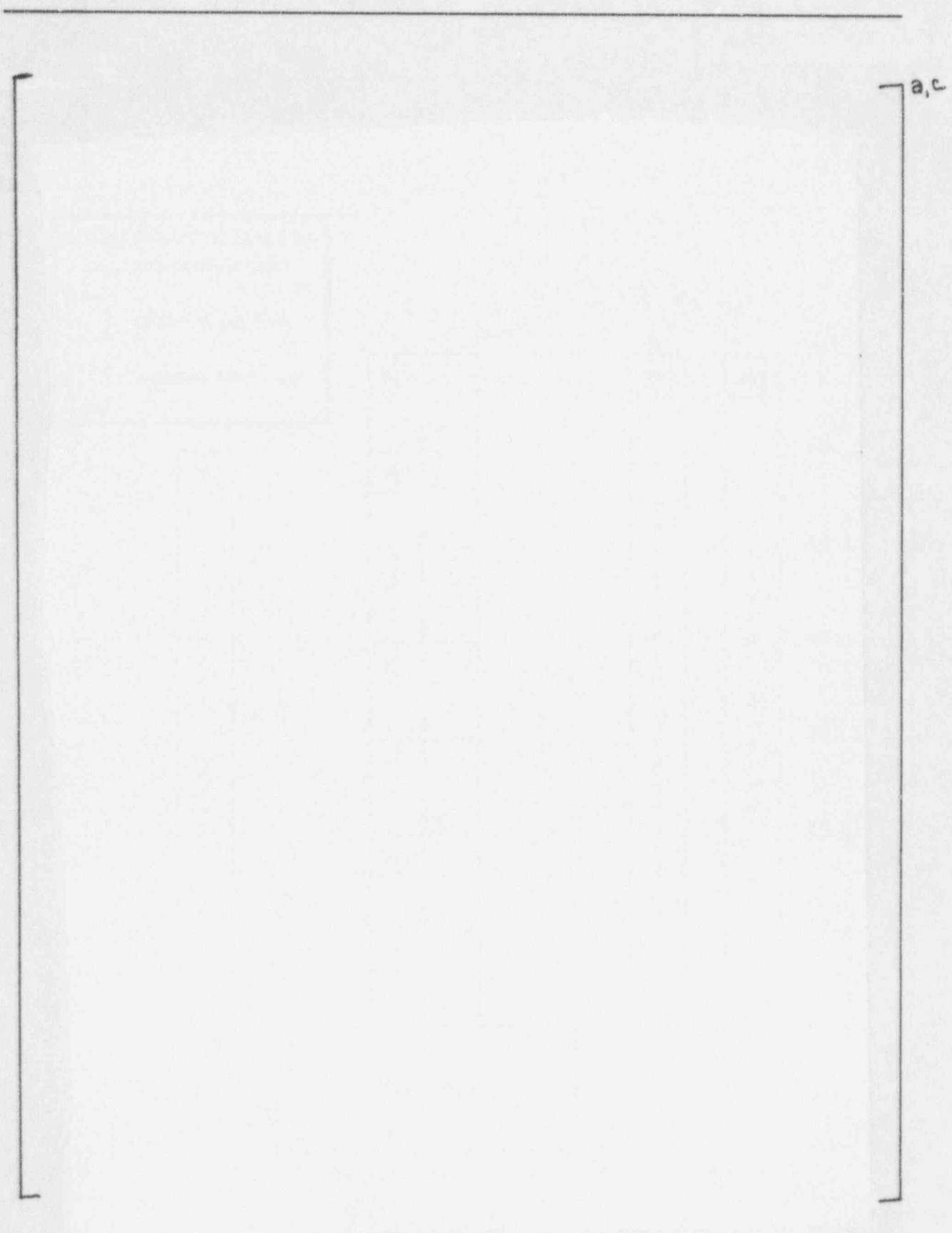


Figure 3.2-2 NOTRUMP Model for Vertical Pipe

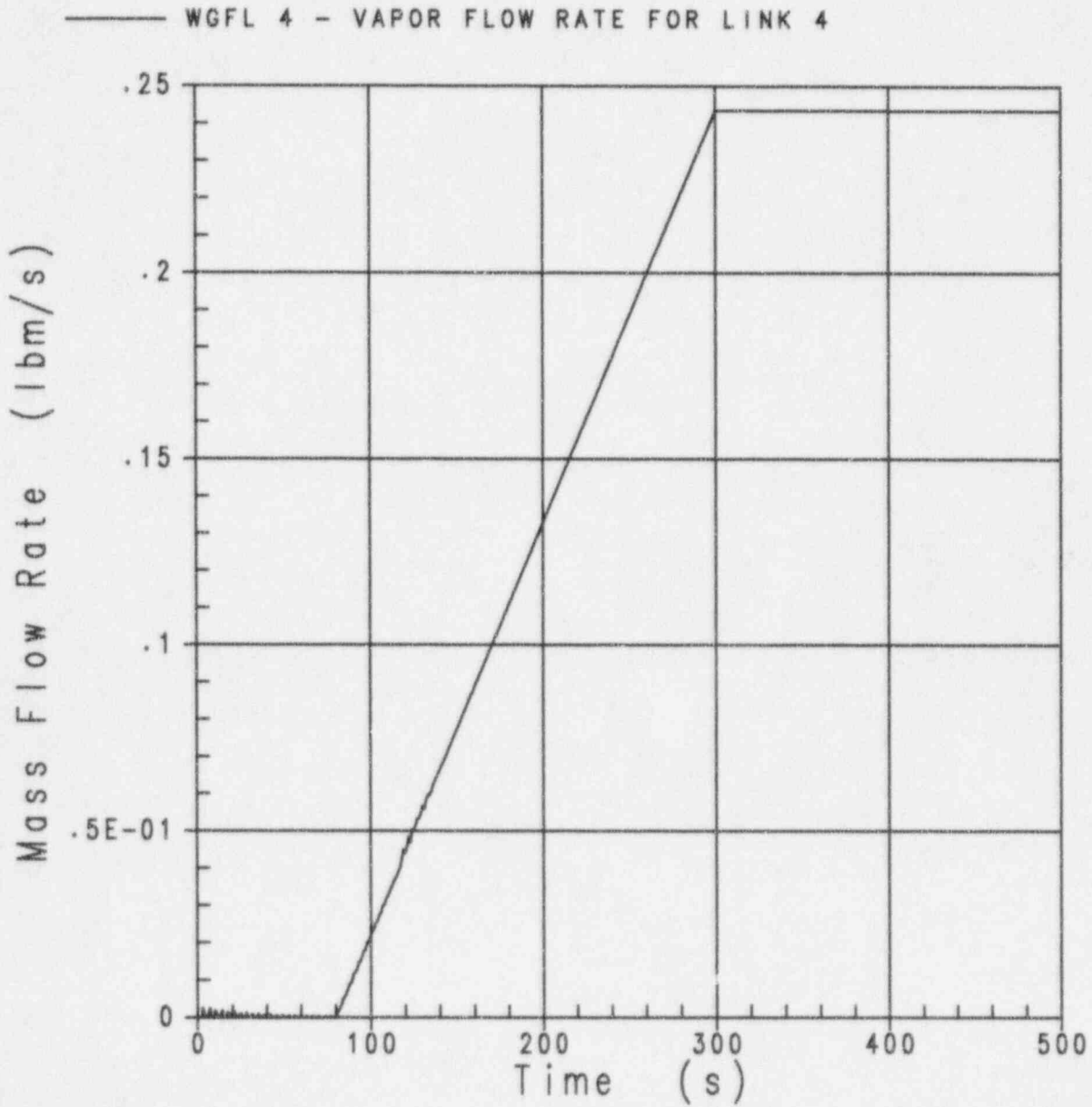


Figure 3.2-3 3-in. Pipe, $W_1 = 0.0587$ lbs/sec., $W_v = 0.2435$ lbs/sec. (20 psia)

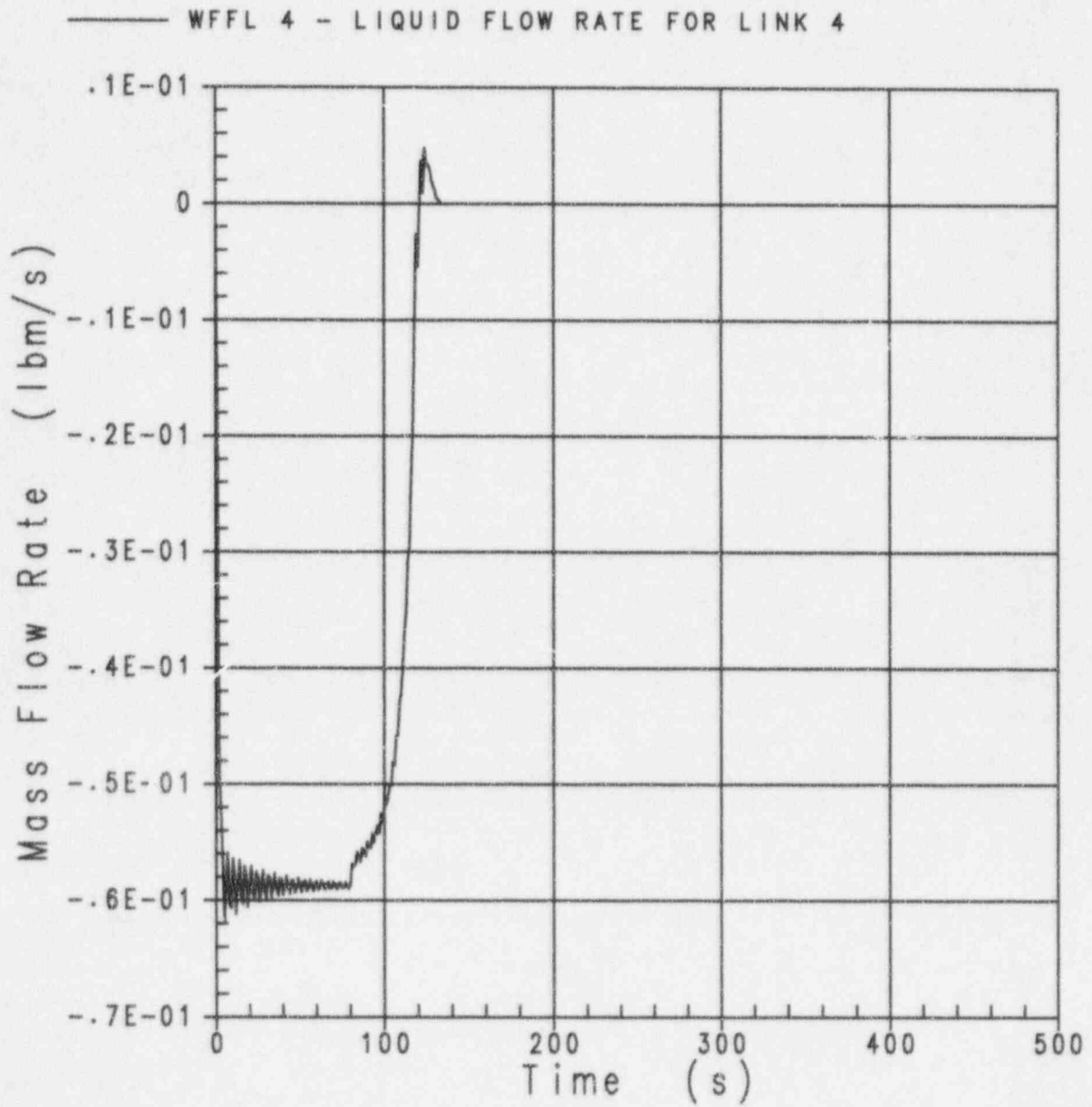


Figure 3.2-4 3-in. Pipe, $W_1 = 0.0587$ lbs/sec., $W_v = 0.2435$ lbs/sec. (20 psia)

— VFMFN 1 - NODE 1 MIX REG VOID FRACTION
 - - - VFMFN 2 - NODE 2 MIX REG VOID FRACTION
 - - - VFMFN 3 - NODE 3 MIX REG VOID FRACTION
 - - - VFMFN 4 - NODE 4 MIX REG VOID FRACTION
 - - - VFMFN 5 - NODE 5 MIX REG VOID FRACTION
 - - - VFMFN 6 - NODE 6 MIX REG VOID FRACTION

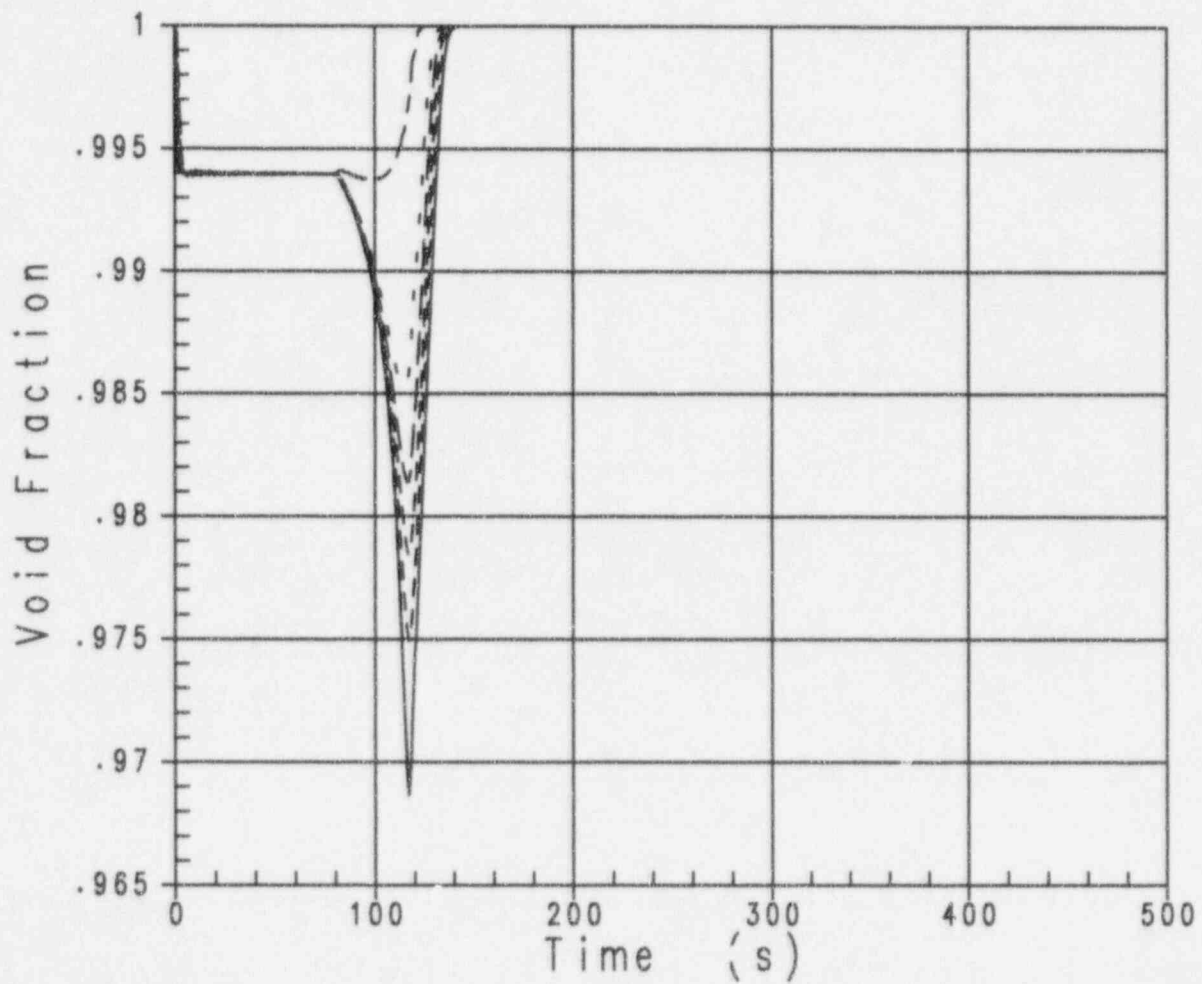


Figure 3.2-5 3-in. Pipe, $W_1 = 0.0587$ lbs/sec., $W_2 = 0.2435$ lbs/sec. (20 psia)

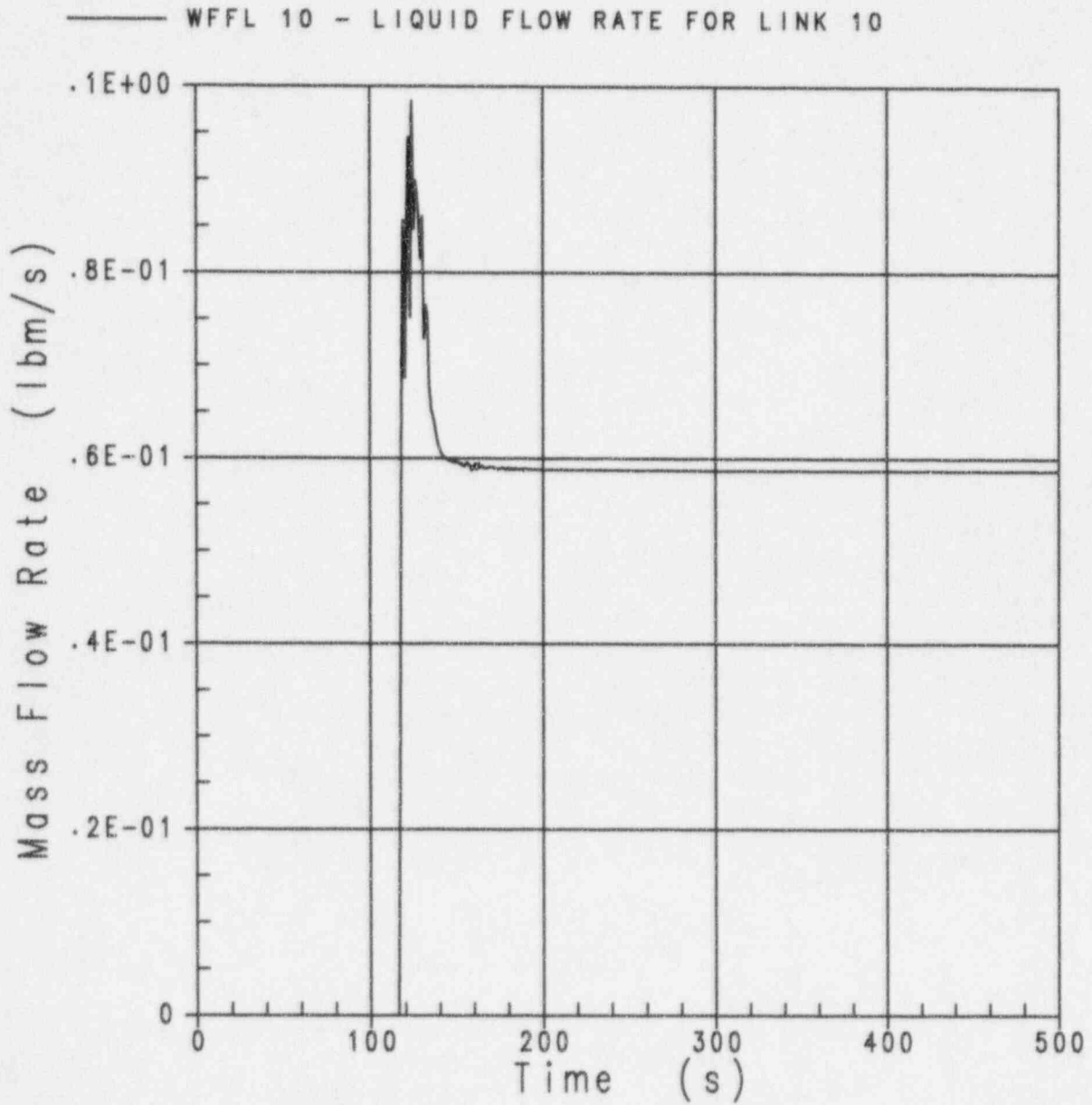


Figure 3.2-6 3-in. Pipe, $W_1 = 0.0587$ lbs/sec., $W_2 = 0.2435$ lbs/sec. (20 psia)

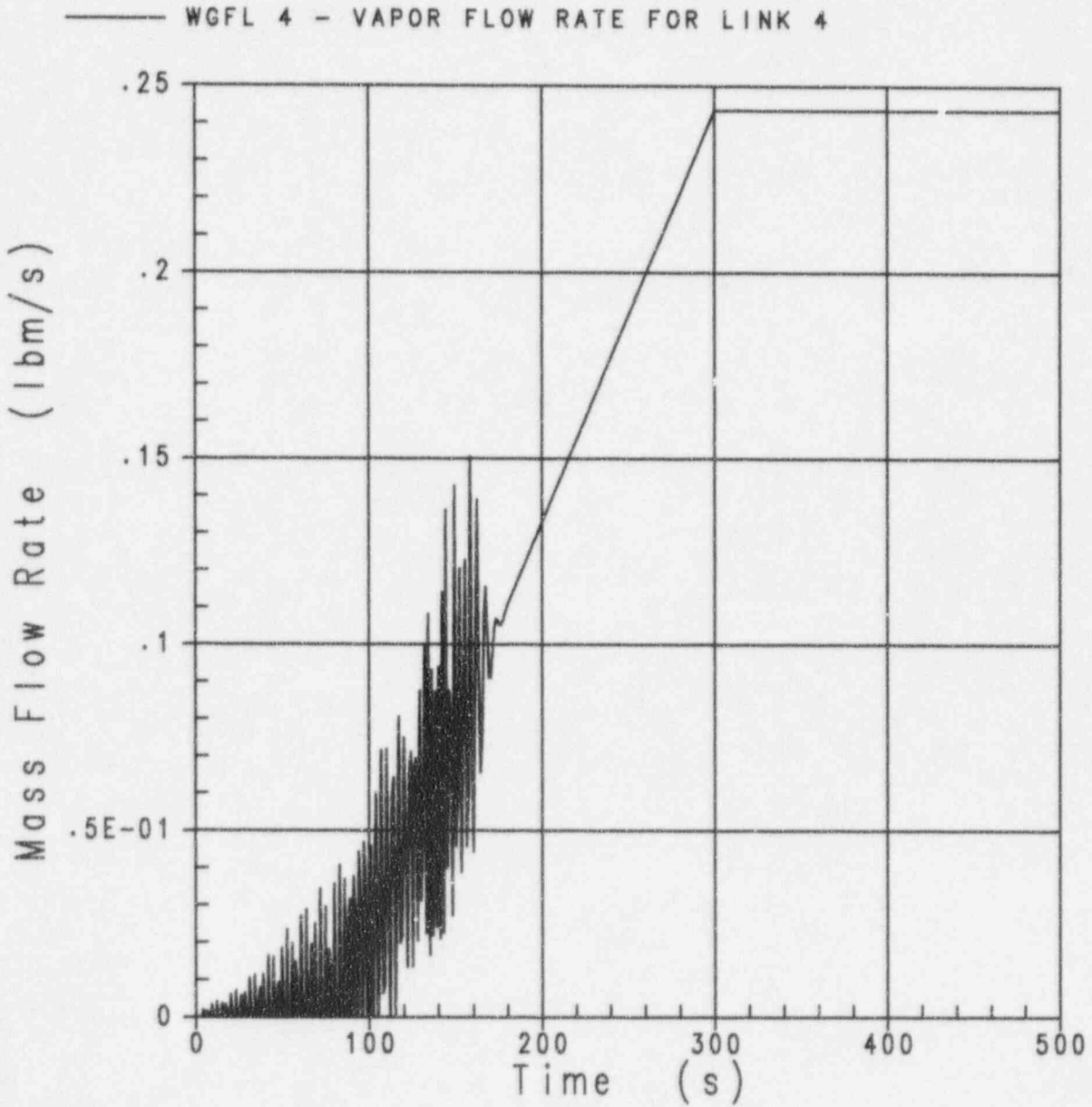


Figure 3.2-7 3-in. Pipe, $W_1 = 0.2937$ lbs/sec., $W_v = 0.2435$ lbs/sec. (20 psia)

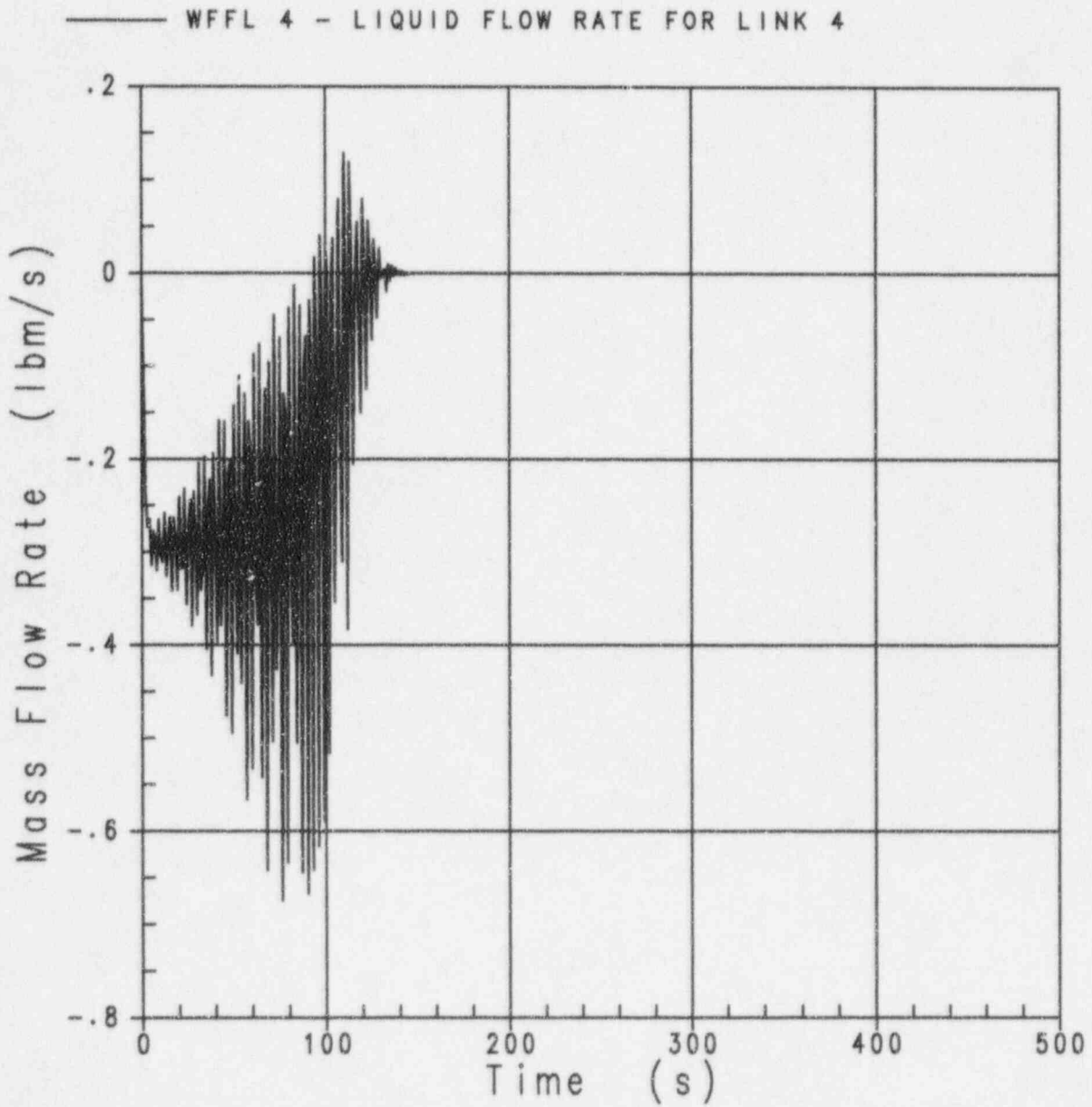


Figure 3.2-8 3-in. Pipe, $W_1 = 0.2937$ lbs/sec., $W_2 = 0.2435$ lbs/sec. (20 psia)

——— VFMFN 1 - NODE 1 MIX REG VOID FRACTION
 - - - - VFMFN 2 - NODE 2 MIX REG VOID FRACTION
 - - - - VFMFN 3 - NODE 3 MIX REG VOID FRACTION
 - - - - VFMFN 4 - NODE 4 MIX REG VOID FRACTION
 - - - - VFMFN 5 - NODE 5 MIX REG VOID FRACTION
 - - - - VFMFN 6 - NODE 6 MIX REG VOID FRACTION

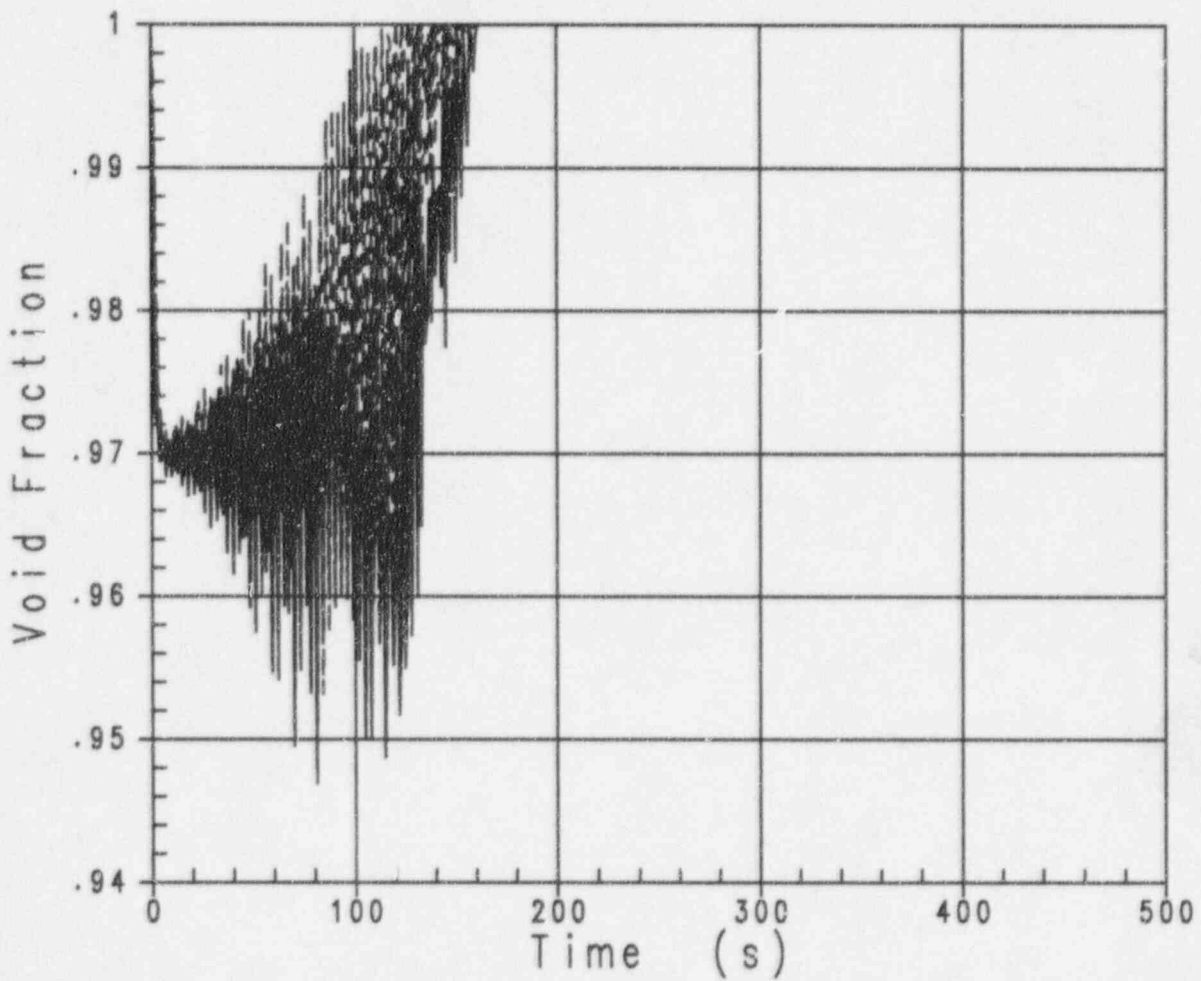


Figure 3.2-9 3-in. Pipe, $W_1 = 0.2937$ lbs/sec., $W_2 = 0.2435$ lbs/sec. (20 psia)

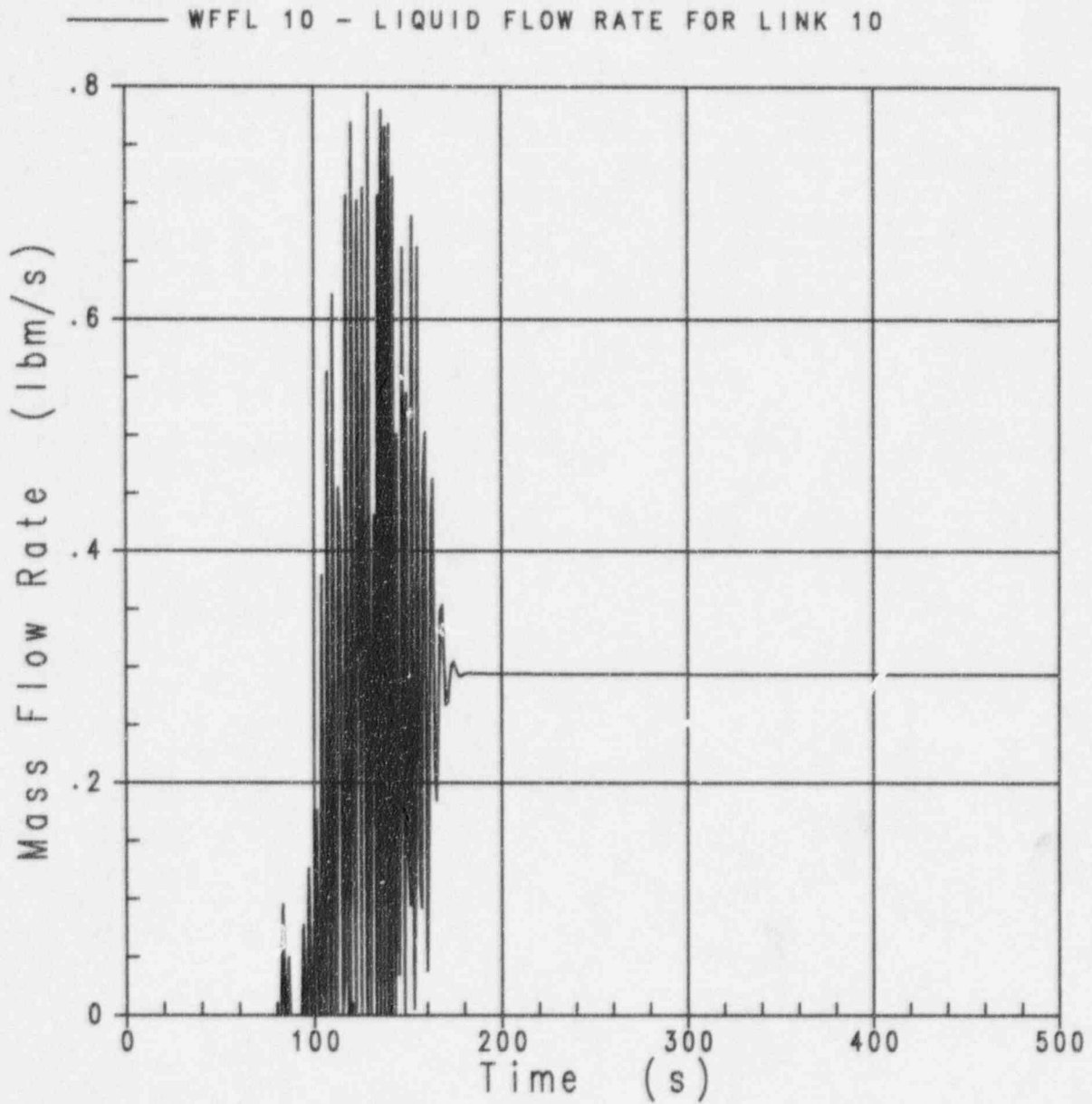


Figure 3.2-10 3-in. Pipe, $W_i = 0.2937$ lbs/sec., $W_v = 0.2435$ lbs/sec. (20 psia)

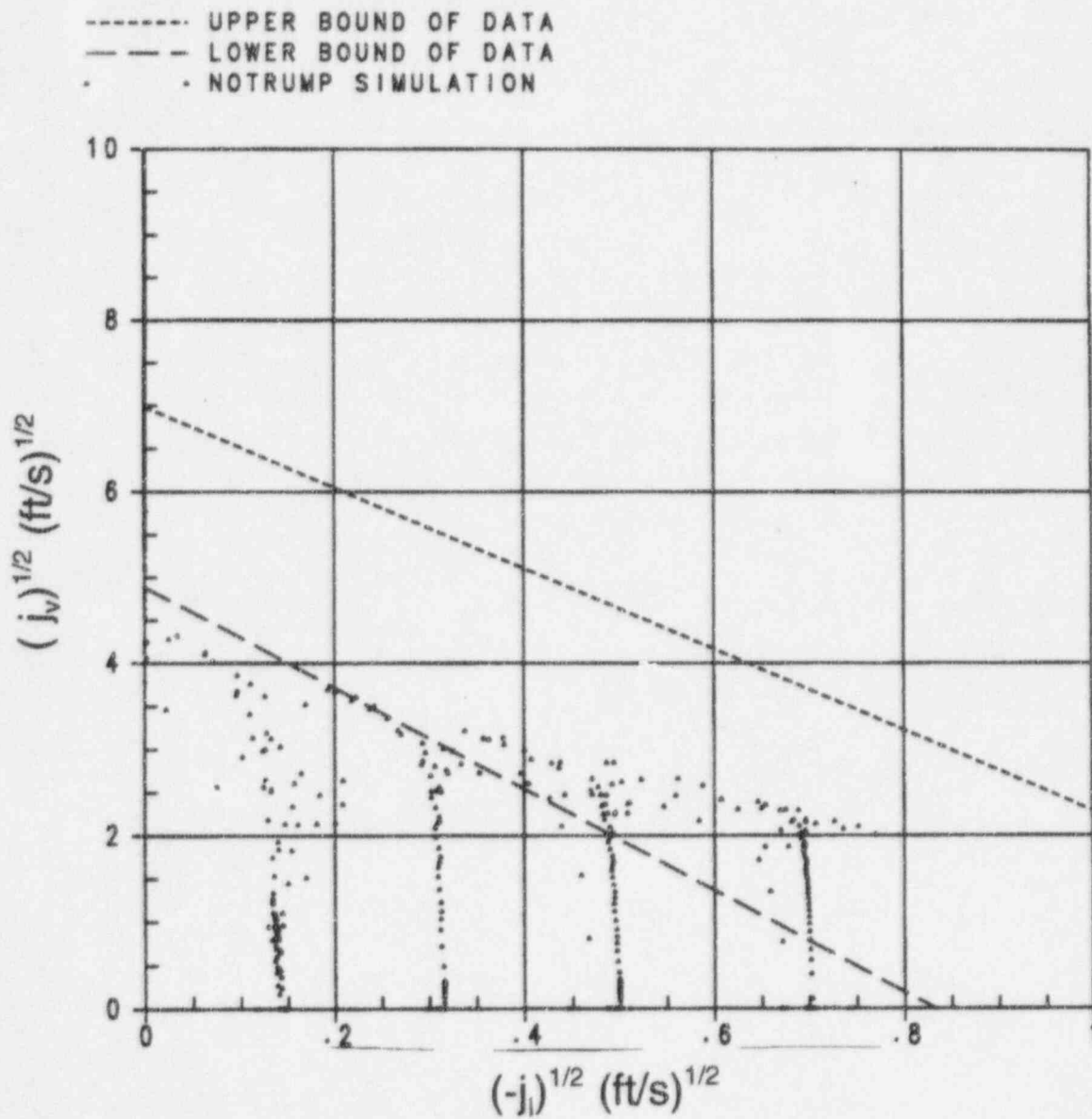


Figure 3.2-11 $j_v^{1/2}$, $j_l^{1/2}$ Predictions Compared with Data Flooding Limits (0.75-in. pipe, 20 psia)

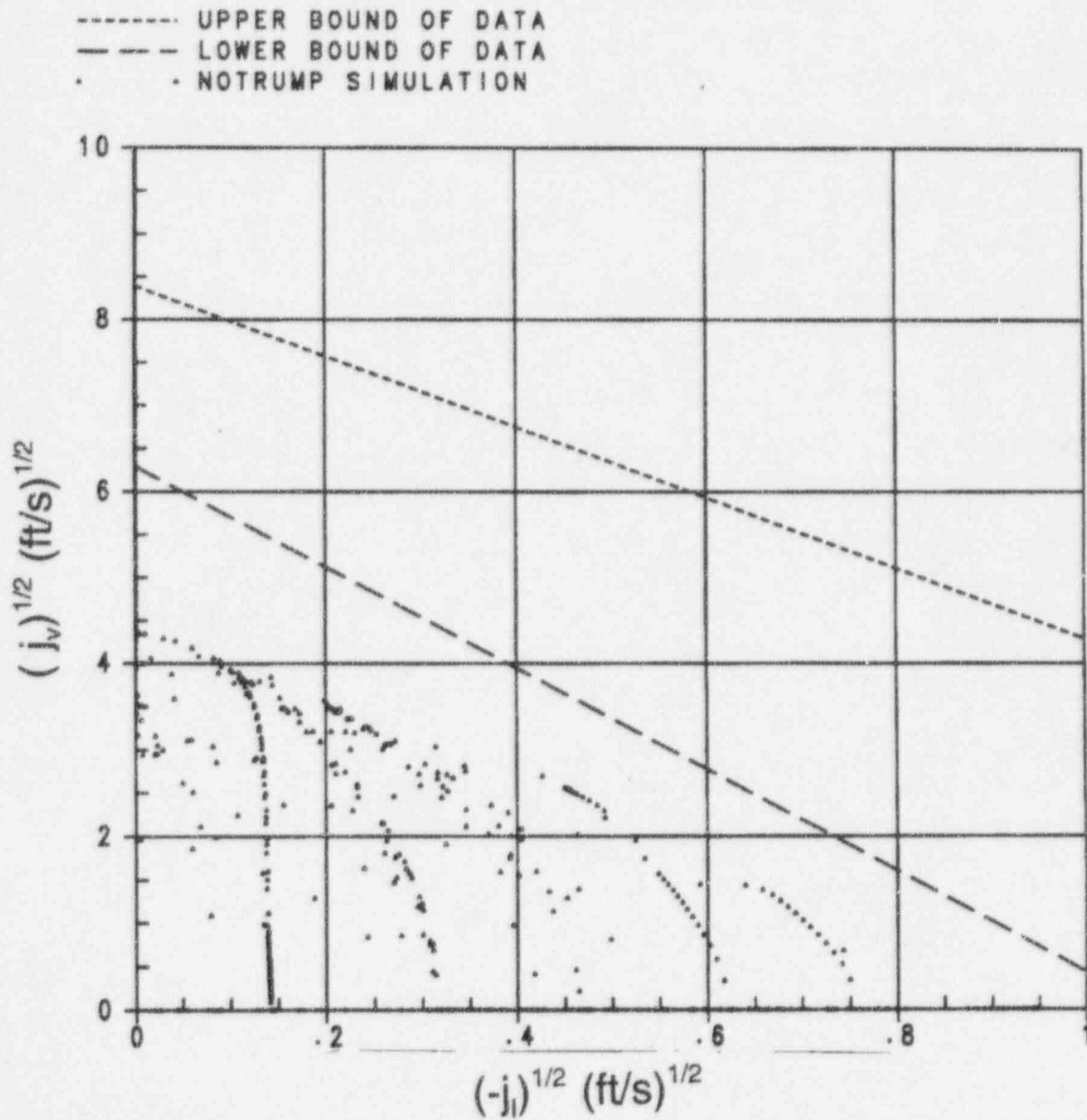


Figure 3.2-12 $j_v^{1/2}$, $j_l^{1/2}$ Predictions Compared with Data Flooding Limits (0.75-in. pipe, 1000 psia)

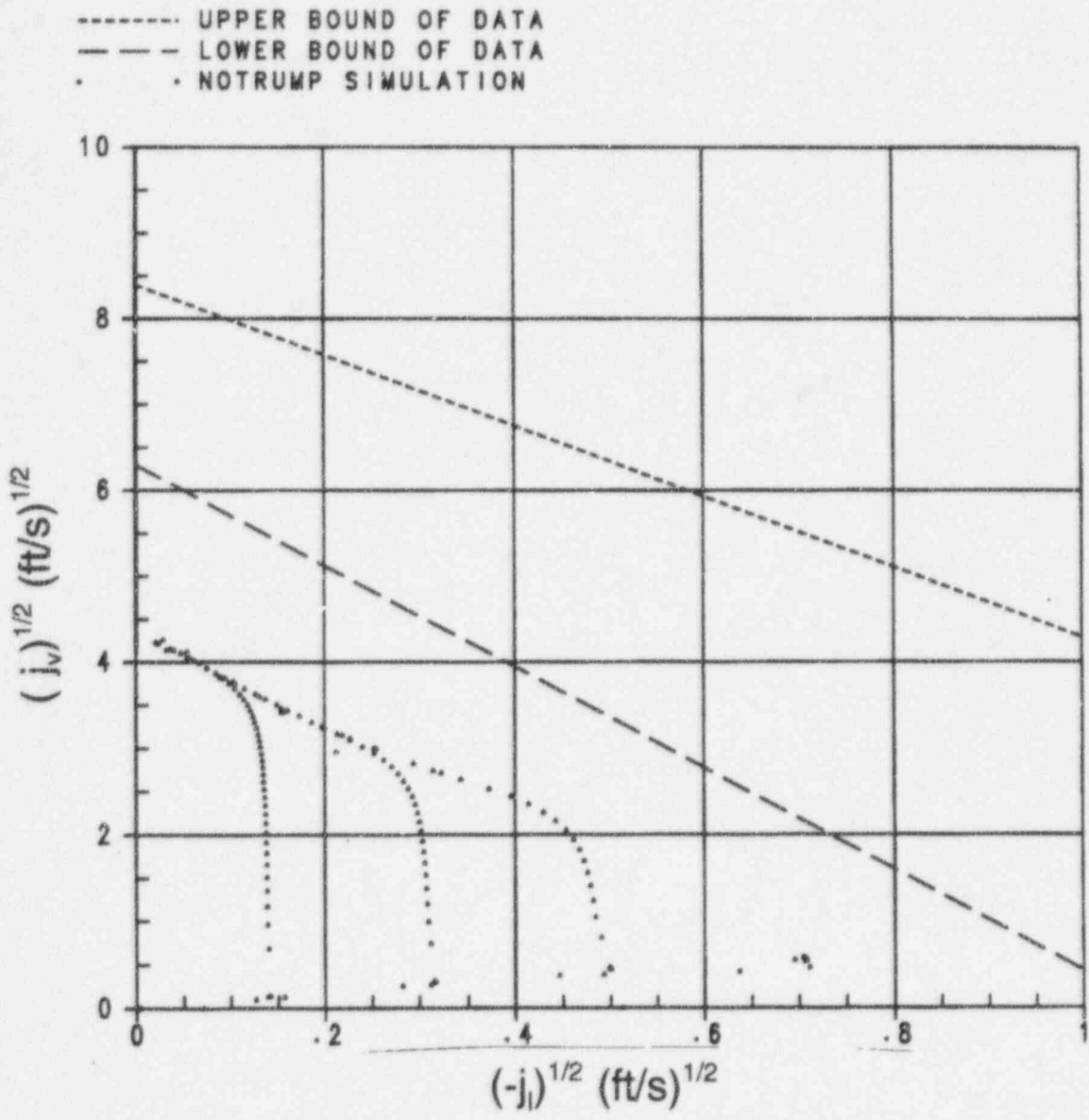


Figure 3.2-13 $j_v^{1/2}$, $j_l^{1/2}$ Predictions Compared with Data Flooding Limits (3-in. pipe, 20 psia)

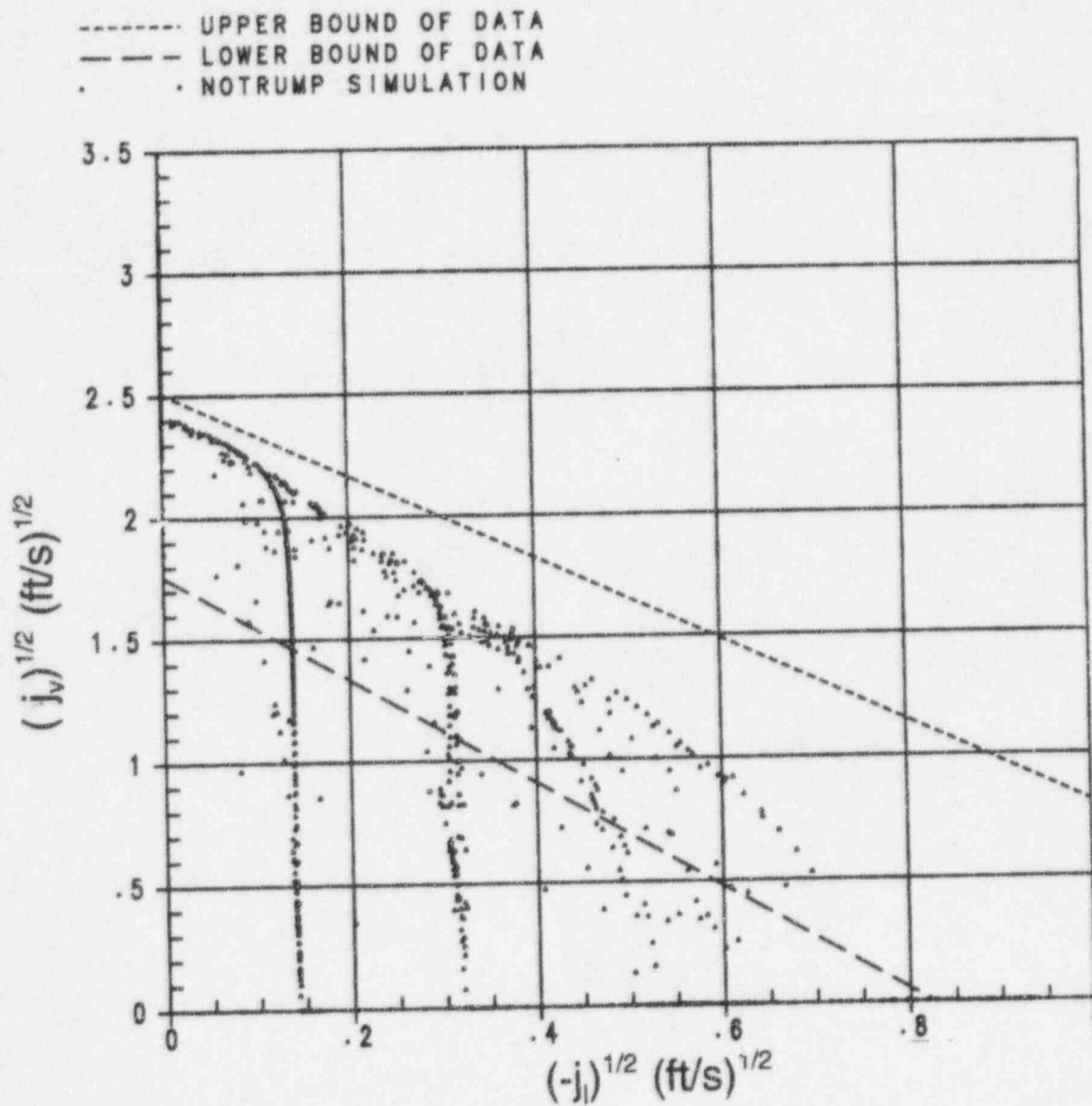


Figure 3.2-14 $j_v^{1/2}$, $j_l^{1/2}$ Predictions Compared with Data Flooding Limits (3-in. pipe, 1000 psia)

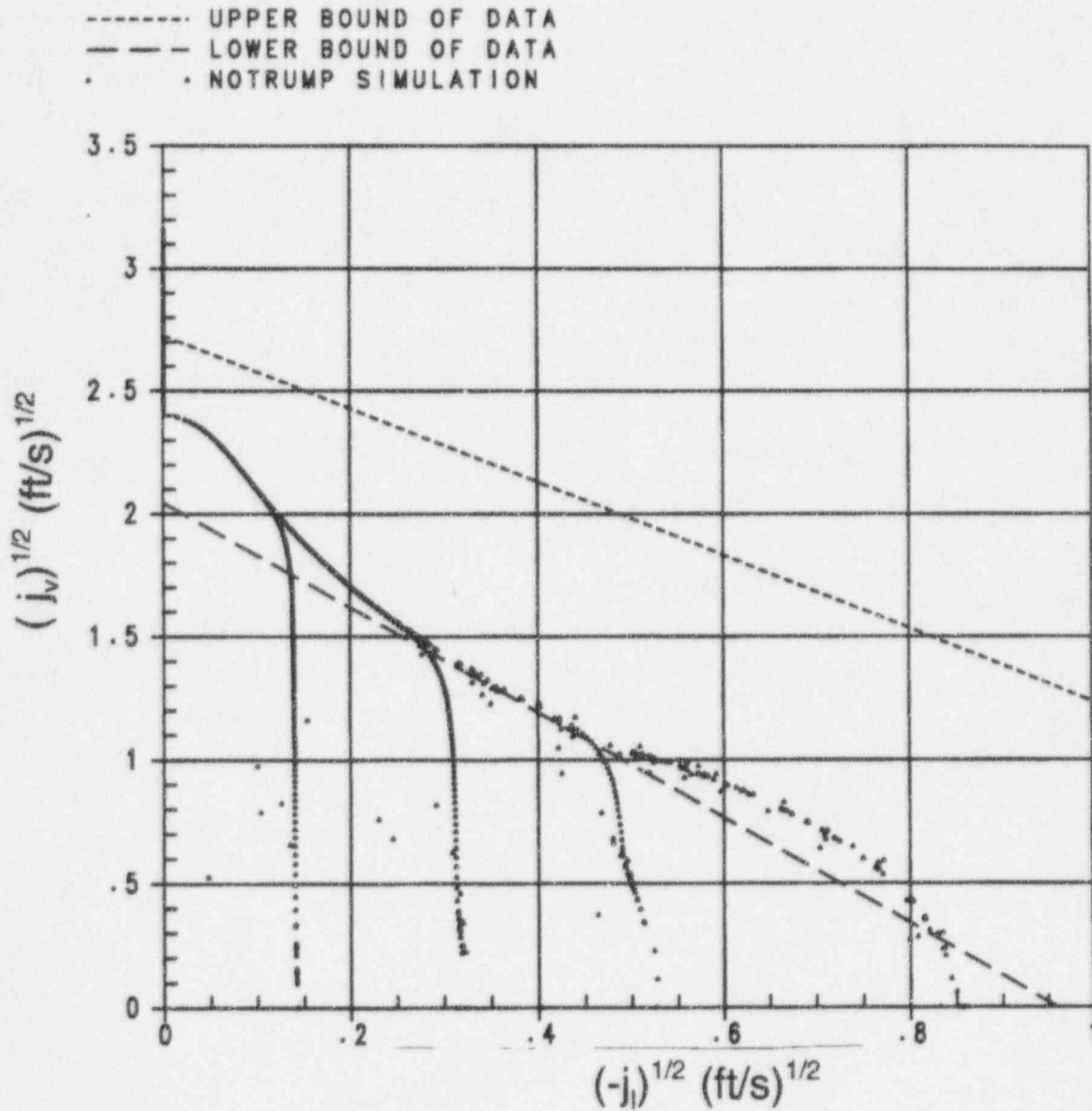


Figure 3.2-15 $j_v^{1/2}, j_l^{1/2}$ Predictions Compared with Data Flooding Limits (2-ft. pipe, 20 psia)

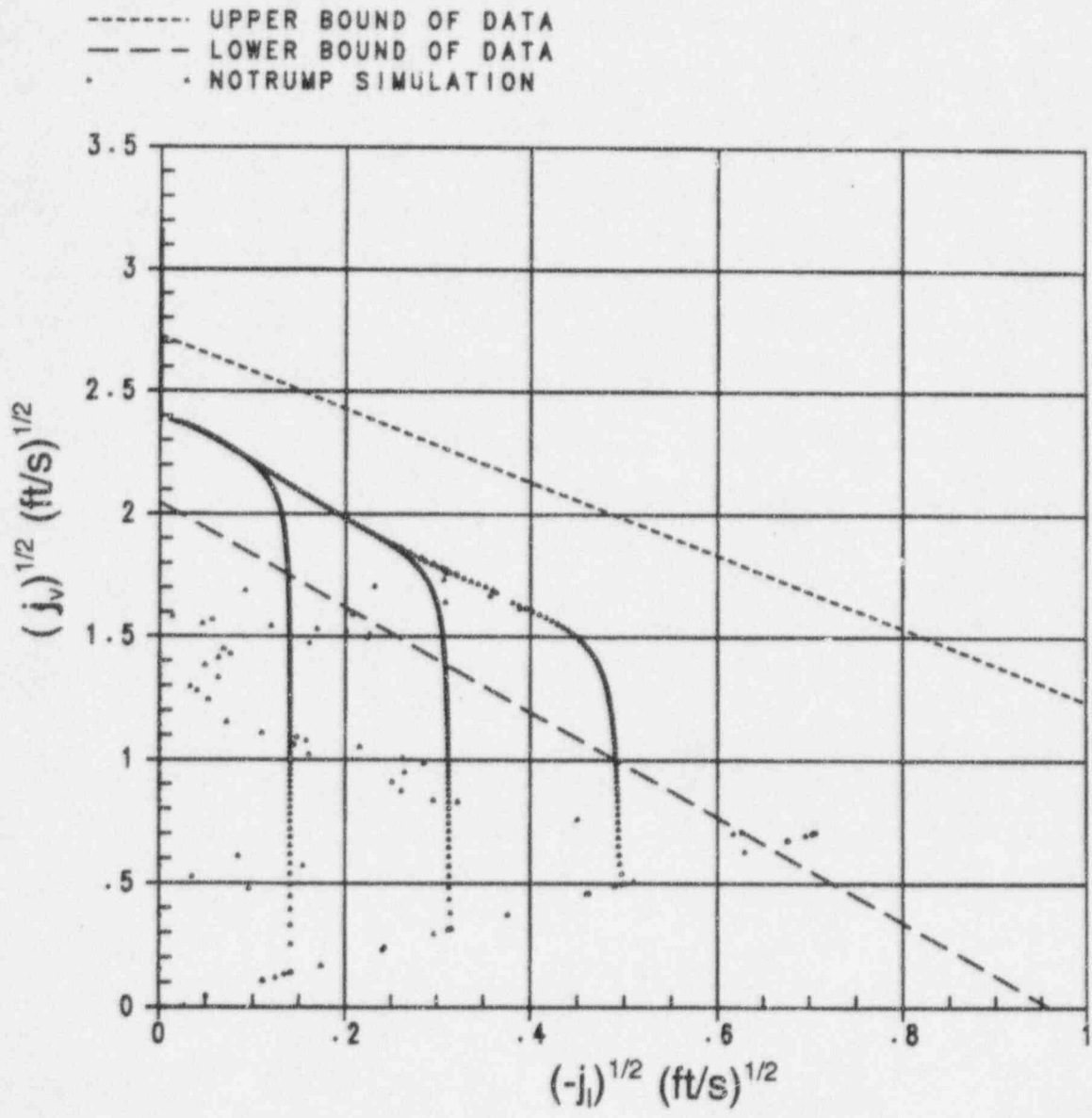


Figure 3.2-16 $j_v^{1/2}, j_l^{1/2}$ Predictions Compared with Data Flooding Limits (2-ft. pipe, 1000 psia)

3.3 Levelizing Drift Flux Model Benchmarking

3.3.1 Introduction

An important flow regime in horizontal channels is the stratified flow regime. Under these conditions, steam can flow countercurrent to the liquid and there is little interaction between the phases. An equally important aspect of these flows is the point at which the stratified flow regime transitions to a slug or bubbly regime. When the transition occurs, the interfacial drag between liquid and vapor increases significantly and the phases are forced to move cocurrently.

The flow regime transition from stratified to slug, or plug, flow was investigated for square channels by Wallis and Dobson [Reference 3.3-1]. They proposed the following criterion:

$$j_v^* = 0.5\alpha^{3/2} \\ = \frac{j_v}{\sqrt{\frac{\Delta\rho g D}{\rho_v}}} \quad (3.3-1)$$

A complete model for transitions in horizontal flow in circular channels was developed by Dukler and Taitel [Reference 3.3-2]. An expression similar to that obtained by Wallis and Dobson [Reference 3.3-1] was developed for the stratified to intermittent boundary, with the constant replaced by a function of the stratified water level.

As pointed out in Reference 3.3-3, the stratified to intermittent boundary defined by the above equation is also equivalent to Wallis's solution to the problem of wave stability in horizontal channel flow [Reference 3.3-4]. This solution defines a region of permissible cocurrent or countercurrent stratified flow in the j_v, j_l plane in which waves on the water surface remain stable. Outside this region, waves become unstable and cause the flow regime to change. Wallis's form of the equation for the wave stability problem is:

$$j_v^{*1/2} + j_l^{*1/2} = 1 \quad (3.3-2)$$

For the Duckler-Taitel flow regime transition, the equation is similar in form, but with different exponents:

$$j_v^{*1/3} + j_l^{*1/3} = 1$$

$$j_v^* = \frac{j_v}{J} = \frac{j_v}{\sqrt{\frac{\Delta\rho g D}{\rho_v}}}$$

$$j_l^* = \frac{\sqrt{\rho_l/\rho_v} j_l}{J} = \frac{j_l}{\sqrt{\frac{\Delta\rho g D}{\rho_l}}} \tag{3.3-3}$$

$$J = \sqrt{\frac{\Delta\rho g D}{\rho_v}}$$

The characteristic velocity is assumed to be a function of the channel diameter, D. In contrast to vertical flow, this relationship is expected to hold at both small and large scales since interfacial disturbances on a horizontal interface are more stable than on a vertical interface due to the additional stabilizing effect of gravity in the horizontal case.

For the Wallis-Dobson transition [Reference 3.3-1], the form is similar but with different constants and exponents:

$$j_v^{*2/3} + j_l^{*2/3} = 0.707 \tag{3.3-4}$$

Equations 3.3-2 to 3.3-4 can be used to represent the stratified flow regime transition boundary. Since Equations 3.3-3 and 3.3-4 more accurately represent the data trends, these are used as benchmarks against which to compare predictions by the NOTRUMP code.

Note that the limits described by the above equations are stability limits, and as such should be viewed as upper limits to the stratified flow regime.

3.3.2 NOTRUMP Horizontal Stratified Model and Flow Transition

NOTRUMP uses []^{ac} to calculate []^{ac} The constitutive model is []^{ac} The constitutive relationship expressed by this []^{ac}

[]^{a,c}

In a horizontal pipe such as a PWR hot leg, the NOTRUMP levelizing model allows countercurrent flow of steam and water. An important test of this model is whether the transition from countercurrent to cocurrent flow is adequately predicted. This transition is equivalent to the flow regime transition from stratified to intermittent or plug flow in a horizontal pipe. A similar test was performed on the WCOBRA/TRAC two-fluid model, as described in Reference 3.3-3. To test this capability in NOTRUMP, a calculational test similar to that performed in Reference 3.3-3 was carried out.

3.3.3 NOTRUMP Horizontal Pipe Model

[]^{a,c}

can flow into node 10 through flowlink 10. Water is injected at constant flow at the location indicated near the left end. Shortly after a steady state is reached (100 sec.), increasing vapor flow is injected at the right end via flowlink 30, reaching a maximum value at 1000 sec. Table 3.3-1 lists the cases calculated. The calculations were performed at two pressures, 1000 and 20 psia.

3.3.4 NOTRUMP Horizontal Flow Results; Leveling Drift Flux

A typical calculation (20 psia, liquid flow = 10 lb/sec.) is shown in Figures 3.3-2 to 3.3-6 for the model shown in Figure 3.3-1. Figure 3.3-2 shows the vapor flow rate at flowlink 3 in the middle of the pipe. Prior to 20 sec. and shortly after, the vapor velocity is low, and liquid flows unimpeded towards the pipe exit and catch tank (see Figure 3.3-3). Figure 3.3-4 shows the liquid flow through flowlink 10, which at this early stage is zero. Figure 3.3-5 shows the liquid level as a function of time in each node, and Figure 3.3-6 shows the level as a function of distance along the pipe for three different times. During the early period (< 100 sec.), the liquid surface is nearly uniform, with a slightly higher level near the dam providing the driving force for flow. The level profile agrees well with the value calculated from a simple weir flow solution (see page 368 of Reference 3.3-5), also shown in Figure 3.3-6.

As the countercurrent flow of vapor continues to increase, the liquid flow in the pipe slows down and eventually reverses (see Figure 3.3-3). The liquid levels increase as liquid flow out of the pipe becomes smaller than liquid flow into the pipe (see Figure 3.3-5). At about 900 sec., the liquid level at the left end of the pipe exceeds the dam height and water begins to flow over the dam (see Figure 3.3-4). Since the vapor flow continues to increase, the pipe continues to empty and levels drop. After the vapor flow reaches a steady-state value at 1000 sec., the pipe levels reach a steady-state value. At the end of the run, the water surface is zero at the pipe outlet and gradually increases to the level of the dam.

Figures 3.3-7 to 3.3-11 show similar plots for a case where the liquid flow is 150 lb/sec. The results are similar in nature to the low flow results.

Figures 3.3-12 to 3.3-16 show results for a case at 1000 psia. The behavior is again similar to the previous cases.

The calculated values of $j_v^{1/2}$ and $j_l^{1/2}$ every second for flowlink 4 are arranged in pairs. All pairs in countercurrent flow are then saved, and the resulting pairs are plotted as points, as shown in Figures 3.3-17 and 3.3-18, along with the data boundaries described by Equations 3.3-3 and 3.3-4. Each "curve" is actually a family of points denoting $j_v^{1/2}$, $j_l^{1/2}$ pairs at different time increments. As time increases from zero, points move in the lower straight line to the right. At the early portion of the transient, the injected steam flow is zero, but volume replacement in the catch tank causes some steam flow in the pipe, hence the increasing vapor flow. As the injected steam flow increases, the liquid flow is initially unaffected (wavy vertical line). As the flooding curve is approached, the liquid flow reduces and the curve moves to the left until the liquid flow goes to zero. The short straight line denotes the period shortly after the vapor flow becomes constant at 1000 sec. when the liquid flow is oscillating.

It can be seen that the flow reversal point (ie, the vapor flow rate at which the water flow rate is no longer countercurrent) predicted by NOTRUMP occurs at a lower vapor flow than indicated by the data.

3.3.5 Conclusion

The levelizing drift flux model used in NOTRUMP is benchmarked using simple calculational tests and compared with well-known flow regime transition models. The NOTRUMP model predicts that countercurrent flow will occur well within the limits allowed by interfacial wave stability. Variations in input flow conditions result in expected behavior over a wide pressure range. Noding variations have little effect on results. This model is therefore considered adequate to predict stratified flow conditions in horizontal pipes.

3.3.6 References

- 3.3-1 Dobson, J. E. and G. B. Wallis, "The Onset of Slugging in Horizontal Stratified Air-Water Flow," *International Journal of Multiphase Flow*, Vol. 1, pp 173-193 (1973).
- 3.3-2 Dukler, A. E. and Y. Taitel, "A Model for Predicting Flow Regime Transitions in Horizontal and Near Horizontal Gas-Liquid Flow," *AIChE Journal*, Vol. 22, No. 1 (January 1976).
- 3.3-3 Bajorek, S. M., et. al, "Westinghouse Code Qualification Document for Best-Estimate Loss-of-Coolant Accident Analysis," WCAP 12945-P, Volume 3, Section 15-1-4-1.
- 3.3-4 Wallis, G. B., *One Dimensional Two Phase Flow*, Mc Graw-Hill (1969).
- 3.3-5 Vernard, J. K., *Elementary Fluid Mechanics*, 4th Edition, John Wiley & Sons (1961).

**TABLE 3.3-1
HORIZONTAL COUNTERCURRENT FLOW LIMIT MODEL
(LEVELIZING) CASES ANALYZED**

Pressure (psia)	Case	Liquid Flow Rate, W_L (lbm/sec.)	Vapor Flow Rate, W_v (lbm/sec.)
20	1	10	0 - 40
	2	50	
	3	150	
1000	1	10	0 - 400
	2	50	
	3	150	

NOTE: Liquid was injected at the following rate:
0.0 - 50.0 sec.----- 0.0 - full flow rate
50.0 sec. - end of transient ----- full flow rate

Vapor was injected at the following rate:
0.0 - 100.0 sec.----- 0.0
100.0 - 1000.0 sec.----- 0.0 - full flow rate
1000.0 sec. - end of transient -- full flow rate

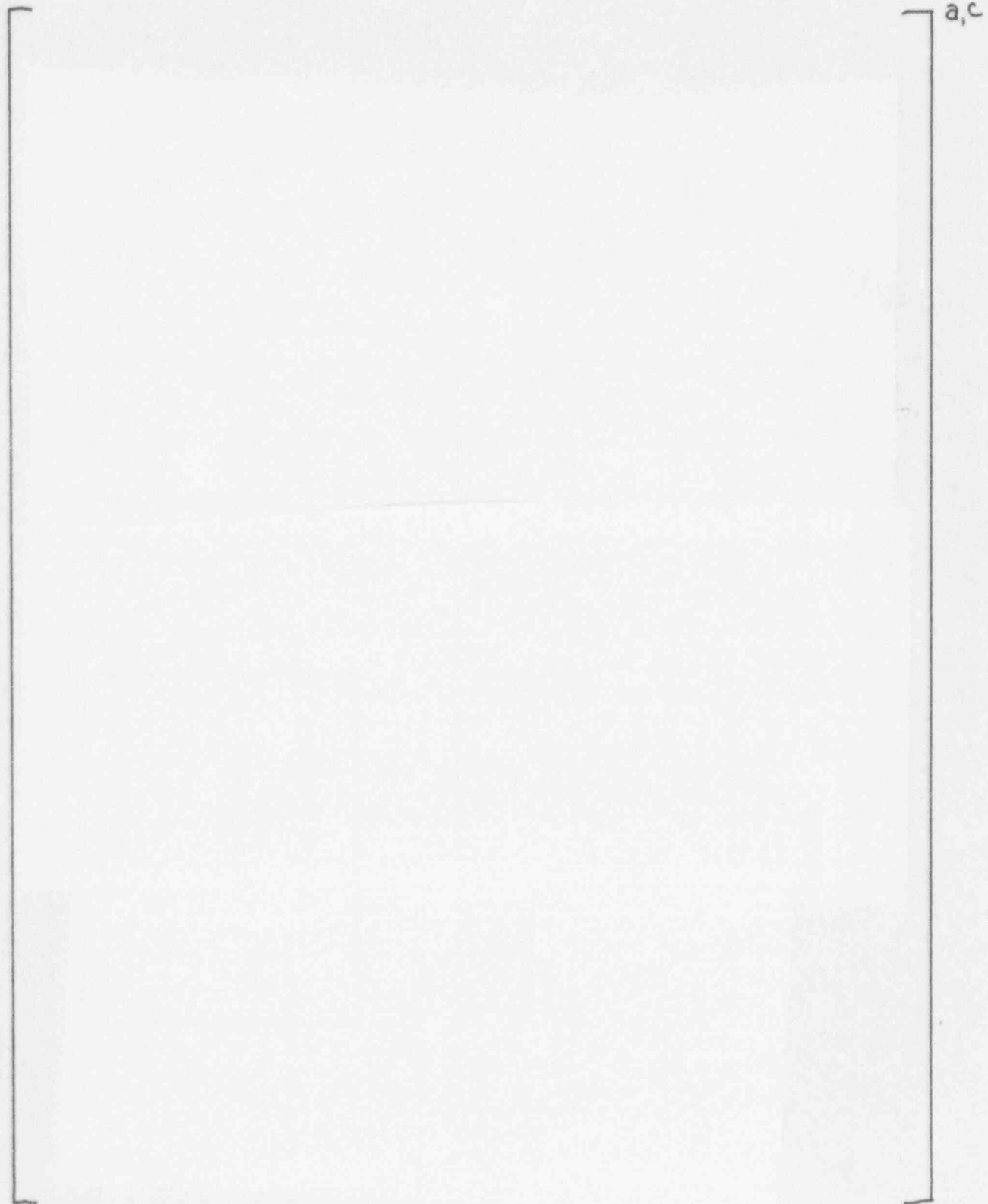


Figure 3.3-1 NOTRUMP Model for Horizontal Pipe

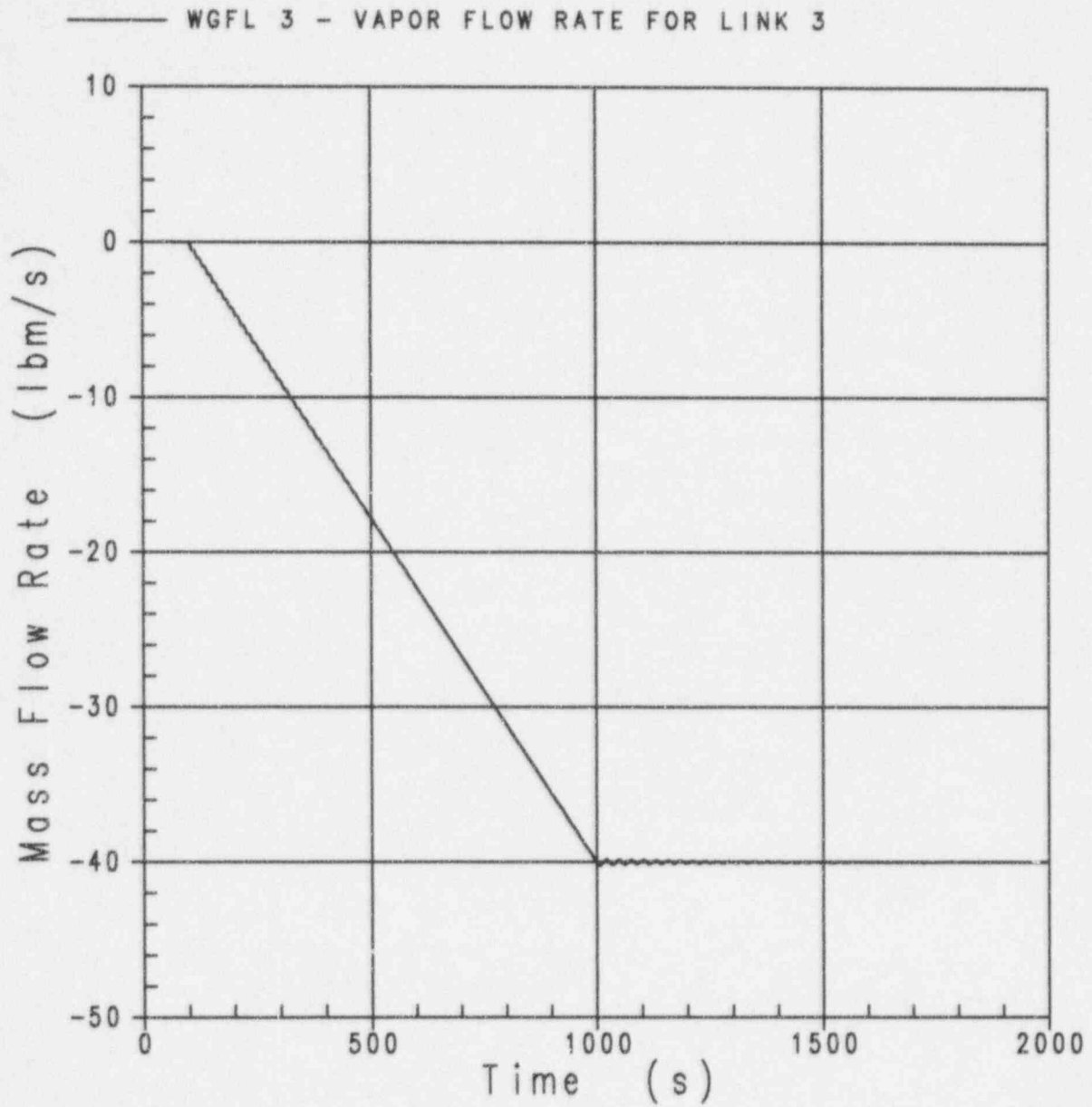


Figure 3.3-2 20 psia, $W_1 = 10$ lbs/sec., $W_2 = 40$ lbs/sec.

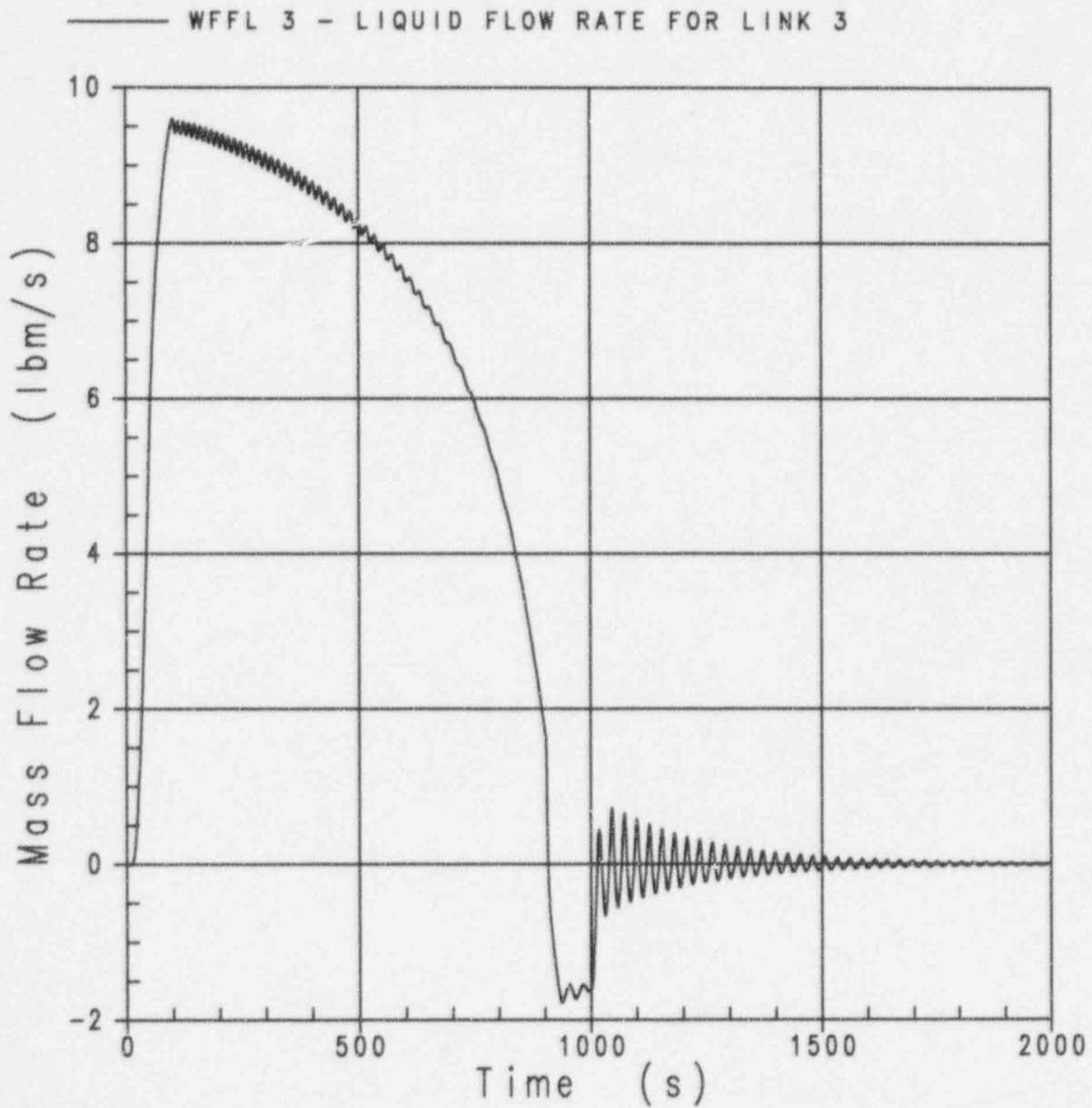


Figure 3.3-3 20 psia, $W_1 = 10$ lbs/sec., $W_2 = 40$ lbs/sec.

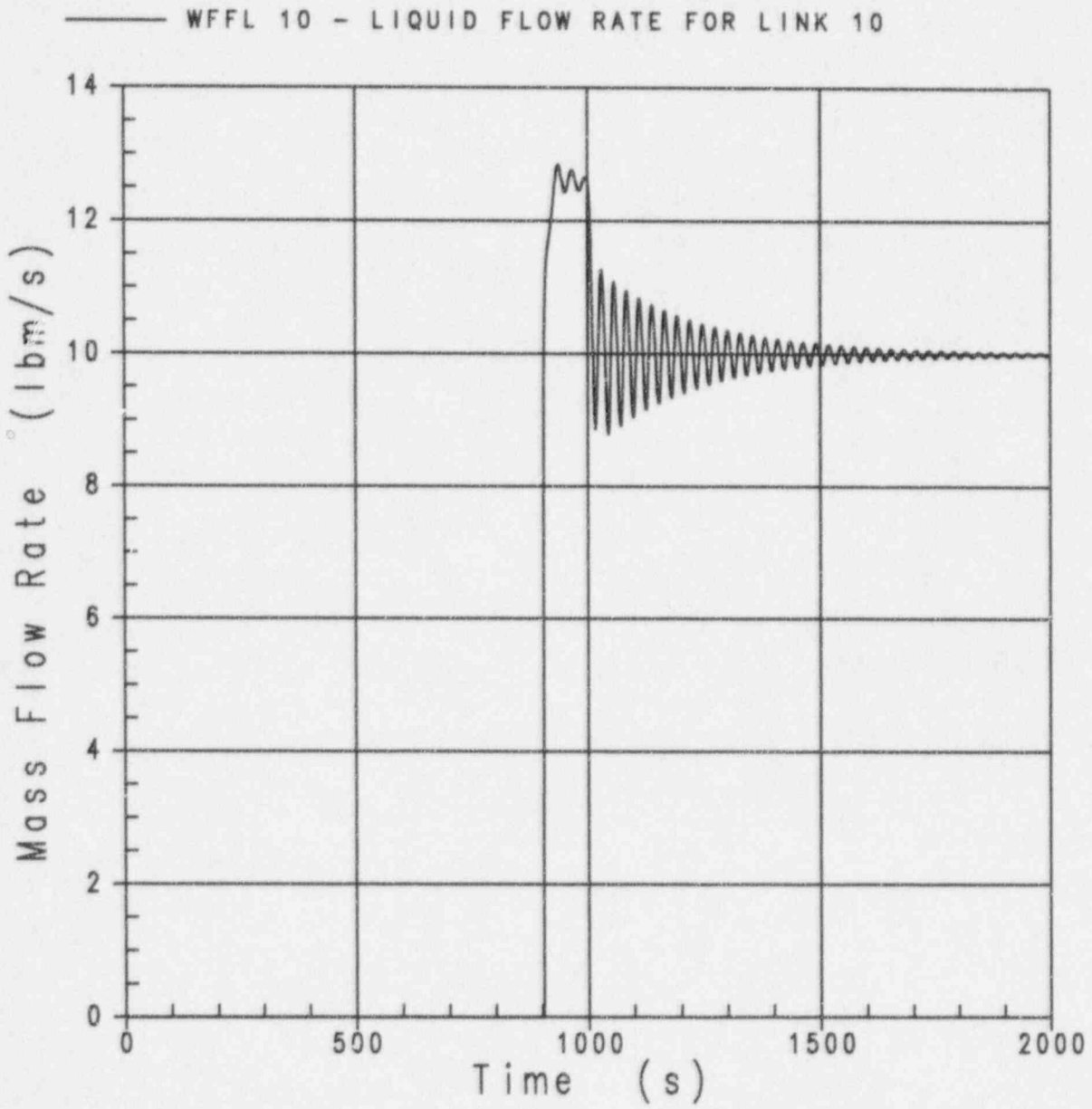


Figure 3.3-4 20 psia, $W_1 = 10$ lbs/sec., $W_v = 40$ lbs/sec.

——— EMIXFN 1 - NODE 1 MIXTURE ELEVATION
 - - - - EMIXFN 2 - NODE 2 MIXTURE ELEVATION
 - - - - EMIXFN 3 - NODE 3 MIXTURE ELEVATION
 - - - - EMIXFN 4 - NODE 4 MIXTURE ELEVATION
 - - - - EMIXFN 5 - NODE 5 MIXTURE ELEVATION
 - - - - EMIXFN 6 - NODE 6 MIXTURE ELEVATION

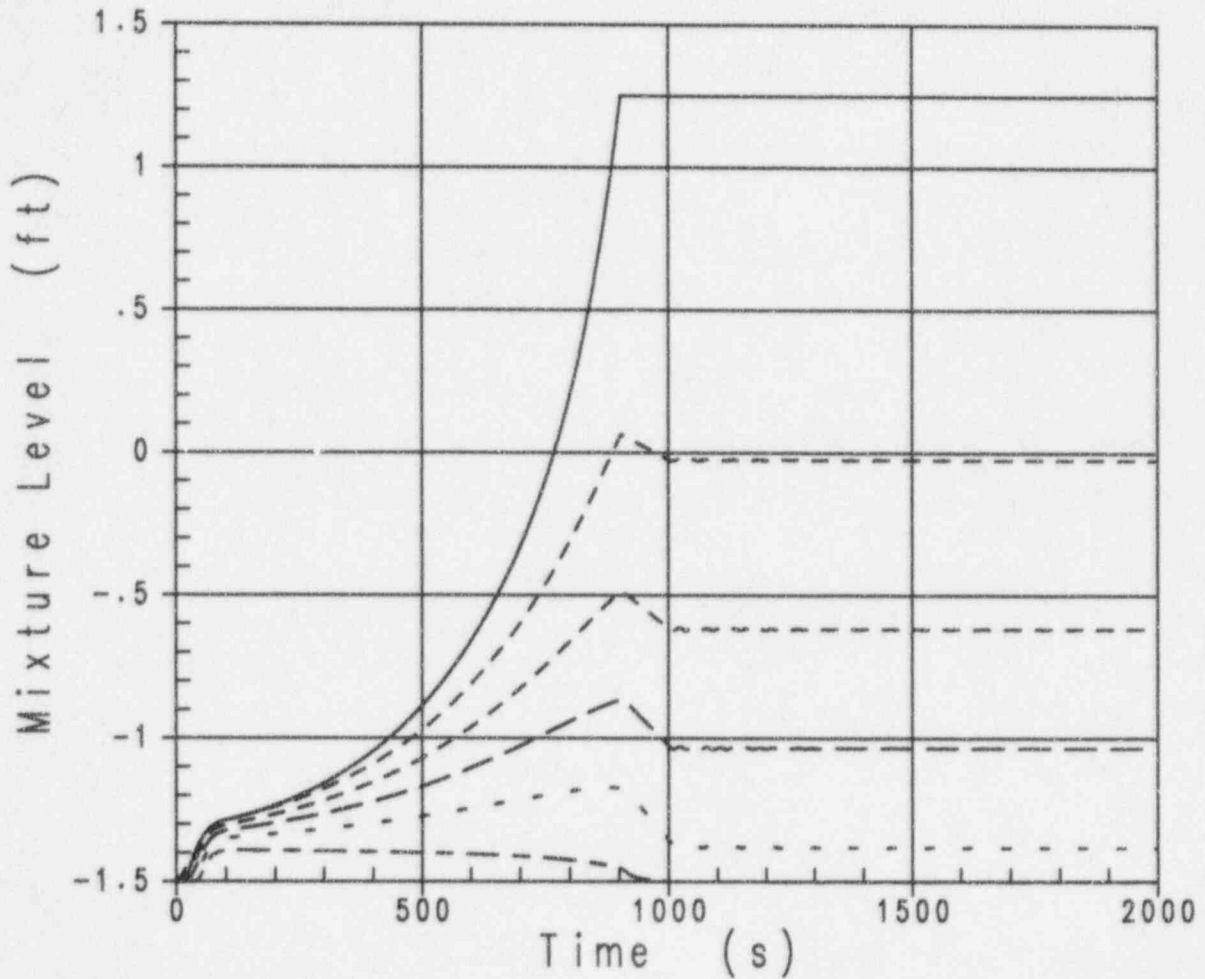


Figure 3.3-5 20 psia, $W_1 = 10$ lbs/sec., $W_v = 40$ lbs/sec.

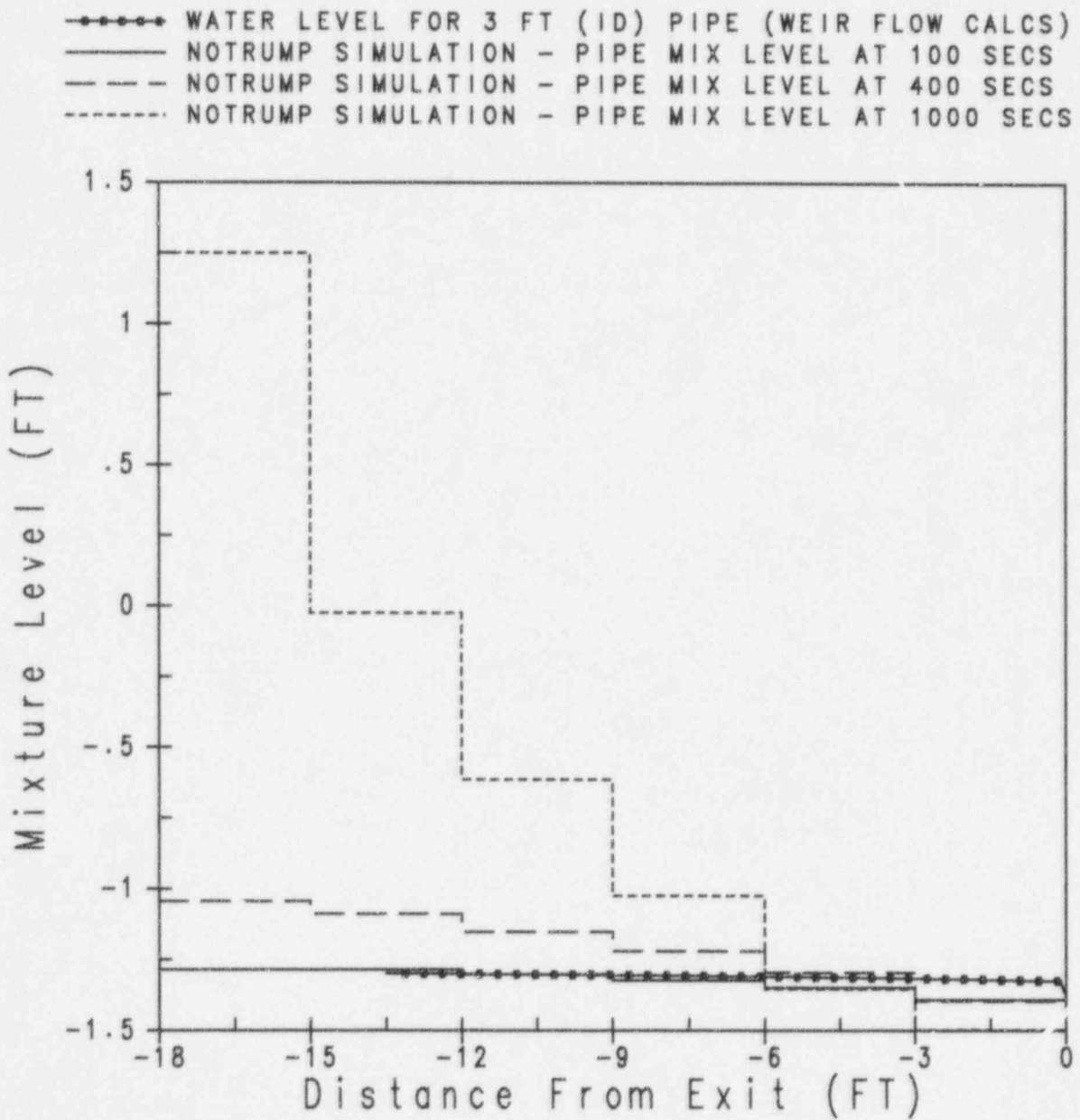


Figure 3.3-6 20 psia, $W_1 = 10$ lbs/sec., $W_v = 40$ lbs/sec.

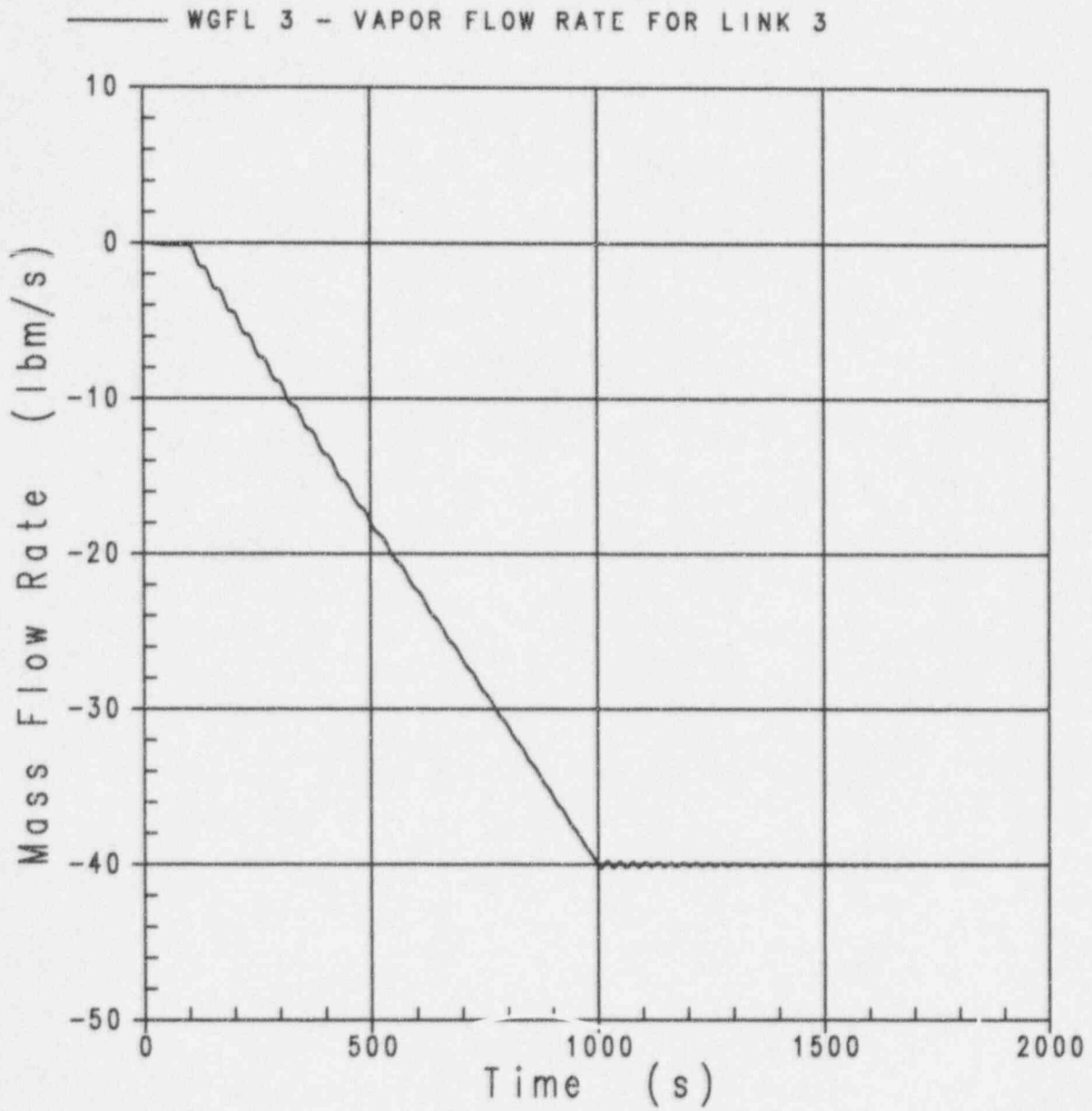


Figure 3.3-7 20 psia, $W_1 = 150$ lbs/sec., $W_2 = 40$ lbs/sec.

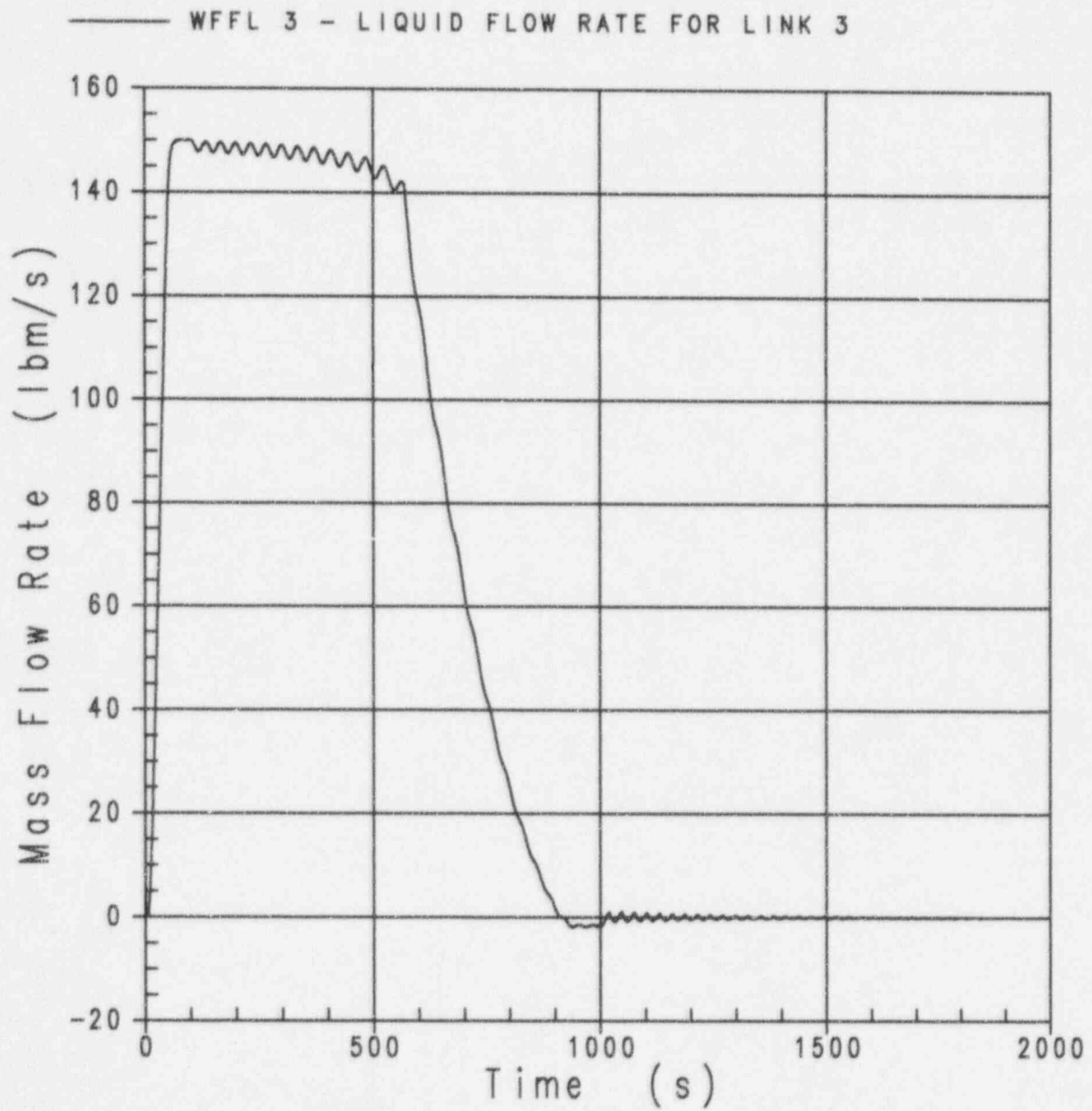


Figure 3.3-8 20 psia, $W_1 = 150$ lbs/sec., $W_2 = 40$ lbs/sec.

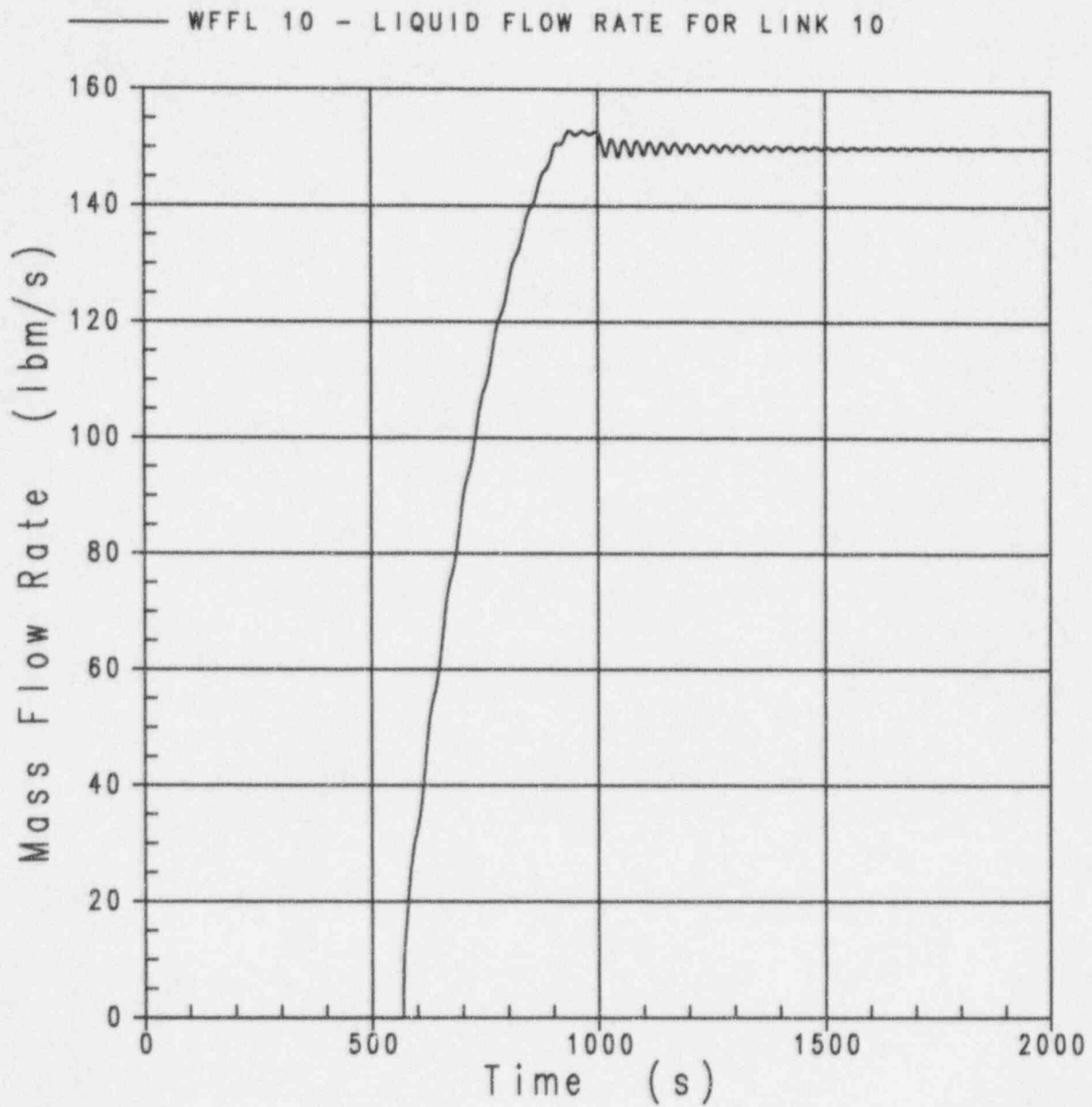


Figure 3.3-9 20 psia, $W_1 = 150$ lbs/sec., $W_2 = 40$ lbs/sec.

——— EMIXFN 1 - NODE 1 MIXTURE ELEVATION
 - - - - EMIXFN 2 - NODE 2 MIXTURE ELEVATION
 - - - - EMIXFN 3 - NODE 3 MIXTURE ELEVATION
 - - - - EMIXFN 4 - NODE 4 MIXTURE ELEVATION
 - - - - EMIXFN 5 - NODE 5 MIXTURE ELEVATION
 - - - - EMIXFN 6 - NODE 6 MIXTURE ELEVATION

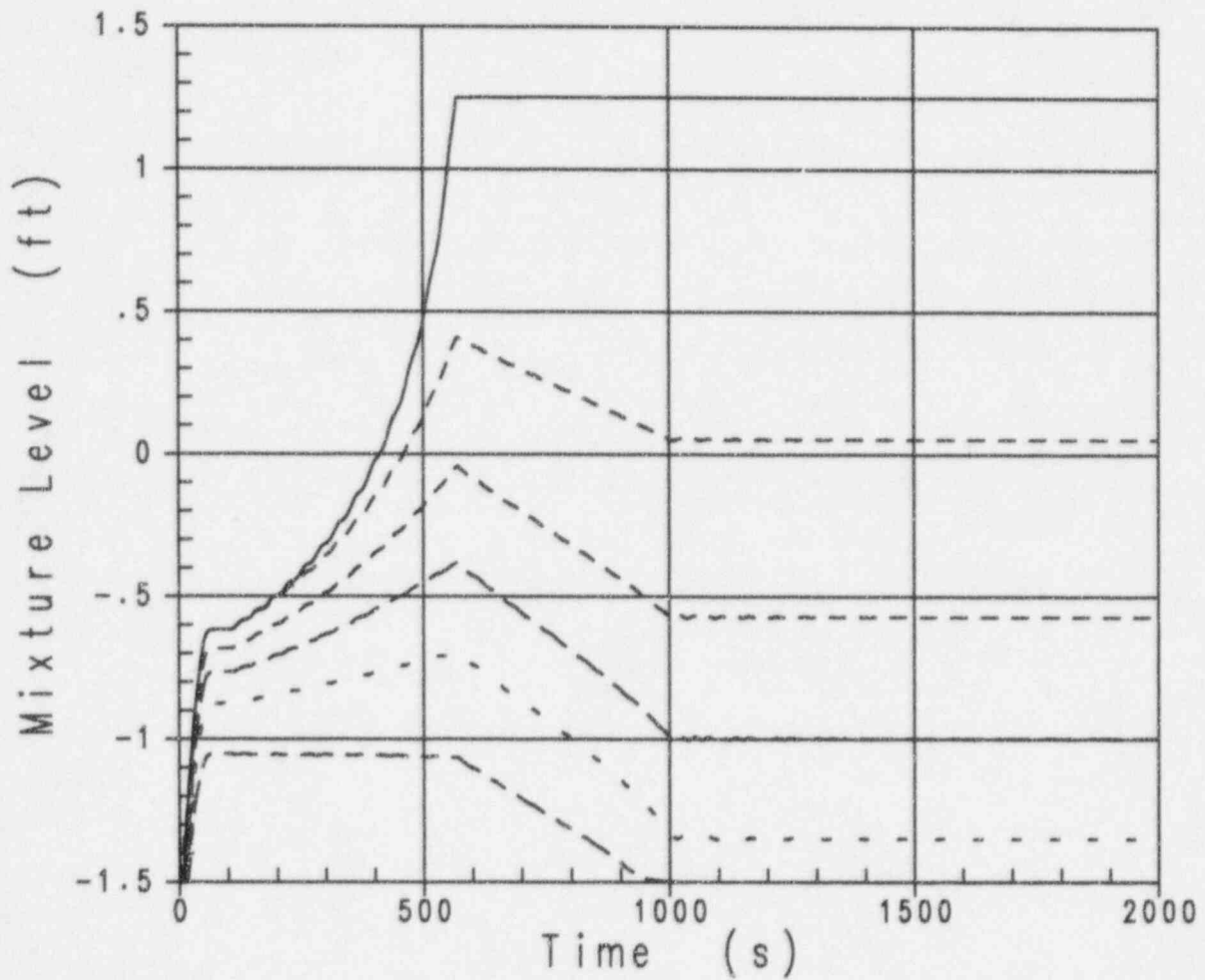


Figure 3.3-10 20 psia, $W_1 = 150$ lbs/sec., $W_v = 40$ lbs/sec.

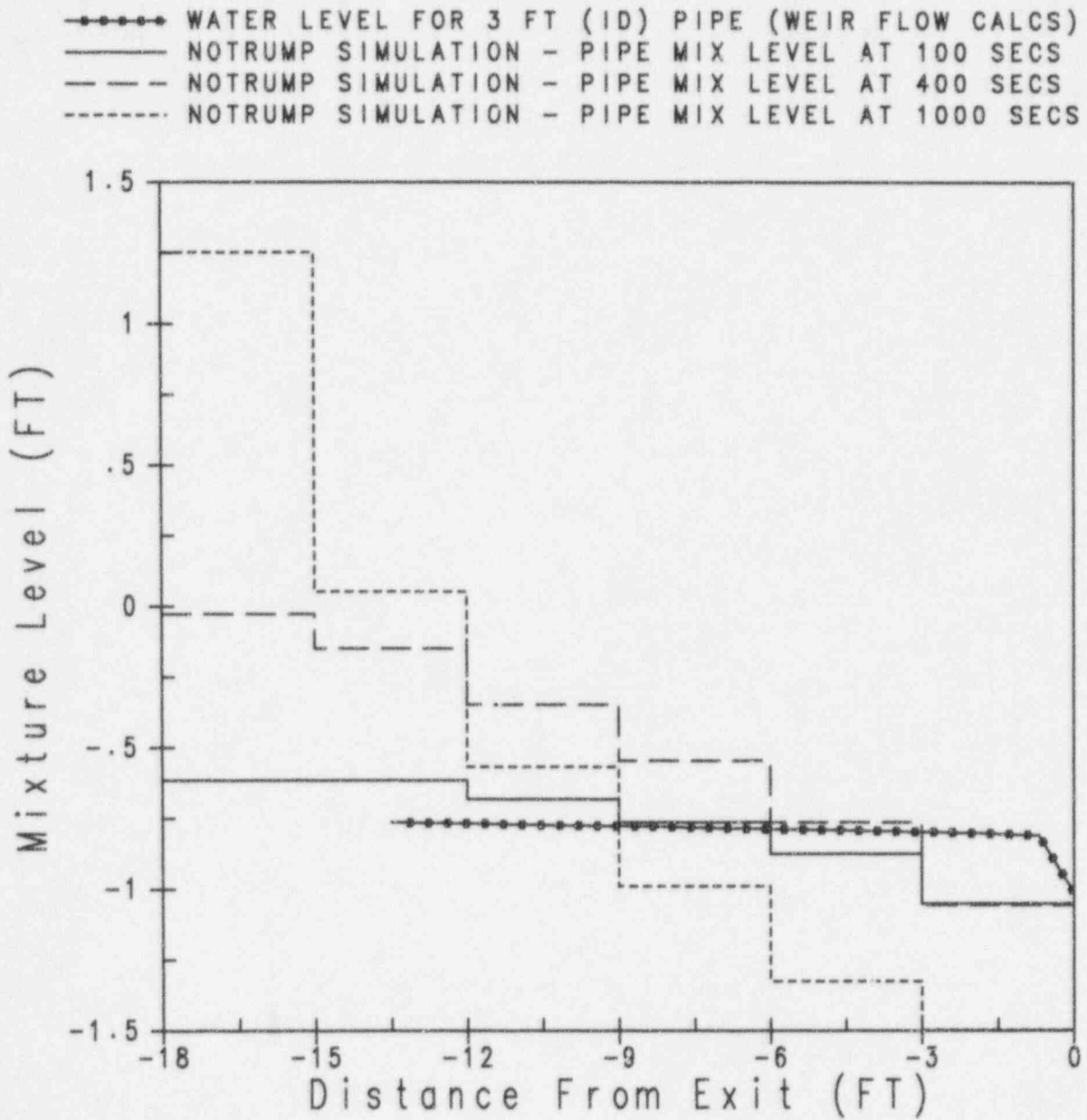


Figure 3.3-11 20 psia, $W_1 = 150$ lbs/sec., $W_2 = 40$ lbs/sec.

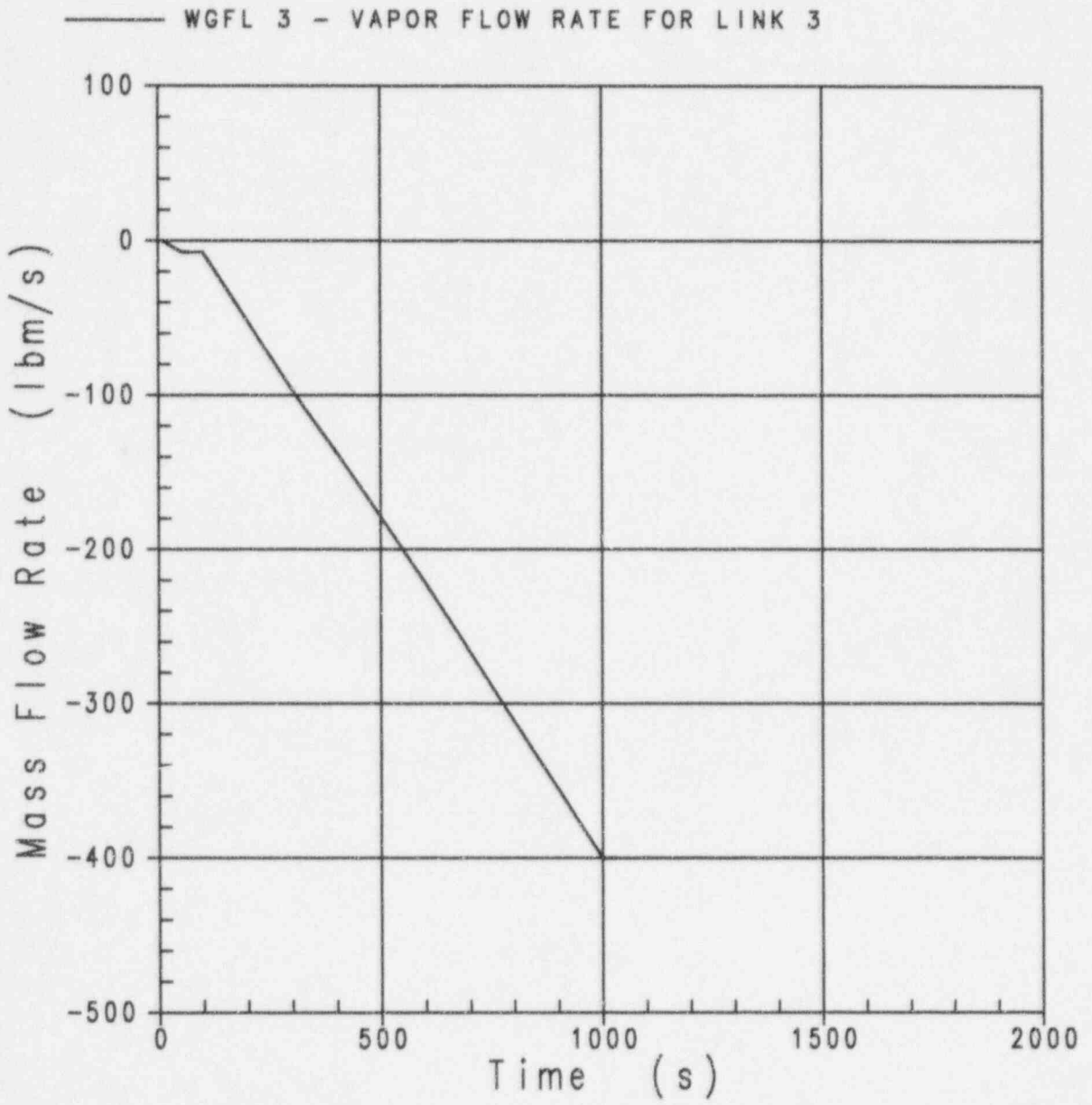


Figure 3.3-12 1000 psia, $W_i = 150$ lbs/sec., $W_v = 400$ lbs/sec

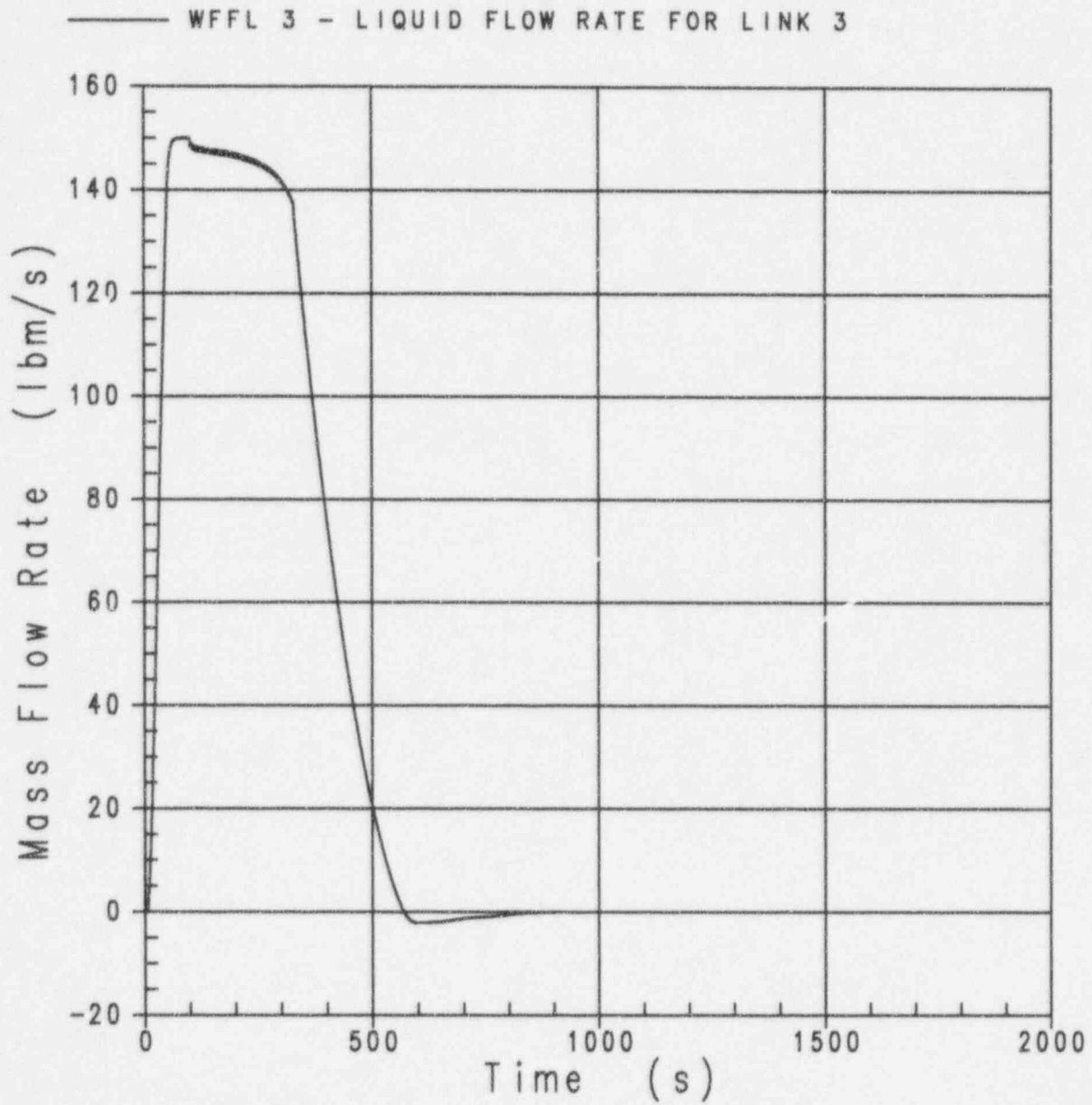


Figure 3.3-13 1000 psia, $W_1 = 150$ lbs/sec., $W_2 = 400$ lbs/sec.

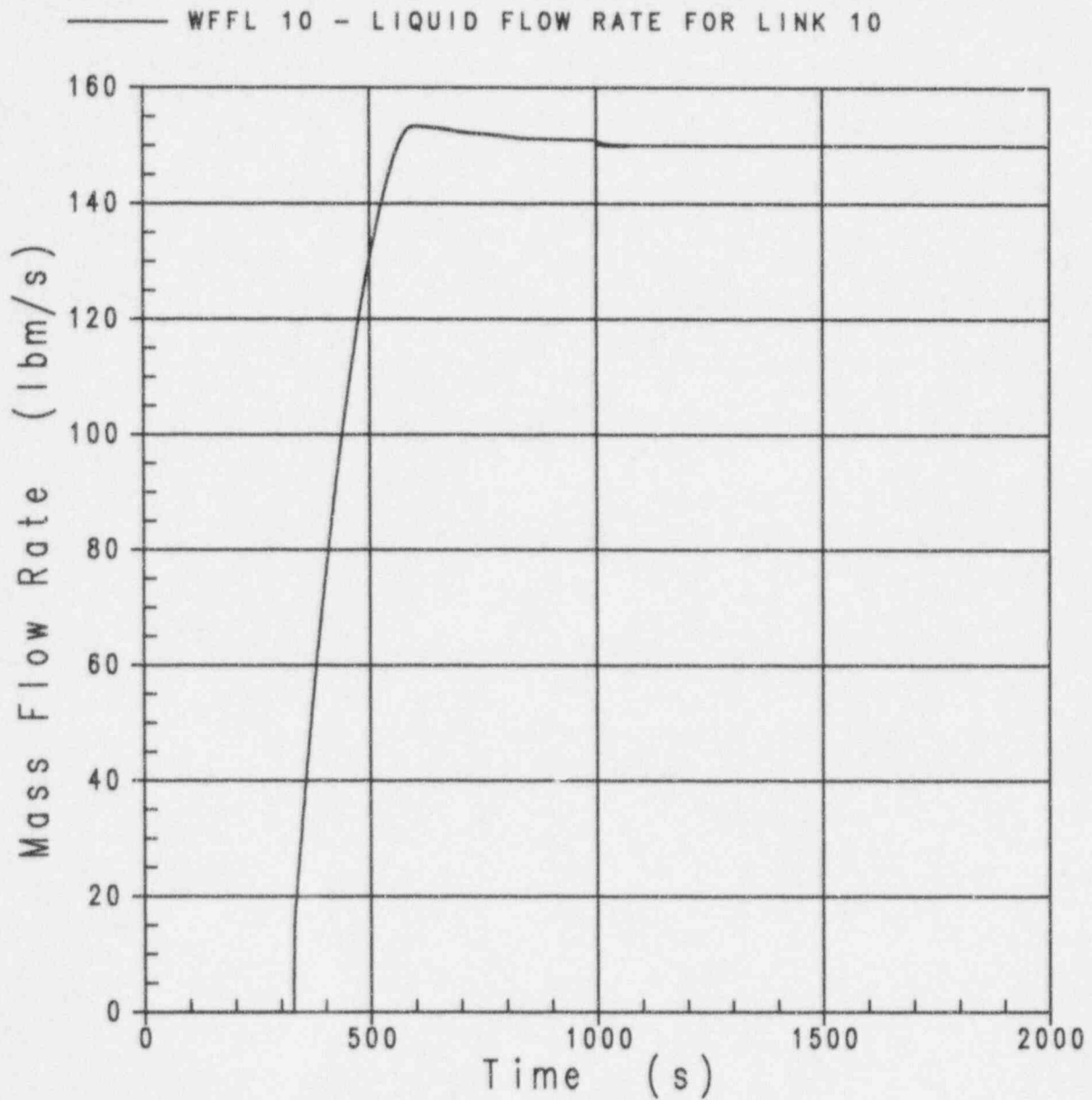


Figure 3.3-14 1000 psia, $W_1 = 150$ lbs/sec., $W_2 = 400$ lbs/sec.

——— EMIXFN 1 - NODE 1 MIXTURE ELEVATION
 - - - - EMIXFN 2 - NODE 2 MIXTURE ELEVATION
 - - - - EMIXFN 3 - NODE 3 MIXTURE ELEVATION
 - - - - EMIXFN 4 - NODE 4 MIXTURE ELEVATION
 - - - - EMIXFN 5 - NODE 5 MIXTURE ELEVATION
 - - - - EMIXFN 6 - NODE 6 MIXTURE ELEVATION

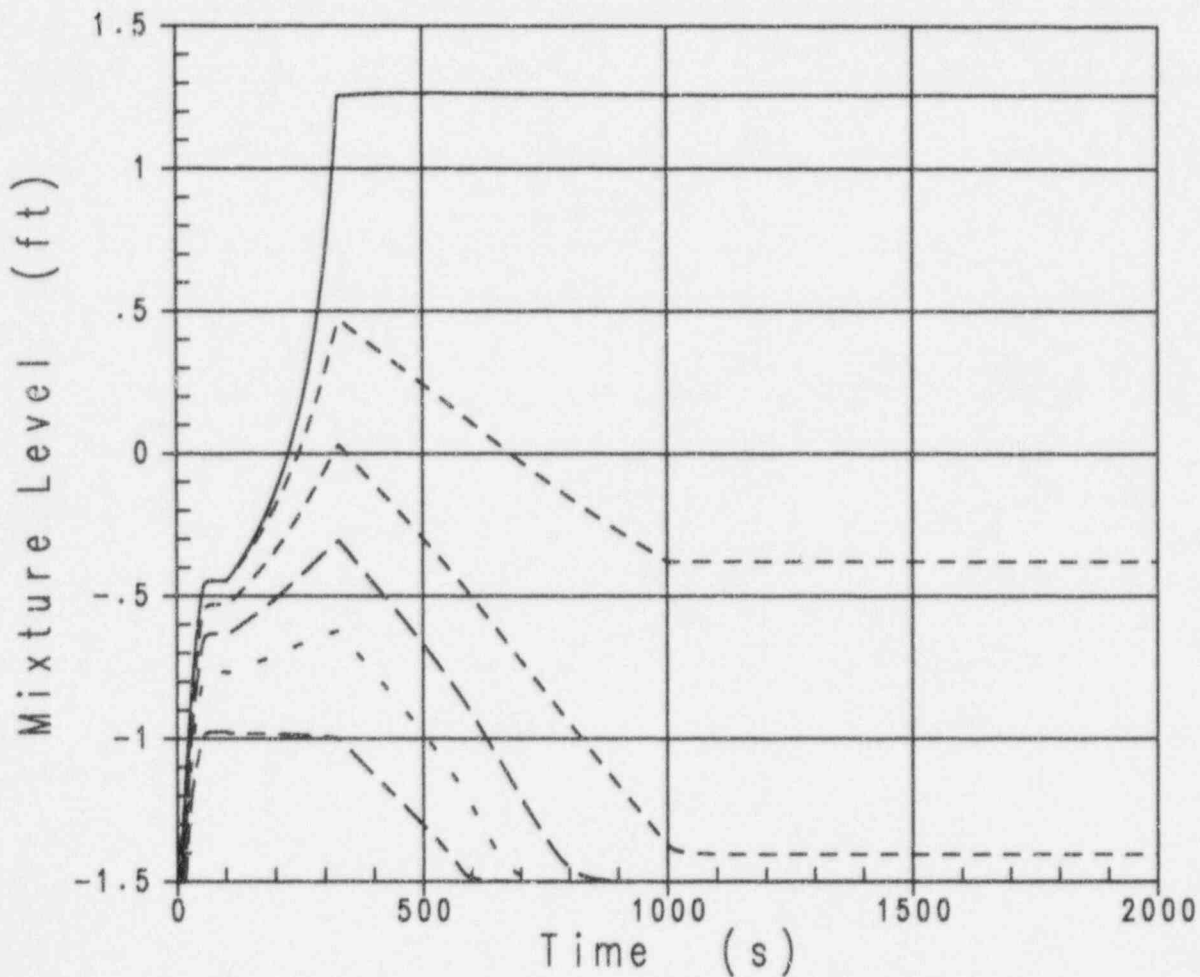


Figure 3.3-15 1000 psia, $W_1 = 150$ lbs/sec., $W_2 = 400$ lbs/sec.

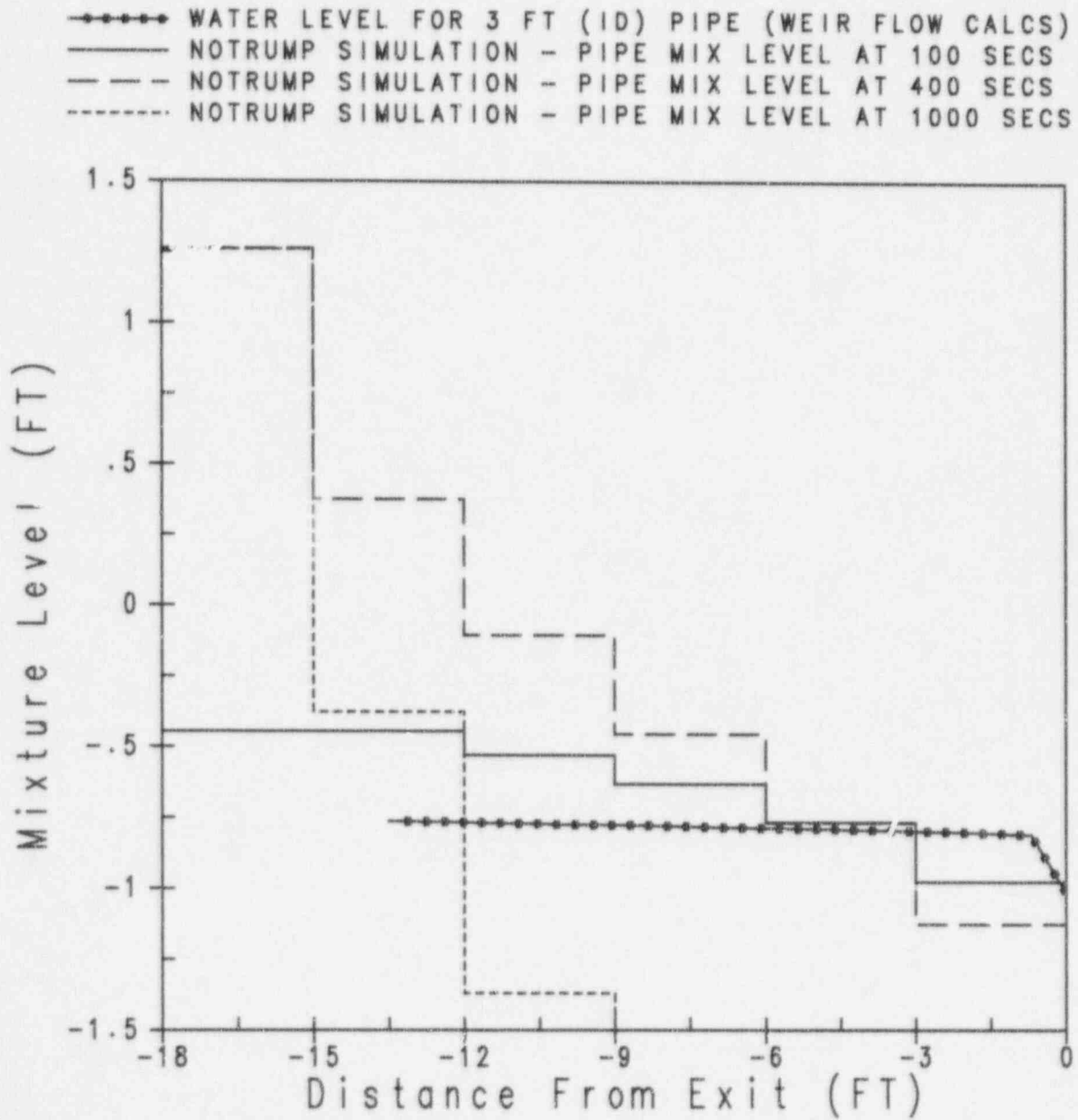


Figure 3.3-16 1000 psia, $W_1 = 150$ lbs/sec., $W_2 = 400$ lbs/sec.

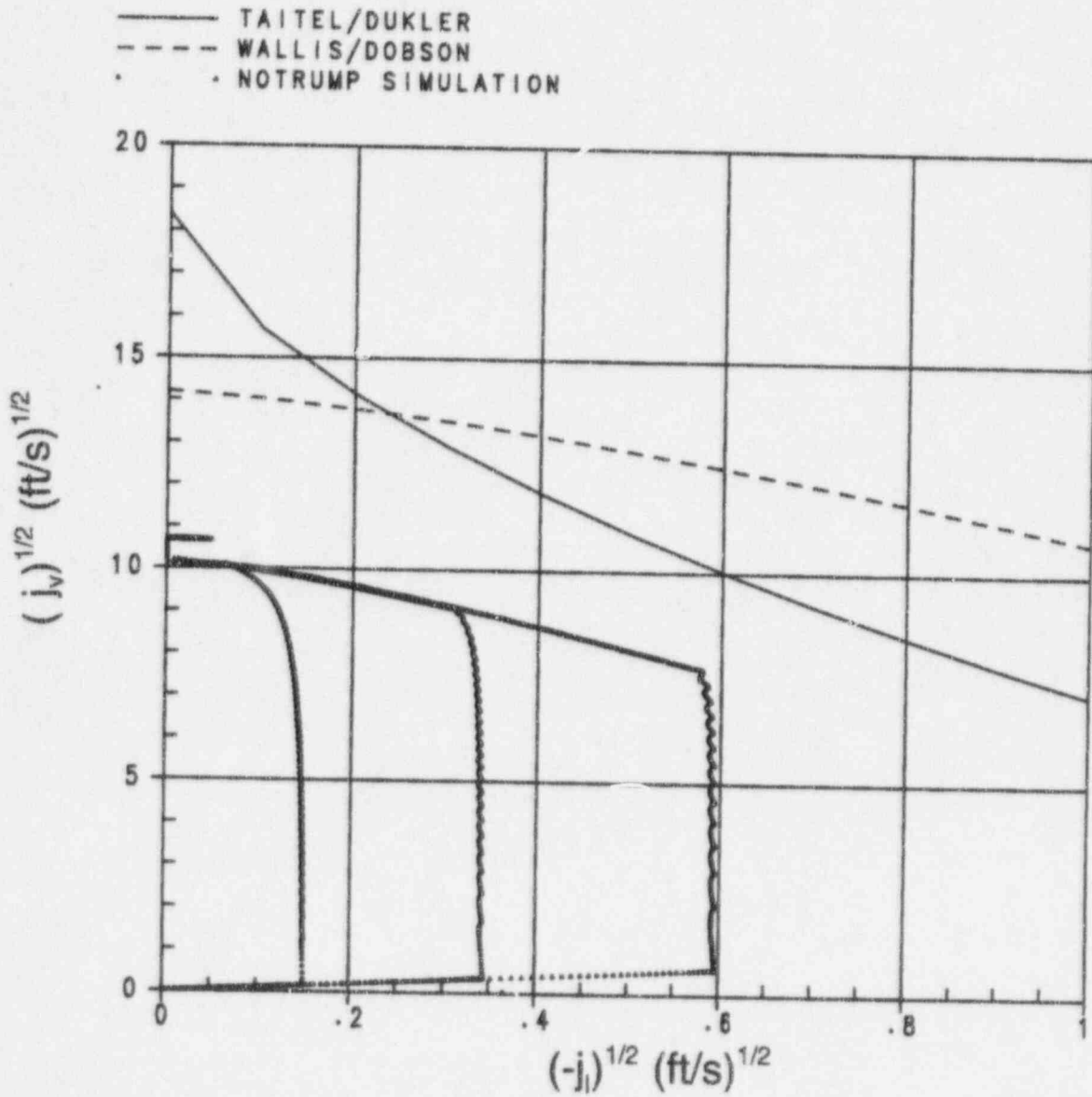


Figure 3.3-17 $j_v^{1/2}$, $j_l^{1/2}$ Predictions Compared with Data Flooding Limits (20 psia)

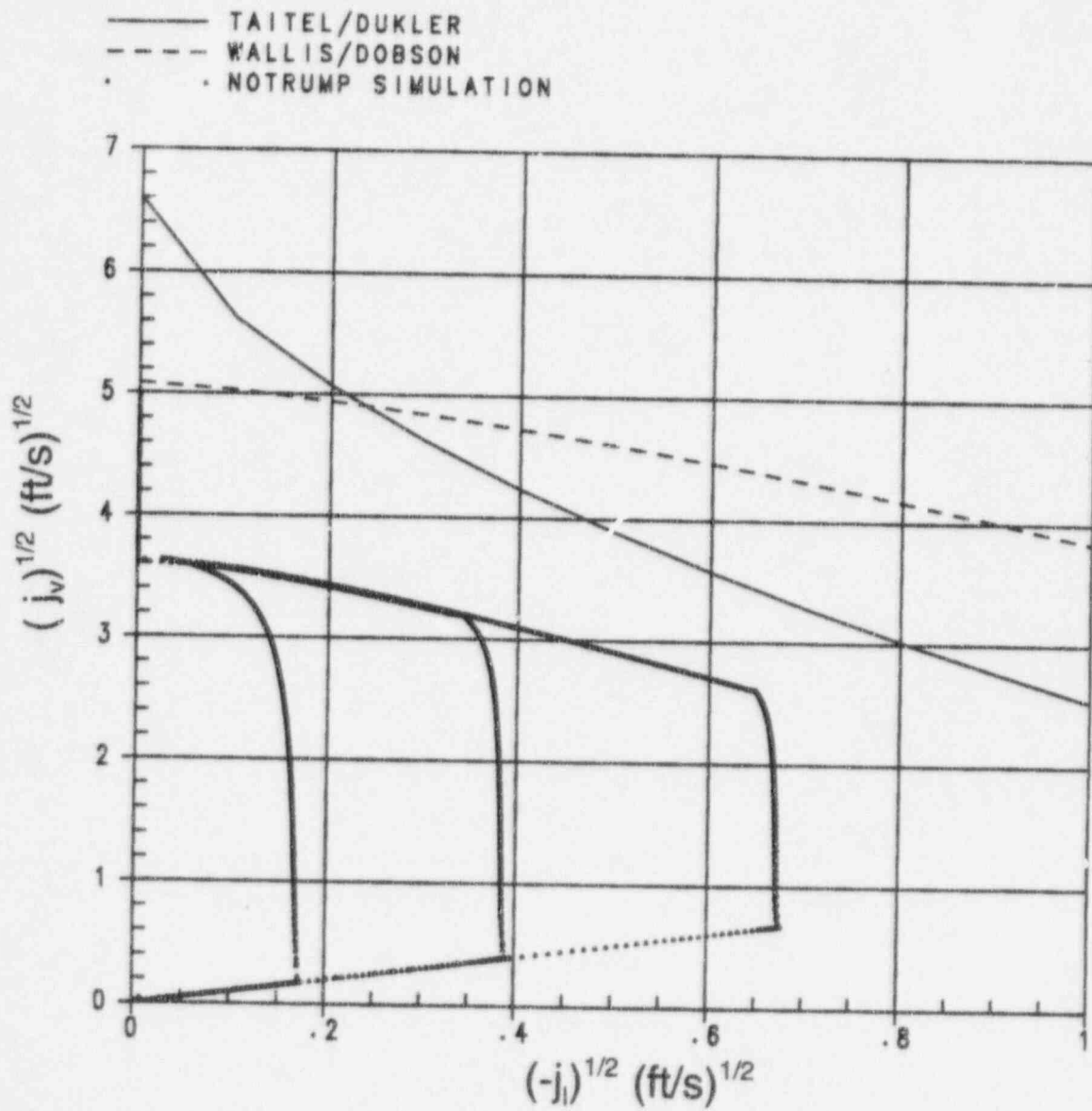


Figure 3.3-18 $j_v^{1/2}$, $j_l^{1/2}$ Predictions Compared with Data Flooding Limits (1000 psia)

3.4 Implicit Treatment of Gravitational Head

The purpose of this benchmark is to verify the implicit treatment of fluid node gravitational head in the solution of the flowlink momentum conservation equations. This is performed with a simulation of an oscillating manometer both with the explicit and implicit treatment of fluid node gravitational head. The pressure imbalances produced by the explicit treatment of fluid node gravitational head were quantified and shown to be virtually eliminated by the implicit treatment.

The NOTRUMP model for this benchmark is a 5-ft. high manometer, and the noding diagram is shown in Figure 3.4-1. One side of the manometer consists of a vertical column of four fluid nodes in



The manometer is initialized to a non-equilibrium condition with a high (4.5 ft.) water level in the column containing the stack of four fluid nodes, and a low (1.5 ft.) water level in the column containing one fluid node. The initial pressure in all fluid nodes is 14.696 psia. This value represents an extreme low that can be reached in AP600 plants and was chosen because the code typically has the most difficulty operating at low pressures. To maximize the piston-like behavior of the oscillating manometer, single-phase fluids are employed. The water is initialized subcooled with a specific enthalpy of 30 Btu/lbm, and the steam is initialized superheated with a specific enthalpy of 1300 Btu/lbm. The initial mass flow rate in all flowlinks was zero. The simulation is run for 5 seconds, both with the explicit and implicit treatment of fluid node gravitational head. For an equivalent comparison of the results, a constant time step size (0.01 seconds) is employed in both runs.

The explicit treatment of fluid node gravitational head can lead to pressure imbalances (and flow instabilities) in surrounding flowlinks if the fluid node density changes rapidly and/or if a water level in the fluid node moves rapidly. This is the case because the fluid node gravitational head, which is calculated at the beginning of a time step, is held constant throughout that time step in the explicit treatment. The implicit treatment of fluid node gravitational head reduces these pressure imbalances because the change in fluid node gravitational head is accounted for in the solution for the new-time central variables.

In the case of the oscillating manometer, the pressure imbalances with the explicit treatment of fluid node gravitational head are primarily due to the rapidly moving water level because the steam and water fluid conditions are essentially constant. The total pressure drop in a flowlink immediately below a rapidly moving water level should differ from the total pressure drop in the flowlinks below

it, which are surrounded by water, in the run with the explicit treatment of fluid node gravitational head. However, in the run with the implicit treatment of fluid node gravitational head, the total pressure drop in a flowlink immediately below a rapidly moving water level should not differ significantly from the total pressure drop in the flowlinks below it, which are surrounded by water. These pressure imbalances caused by the explicit treatment of fluid node gravitational head are quantified in the analysis of the results below.

Figures 3.4-2 and 3.4-3 show plots of the manometer water levels (in both columns) for the explicit and implicit treatment of fluid node gravitational head, respectively, and illustrate the oscillating behavior of the manometer in the runs. To study the pressure imbalances in flowlinks resulting from the explicit treatment of fluid node gravitational head, flowlinks 3 and 4, which are in the vertical column of the manometer that contains the stack of four fluid nodes, were chosen. Figures 3.4-4 and 3.4-5 show plots of the total pressure drop in flowlinks 3 and 4 together with the water level in the stack, for the explicit and implicit treatment of fluid node gravitational head, respectively. Note that perturbations appear in the flowlink pressure drop results of both runs. The perturbations were investigated and found to occur in the fluid node pressures, due to the incompressibility of the subcooled water in the manometer, and were also related to water levels crossing node boundaries. These phenomena were found to be unrelated to the fluid node gravitational head model and are discussed briefly at the end of this section for completeness.

To illustrate the pressure imbalances caused by the explicit treatment of fluid node gravitational head, the initial draining period of the stack is examined. Figures 3.4-6 and 3.4-7 show replots of the results from Figures 3.4-4 and 3.4-5, respectively, with the time scale expanded for the time period 0 to 0.35 seconds to study the initial draining of the water level into fluid node 3. Disregarding the perturbations that occur in both runs when the water level crosses into fluid node 3, from Figure 3.4-6 the pressure imbalance in flowlink 3 due to the explicit treatment of fluid node gravitational head (in fluid node 3) is observed to occur from approximately 0.3 to 0.35 seconds, during which time the total pressure drop in flowlink 3 differs from the total pressure drop in flowlink 4. From Figure 3.4-7, this pressure imbalance is observed to be virtually eliminated by the implicit treatment of fluid node gravitational head. This is more clearly shown in Figures 3.4-8 and 3.4-9, which show replots of the results of Figures 3.4-6 and 3.4-7, respectively, with the time scale expanded for the time period 0.3 to 0.35 seconds. Figure 3.4-10 shows the difference between the total pressure drop in flowlink 4 and flowlink 3 for this time period for the run with the explicit treatment of fluid node gravitational head. The pressure imbalance in flowlink 3 that exists with the explicit treatment of fluid node gravitational head during the time period 0.3 to 0.35 seconds is therefore quantified in Figure 3.4-10. A hand calculational check was performed that verified the pressure imbalance in flowlink 3 that is quantified in Figure 3.4-11.

For completeness, the perturbations in the fluid node pressures are discussed briefly. As stated above, these perturbations were found to be due to the incompressibility of the subcooled water in the manometer and were also related to water levels crossing node boundaries. To illustrate this, the manometer case with the implicit treatment of fluid node gravitational head was modified to initialize

the mixture regions at saturated conditions, with a specific enthalpy of 200 Btu/lbm, which is just above the specific enthalpy of saturated water ($h_f \approx 180$ Btu/lbm at 14.696 psia). The pressure in fluid nodes 3 and 4 were chosen to study the perturbations. For the manometer case with the implicit treatment of fluid node gravitational head with subcooled mixture regions, Figure 3.4-11 shows the pressure in fluid nodes 3 and 4 together with the water level in the stack with the time scale expanded for the time period 0 to 0.6 seconds to study the initial draining of the water level into fluid nodes 3 and 4. Similarly, for the manometer case with the implicit treatment of fluid node gravitational head with saturated mixture regions, Figure 3.4-12 shows the pressure in fluid nodes 3 and 4 together with the water level in the stack with the time scale expanded for the time period 0 to 0.6 seconds. Comparison of Figures 3.4-11 and 3.4-12 shows that fluid node pressures initially change more in the subcooled case, as expected due to the incompressibility of the fluid. As the mixture level crosses the fluid node boundaries, both cases exhibit perturbations, but they are larger in the subcooled case. However, both cases quickly recover and reach the same results.

To show that this is not a concern, the manometer case with the implicit treatment of fluid node gravitational head with subcooled mixture regions was modified to use a smaller time step size that is more representative of the typical Δt scenario under which the code is used. For this case, Figure 3.4-13 shows the pressure in fluid nodes 3 and 4 together with the water level in the stack with the time scale expanded for the time period 0 to 0.6 seconds. These results show that the fluid node pressure perturbations are reduced, both in magnitude and duration. In addition, comparison of Figures 3.4-11 and 3.4-13 indicates that both cases yield approximately the same results in the time period of interest.

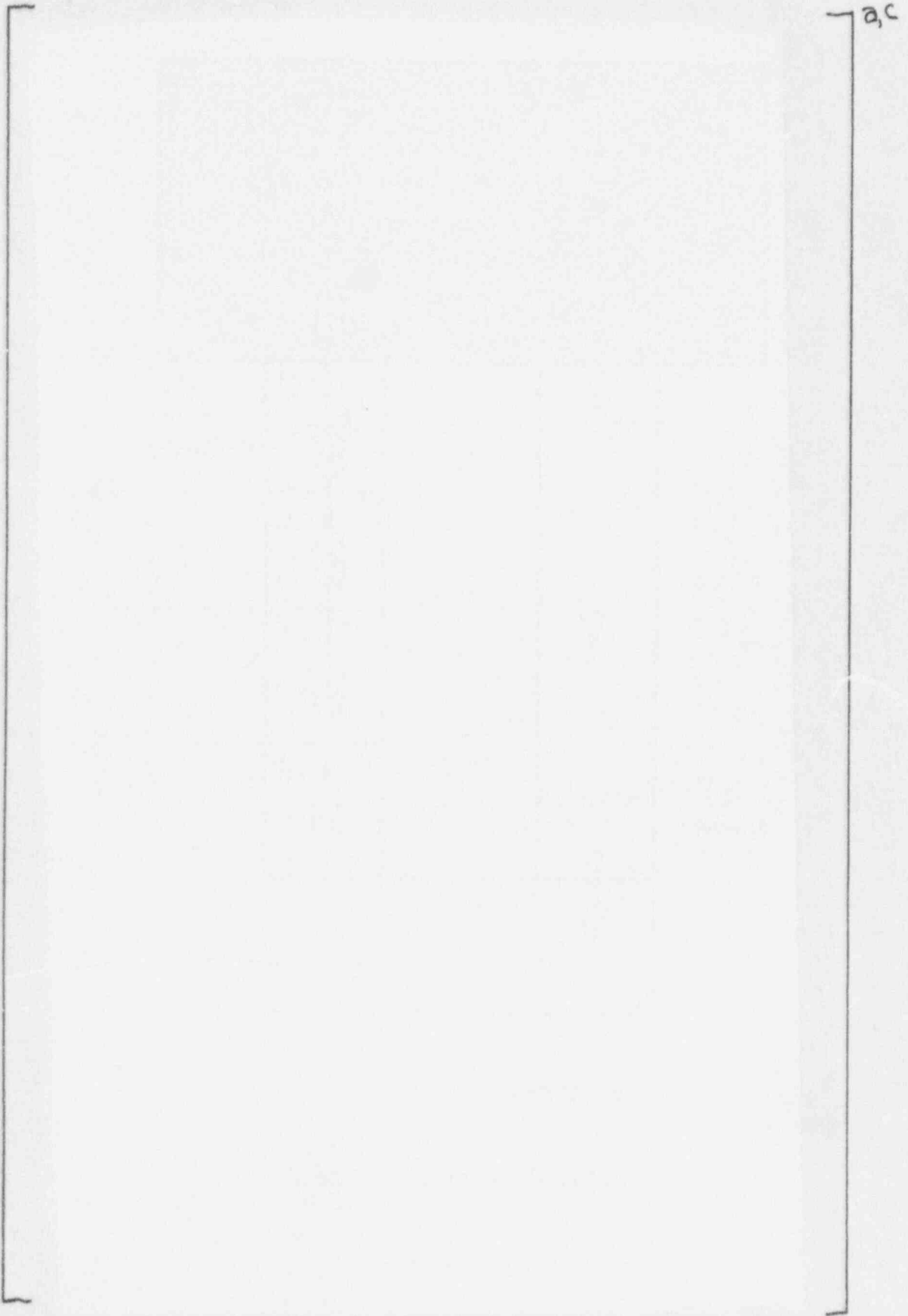


Figure 3.4-1 Noding Diagram for NOTRUMP Manometer Simulation

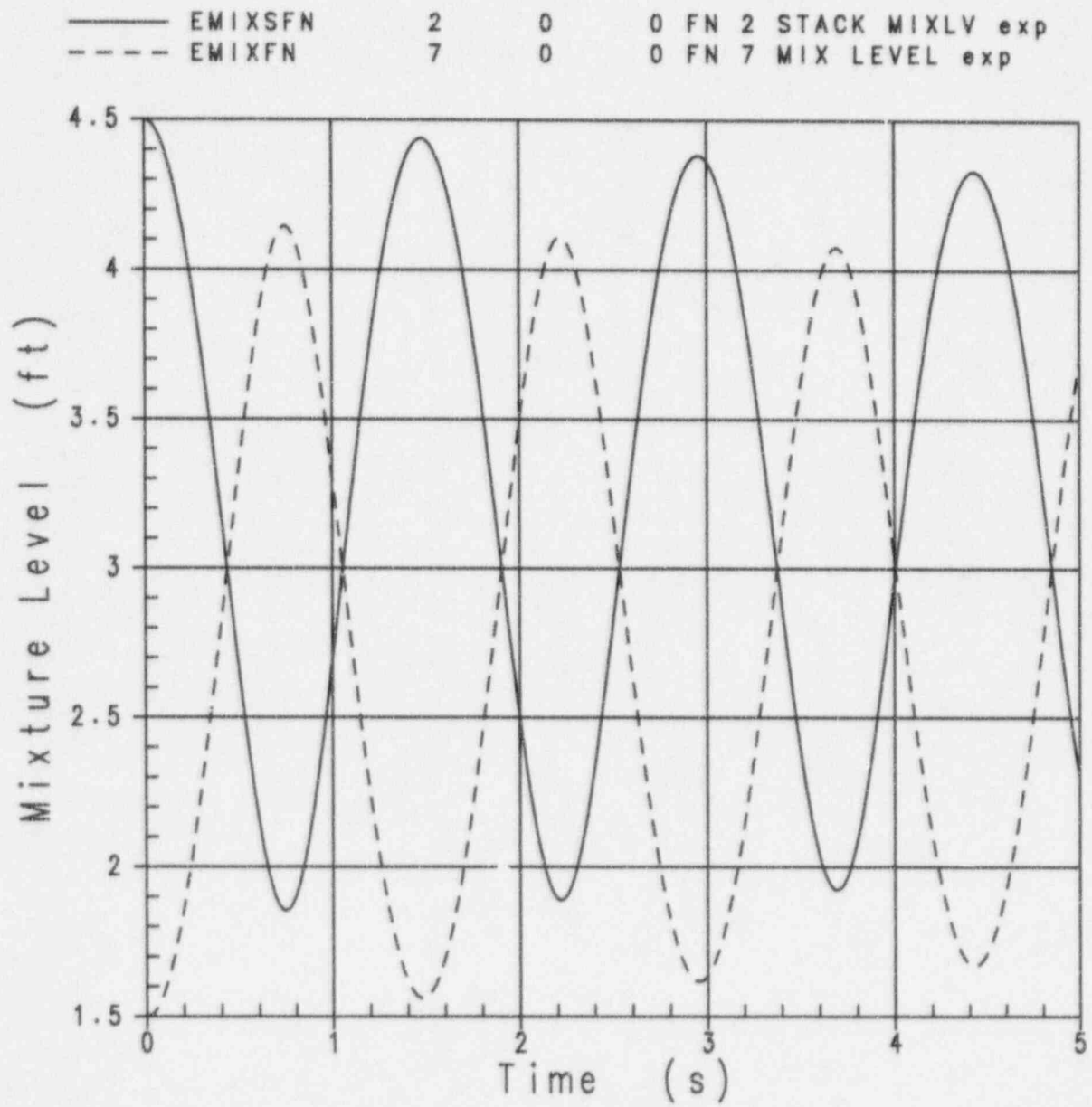


Figure 3.4-2 Explicit Gravitational Head - Manometer Water Levels

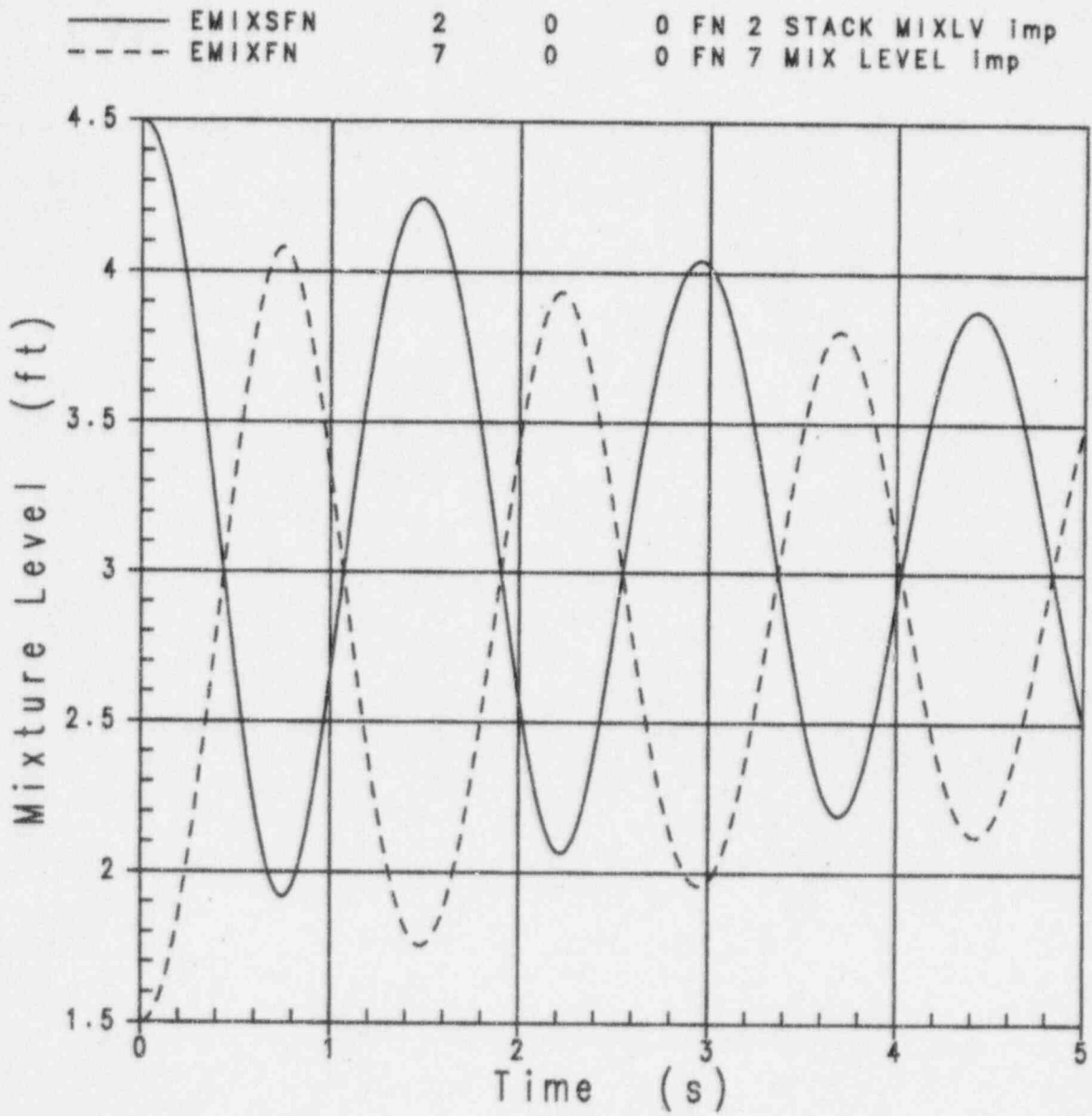


Figure 3.4-3 Implicit Gravitational Head - Manometer Water Levels

Differential Pressure (psi)							
—	DPTOTFL	3	0	0	FL 3	DELTA P	TOT exp
- - -	DPTOTFL	4	0	0	FL 4	DELTA P	TOT exp
Mixture Level (ft)							
- - - -	EMIXSFN	2	0	0	FN 2	STACK	MIXLV exp

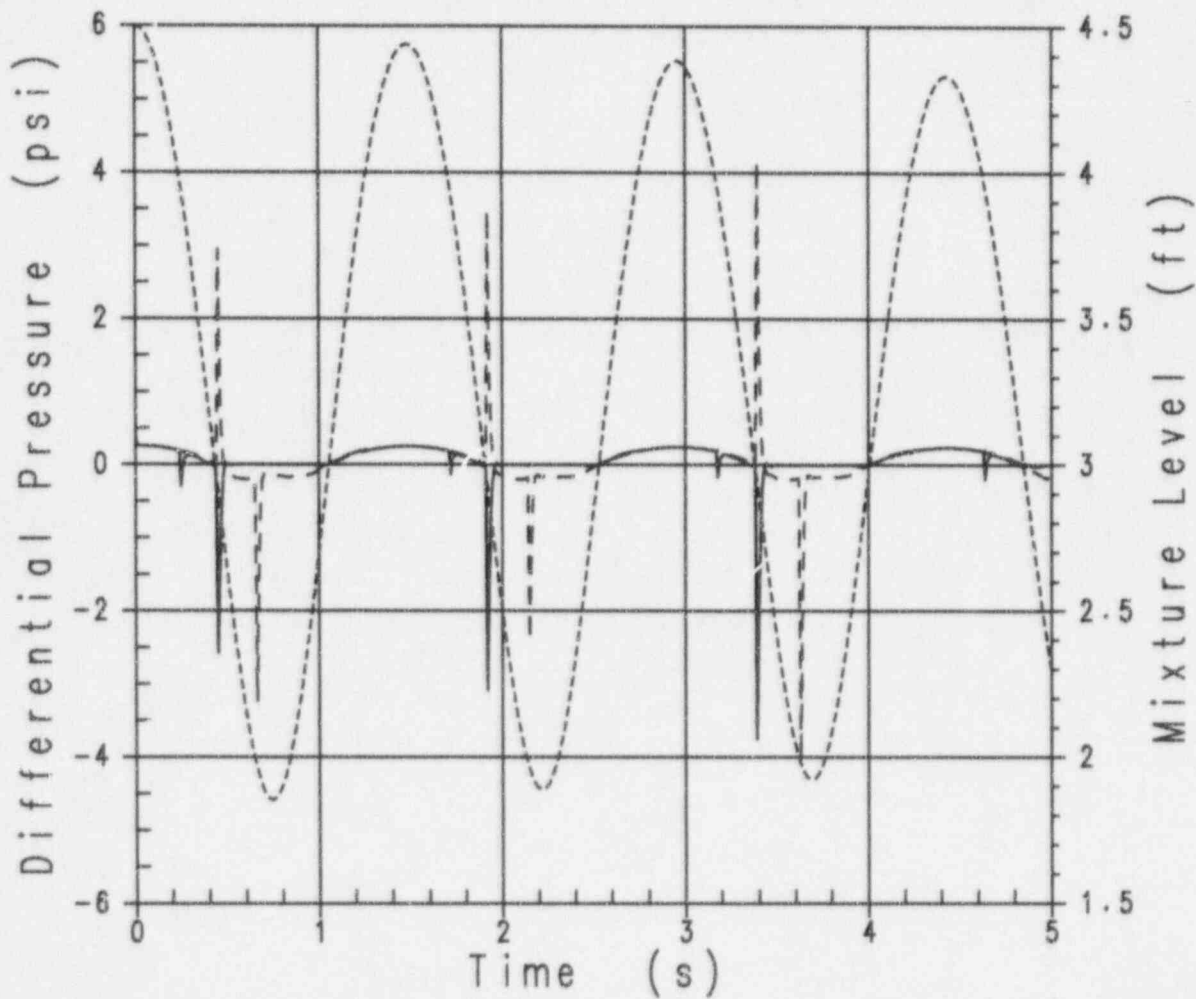


Figure 3.4-4 Explicit Gravitational Head - Flowlinks 3 and 4 Total Pressure Drop with Stack Water Level

Differential Pressure (psi)		Mixture Level (ft)	
—	DPTOTFL 3	0	0 FL 3 DELTA P TOT imp
- - - -	DPTOTFL 4	0	0 FL 4 DELTA P TOT imp
- - - - -	EMIXSFN 2	0	0 FN 2 STACK MIXLV imp

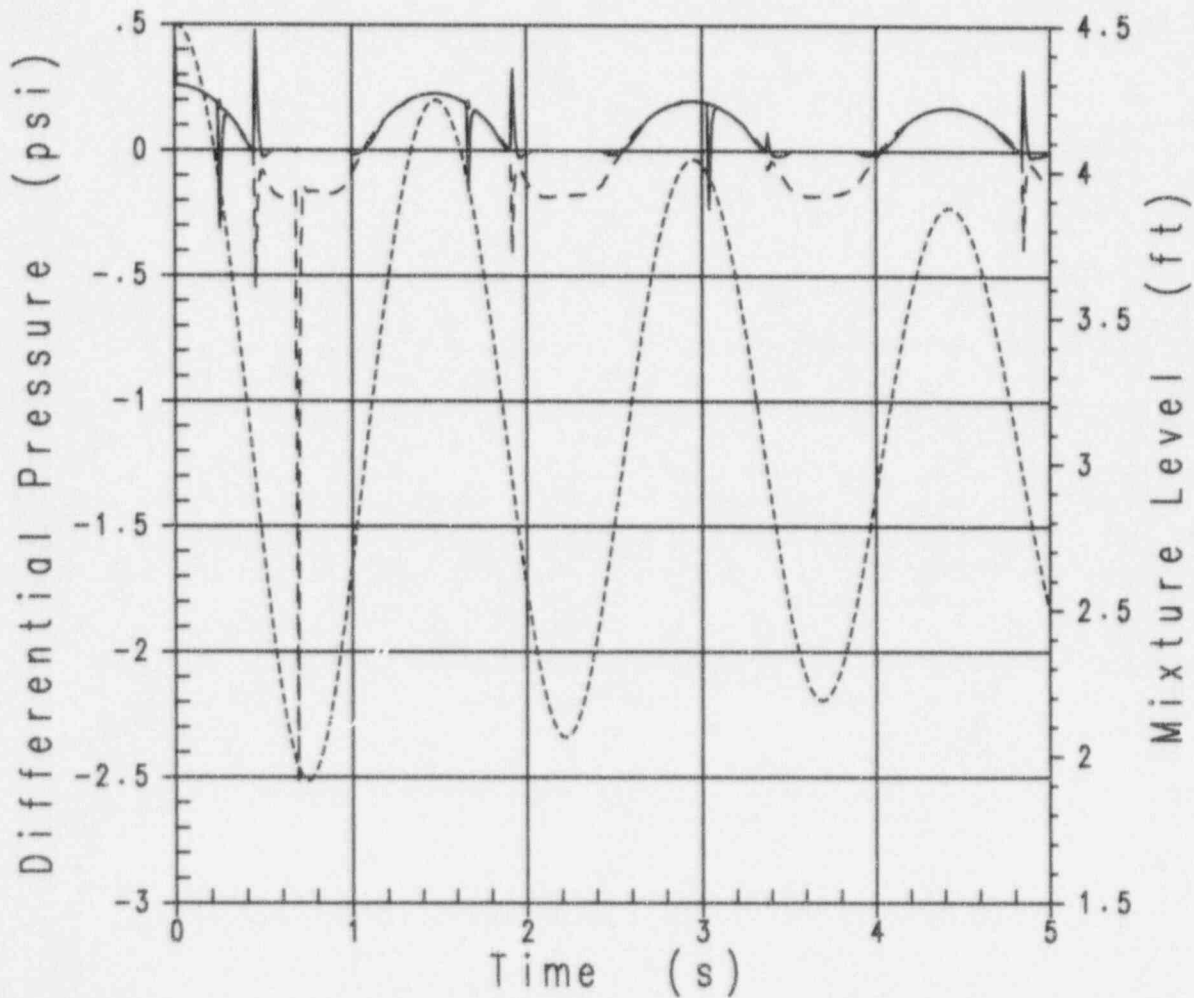


Figure 3.4-5 Implicit Gravitational Head - Flowlinks 3 and 4 Total Pressure Drop with Stack Water Level

Differential Pressure (psi)									
—	DPTOTFL	3	0	0	FL 3	DELTA P	TOT	exp	
- - -	DPTOTFL	4	0	0	FL 4	DELTA P	TOT	exp	
Mixture Level (ft)									
- - - -	EMIXSFN	2	0	0	FN 2	STACK	MIXLV	exp	

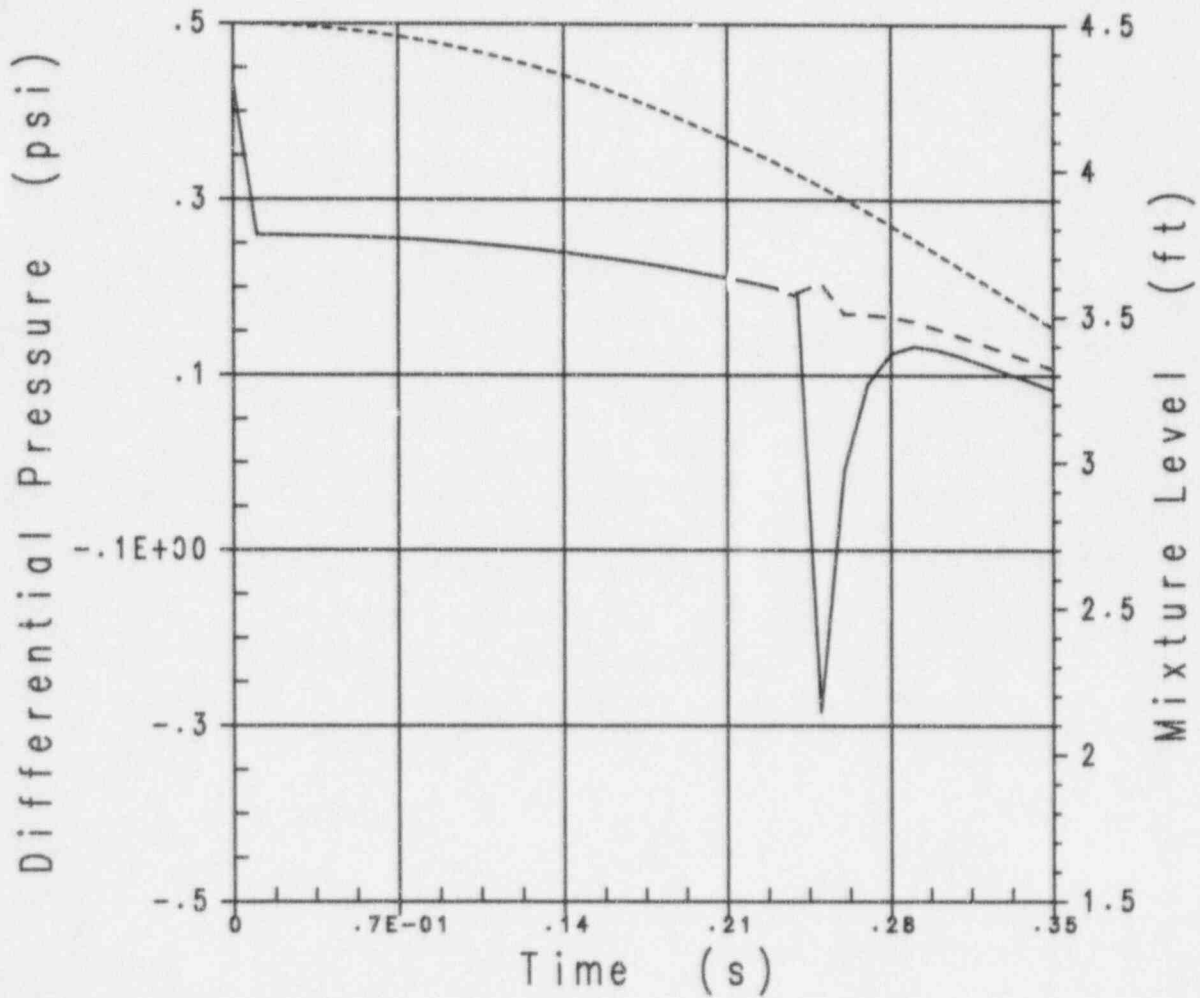


Figure 3.4-6 Explicit Gravitational Head - Flowlinks 3 and 4 Total Pressure Drop with Stack Water Level (Expanded Time Scale 0 to 0.35 Seconds)

Differential Pressure (psi)									
—	DPTOTFL	3	0	0	FL 3	DELTA P	TOT	Imp	
- - - -	DPTOTFL	4	0	0	FL 4	DELTA P	TOT	Imp	
Mixture Level (ft)									
- - - - -	EMIXSFN	2	0	0	FN 2	STACK	MIXLV	Imp	

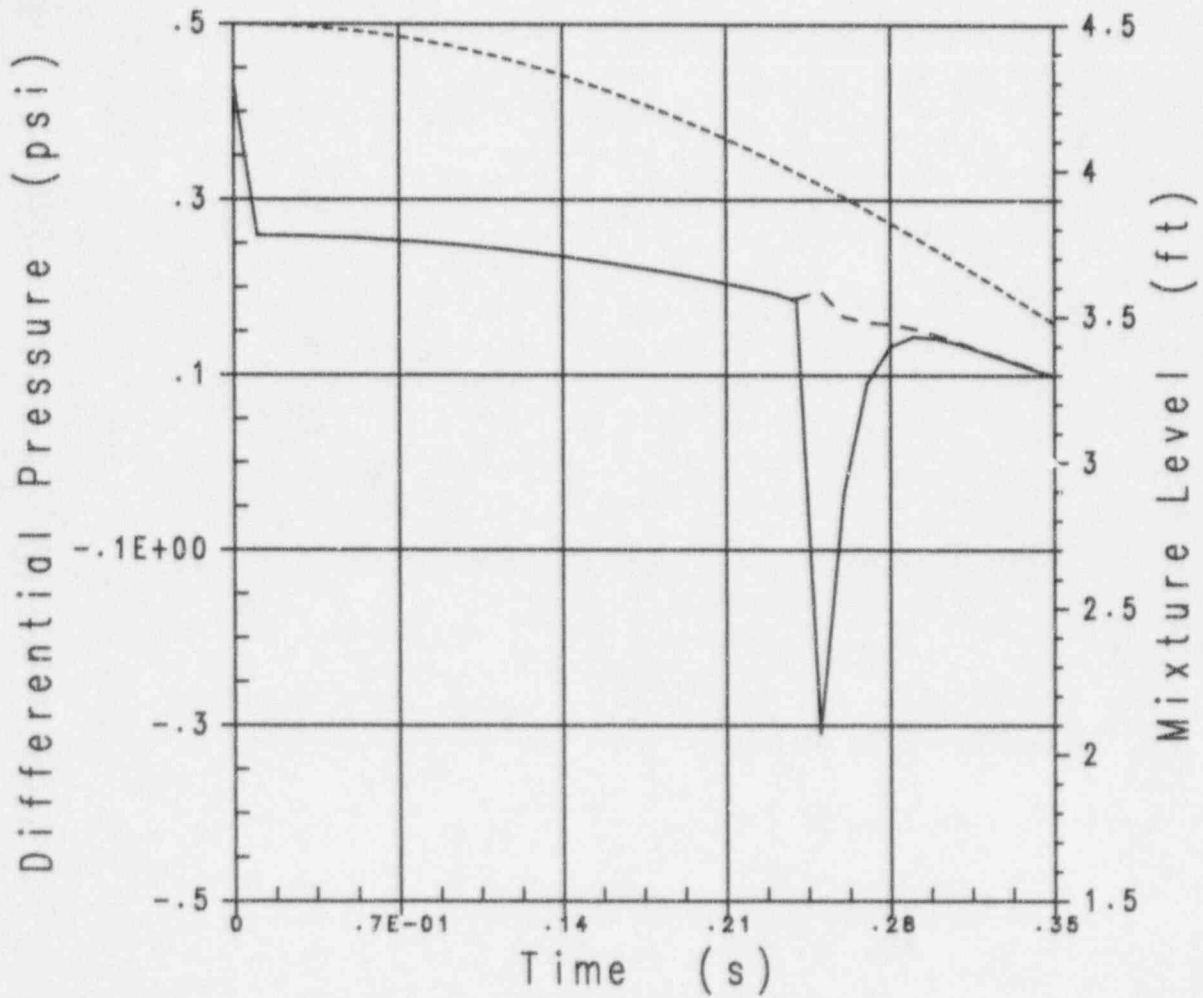


Figure 3.4-7 Implicit Gravitational Head - Flowlinks 3 and 4 Total Pressure Drop with Stack Water Level (Expanded Time Scale 0 to 0.35 Seconds)

Differential Pressure (psi)							
————	DPTOTFL	3	0	0	FL 3	DELTA P	TOT exp
-----	DPTOTFL	4	0	0	FL 4	DELTA P	TOT exp
Mixture Level (ft)							
-----	EMIXSFN	2	0	0	FN 2	STACK	MIXLV exp

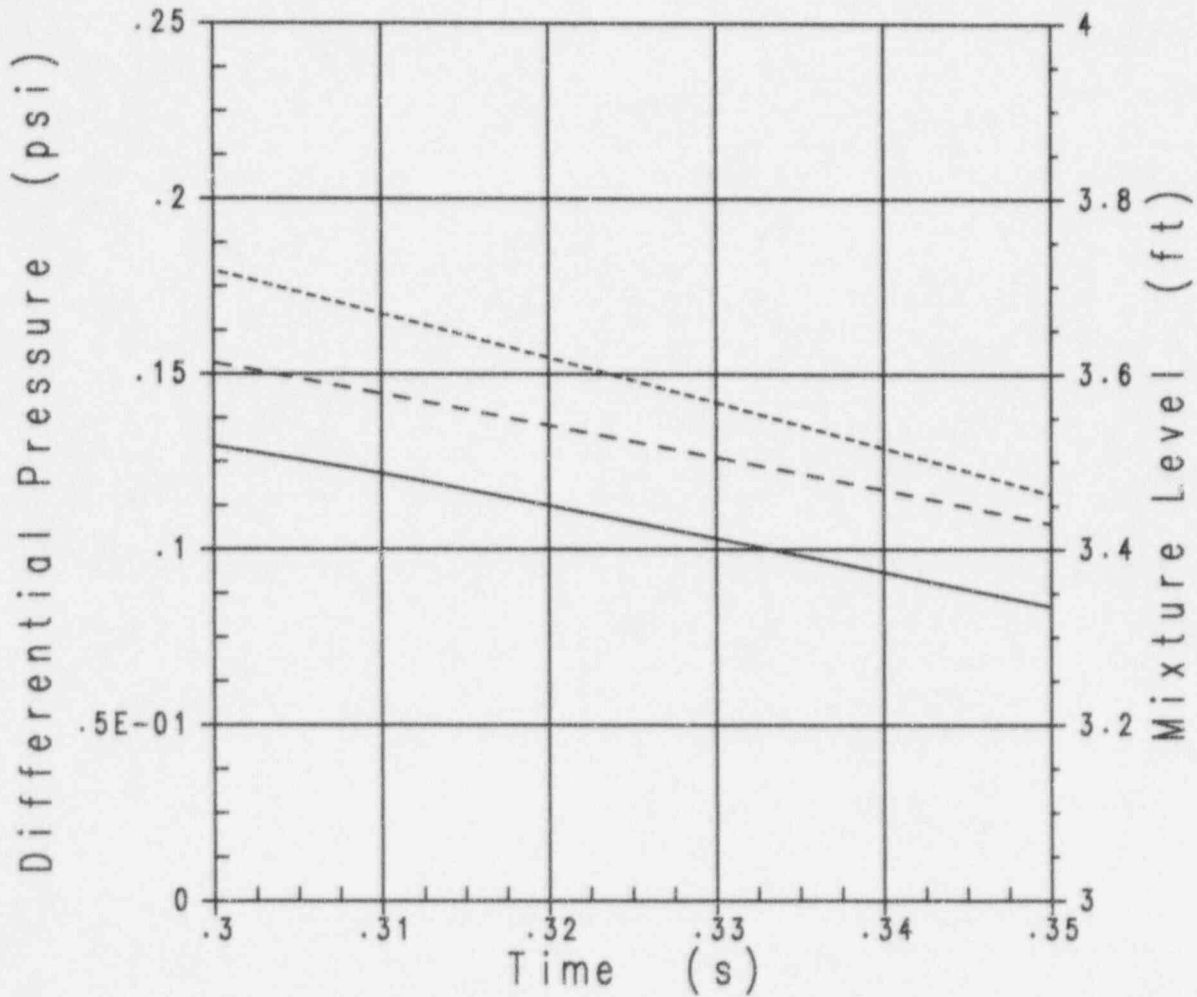


Figure 3.4-8 Explicit Gravitational Head - Flowlinks 3 and 4 Total Pressure Drop with Stack Water Level (Expanded Time Scale 0.3 to 0.35 Seconds)

Differential Pressure (psi)									
—	DPTOTFL	3	0	0	FL 3	DELTA P	TOT	imp	
- - -	DPTOTFL	4	0	0	FL 4	DELTA P	TOT	imp	
Mixture Level (ft)									
- - - - -	EMIXSFN	2	0	0	FN 2	STACK	MIXLV	imp	

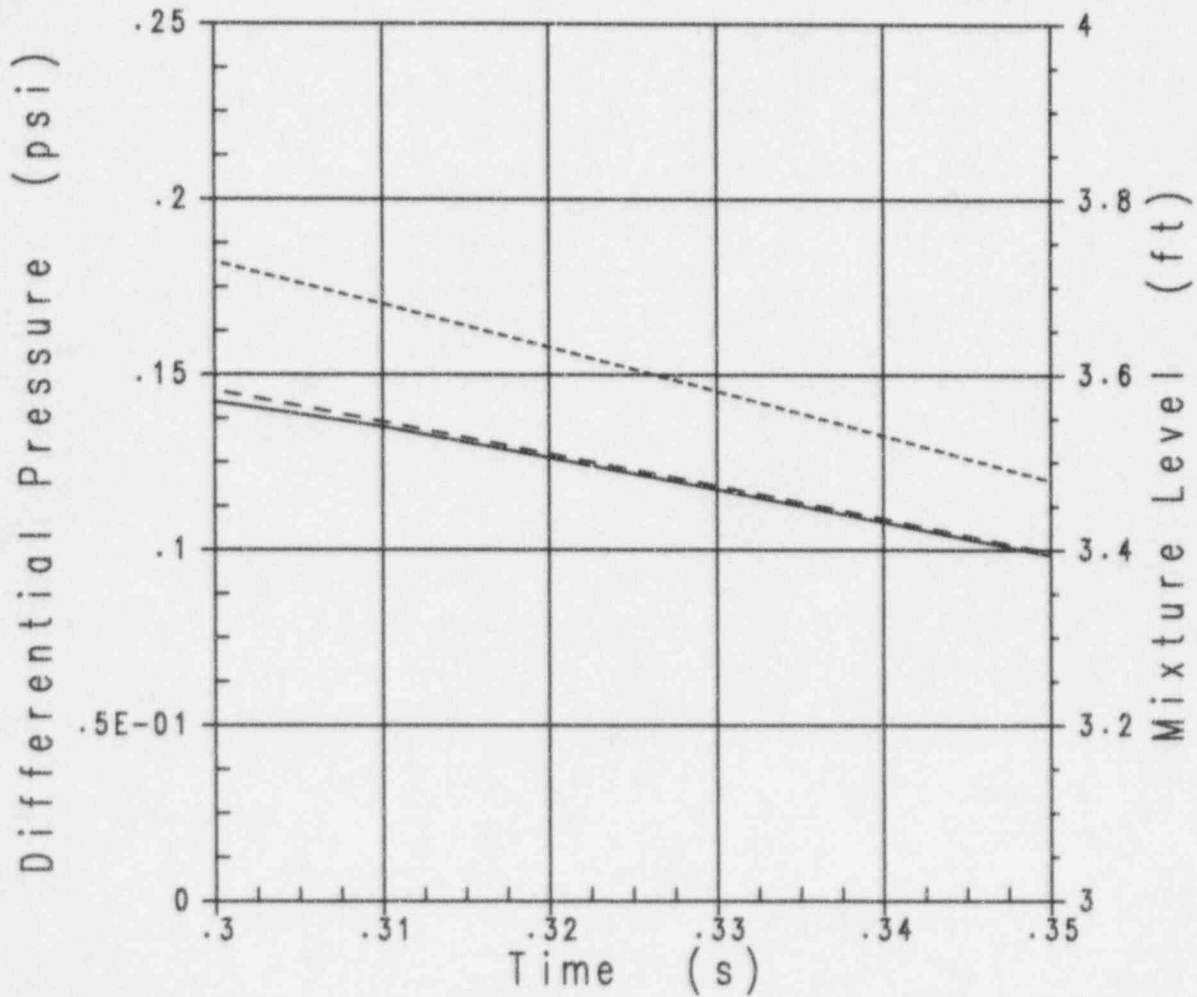


Figure 3.4-9 Implicit Gravitational Head - Flowlinks 3 and 4 Total Pressure Drop with Stack Water Level (Expanded Time Scale 0.3 to 0.35 Seconds)

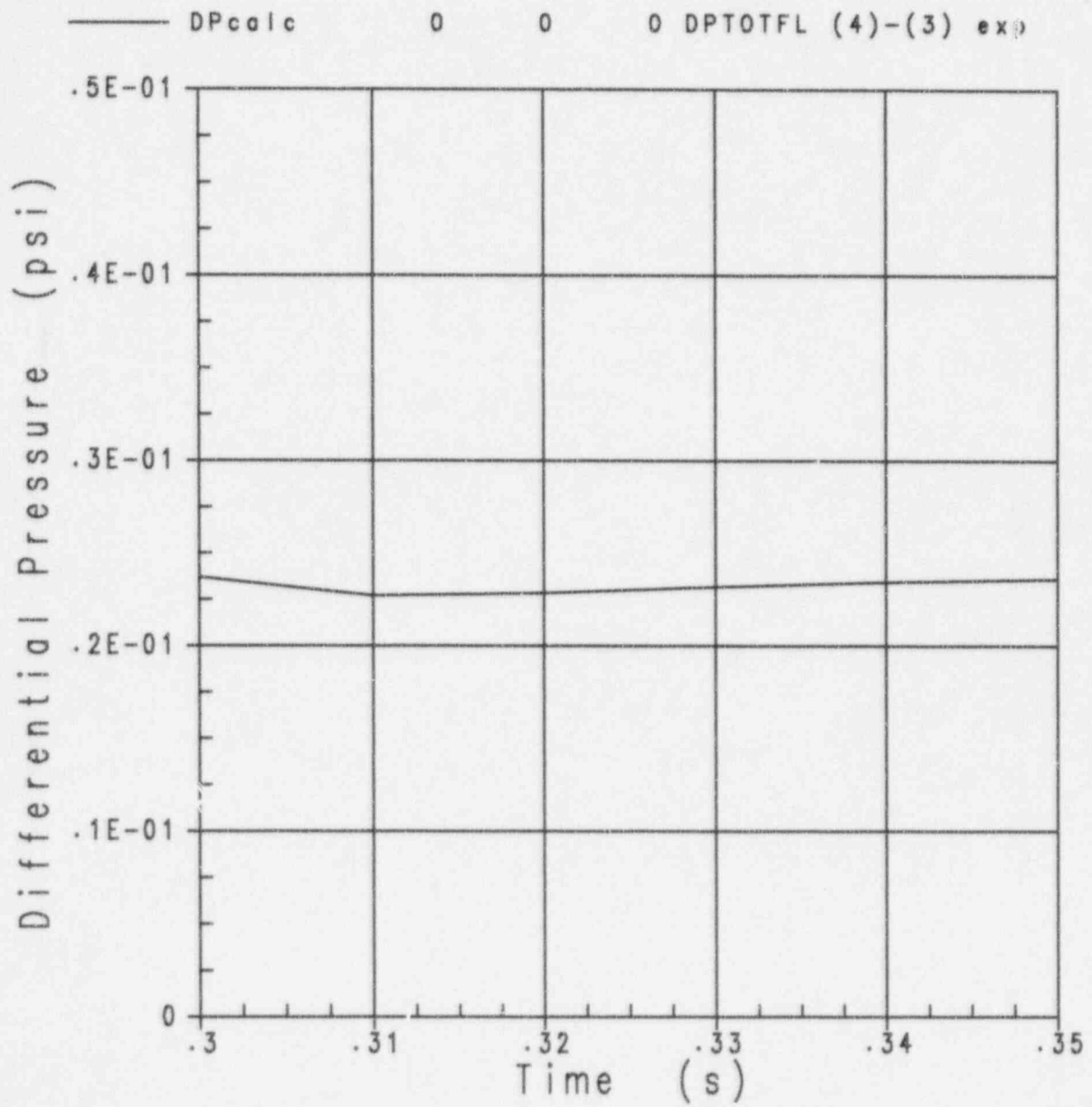


Figure 3.4-10 Explicit Gravitational Head - Difference Between Total Pressure Drop in Flowlinks 4 and 3 (Expanded Time Scale 0.3 to 0.35 Seconds)

Pressure (psia)					
—— PFN	3	0	0	FN 3	PRESSURE sub
---- PFN	4	0	0	FN 4	PRESSURE sub
Mixture Level (ft)					
- - - - EMIXSFN	2	0	0	FN 2	STACK MIXLV sub

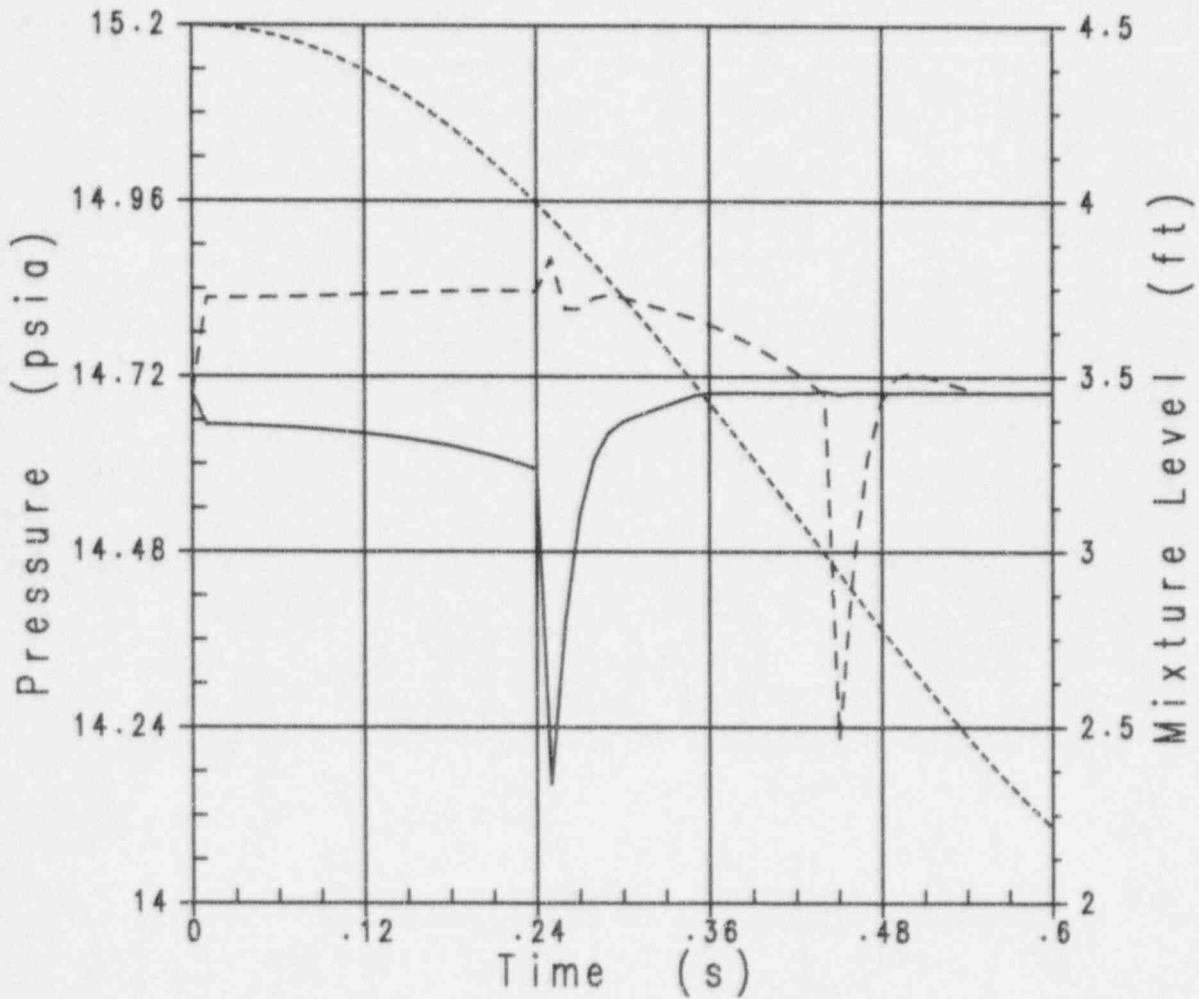


Figure 3.4-11 Implicit Gravitational Head with Subcooled Mixture Regions - Fluid Nodes 3 and 4 Pressure (Expanded Time Scale 0 to 0.6 Seconds)

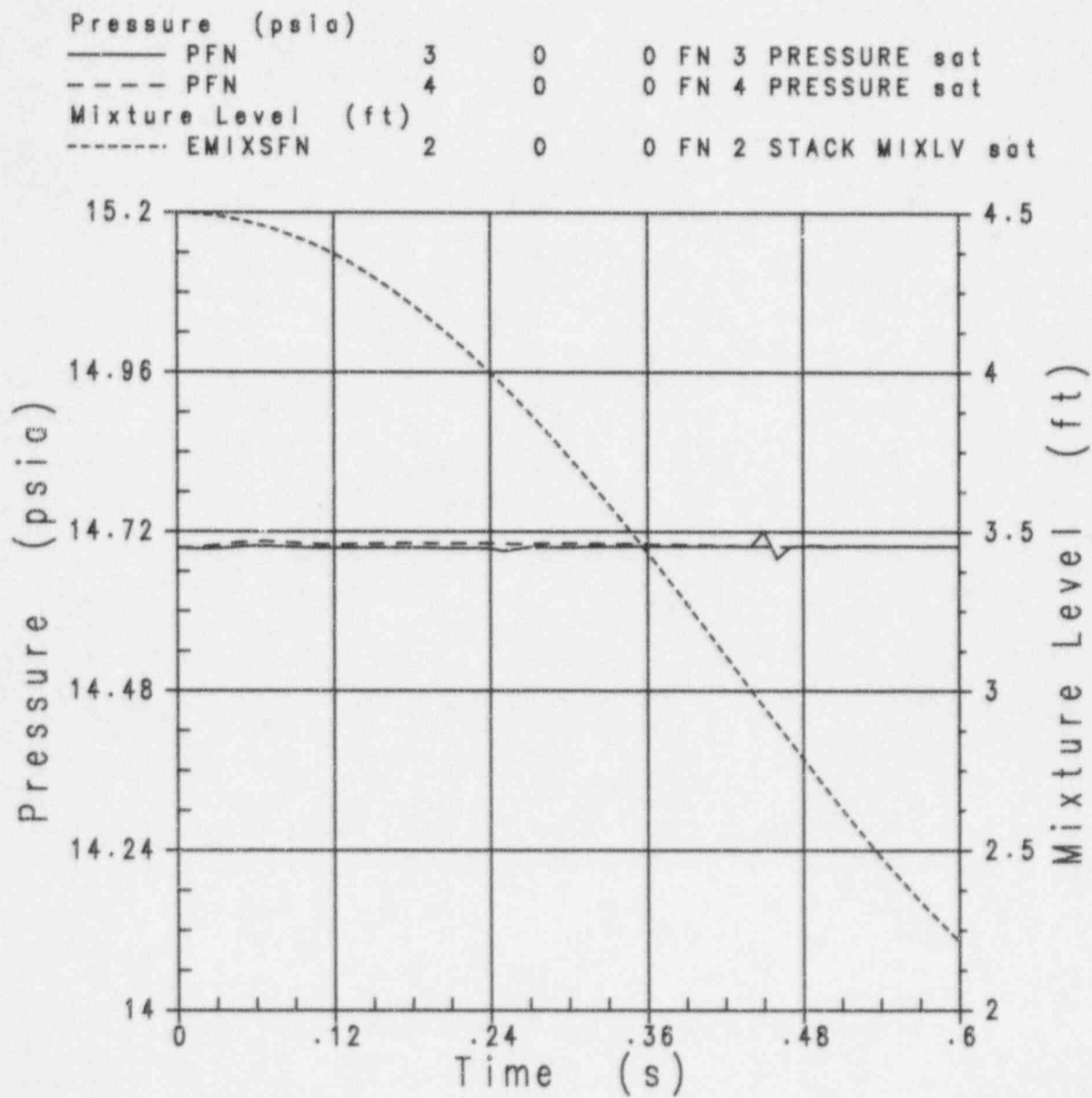


Figure 3.4-12 Implicit Gravitational Head with Saturated Mixture Regions - Fluid Nodes 3 and 4 Pressure (Expanded Time Scale 0 to 0.6 Seconds)

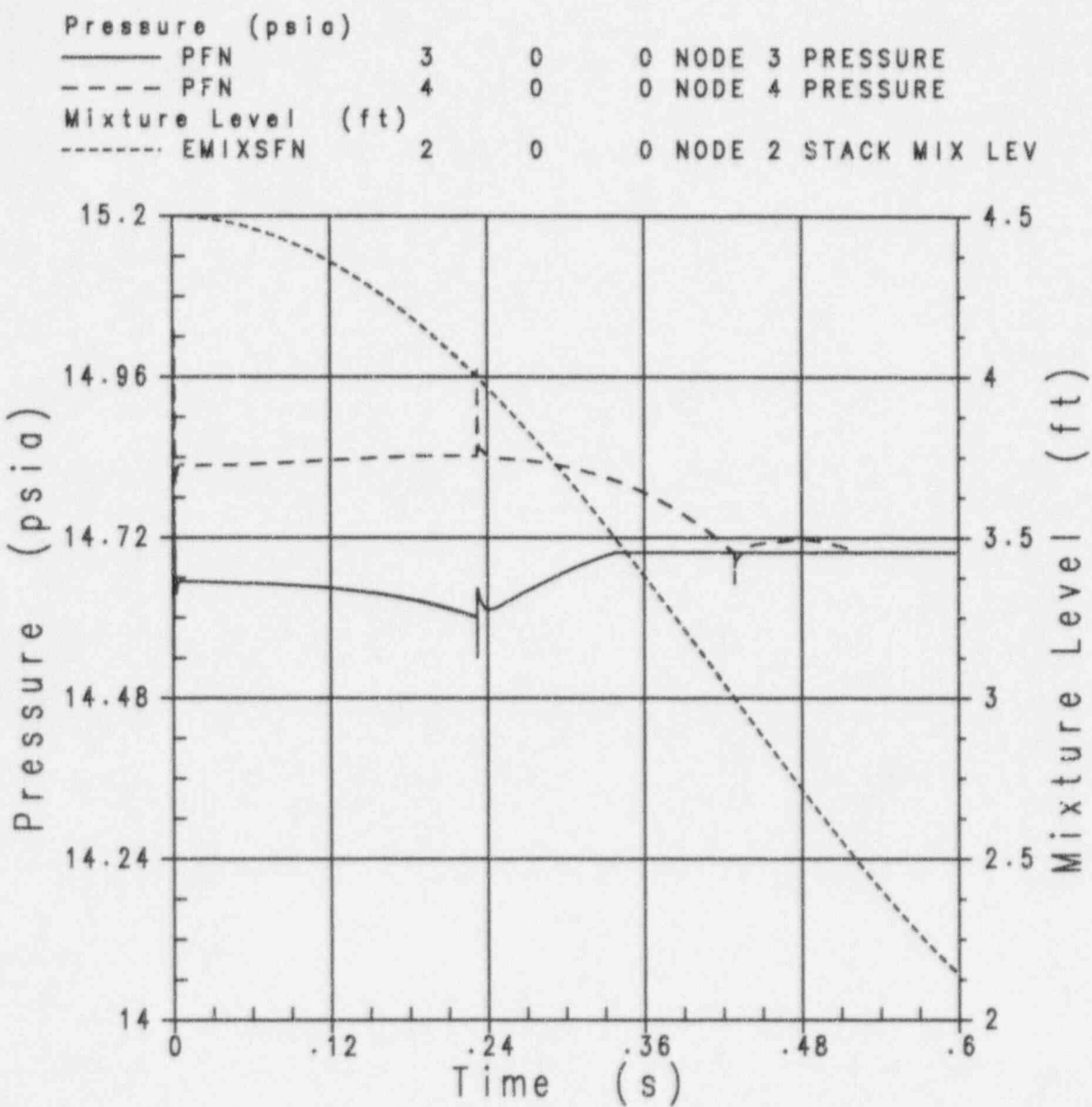


Figure 3.4-13 Implicit Gravitational Head with Subcooled Mixture Regions - Fluid Nodes 3 and 4 Pressure (Reduced Time Step Size; Expanded Time Scale 0 to 0.6 Seconds)

3.5 Net Volumetric Flow-Based Momentum Equation

To assess the logic of the net volumetric flow-based momentum equation, a portion of an AP600 plant calculation is used. The calculation is performed with the logic turned off then on. Multiplots are provided for two cases for the system pressure and mass flow rates in the flowlinks connecting the loops to the vessel. In addition, a simple problem is performed to verify that the volumetric flow-based flowlink model calculates the correct mass flow when the volume flow is specified. The problem analyzed is a horizontal, frictionless pipe through which flow is maintained at a constant velocity (constant volumetric flow) as the density of the inlet steam/water mixture is varied. The results of the plant calculation and benchmark test performed to validate the model are provided in the following paragraphs.

3.5.1 AP600 Plant Transient

A sensitivity study was performed on the AP600 plant to assess the effects of the volumetric flow-based momentum equation and the original mass flow-based momentum equation. This was accomplished by running an AP600 plant transient with the volumetric flow-based momentum turned on and re-running the transient with the mass-based momentum turned on. The transient simulating a 2-in. cold leg break in the passive residual heat removal (PRHR) loop was chosen since this transient is sufficiently long to show any differences.

From the comparison of results of these two runs, it can be seen that the system pressure is similar between the two cases up to the point when automatic depressurization system (ADS) 1 is actuated (see Figure 3.5-1). For the volumetric flow-based case, ADS 1 actuation occurs at approximately 990 sec., while for the mass flow-based case, ADS 1 actuation occurs at approximately 810 sec., 180 sec. earlier. This is caused by a delay in the time when vapor flows to the top of the core makeup tank (CMT) balance line, allowing the CMT to start draining for the volumetric flow-based case.

In addition to the similarity in system pressure up until ADS 1 actuation occurs, the system flow rates between the loops and vessel also show similar trends. Figures 3.5-2 to 3.5-13 compare the loop-to-vessel flow rates and contain overlays of the volumetric and mass flow-based runs. From these figures, it can be seen that the liquid and vapor mass flow rates are similar for both runs in each of the flowlinks connecting the vessel and loops. Fluctuations occur occasionally in the mass flow-based case, such as at approximately 800 sec. of Figure 3.5-2, which indicates that this case behaves unrealistically at times. The mass flow-based case does not run to completion because complications resulted in run termination at approximately 1700 sec. The volumetric flow-based momentum equation allows the transient simulation to run to its specified end time.

3.5.2 Demonstration Problem

The purpose of this benchmark test is to demonstrate the net volumetric flow-based momentum equation implemented in NOTRUMP. This is done by simulating flow through a horizontal, frictionless pipe modeled by 12 homogeneous nodes. A constant-velocity flow rate of 10 ft./sec. is maintained throughout the simulation while the void fraction of the beginning node is ramped linearly from zero to 0.9 over a 1-sec. time interval. By using the volumetric flow-based momentum equation, flow through the interior fluid nodes making up the horizontal pipe should remain close to 10 ft./sec. while the density gradient propagates downstream with no major perturbations in pressure. Figure 3.5-14 shows the noding diagram for this problem.

The flow rate is initialized at a constant velocity of 10 ft./sec. with a quality of one. This translates into an initial mass flow rate of 455 lbm/sec. for the initial system pressure of 50 psia. After running the problem at this constant liquid mass flow rate for 10 sec., the void fraction of the fluid entering the system is ramped linearly from zero to 0.9. Therefore, the liquid mass flow rate entering the pipe at the end of the void fraction ramp time is 46.3 lbm/sec. The results of this calculation are shown in Figures 3.5-15 through 3.5-18.

Figure 3.5-15 illustrates the void fraction ramp that starts the transient to be simulated. As described above, the void fraction ramp is increased from an initial value of zero up to 0.9 over a 1-sec. time interval.

Figure 3.5-16 shows the corresponding mass flow rate of the liquid through the horizontal, frictionless pipe as the density of the fluid entering the beginning node is varied according to Figure 3.5-15. Therefore, the liquid mass flow rate decreases from 455 lbm/sec. to 46.3 lbm/sec. over the 1-sec. ramp time interval.

The pressure in the system remains nearly constant at 50 psia throughout the transient, which provides evidence that the volumetric flow-based momentum equation is functioning properly. Figure 3.5-17 provides the velocity of the flow through the system. As expected, the velocity remains approximately constant at 10 ft./sec. throughout the transient.

In conclusion, the volumetric flow-based momentum equation implemented in NOTRUMP performs as expected.

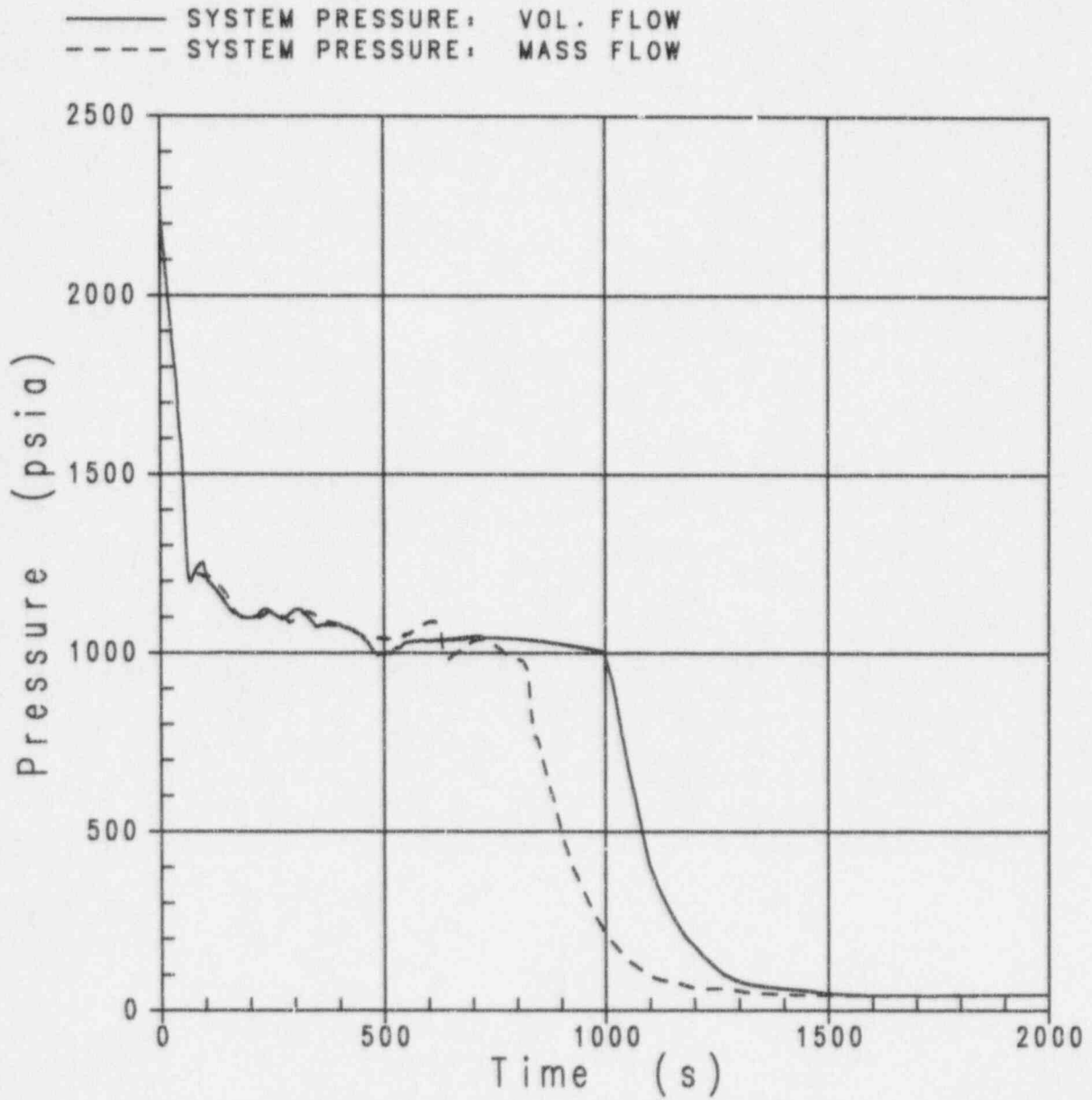


Figure 3.5-1 Reactor Coolant System Pressure

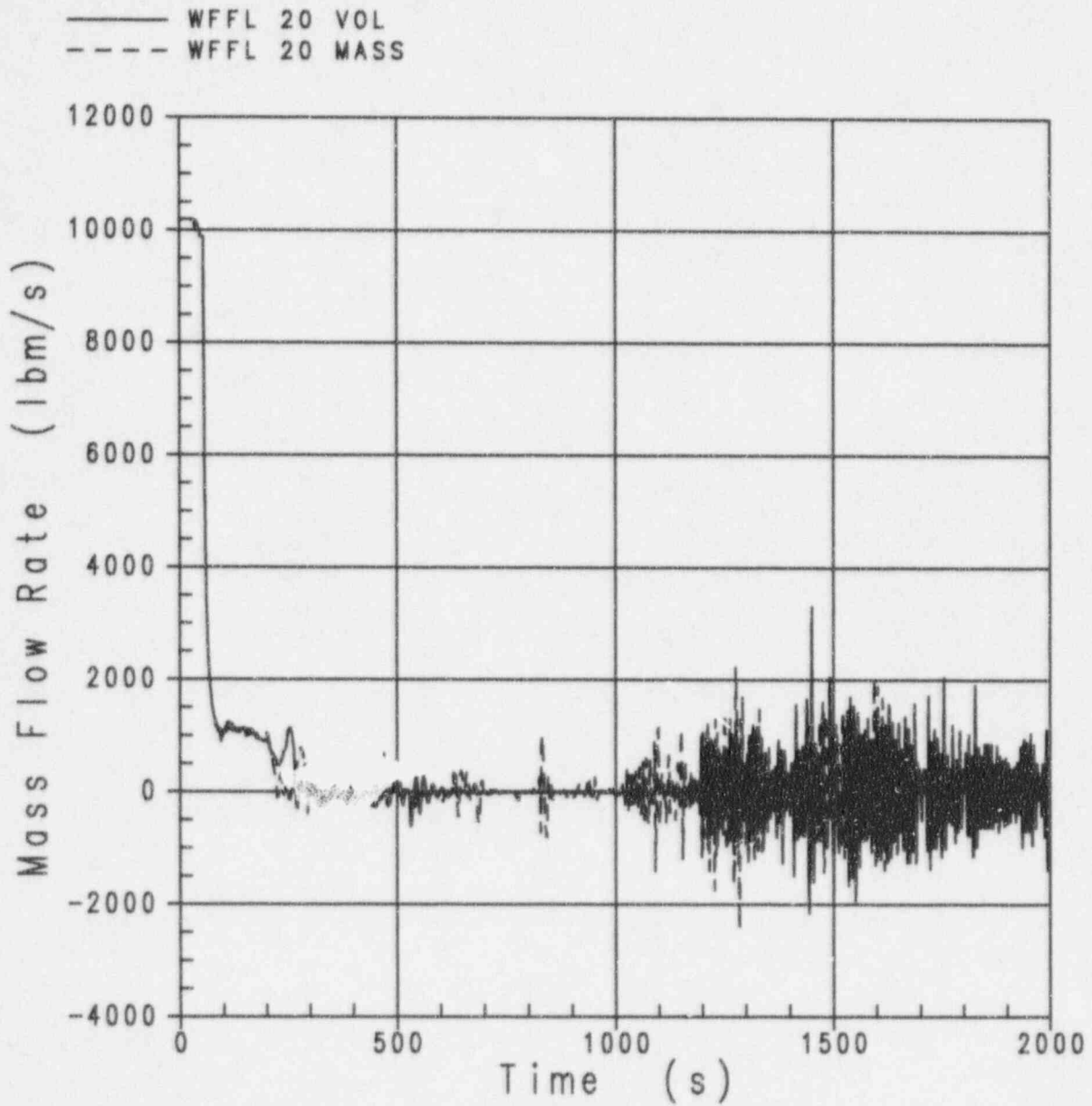


Figure 3.5-2 Comparison of Liquid Mass Flow Rates for Hot Leg 1

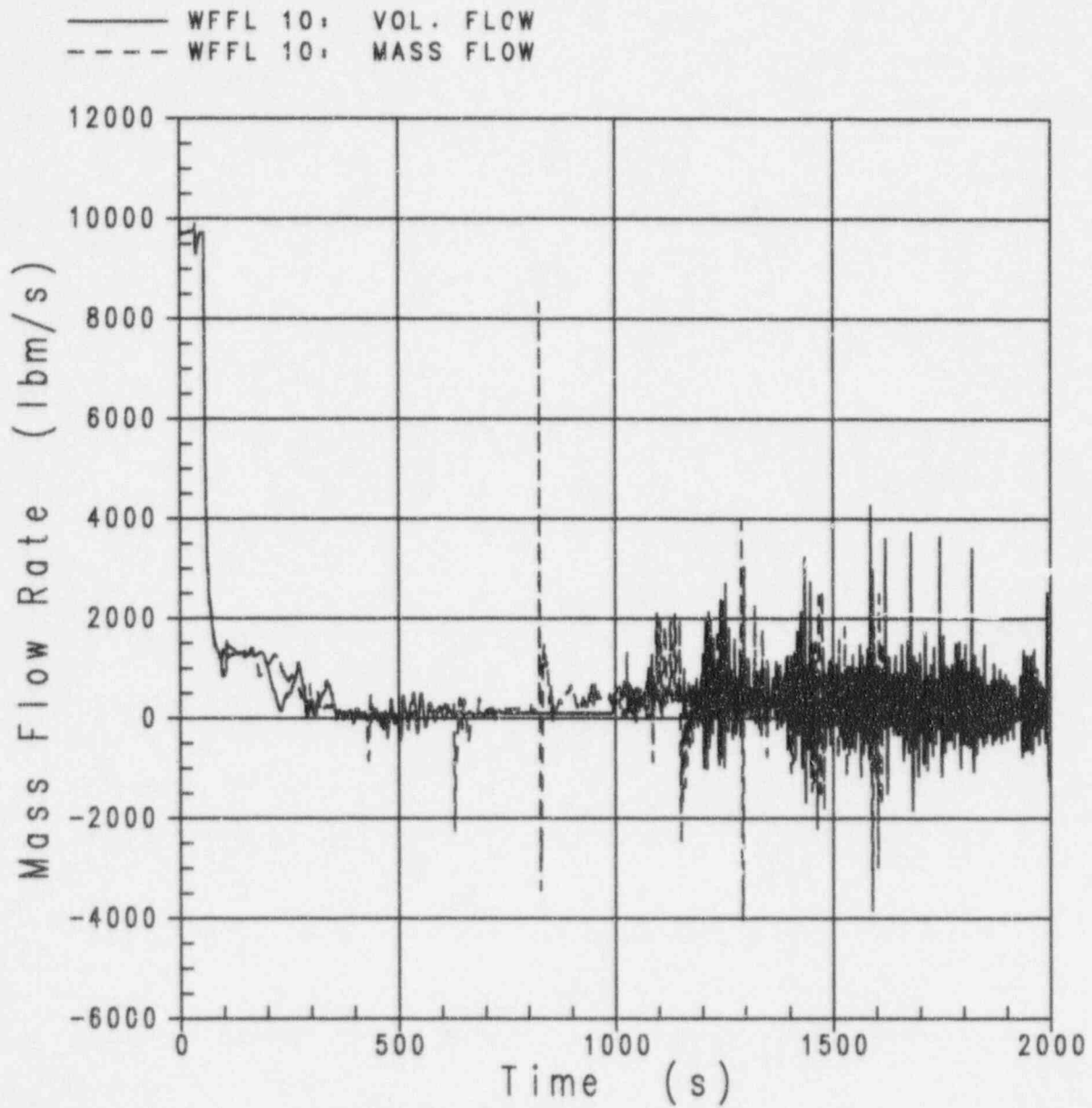


Figure 3.5-3 Comparison of Liquid Mass Flow Rates for Hot Leg 2

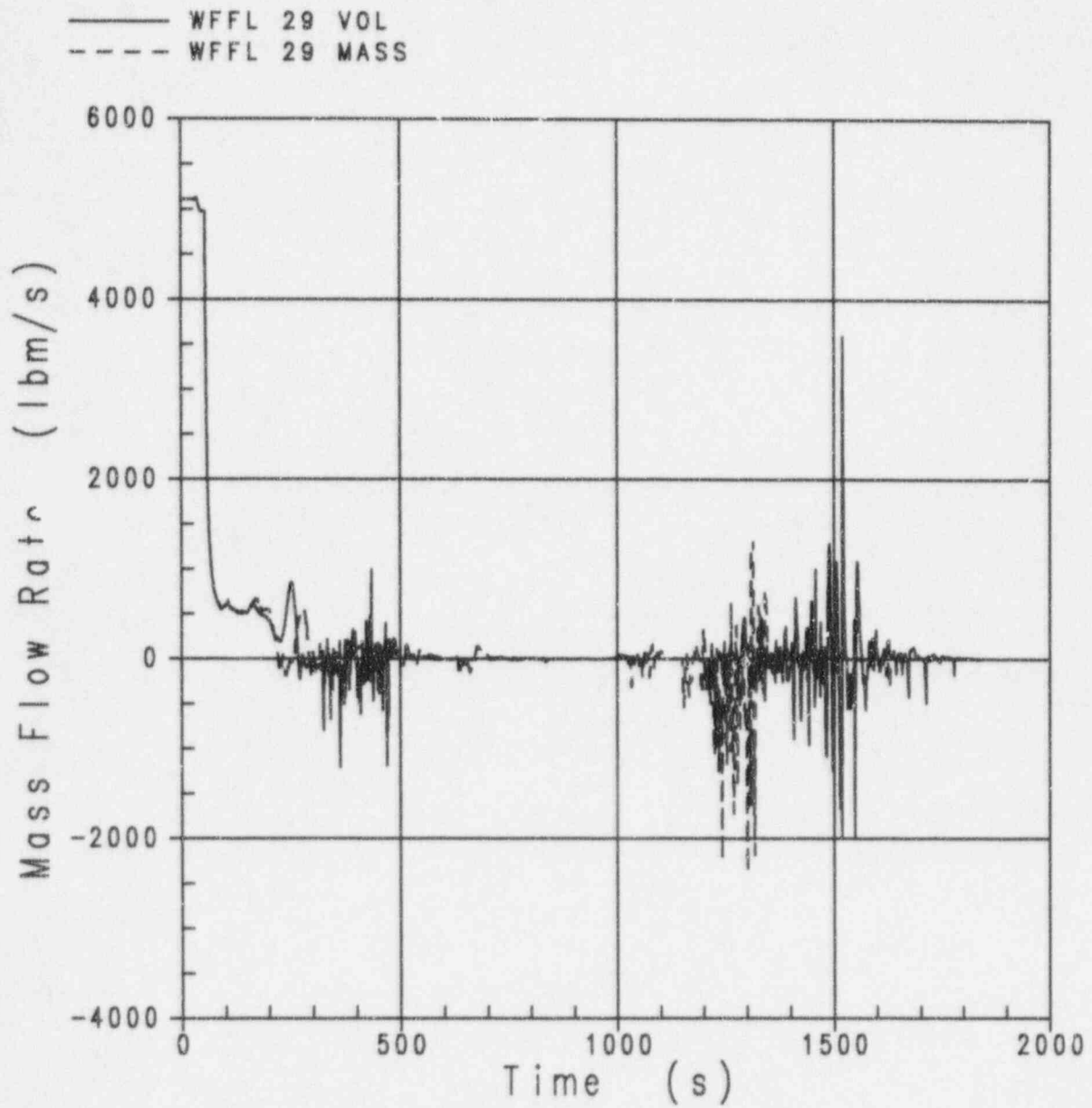


Figure 3.5-4 Comparison of Liquid Mass Flow Rates for Cold Leg 1

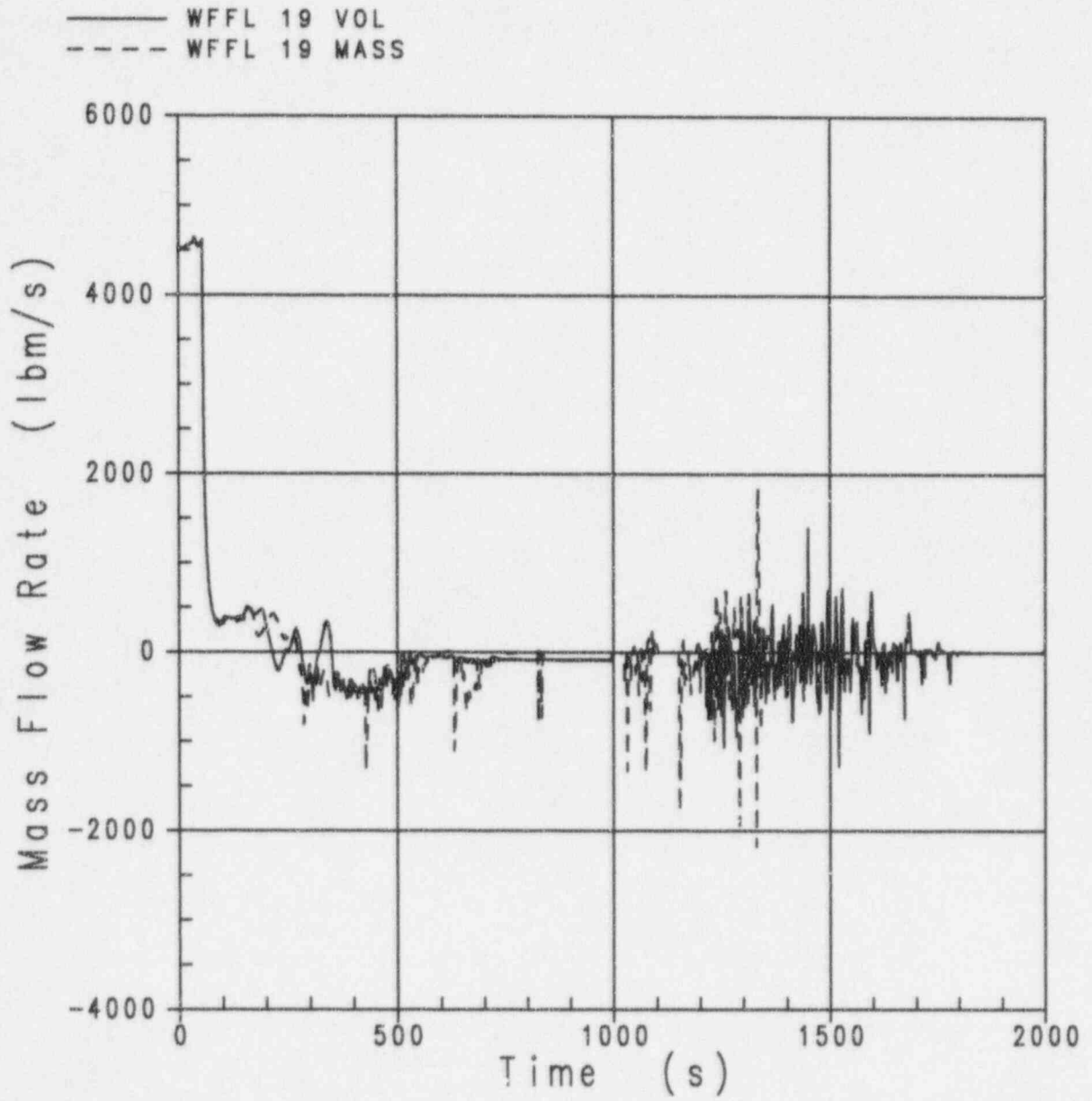


Figure 3.5-5 Comparison of Liquid Mass Flow Rates for Cold Leg 2

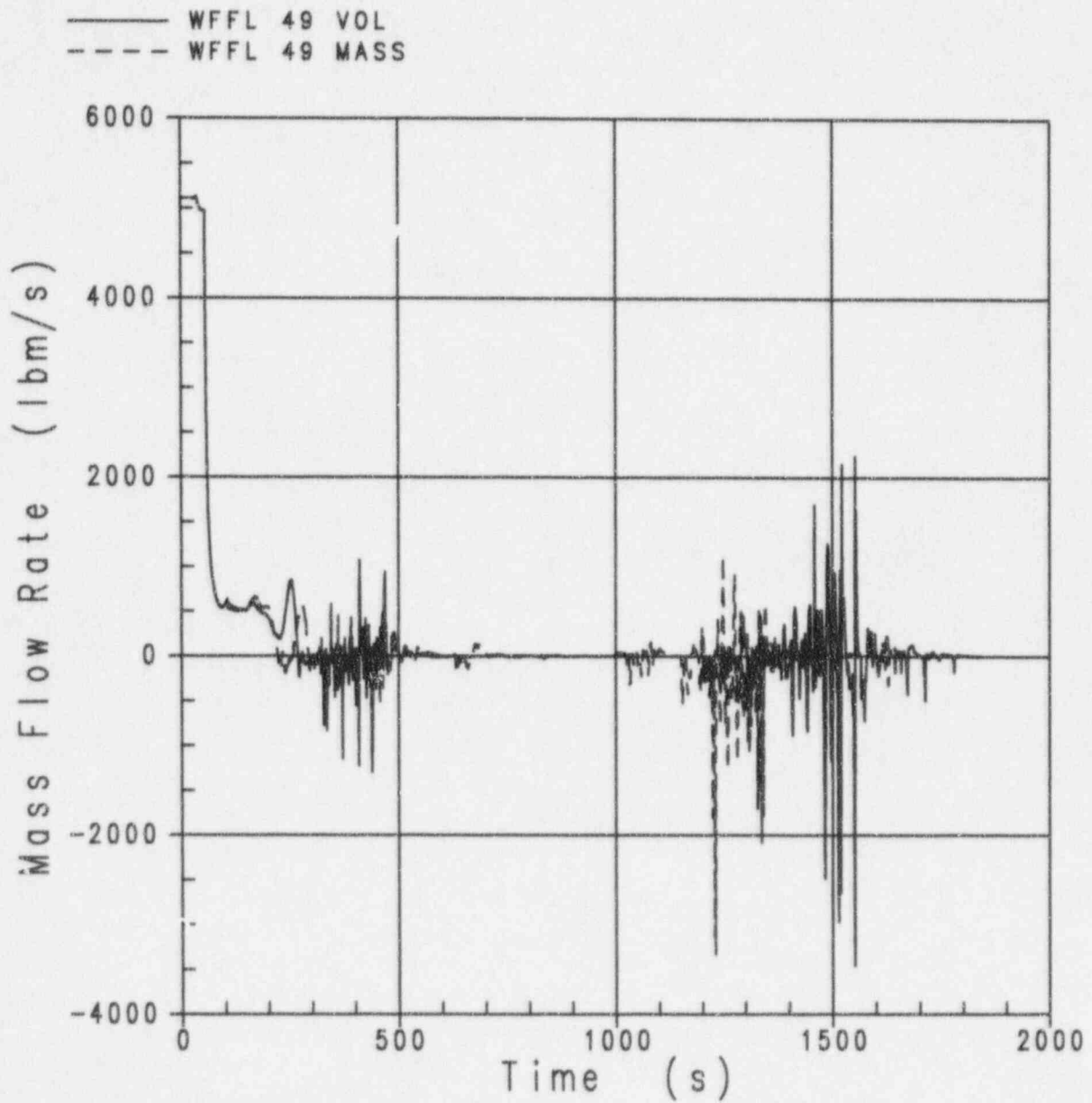


Figure 3.5-6 Comparison of Liquid Mass Flow Rates for Cold Leg 3

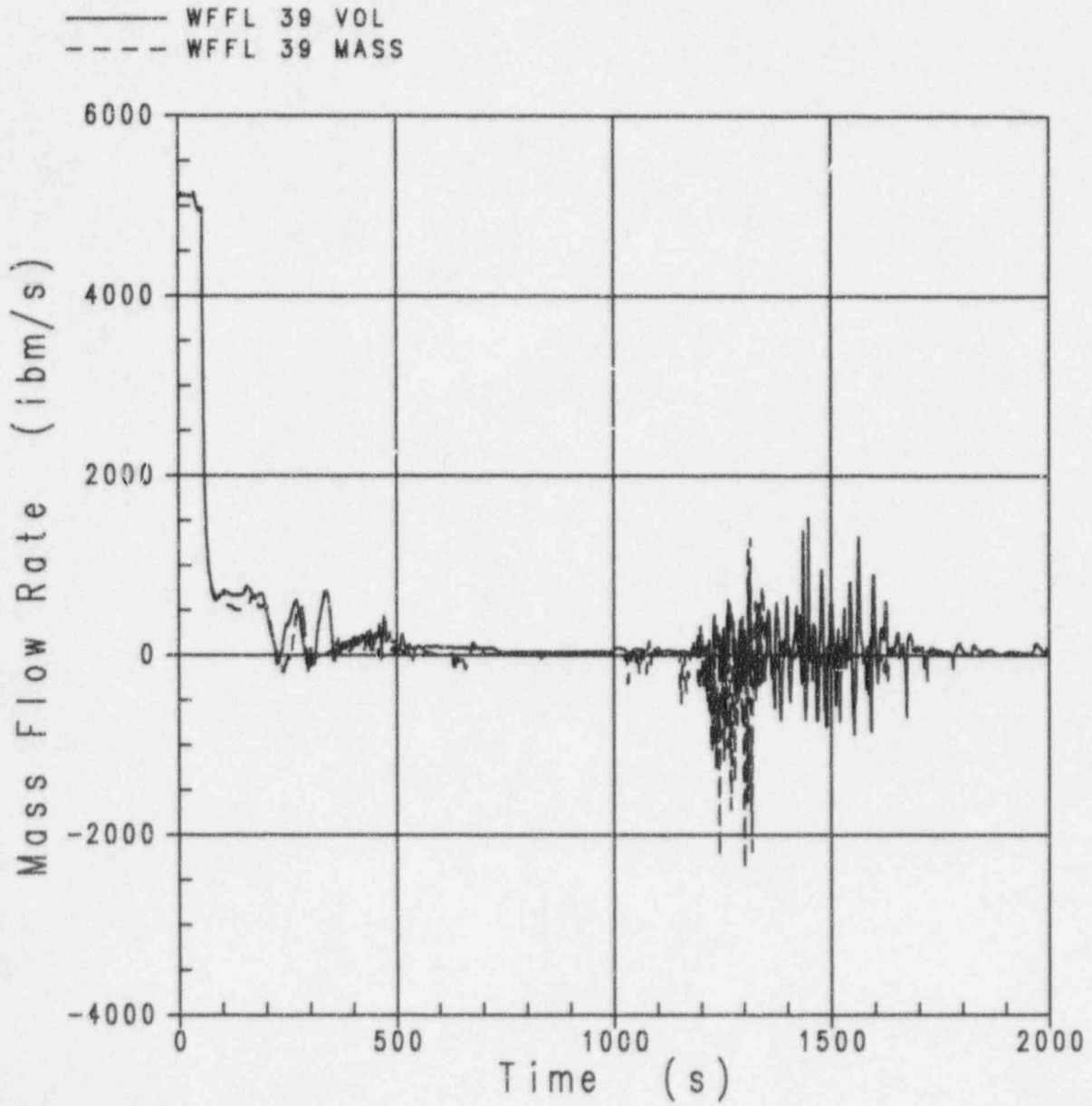


Figure 3.5-7 Comparison of Liquid Mass Flow Rates for Cold Leg 4

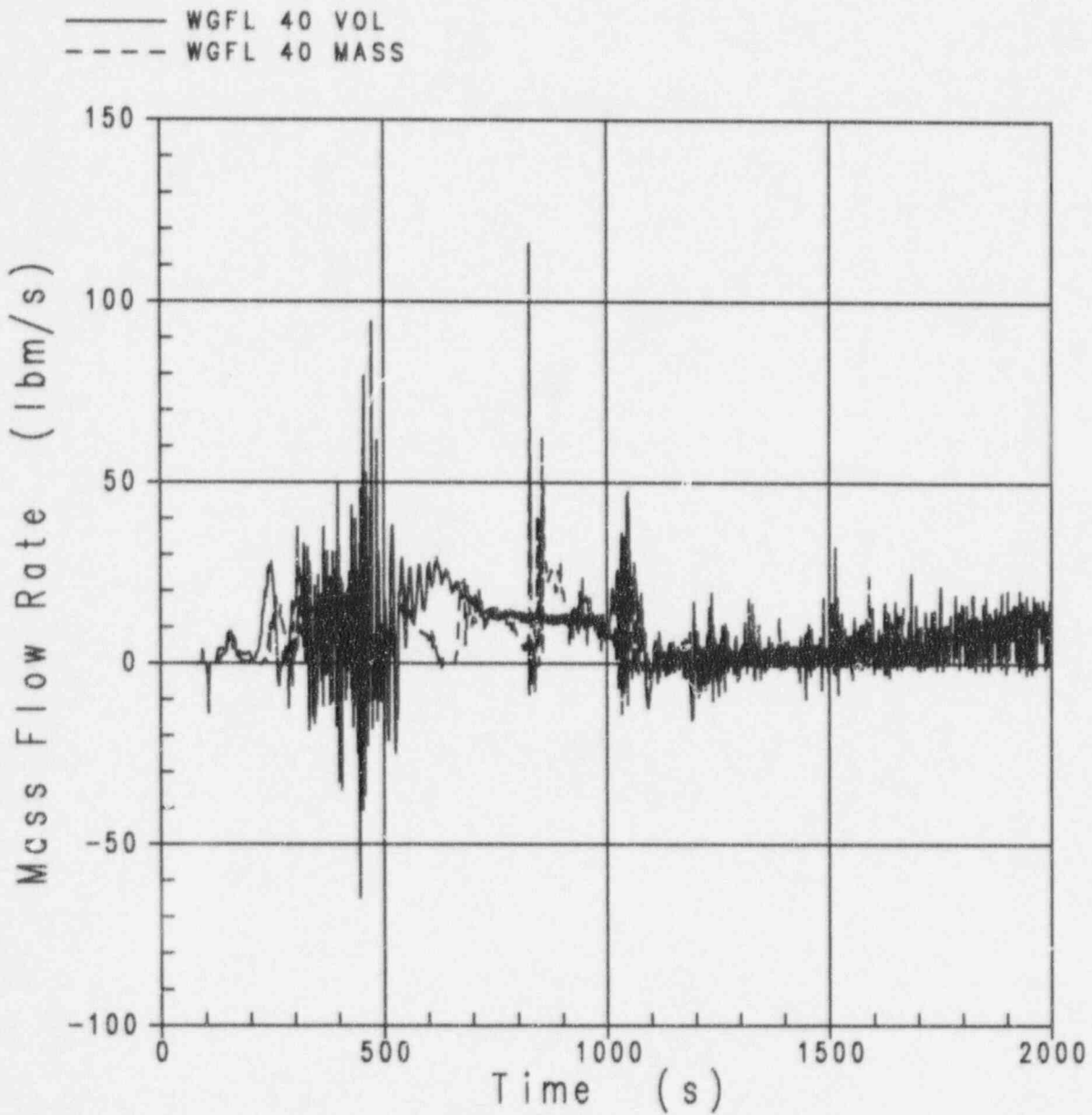


Figure 3.5-8 Comparison of Vapor Mass Flow Rates for Hot Leg 1

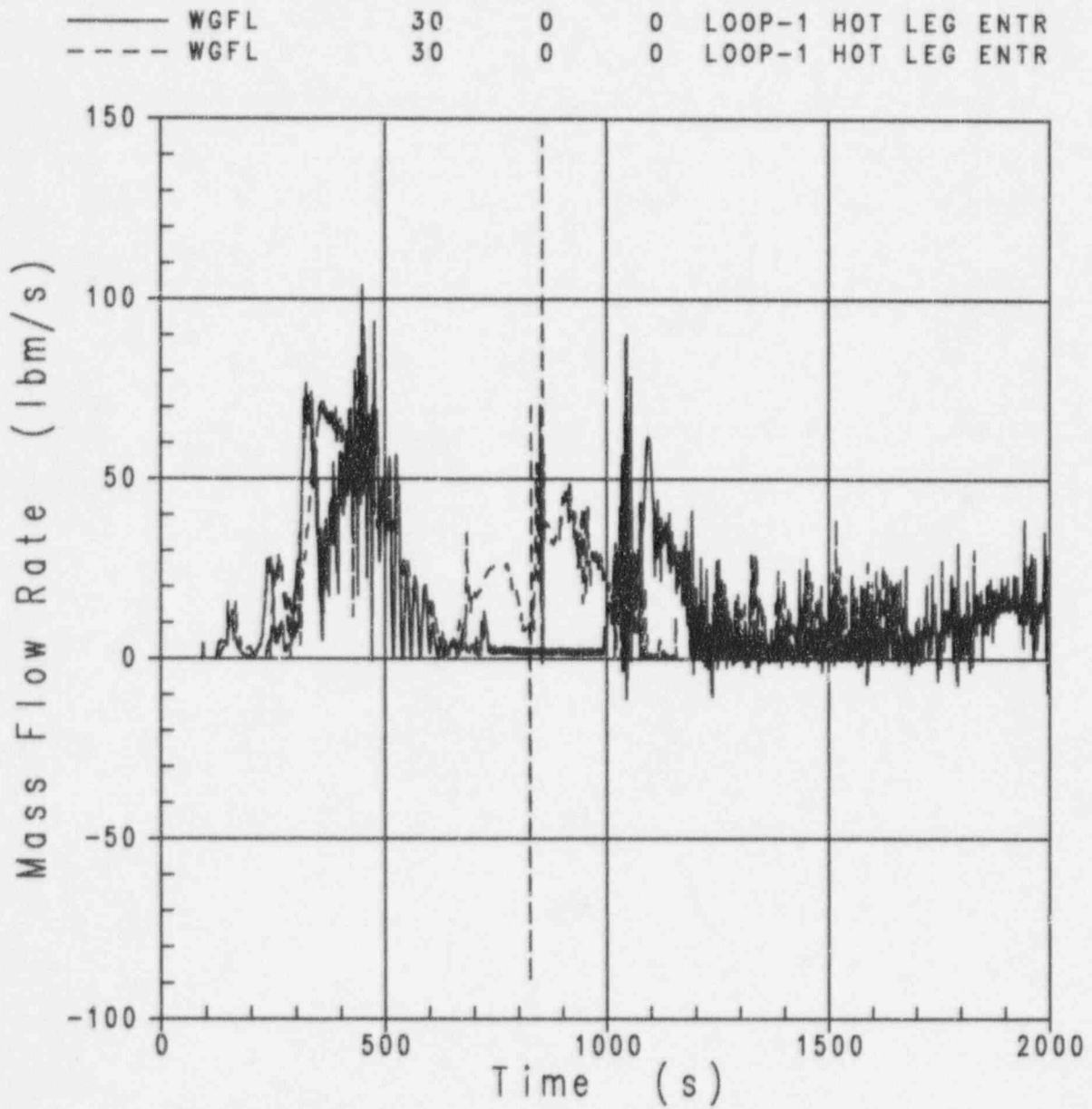


Figure 3.5-9 Comparison of Vapor Mass Flow Rates for Hot Leg 2

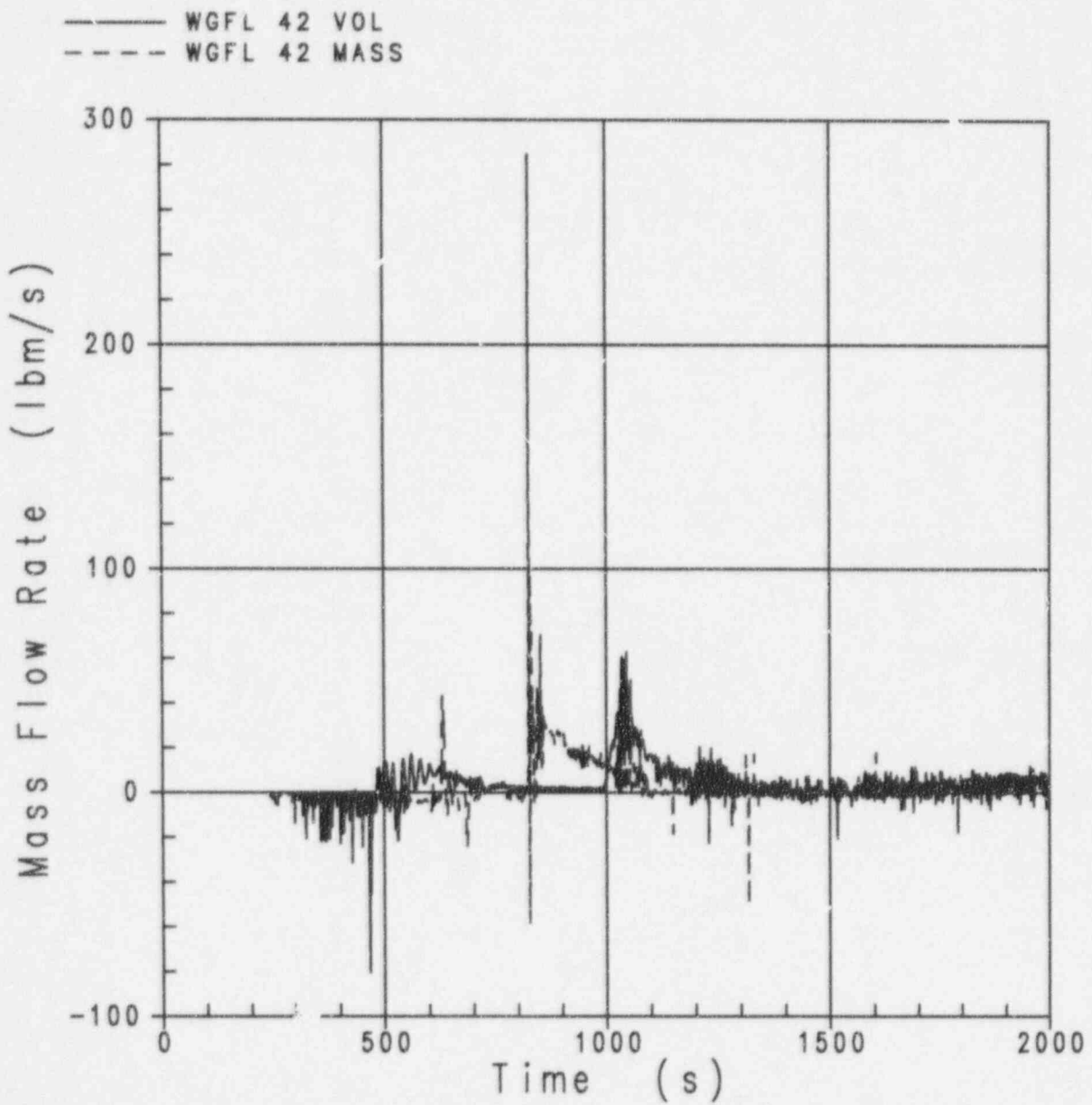


Figure 3.5-10 Comparison of Vapor Mass Flow Rates for Cold Leg 1

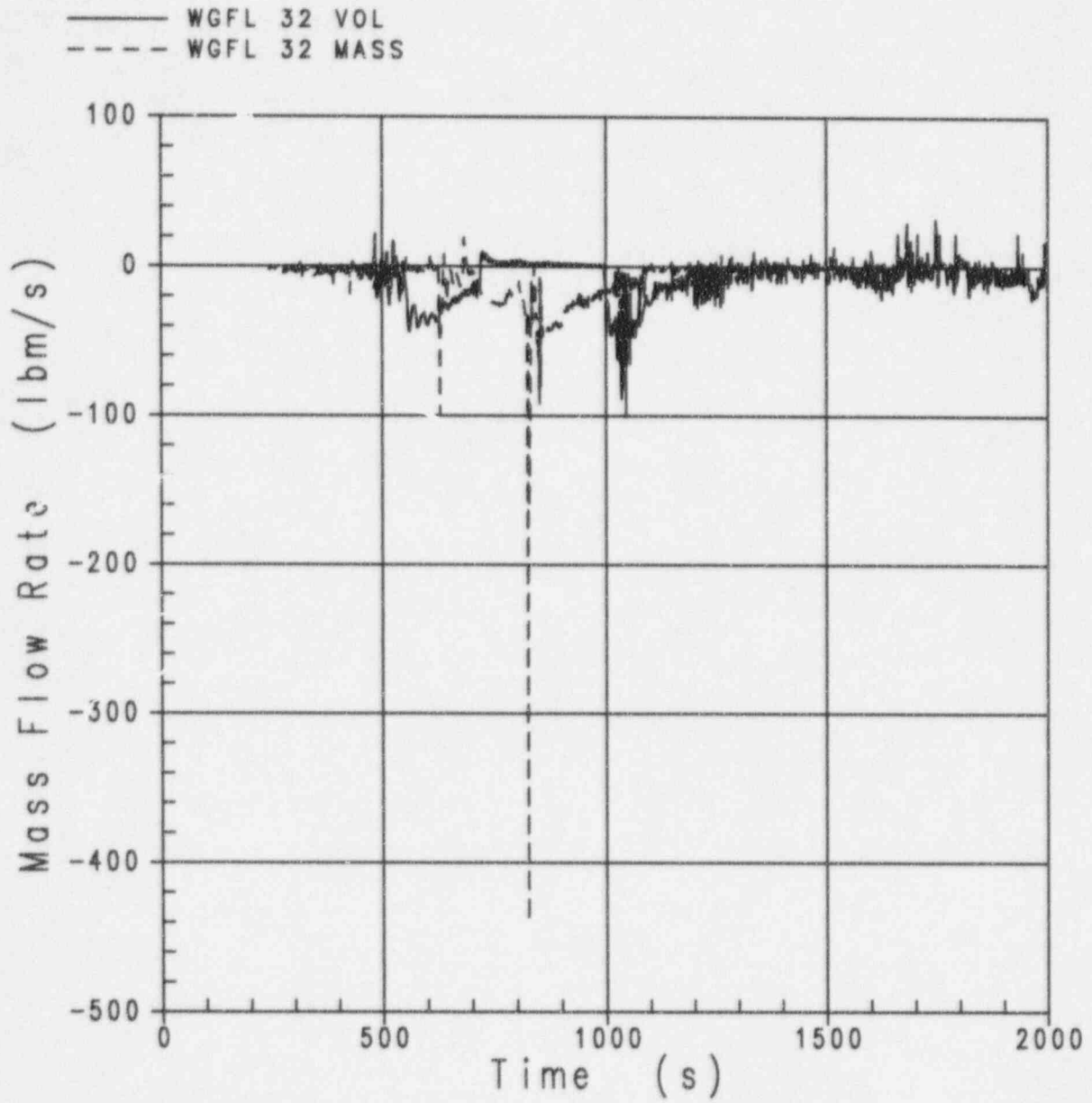


Figure 3.5-11 Comparison of Vapor Mass Flow Rates for Cold Leg 2

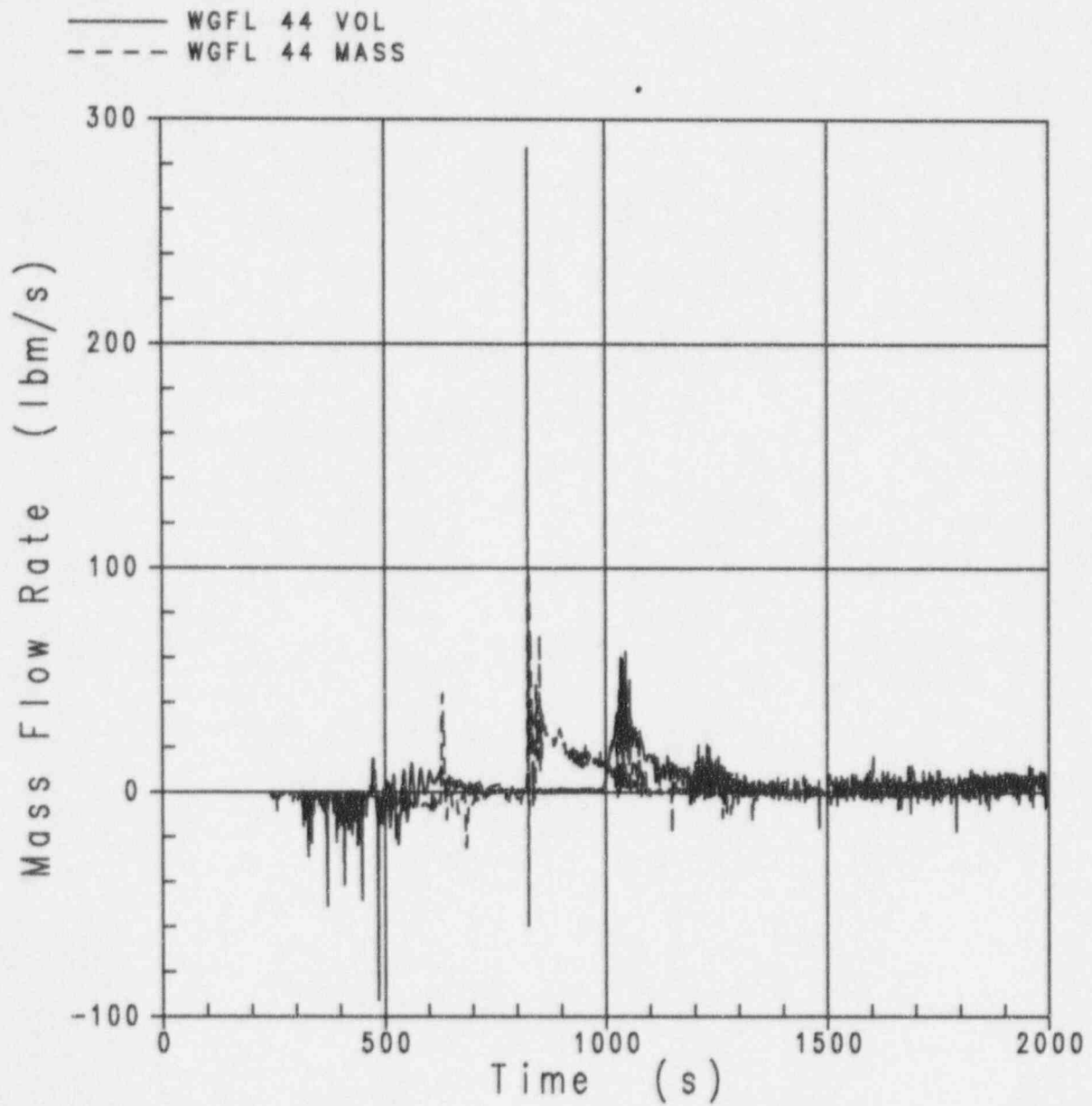


Figure 3.5-12 Comparison of Vapor Mass Flow Rates for Cold Le_3

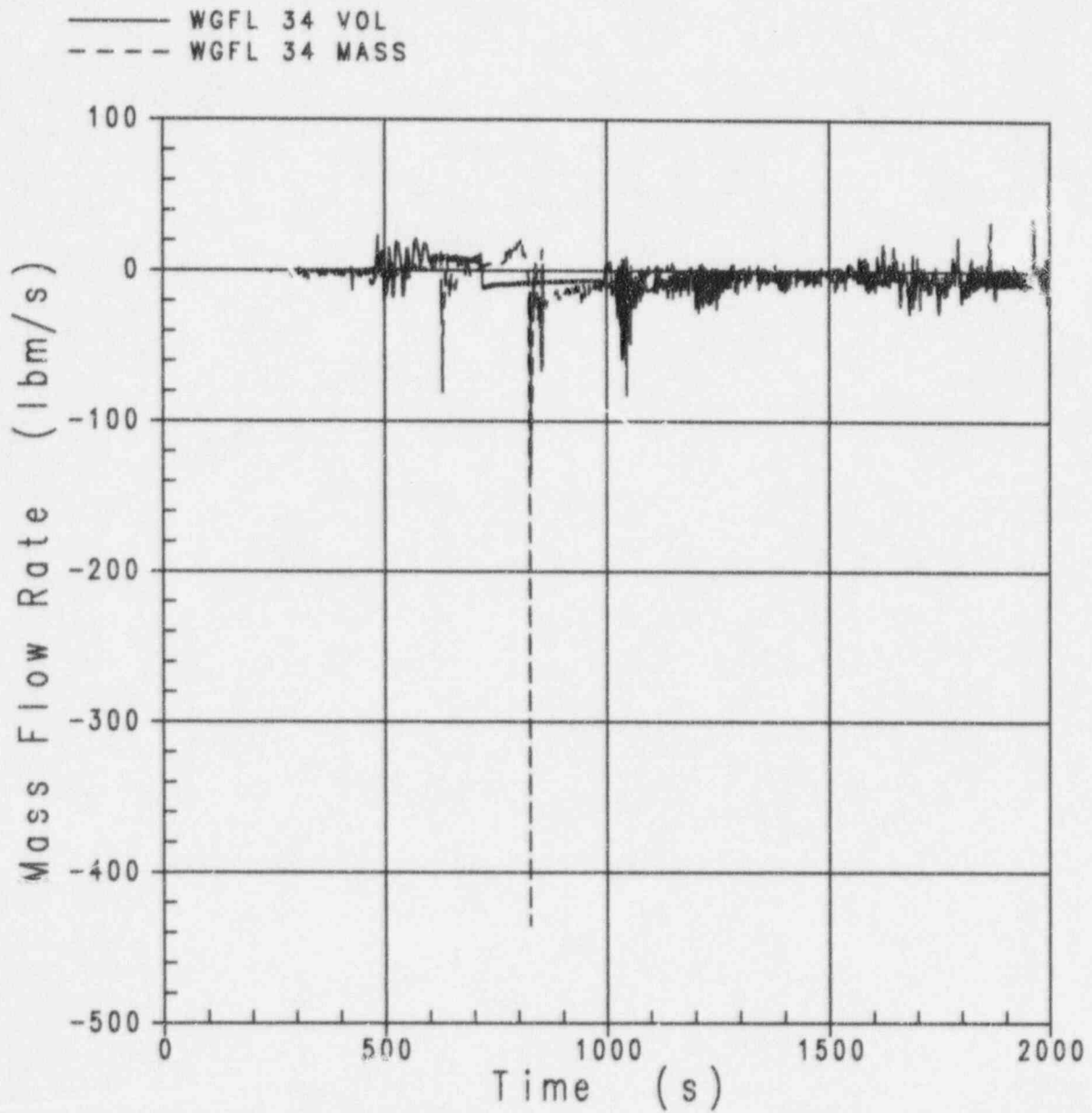


Figure 3.5-13 Comparison of Vapor Mass Flow Rates for Cold Leg 4



Figure 3.5-14 NOTRUMP Model for Demonstration Problem

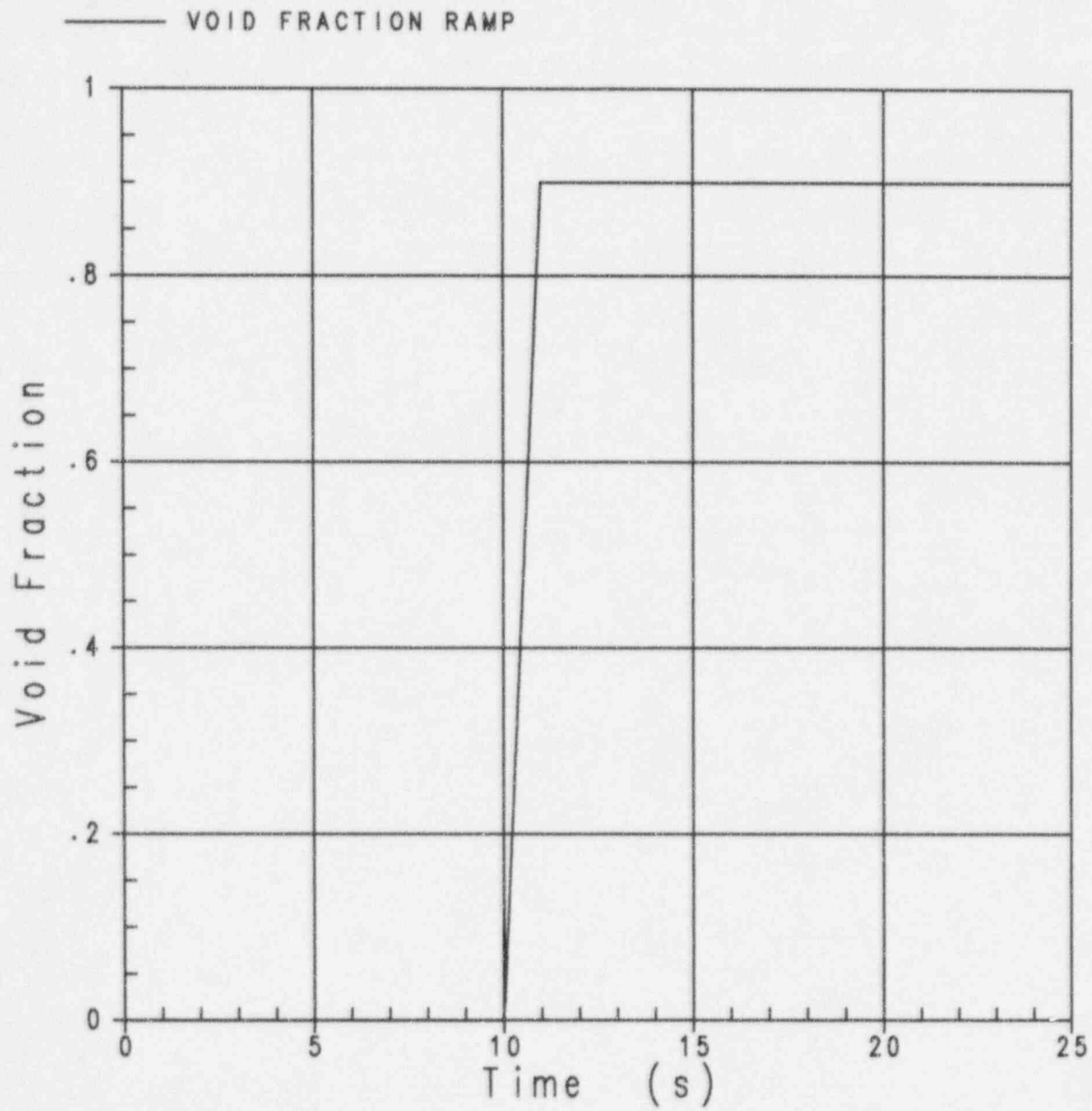


Figure 3.5-15 Void Fraction

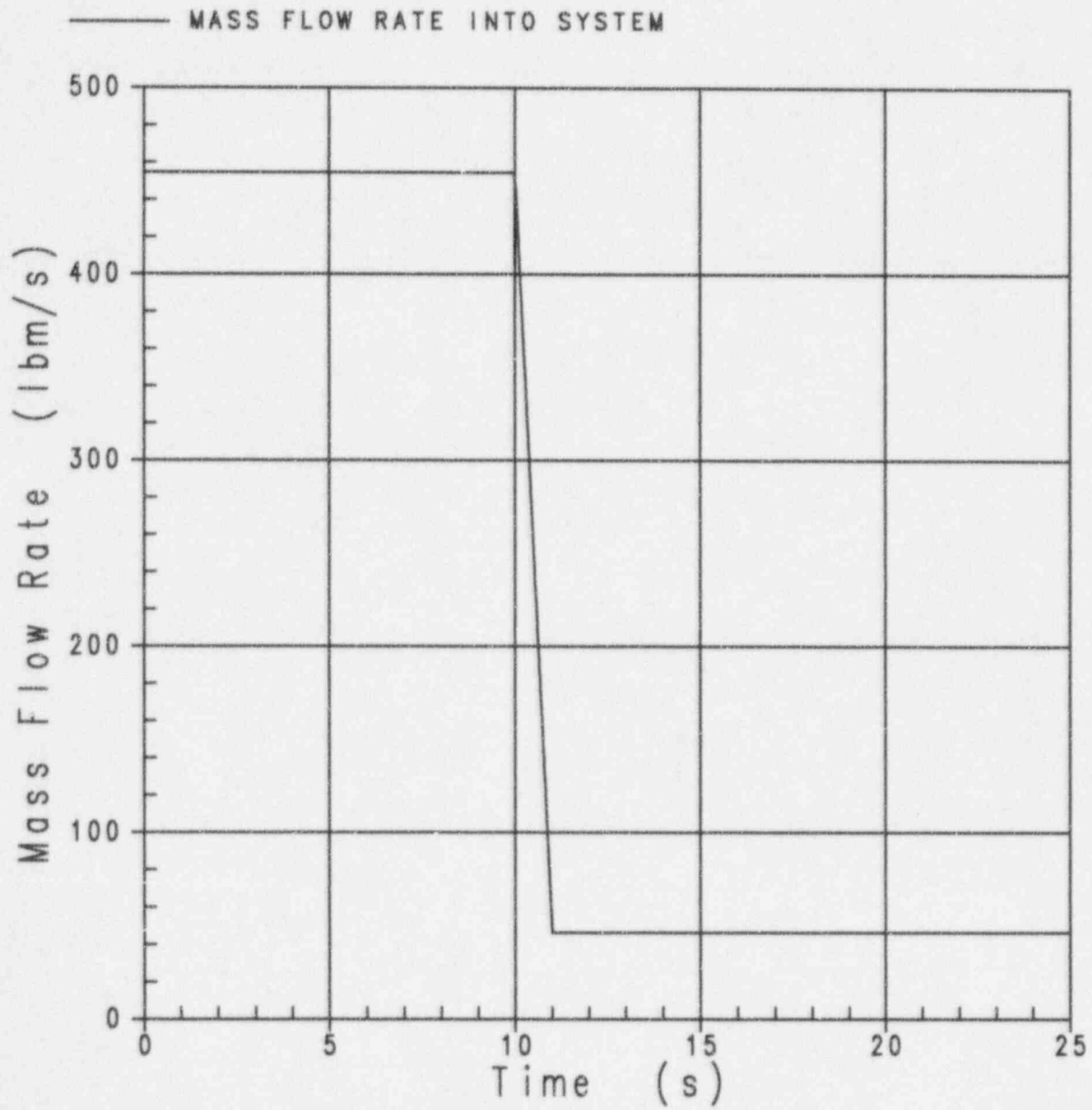


Figure 3.5-16 Mass Flow Rate into System

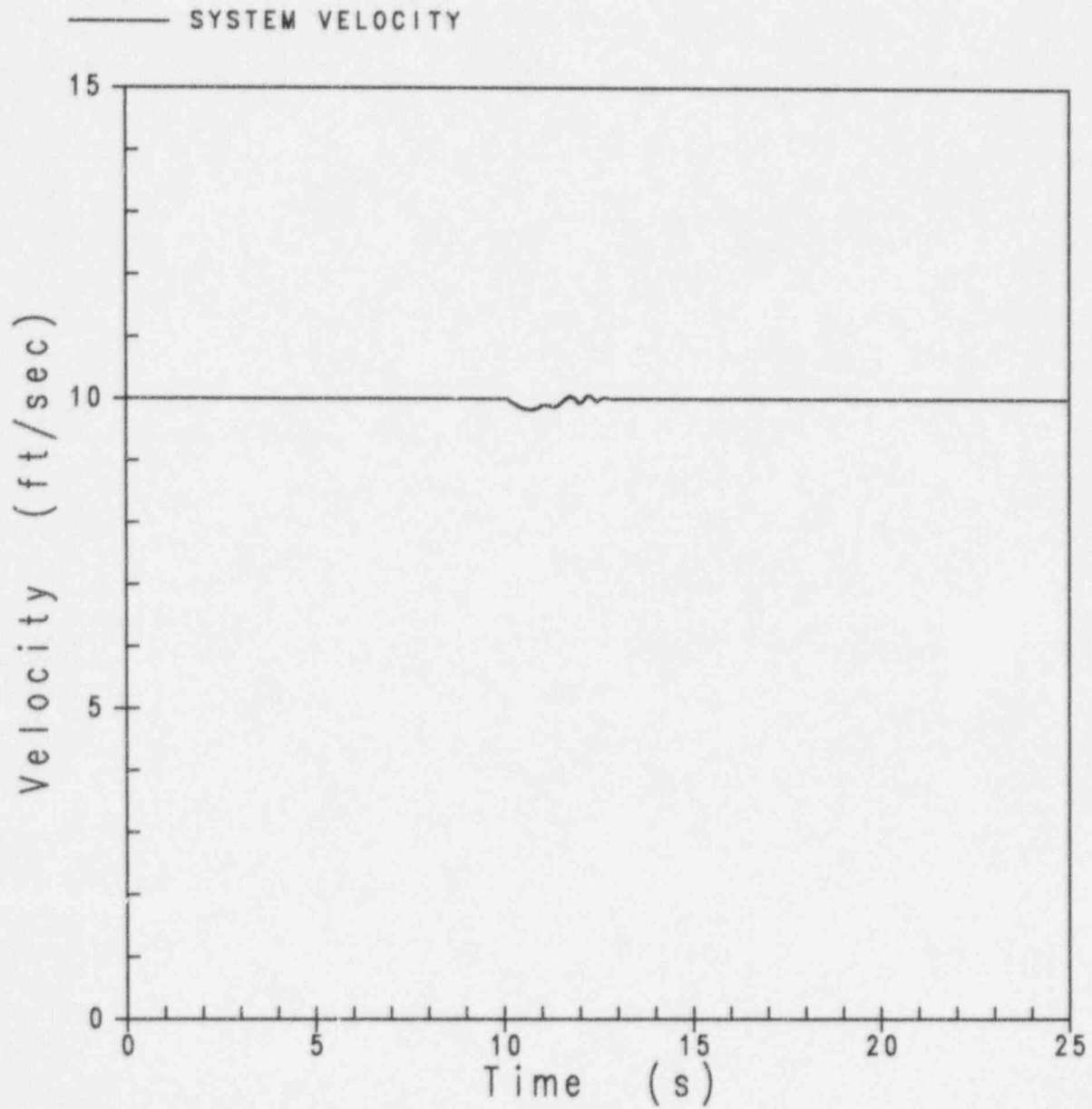


Figure 3.5-17 Velocity

3.6 Implicit Bubble Rise Model

The purpose of this test is to demonstrate the results of the implicit treatment of bubble rise in calculations. This is done by simulating a constant pressure boil-off problem with both the existing explicit treatment of bubble rise and the new implicit treatment of bubble rise.

The NOTRUMP model for this test consists of a two-node stack connected at the top to a constant pressure boundary node. Heat is applied to the bottom node in the stack, which allows the froth level to swell well into the upper node. The noding diagram for this problem is shown in Figure 3.6-1.

The nodes are initialized with a stack water level of 1.5 ft., a water mass of approximately 66 lbm, and an initial enthalpy of 298.4 Btu/lbm, which is the enthalpy at a saturation pressure of 100 psia. Heat is then applied to the bottom node at a constant rate of 25 Btu/sec. for the entire transient. The test is performed until the boil-off results in a mixture level well into the lower node.

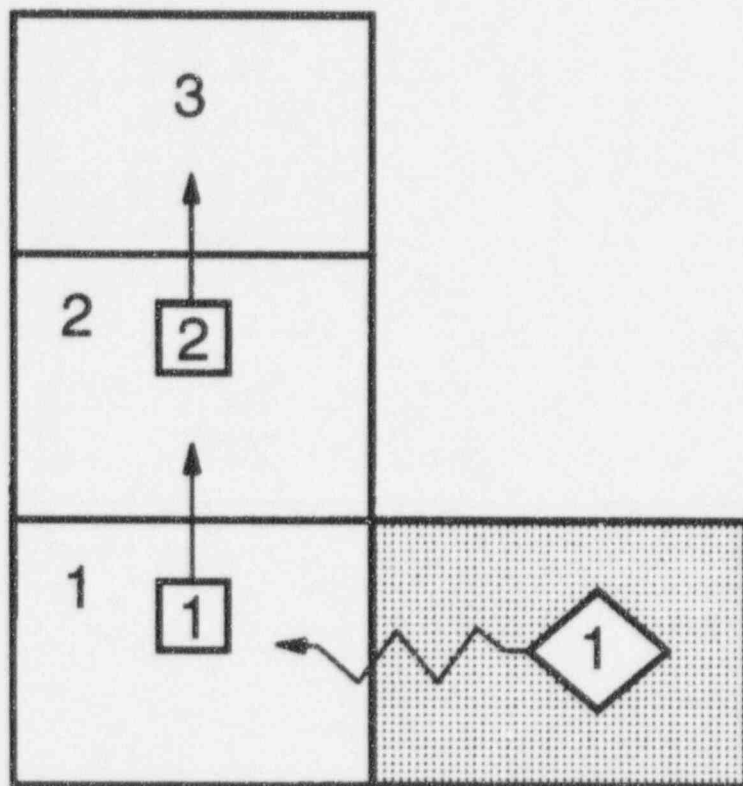
Results of the two calculations are presented in Figures 3.6-2 through 3.6-8.

The mixture level of the two-node stack is presented in Figure 3.6-2. In contrast to the explicit bubble rise model, the implicit bubble rise model results in a smooth transition as the mixture level crosses the node boundary at an elevation of 1 ft. The smooth transition represents the desired result, as there is no physical mechanism at the node boundary to cause the mixture level hanging behavior or discontinuity at the node boundary as seen in the explicit bubble rise model.

Figures 3.6-3 and 3.6-4 illustrate the mixture region void fractions for the explicit and implicit bubble rise models, respectively. The explicit bubble rise model predicts an increasing void fraction in the upper node mixture region as it drains (see Figure 3.6-3). However, for the implicit bubble rise model, shown in Figure 3.6-4, the upper node void fraction matches the lower node void fraction up to the time when the upper node drains. Thus, the implicit bubble rise model correctly predicts the mixture region void fraction of a node being drained.

One other aspect of the implicit bubble rise model is its stability when the model convects more bubble mass out of a region during a time step than exists in the region at the beginning of the time step, i.e., the material courant limit is violated. For the explicit bubble rise model, a limit is placed on the code so that the material courant limit can not be violated (see Figure 3.6-5). However, Figure 3.6-6 depicts the implicit bubble rise model, which allows the material courant limit to be violated. During the time period that the material courant limit is violated, the code continues to show no instability in calculated pressure or flow (see Figures 3.6-7 and 3.6-8, respectively).

In conclusion, the implicit bubble rise model performs as expected and increases the robustness of the NOTRUMP bubble rise calculation.



- Interior Fluid Node

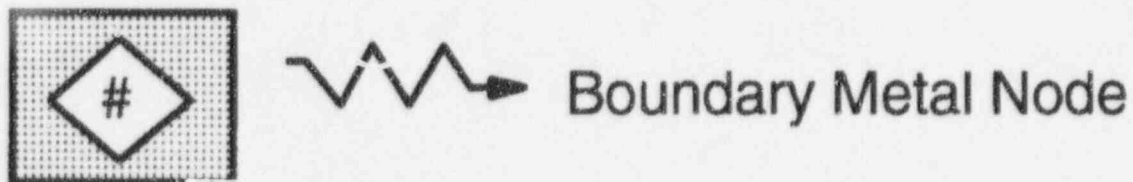
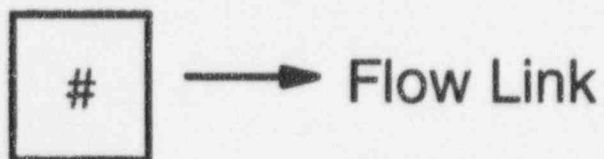


Figure 3.6-1 NOTRUMP Model for Boil-Off Problem

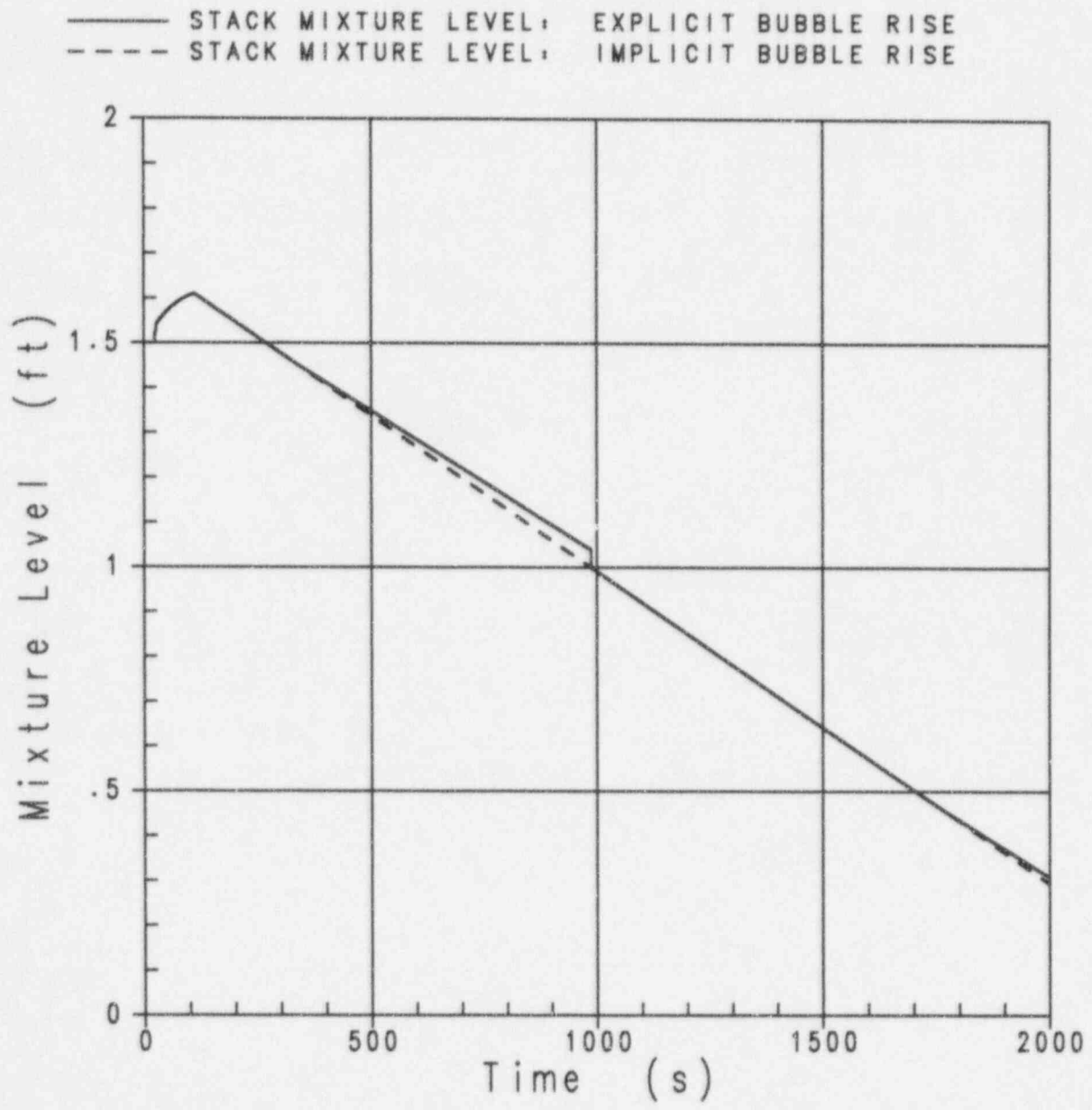


Figure 3.6-2 Mixture Levels

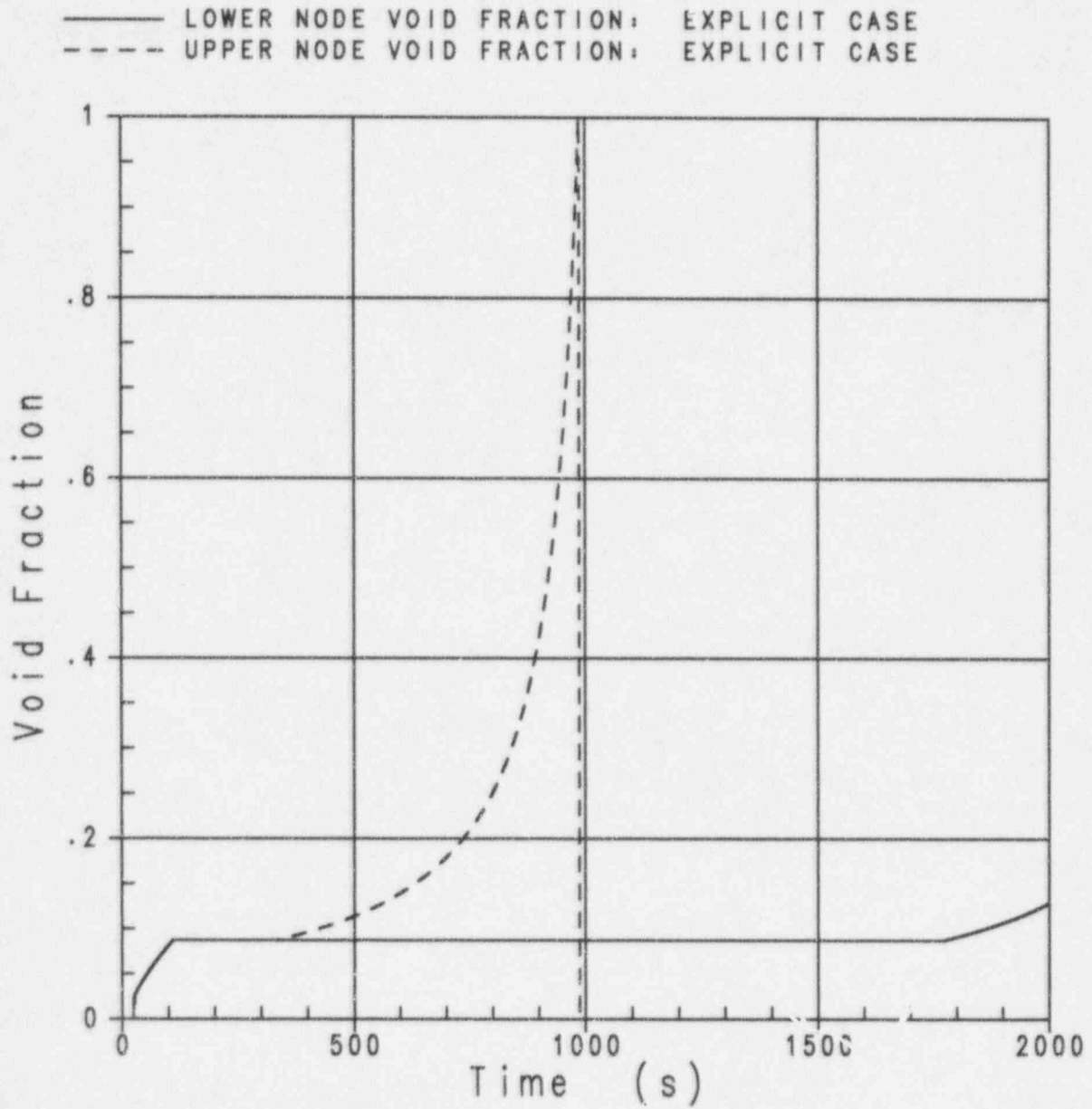


Figure 3.6-3 Void Fractions

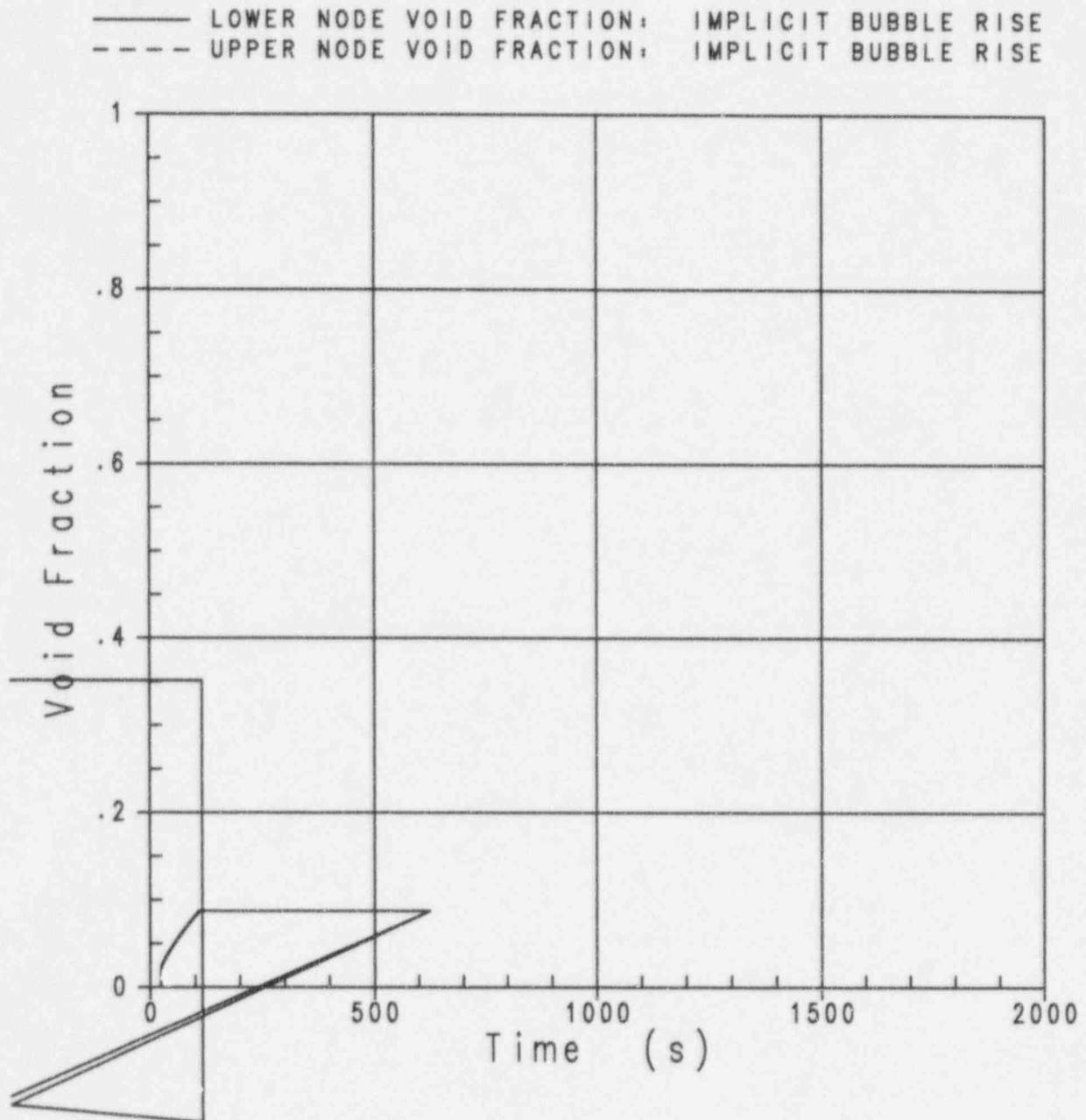


Figure 3.6-4 Void Fractions

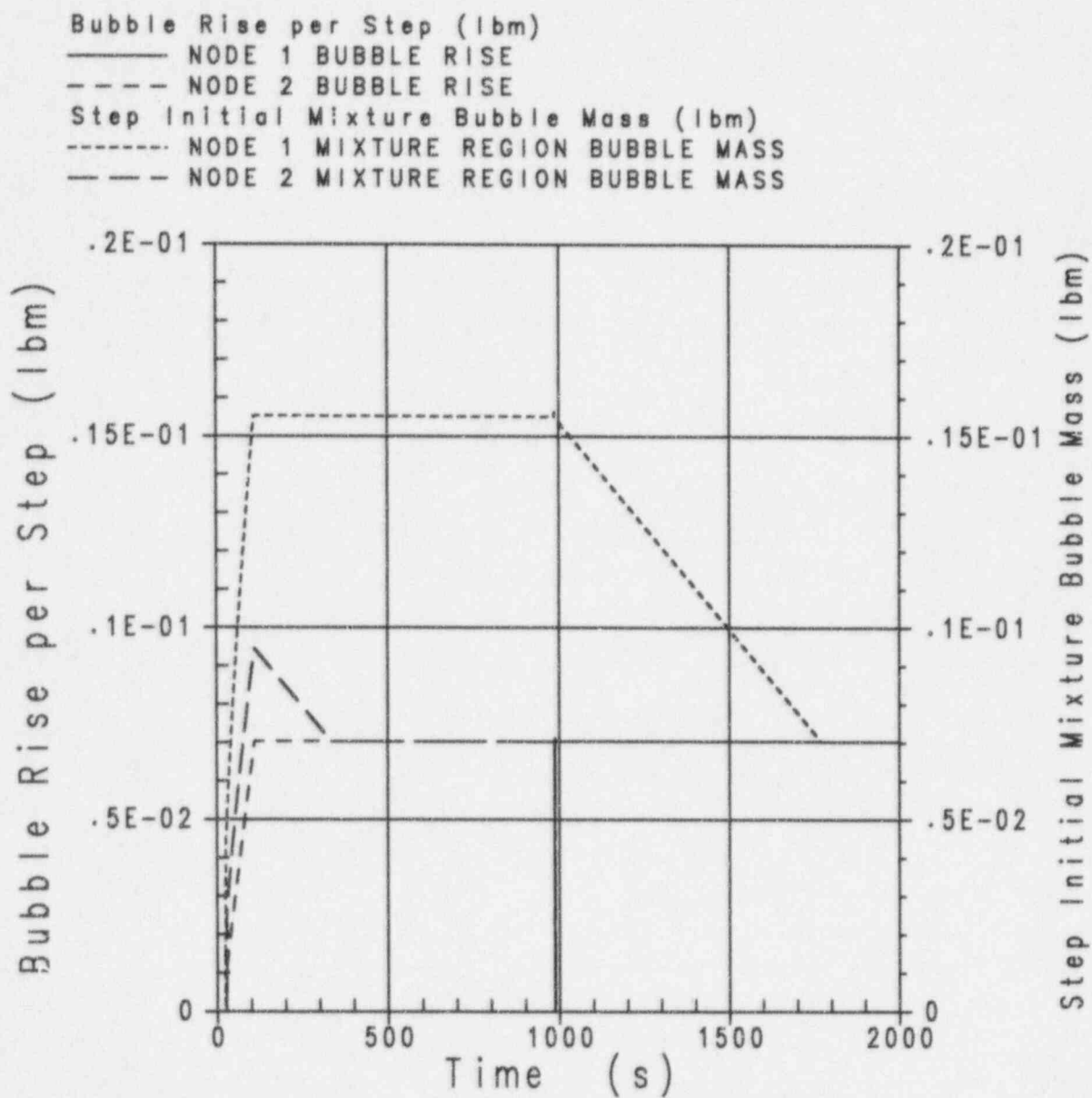


Figure 3.6-5 Bubble Rise per Step and Step Initial Mixture Bubble Mass (Explicit Bubble Rise)

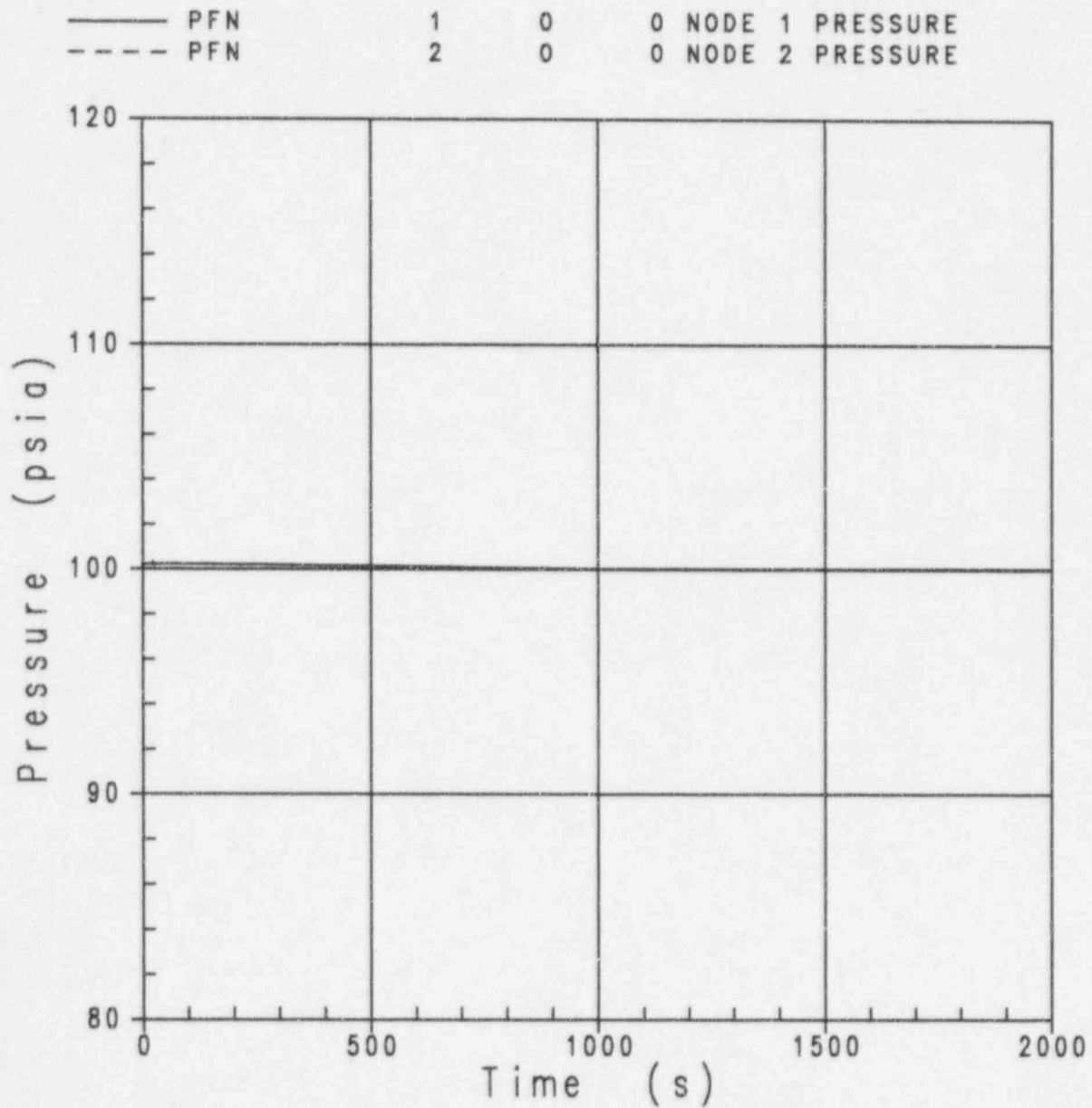


Figure 3.6-7 Node Pressures with Implicit Bubble Rise

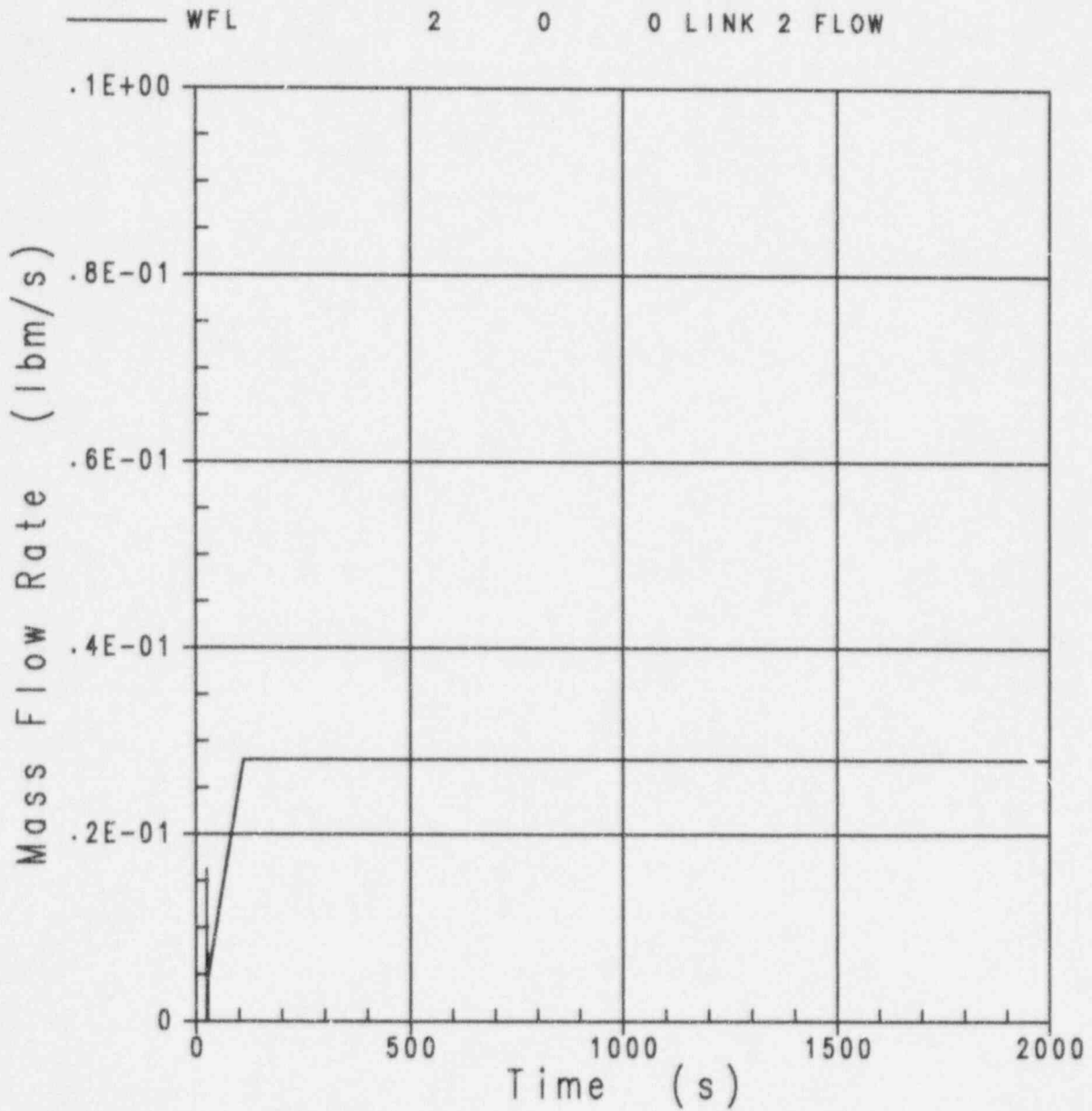


Figure 3.6-8 Link 2 Flow Rate with Implicit Bubble Rise

3.7 Main Coolant Pump Model

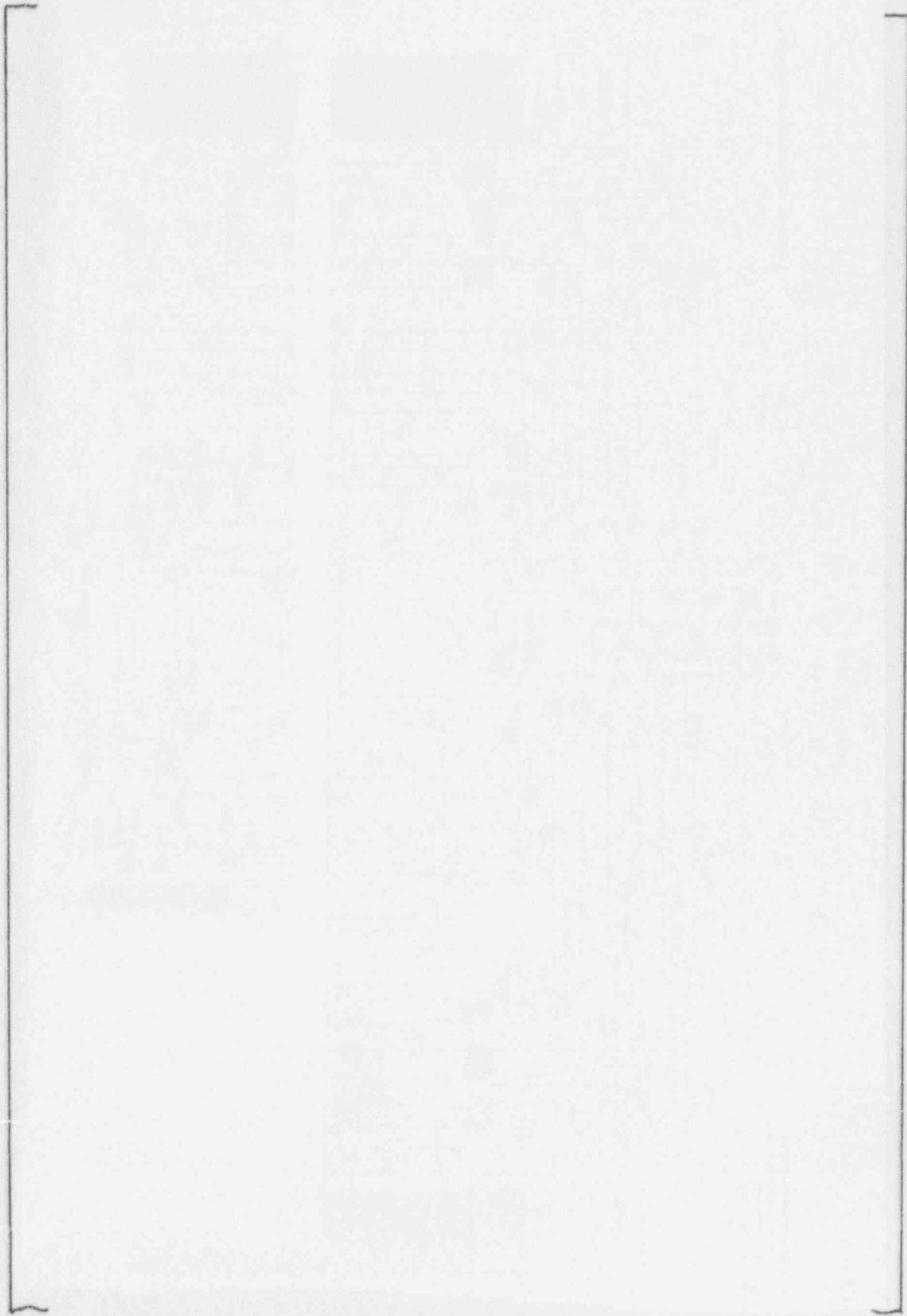
The purpose of this test is to assess the effects of changes to the main coolant pump model. The coding changes mainly affect the calculations while the pump is operating and the pump coastdown after the pumps trip. Therefore, an AP600 plant calculation is performed through the completion of the main coolant pump coastdown. This calculation is performed twice, once with and once without the new pump model actuated.

The NOTRUMP model of the AP600 plant used for this test is the same as that contained in the preliminary FSAR calculations. The noding diagram is shown in Figure 3.7-1. The test case chosen is a 2-in. cold leg break (break in node 19).

Results

The break is assumed to occur at time zero. Reactor trip is modeled to occur when the reactor coolant system (RCS) pressure decreases to 1800 psia with approximately a 2.5-sec. delay once the setpoint is reached. The main coolant pumps are modeled to trip approximately 16 sec. after the RCS pressure decreases to 1700 psia. For both cases, the reactor trip setpoint is reached at approximately 32.5 sec. with a resultant trip at approximately 35 sec., and the main coolant pump trip setpoint is reached at approximately 39 sec. with a resultant trip at approximately 55 sec. Both cases are terminated at 300 sec., after the coastdown is completed and the pump model has ceased having a significant effect on the results.

Results of the two calculations are presented in Figures 3.7-2 through 3.7-6, which show the pressurizer pressure and mass flow rates through a pump to a cold leg on each loop. There is no noticeable difference in the calculated results of system pressure and flow rates through the time the pump model is expected to have an influence on results. Therefore, the changes to the pump model, while making the calculations more robust, do not significantly affect the results.



a,c

Figure 3.7-1 Plant Noding Diagram

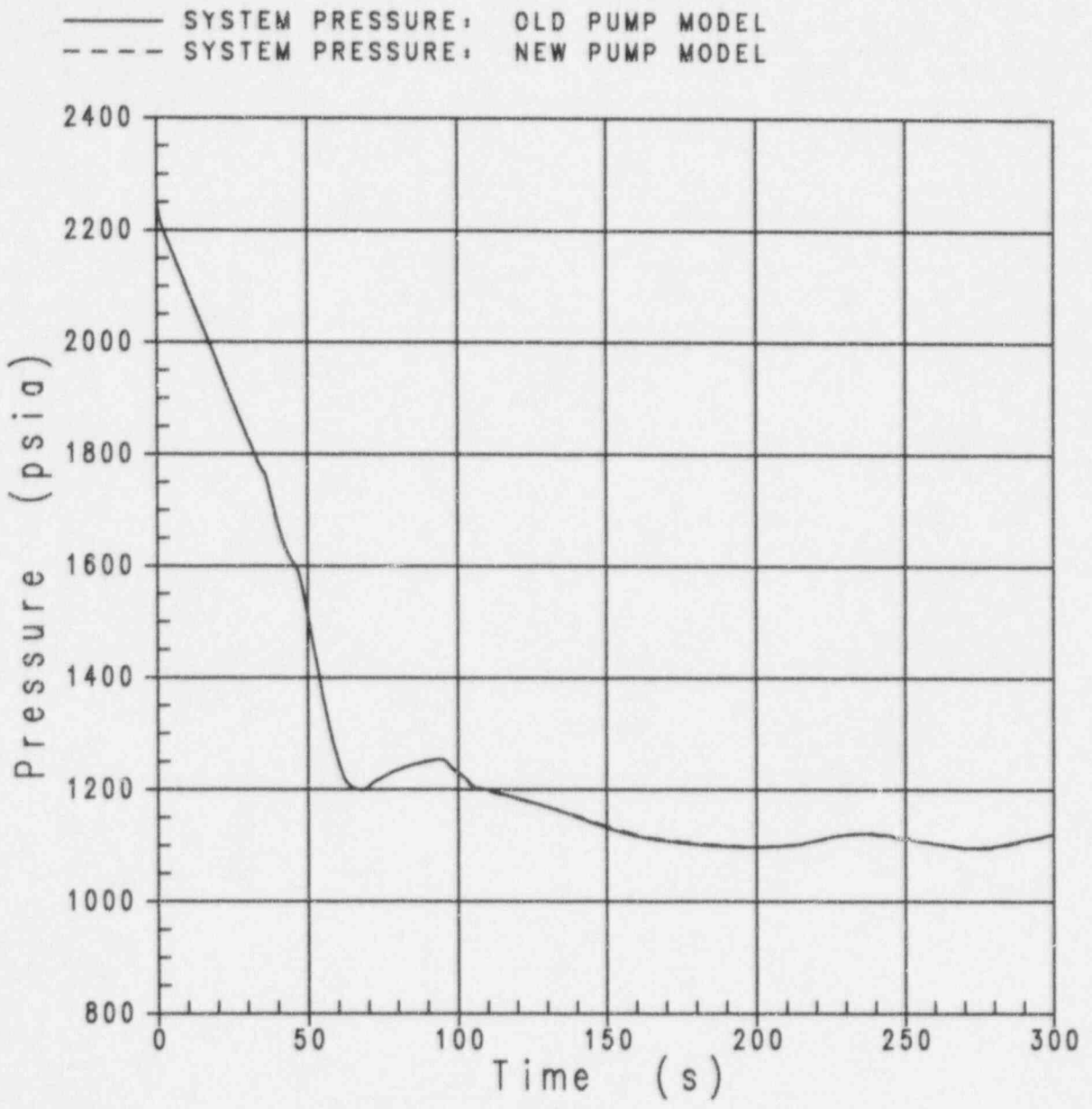


Figure 3.7-2 Pressurizer Pressure

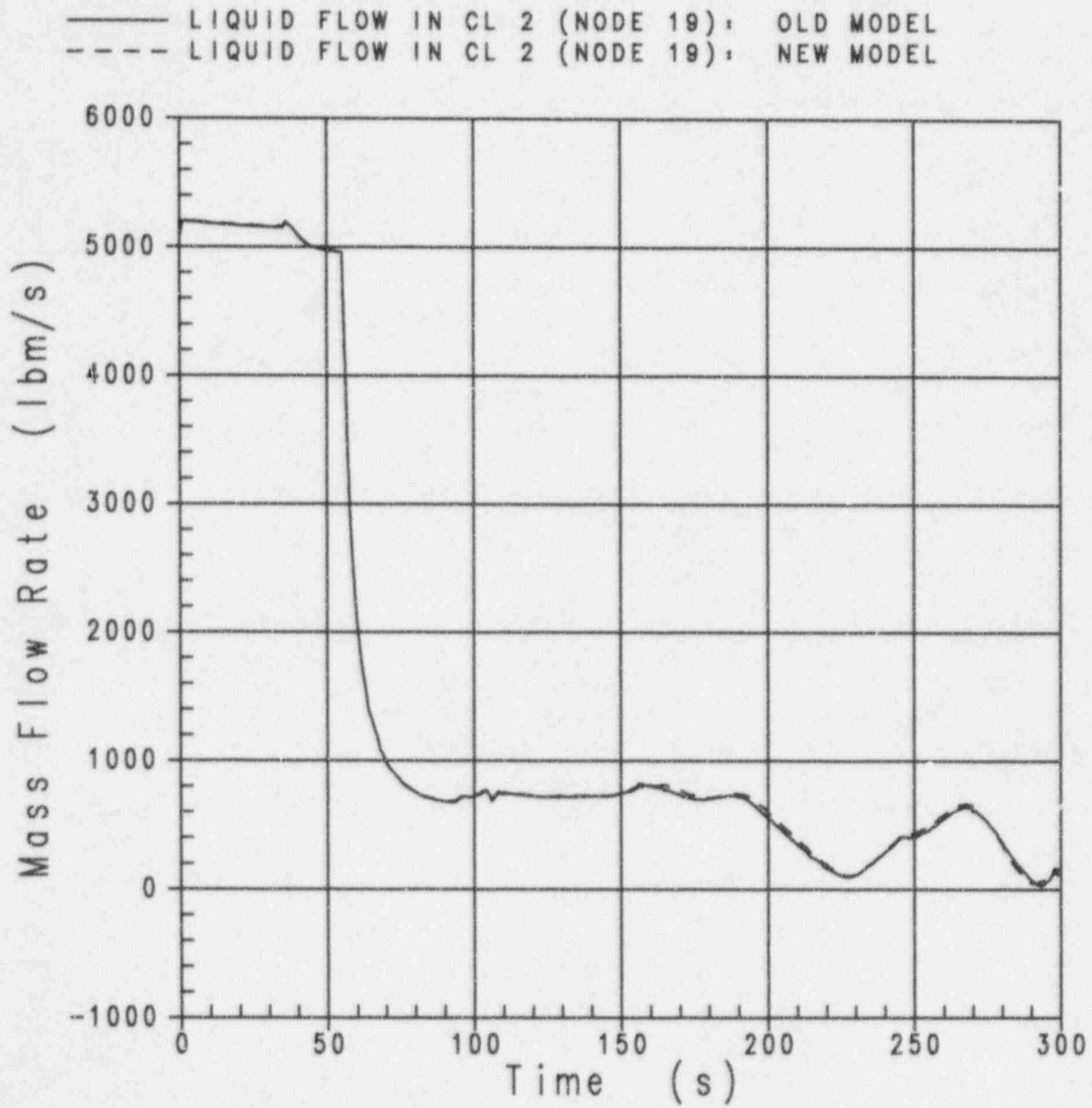


Figure 3.7-3 Mass Flow into Cold Leg 2

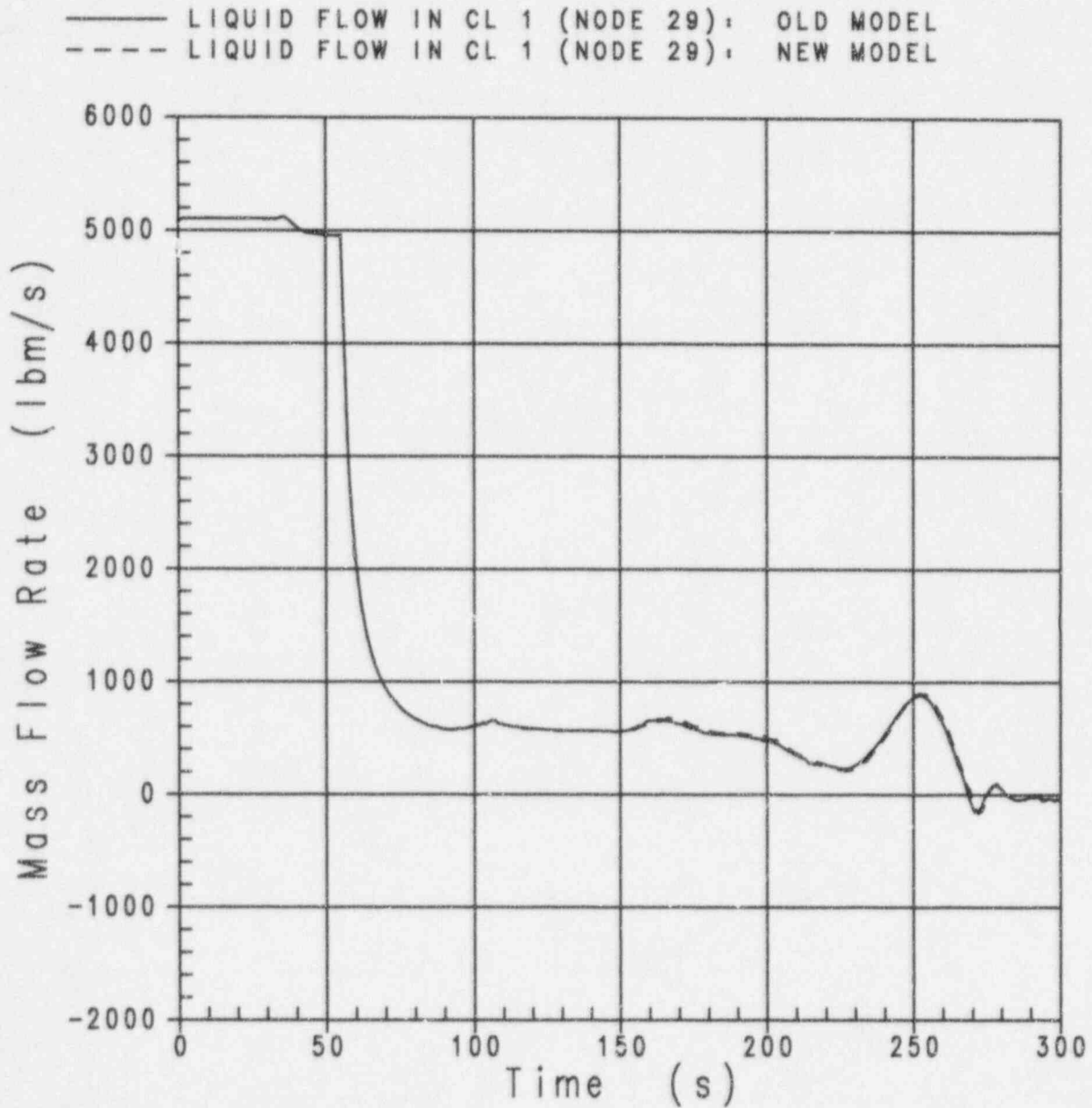


Figure 3.7-4 Mass Flow into Cold Leg 1

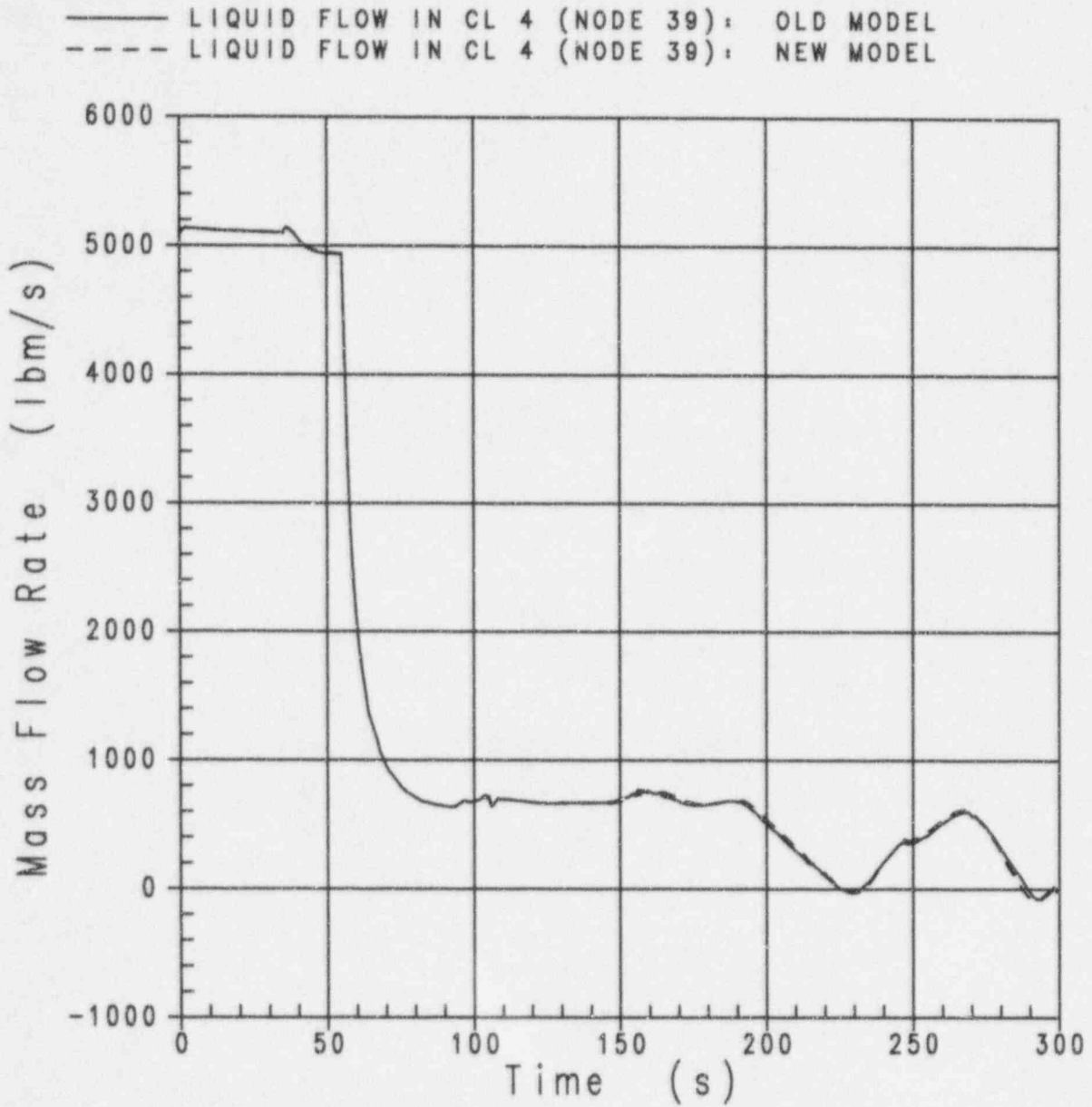


Figure 3.7-5 Mass Flow into Cold Leg 4

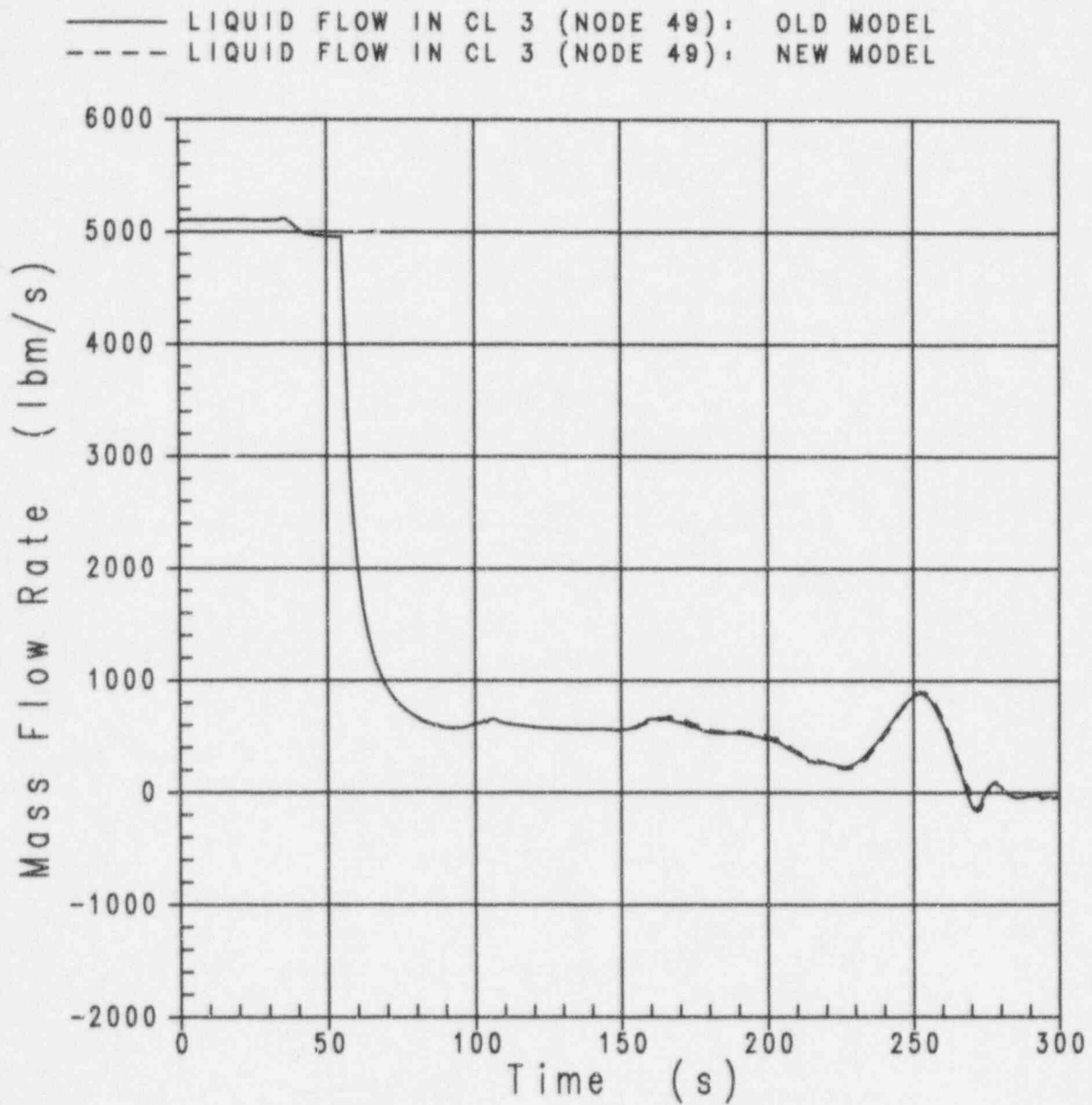


Figure 3.7-6 Mass Flow into Cold Leg 3

3.8 Fluid Node Stacking Logic

The purpose of this benchmark is to demonstrate the fluid node stacking logic for both a single-phase and a two-phase problem. The oscillating manometer simulation with the implicit treatment of fluid node gravitational head, which is described in Section 3.4, is used as the single-phase problem. The demonstration of the fluid node stacking logic for this test is contained in Subsection 3.8.1. For the two-phase problem, the constant-pressure boil-off simulation with the implicit treatment of bubble rise, which is described in Section 3.6, is used. The fluid node stacking logic demonstration for this test is contained in Subsection 3.8.2.

3.8.1 Single-Phase Oscillating Manometer Problem

In the single-phase oscillating manometer problem, the stack is comprised of fluid nodes 2 through 5, which are connected by point-contact flowlinks 2 through 4, as shown in the noding diagram in Figure 3.4-1. The water level in the stack moves rapidly in this problem. To demonstrate the operation of fluid node stacking, the initial draining and refilling period of the stack, which occurs during the first 1.5 seconds of the simulation, is studied.

The stack water level is initialized to 4.5 ft., which is within fluid node 2, and the stack begins to drain at a time of 0 seconds. Figure 3.8-1 shows the water level in the stack. During the entire simulation, the stack water level exhibits smooth behavior as it traverses the fluid node boundaries. Table 3.8-1 summarizes the stack draining and filling events. These events are then checked with a study of the results of key stack fluid node and flowlink quantities, beginning with the stack fluid node region masses, as discussed below.

Figure 3.8-2 shows the mixture region mass in fluid nodes 2 through 5, together with the stack water level as a function of time.

Figure 3.8-3 shows the vapor region mass in fluid nodes 2 through 5, together with the stack water level.

As shown in the figures, the behavior of the stack fluid node mixture and vapor region masses is consistent with the draining and filling events summarized in Table 3.8-1. During the entire simulation, the fluid node region masses exhibit smooth behavior as regions are either created or removed. Next, the stack fluid node region specific enthalpies are studied.

Figure 3.8-4 shows the mixture region specific enthalpy in fluid nodes 2 through 5, together with the stack water level. From Figure 3.8-4, when a mixture region exists in a fluid node, the calculated mixture region specific enthalpy is equal to 30 Btu/lbm, the value that all mixture regions are initialized to. Also, when a mixture region does not exist in a fluid node, by code convention the mixture region specific enthalpy is set equal to the specific enthalpy of saturated water, approximately 181 Btu/lbm in this problem.

Figure 3.8-5 shows the vapor region specific enthalpy in fluid nodes 2 through 5, together with the stack water level. From Figure 3.8-5, when a vapor region exists in a fluid node, the calculated vapor region specific enthalpy is equal to approximately 1300 Btu/lbm, the value that all vapor regions are initialized to. Also, when a vapor region does not exist in a fluid node, the vapor region specific enthalpy value is set equal to the specific enthalpy of saturated steam, approximately 1150 Btu/lbm in this problem. Slight deviations from 1300 Btu/lbm in the vapor region specific enthalpy in fluid nodes 3, 4, and 5 occur due to the fact that vapor regions are created at saturated steam conditions in the fluid node stacking logic calculations, and that the vapor regions are sensitive (more so than the mixture regions) to the small amount of internally calculated interfacial mass and energy that is transferred between the regions of a fluid node. For example, after 0.23 seconds, the vapor region specific enthalpy in fluid node 3 increases and gradually approaches 1300 Btu/lbm, as illustrated in Figure 3.8-6 (which shows the vapor region specific enthalpy in fluid node 3 together with the stack water level, with the time scale expanded for the time period 0.2 to 0.3 seconds).

Thus, the behavior of the stack fluid node mixture and vapor region specific enthalpies is consistent with the draining and filling events summarized in Table 3.8-1. The transitions as regions are either created or removed occur smoothly. Next, the stack flowlink mass flow rates are studied.

Figure 3.8-7 shows the liquid mass flow rate in flowlinks 2 through 5, together with the stack water level. Flowlinks 2 through 4 reside within the stack, and flowlink 5 exits the bottom of the stack. From Figure 3.8-7, as the stack begins to drain at 0 seconds, the liquid mass flow rates in flowlinks 2 through 5 begins to increase together at the same value. At 0.23 seconds, the liquid mass flow rate in flowlink 2 decreases to zero. The liquid mass flow rates in flowlinks 3 through 5 continue to increase together, and at 0.43 seconds, the liquid mass flow rate in flowlink 3 decreases to zero. The liquid mass flow rates in flowlinks 4 and 5 then begin to decrease together, and at 0.64 seconds, the liquid mass flow rate in flowlink 4 decreases to zero. At 0.74 seconds, as the water level in the stack decreases to its lowest value and the stack begins refilling, the liquid mass flow rate in flowlink 5 transitions from positive to negative, and continues to decrease (i.e., it continues to increase in magnitude in the negative direction). At 0.83 seconds, the liquid mass flow rate in flowlink 4 decreases from zero to a negative value equal to that of the liquid mass flow rate in flowlink 5. At 1.05 seconds, the liquid mass flow rate in flowlink 3 decreases from zero to a negative value equal to that of the liquid mass flow rate in flowlinks 4 and 5. The liquid mass flow rates in flowlinks 3 through 5 then begin to increase together, and at 1.26 seconds, the liquid mass flow rate in flowlink 2 decreases from zero to a negative value equal to that of the liquid mass flow rates in flowlinks 3 through 5. The liquid mass flow rates in flowlinks 2 through 5 continue to increase together, and cross through zero at 1.47 seconds as the stack transitions from filling back to draining.

Figure 3.8-8 shows the vapor mass flow rates in flowlinks 1 through 4, together with the stack water level. Flowlinks 2 through 4 reside within the stack, and flowlink 1 enters the top of the stack. From Figure 3.8-8, as the stack begins to drain at 0 seconds, the vapor mass flow rates in flowlink 1 begins to increase, and the vapor mass flow rates in flowlinks 2 through 4 remain at zero. At 0.23 seconds, the vapor mass flow rate in flowlink 2 increases to a value equal to that of the vapor mass flow rate in

flowlink 1, while the vapor mass flow rates in flowlinks 3 and 4 remain at zero. At 0.43 seconds, the vapor mass flow rate in flowlink 3 increases to a value equal to that of the vapor mass flow rate in flowlinks 1 and 2, while the vapor mass flow rate in flowlink 4 remains at zero. The vapor mass flow rates in flowlinks 1 through 3 then begin to decrease together, and at 0.64 seconds, the vapor mass flow rate in flowlink 4 increases from zero to a value equal to that of the vapor mass flow rates in flowlinks 1 through 3. At 0.74 seconds, as the water level in the stack decreases to its lowest value and the stack begins refilling, the vapor mass flow rates in flowlinks 1 through 4 transition from positive to negative and continue to decrease (i.e., they continue to increase in magnitude in the negative direction). At 0.83 seconds, the vapor mass flow rate in flowlink 4 increases to zero, and the vapor mass flow rates in flowlinks 1 through 3 continue to decrease. At 1.05 seconds, the vapor mass flow rate in flowlink 3 increases to zero. The vapor mass flow rates in flowlinks 1 and 2 then begin to increase together. At 1.26 seconds, the vapor mass flow rate in flowlink 2 increases to zero. The vapor mass flow rate in flowlink 1 continues to increase, and crosses through zero at 1.47 seconds as the stack transitions from filling back to draining.

Thus, the behavior of the stack flowlink liquid and vapor mass flow rates is consistent with the draining and filling events summarized in Table 3.8-1. During the entire simulation, the flowlink mass flow rates exhibit smooth behavior as the stack water level crosses fluid node boundaries. Next, the stack fluid node pressures are studied.

Figure 3.8-9 shows the pressure in fluid nodes 2 through 5, together with the stack water level. The stack fluid node pressures exhibit smooth behavior during the simulation, except for when the stack water level crosses fluid node boundaries. These pressure perturbations are found to be due to the incompressibility of the subcooled water in the manometer and are more pronounced as the water level crosses the fluid node boundaries (see the investigation at the end of Section 3.4).

3.8.2 Two-Phase Constant-Pressure Boil-Off Problem

In the two-phase constant-pressure boil-off problem, the stack is comprised of interior fluid nodes 1 and 2, which are connected by point-contact flowlink 1, as shown in the noding diagram in Figure 3.6-1. The mixture level in the stack moves slowly in this problem when compared to the single-phase manometer test described in Subsection 3.8.1. To demonstrate the operation of fluid node stacking, the entire period during which the stack drains, i.e., the first 2400 seconds of the simulation, is studied.

Figure 3.8-10 shows the mixture level in the stack. The stack mixture level is initialized to 1.5 ft., which is within fluid node 2. After an initial increase in the stack mixture level, the stack begins to drain at 110 seconds. At 985 seconds, the stack mixture level decreases to 1 ft. and passes from fluid node 2 to fluid node 1. At 2400 seconds, the stack mixture level decreases to approximately 0 ft., so that the stack is almost completely drained. During the entire simulation, the stack mixture level exhibits smooth behavior, most notably as it crosses the boundary between fluid nodes 1 and 2. A study of the results of key stack fluid node and flowlink quantities was performed, as discussed below.

Figure 3.8-11 shows the mixture region volume in fluid nodes 1 and 2, together with the stack mixture level. The mixture region volume in fluid node 2 increases initially, begins to decrease at 110 seconds, and reaches zero at 985 seconds. At this time, the mixture region volume in fluid node 1 begins to decrease. Figure 3.8-12 shows the vapor region volume in fluid nodes 1 and 2, together with the stack mixture level. The vapor region volume in fluid node 2 decreases initially, begins to increase at 110 seconds, and reaches its maximum value (the fluid node total volume) at 985 seconds. At this time, the vapor region volume in fluid node 1 begins to increase. The behavior of the fluid node region volumes is smooth as regions are either created or removed.

Figure 3.8-13 shows the mixture region specific enthalpy in fluid nodes 1 and 2, together with the stack mixture level. As noted in the discussion of the single-phase manometer problem in Subsection 3.8.1, by code convention the specific enthalpy of a nonexistent mixture region is set equal to the specific enthalpy of saturated water. This is observed for the mixture region specific enthalpy in fluid node 2 at 985 seconds, as the region disappears. Figure 3.8-14 shows the vapor region specific enthalpy in fluid nodes 1 and 2, together with the stack mixture level. As also noted in the discussion of Subsection 3.8.1, by code convention the specific enthalpy of a nonexistent vapor region is set equal to the specific enthalpy of saturated steam. This is observed for the vapor region specific enthalpy in fluid node 1 from 0 to 985 seconds, before the region is created. The stack fluid node region specific enthalpies exhibit smooth behavior and do not change significantly during the entire simulation.

Figure 3.8-15 shows the mixture region quality in fluid nodes 1 and 2, together with the stack mixture level. In a manner analogous to and consistent with what is performed for mixture region specific enthalpies, by code convention the quality of a nonexistent mixture region is set equal to zero. This is observed for the mixture region quality in fluid node 2 at 985 seconds, as the region disappears. Figure 3.8-16 shows the vapor region quality in fluid nodes 1 and 2, together with the stack mixture level. Also in a manner analogous to and consistent with what is performed for vapor region specific enthalpies, by code convention the quality of a nonexistent vapor region is set equal to one. This is observed for the vapor region quality in fluid node 1 from 0 to 985 seconds, before the region is created. The stack fluid node region qualities exhibit smooth behavior and change negligibly during the entire simulation.

Figure 3.8-17 shows the liquid mass flow rate in flowlink 1, together with the stack mixture level, and Figure 3.8-18 shows a replot of Figure 3.8-17 with an expanded y-axis scale for the liquid mass flow rate in flowlink 1 to enable detailed study of the pertinent behavior. After undergoing an initial perturbation, the liquid mass flow rate in flowlink 1 remains constant at a small negative value beginning at 110 seconds. At 985 seconds, as the stack mixture level drains from fluid node 2 to fluid node 1, the liquid mass flow rate in flowlink 1 increases to zero (i.e., it decreases in magnitude, while remaining in the negative direction, until it reaches zero) and remains there for the rest of the simulation. Figure 3.8-19 shows the vapor mass flow rate in flowlink 1, together with the stack mixture level. The vapor mass flow rate in flowlink 1 increases initially then remains essentially constant from 110 seconds to the end of the simulation. A change in the vapor mass flow rate in

flowlink 1 occurs at 985 seconds as the flow transitions from countercurrent to all vapor upflow. Thus, the stack flowlink liquid and vapor mass flow rates exhibit smooth behavior as the stack mixture level crosses the boundary between fluid nodes 1 and 2.

Figure 3.8-20 shows the pressure in fluid nodes 1 and 2, together with the stack mixture level. The stack fluid node pressures do not change significantly during the entire simulation; they exhibit smooth behavior, most notably as the stack mixture level crosses the fluid node boundaries.

This concludes the demonstration of the fluid node stacking logic, which shows that the stack mixture level moves smoothly from node to node as the inventory in the system increases or decreases.

TABLE 3.8-1
SUMMARY OF THE STACK DRAINING AND
FILLING EVENTS FOR THE FIRST 1.5 SECONDS OF
THE SINGLE-PHASE OSCILLATING MANOMETER SIMULATION

Time (sec.)	Stack Water Level (ft.)	Stack Draining/Filling Status	Fluid Node with Water Level
0	4.5	Initiate draining	2
0.23	4	Draining	Transition 2 to 3
0.43	3	Draining	Transition 3 to 4
0.64	2	Draining	Transition 4 to 5
0.74	1.86	Transition from draining to filling	5
0.83	2	Filling	Transition 5 to 4
1.05	3	Filling	Transition 4 to 3
1.26	4	Filling	Transition 3 to 2
1.47	4.41	Transition from filling to draining	2

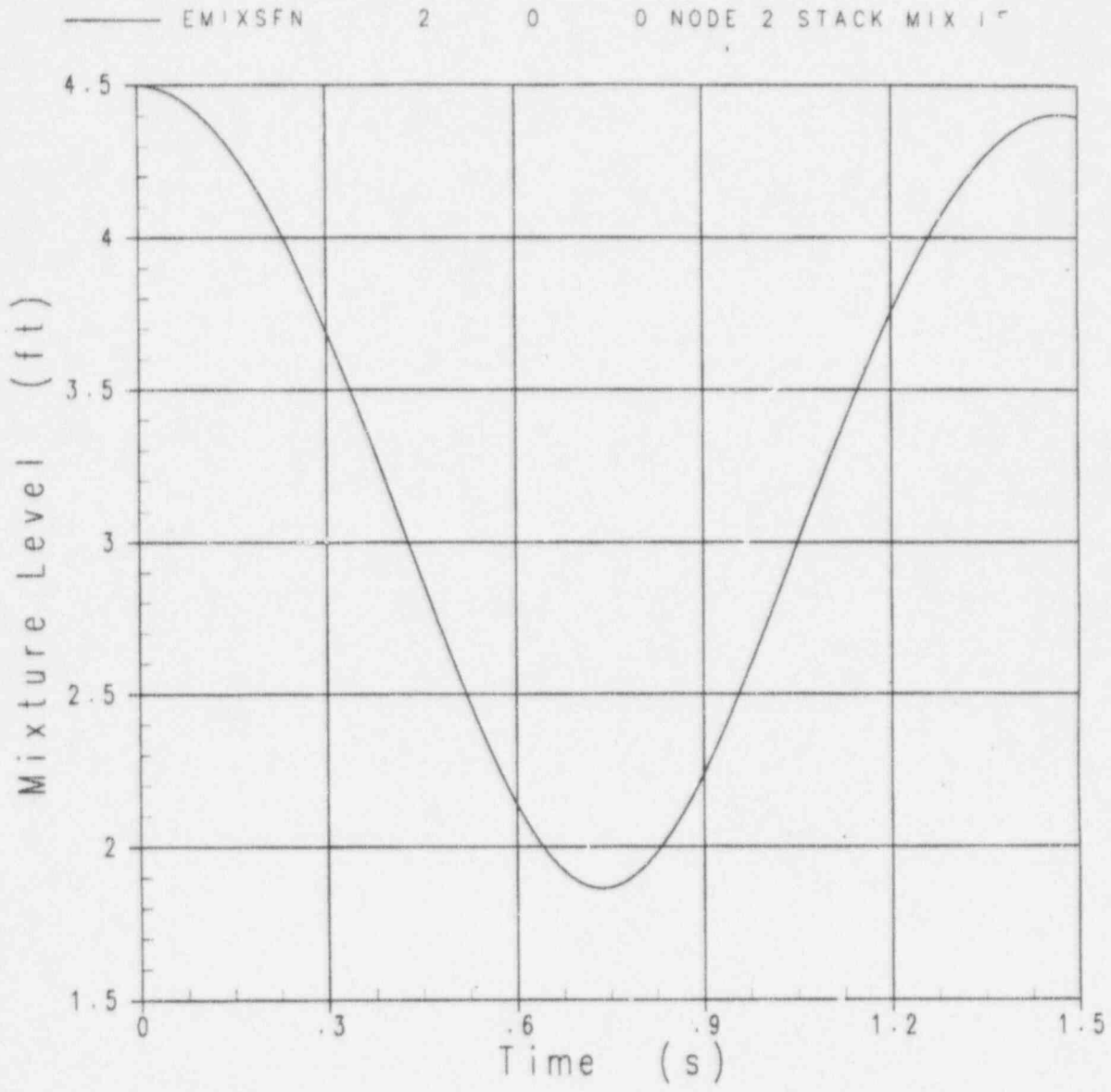


Figure 3.8-1 Single-Phase Oscillating Manometer Case: Stack Mixture Level

Mass (lbm)									
————	TMMFN	2	0	0	NODE 2	MIX	REG	MASS	
-----	TMMFN	3	0	0	NODE 3	MIX	REG	MASS	
- - - -	TMMFN	4	0	0	NODE 4	MIX	REG	MASS	
-----	TMMFN	5	0	0	NODE 5	MIX	REG	MASS	
Mixture Level (ft)									
-----	EMIXSFN	2	0	0	NODE 2	STACK	MIX	LEV	

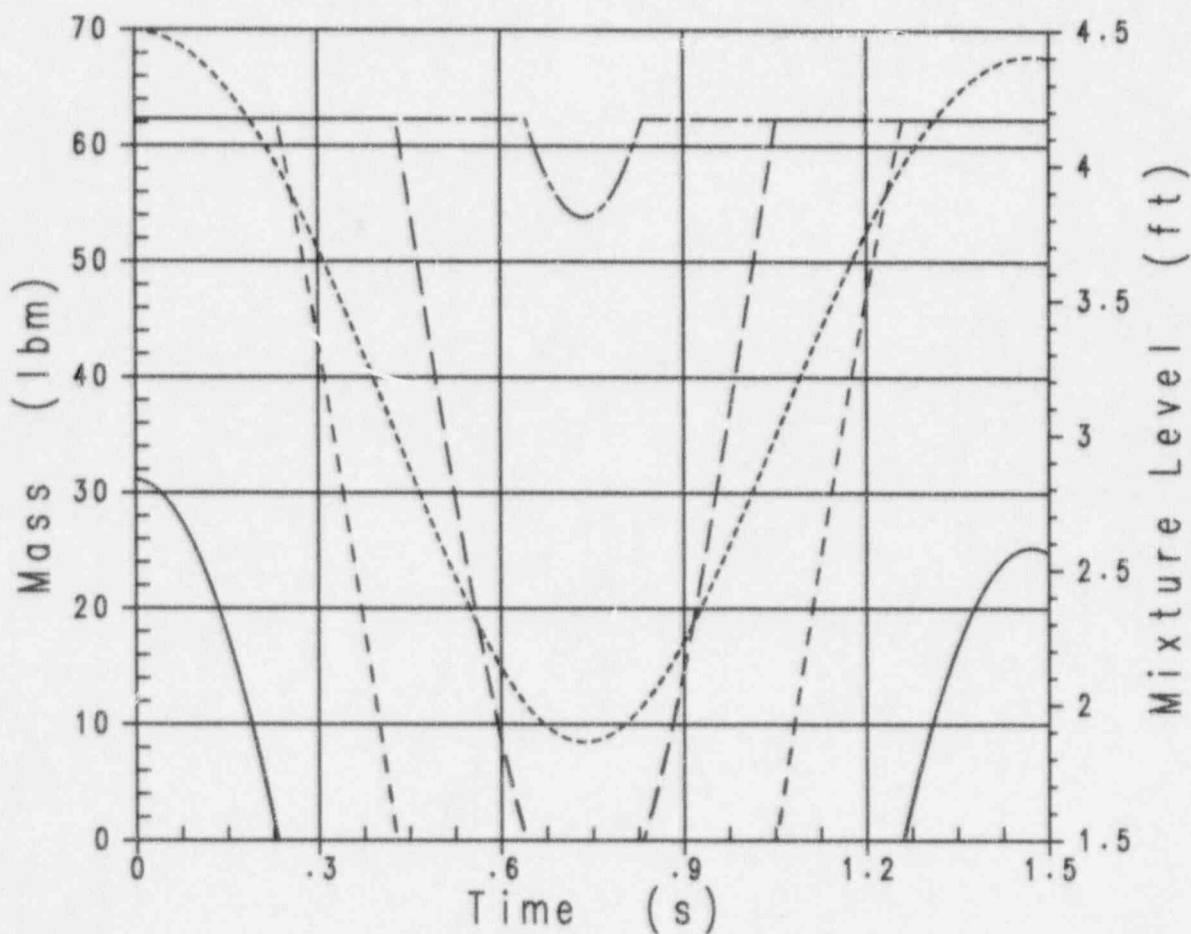


Figure 3.8-2 Single-Phase Oscillating Manometer Case: Stack Node Mixture Region Masses with Stack Mixture Level

Mass (lbm)									
—	TMVFN	2	0	0	NODE 2	VAP	REG	MASS	
- - - -	TMVFN	3	0	0	NODE 3	VAP	REG	MASS	
- - - -	TMVFN	4	0	0	NODE 4	VAP	REG	MASS	
- - - -	TMVFN	5	0	0	NODE 5	VAP	REG	MASS	
Mixture Level (ft)									
- - - - -	EMIXSFN	2	0	0	NODE 2	STACK	MIX	LEV	

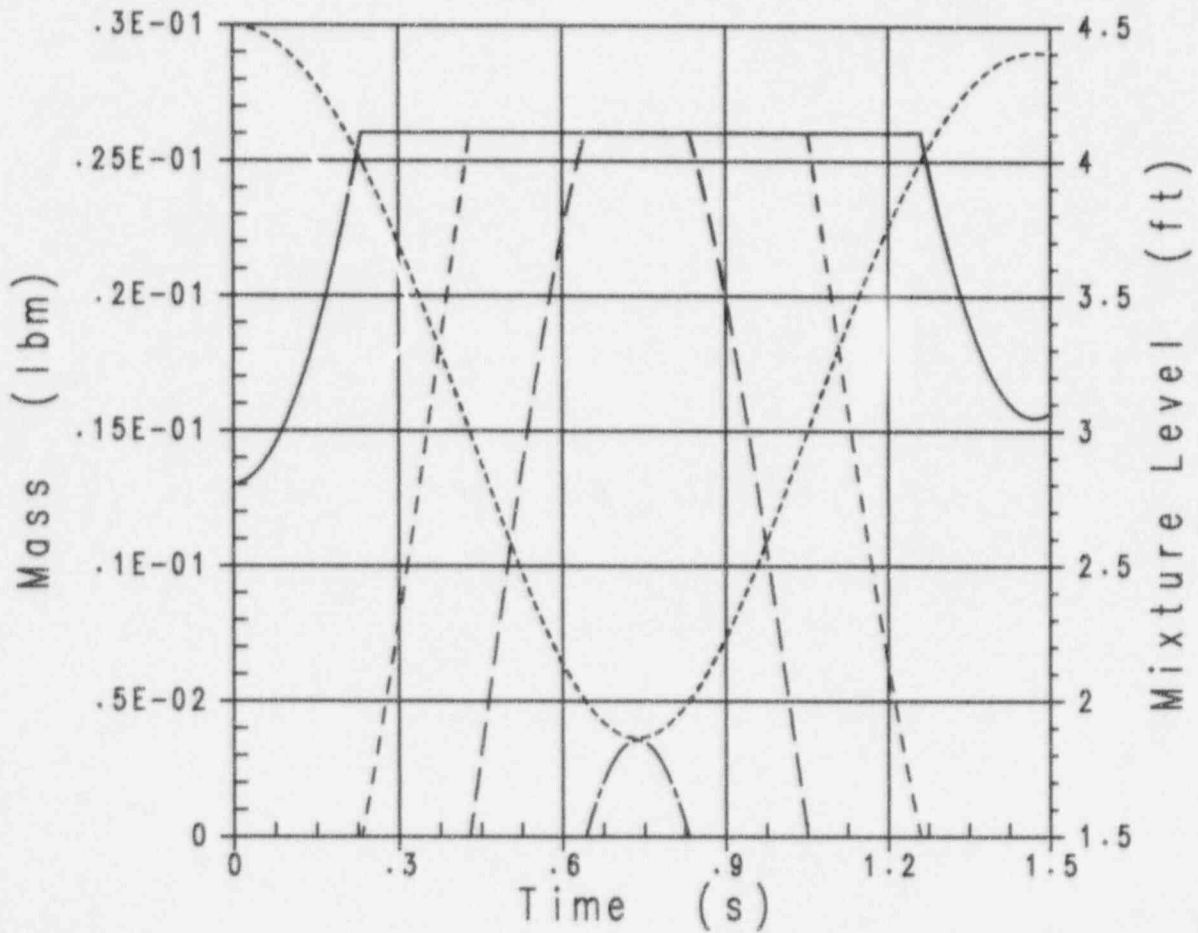


Figure 3.8-3 Single-Phase Oscillating Manometer Case: Stack Node Vapor Region Masses with Stack Mixture Level

Mixture Enthalpy (Btu/lbm)							
————	SHMFN	2	0	0	NODE 2	MIX REG	ENTHP
----	SHMFN	3	0	0	NODE 3	MIX REG	ENTHP
----	SHMFN	4	0	0	NODE 4	MIX REG	ENTHP
----	SHMFN	5	0	0	NODE 5	MIX REG	ENTHP
Mixture Level (ft)							
-----	EMIXSFN	2	0	0	NODE 2	STACK	MIX LEV

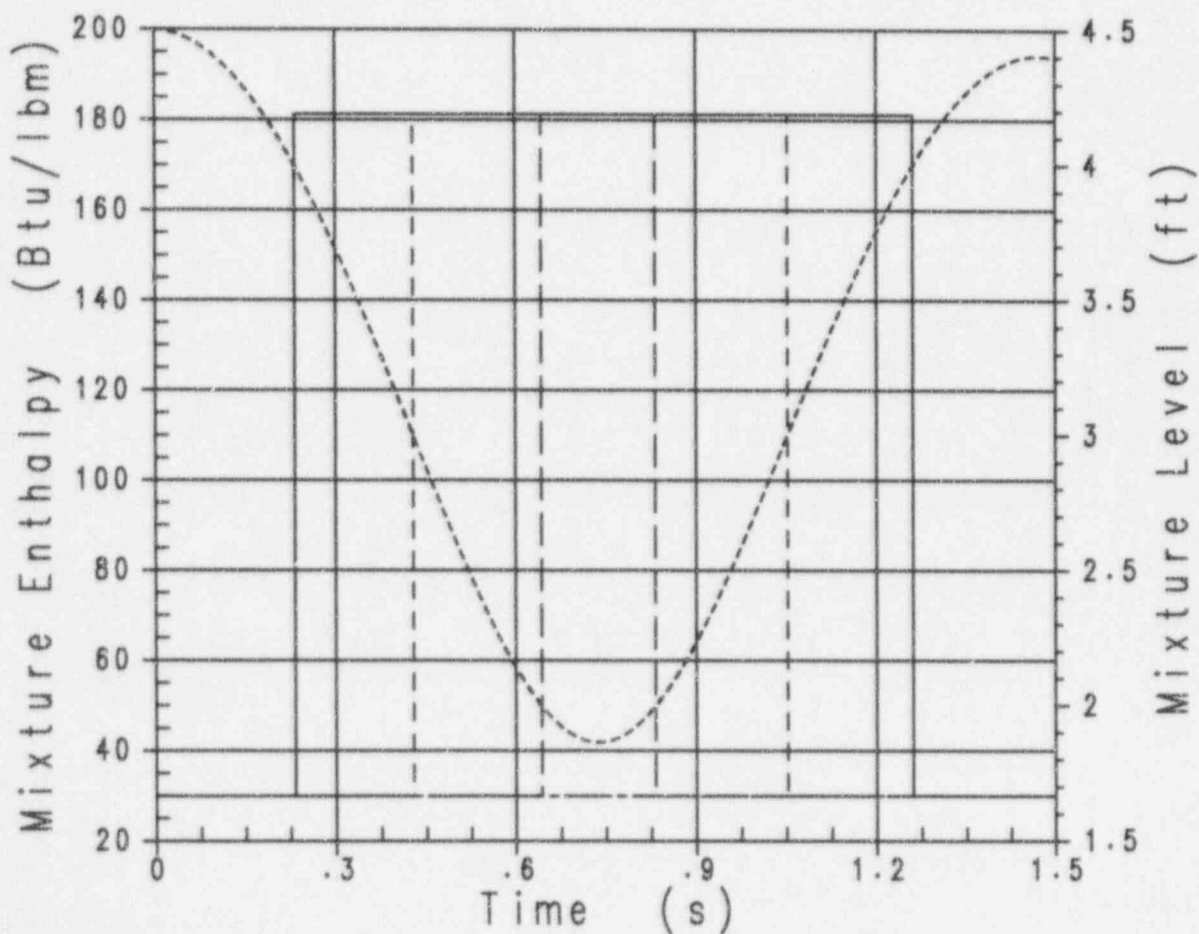


Figure 3.8-4 Single-Phase Oscillating Manometer Case: Stack Node Mixture Region Specific Enthalpies with Stack Mixture Level

Enthalpy (Btu/lbm)									
————	SHVFN	2	0	0	NODE 2	VAP	REG	ENTHP	
-----	SHVFN	3	0	0	NODE 3	VAP	REG	ENTHP	
-----	SHVFN	4	0	0	NODE 4	VAP	REG	ENTHP	
-----	SHVFN	5	0	0	NODE 5	VAP	REG	ENTHP	
Mixture Level (ft)									
-----	EMIXSFN	2	0	0	NODE 2	STACK	MIX	LEV	

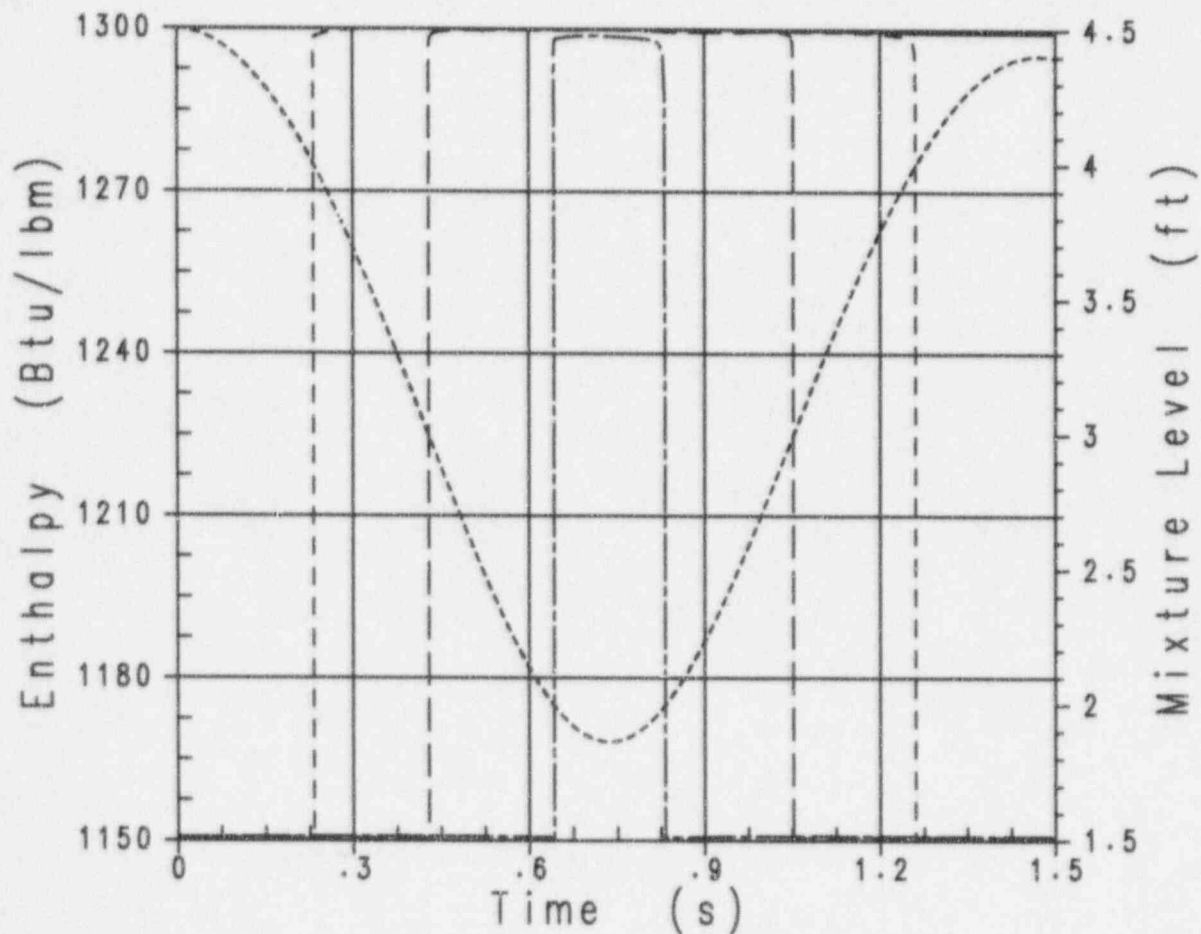


Figure 3.8-5 Single-Phase Oscillating Manometer Case: Stack Node Vapor Region Specific Enthalpies with Stack Mixture Level

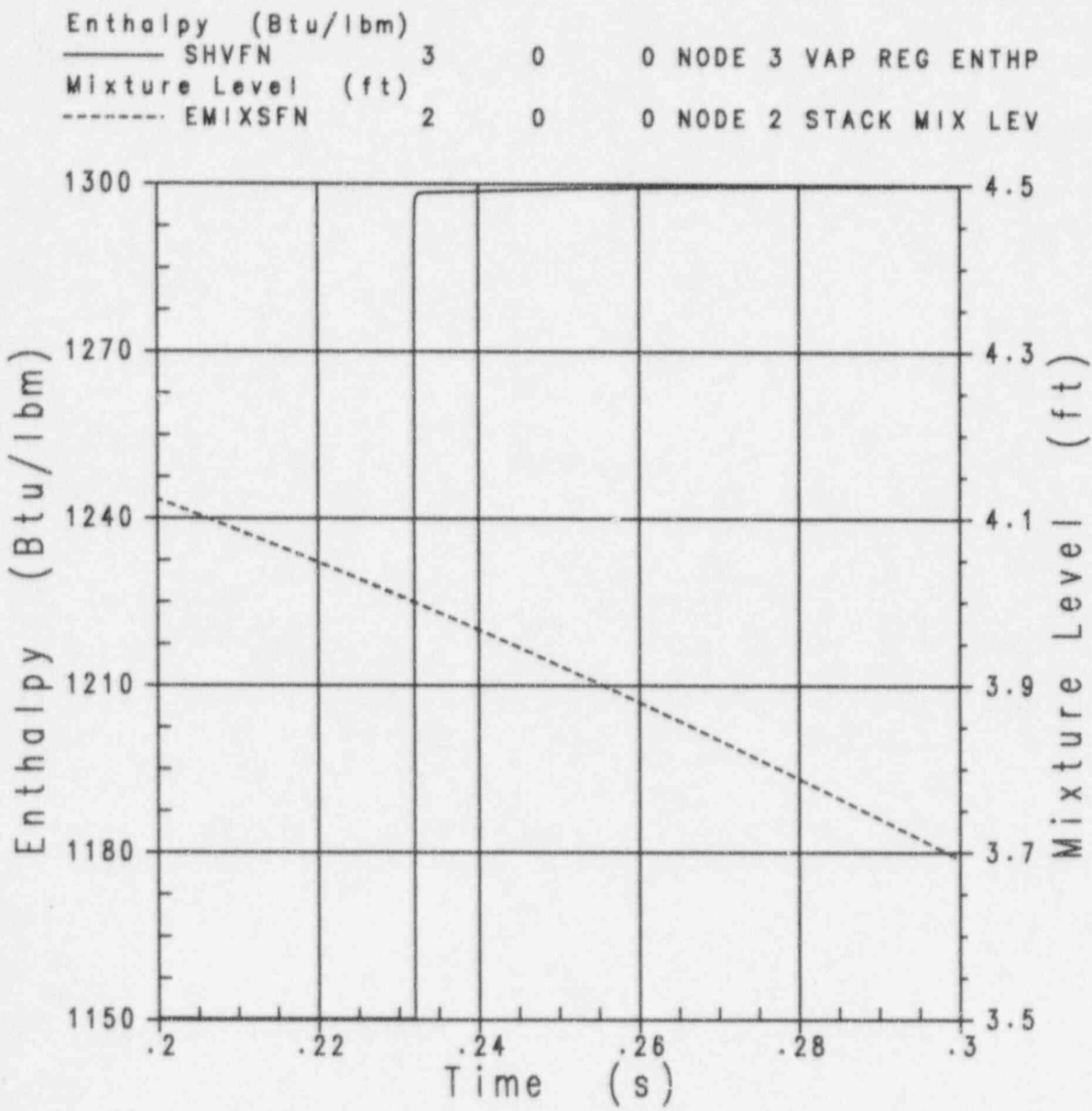


Figure 3.8-6 Single-Phase Oscillating Manometer Case: Stack Node 3 Vapor Region Specific Enthalpy with Stack Mixture Level (with Expanded Time Scale 0.2 to 0.3 Seconds)

Mass Flow Rate (lbm/s)					
————	WFFL 2	0	0	LINK 2	LIQ FLOW RATE
-----	WFFL 3	0	0	LINK 3	LIQ FLOW RATE
- - - -	WFFL 4	0	0	LINK 4	LIQ FLOW RATE
————	WFFL 5	0	0	LINK 5	LIQ FLOW RATE
Mixture Level (ft)					
-----	EMIXSFN 2	0	0	NODE 2	STACK MIX LEV

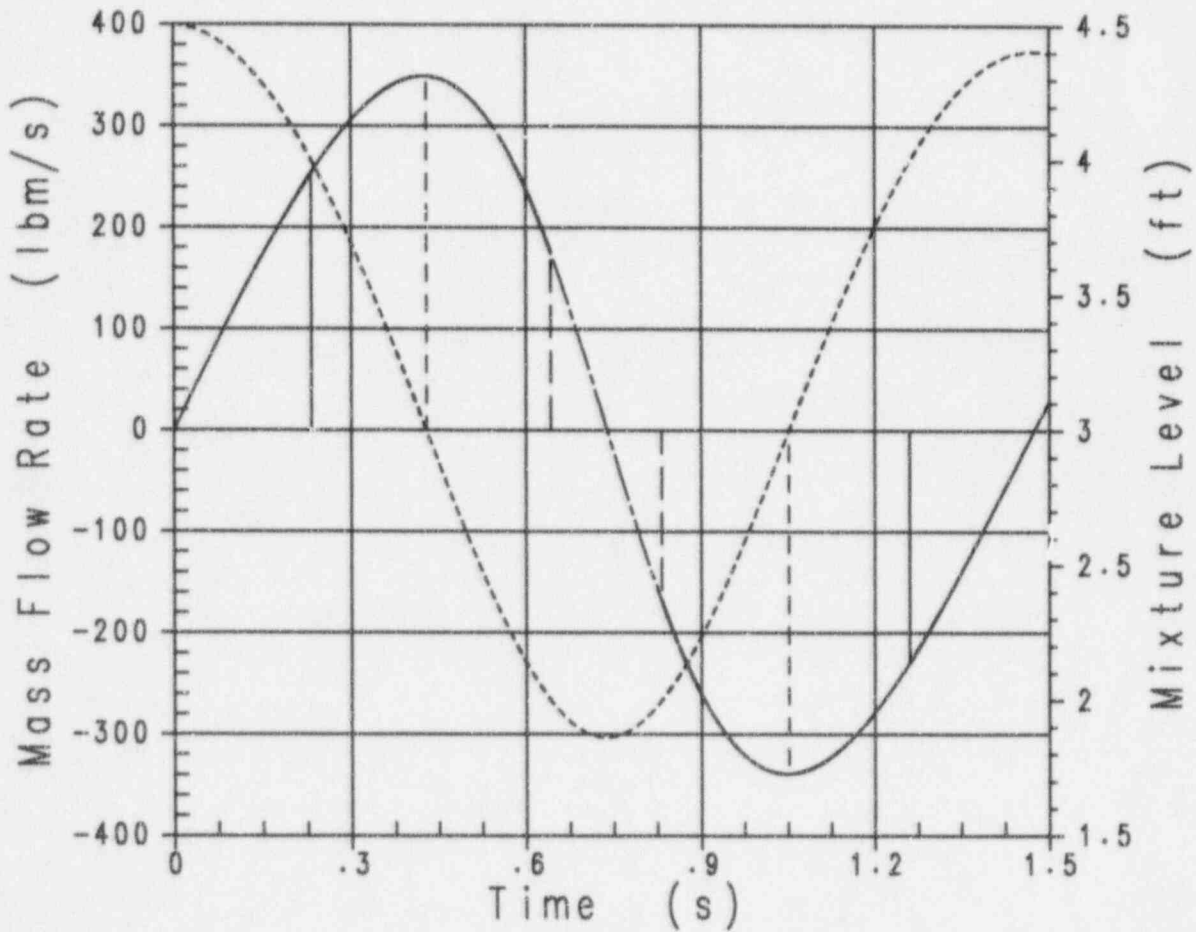


Figure 3.8-7 Single-Phase Oscillating Manometer Case: Stack Flowlink Liquid Mass Flow Rates with Stack Mixture Level

Mass Flow Rate (lbm/s)					
—	WGFL	1	0	0	LINK 1 VAP FLOW RATE
- - - -	WGFL	2	0	0	LINK 2 VAP FLOW RATE
- - - -	WGFL	3	0	0	LINK 3 VAP FLOW RATE
- - - -	WGFL	4	0	0	LINK 4 VAP FLOW RATE
Mixture Level (ft)					
- - - - -	EMIXSFN	2	0	0	NODE 2 STACK MIX LEV

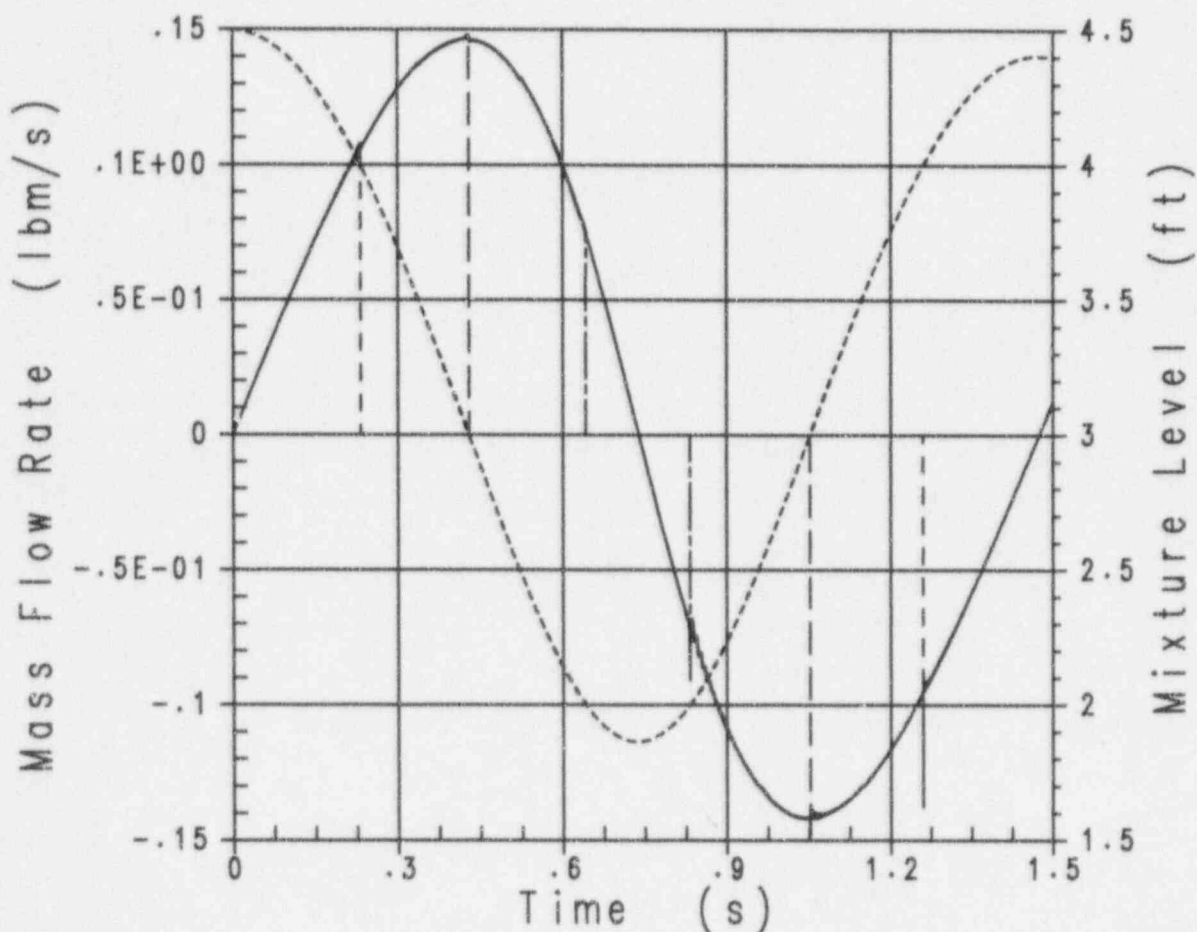


Figure 3.8-8 Single-Phase Oscillating Manometer Case: Stack Flowlink Vapor Mass Flow Rates with Stack Mixture Level

Pressure (psia)						
————	PFN	2	0	0	NODE 2	PRESSURE
-----	PFN	3	0	0	NODE 3	PRESSURE
- - - -	PFN	4	0	0	NODE 4	PRESSURE
————	PFN	5	0	0	NODE 5	PRESSURE
Mixture Level (ft)						
-----	EMIXSFN	2	0	0	NODE 2	STACK MIX LEV

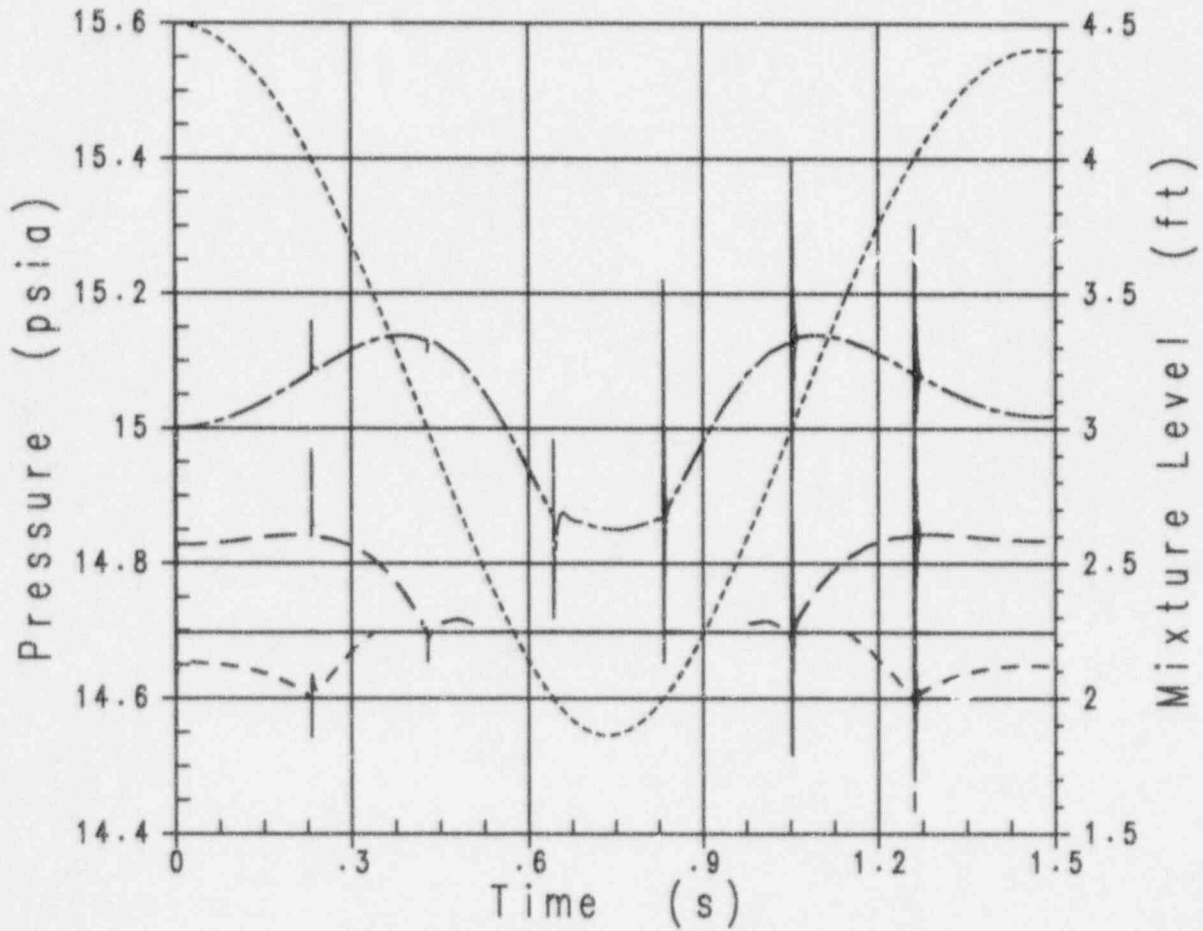


Figure 3.8-9 Single-Phase Oscillating Manometer Case: Stack Node Pressures with Stack Mixture Level

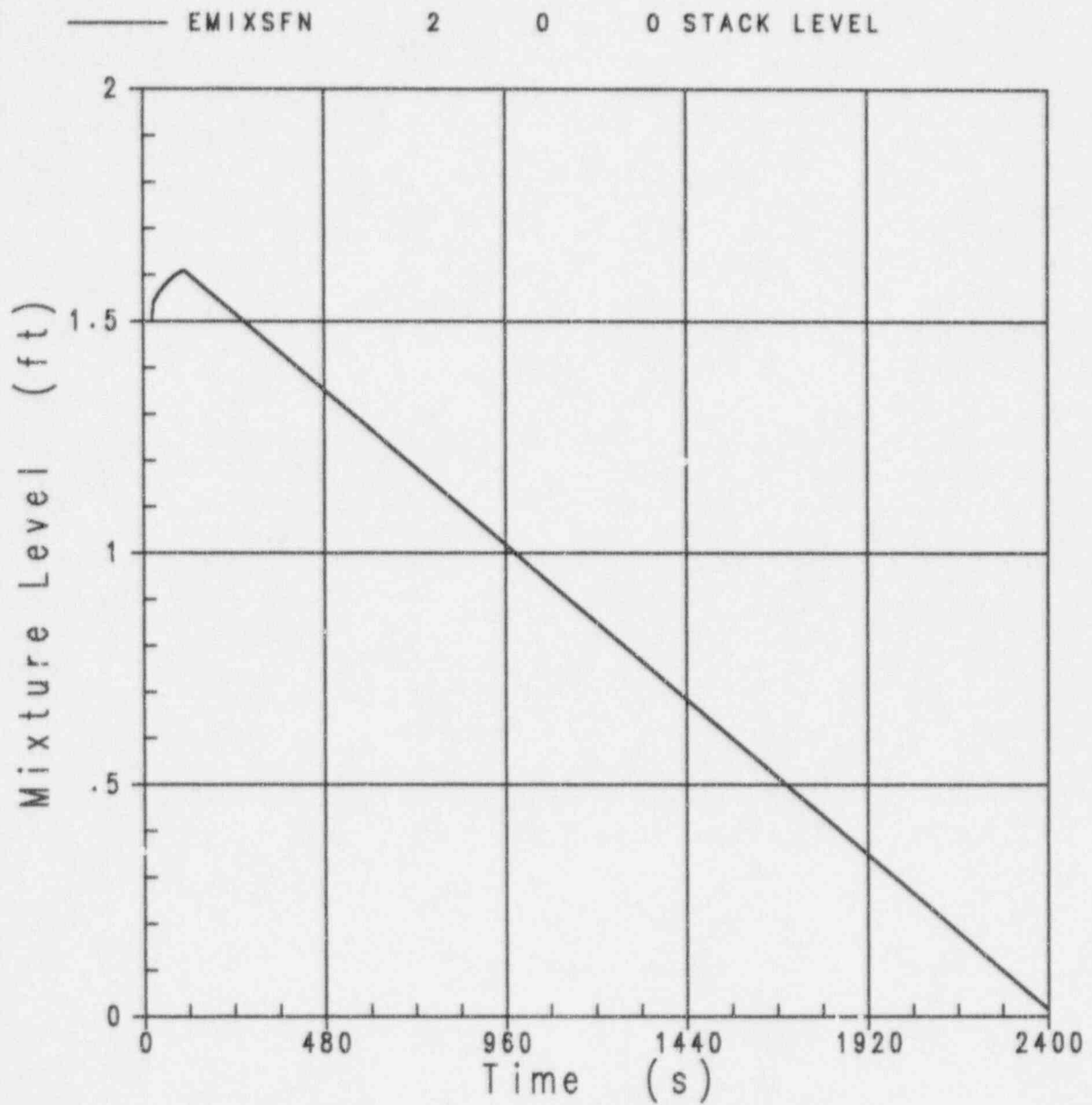


Figure 3.8-10 Two-Phase Constant-Pressure Boil-Off Case: Stack Mixture Level

Volume (ft ³)				
— VMFN	1	0	0	NODE 1 MIX VOLUME
- - - VMFN	2	0	0	NODE 2 MIX VOLUME
Mixture Level (ft)				
- - - - - EMIXSFN	2	0	0	STACK LEVEL

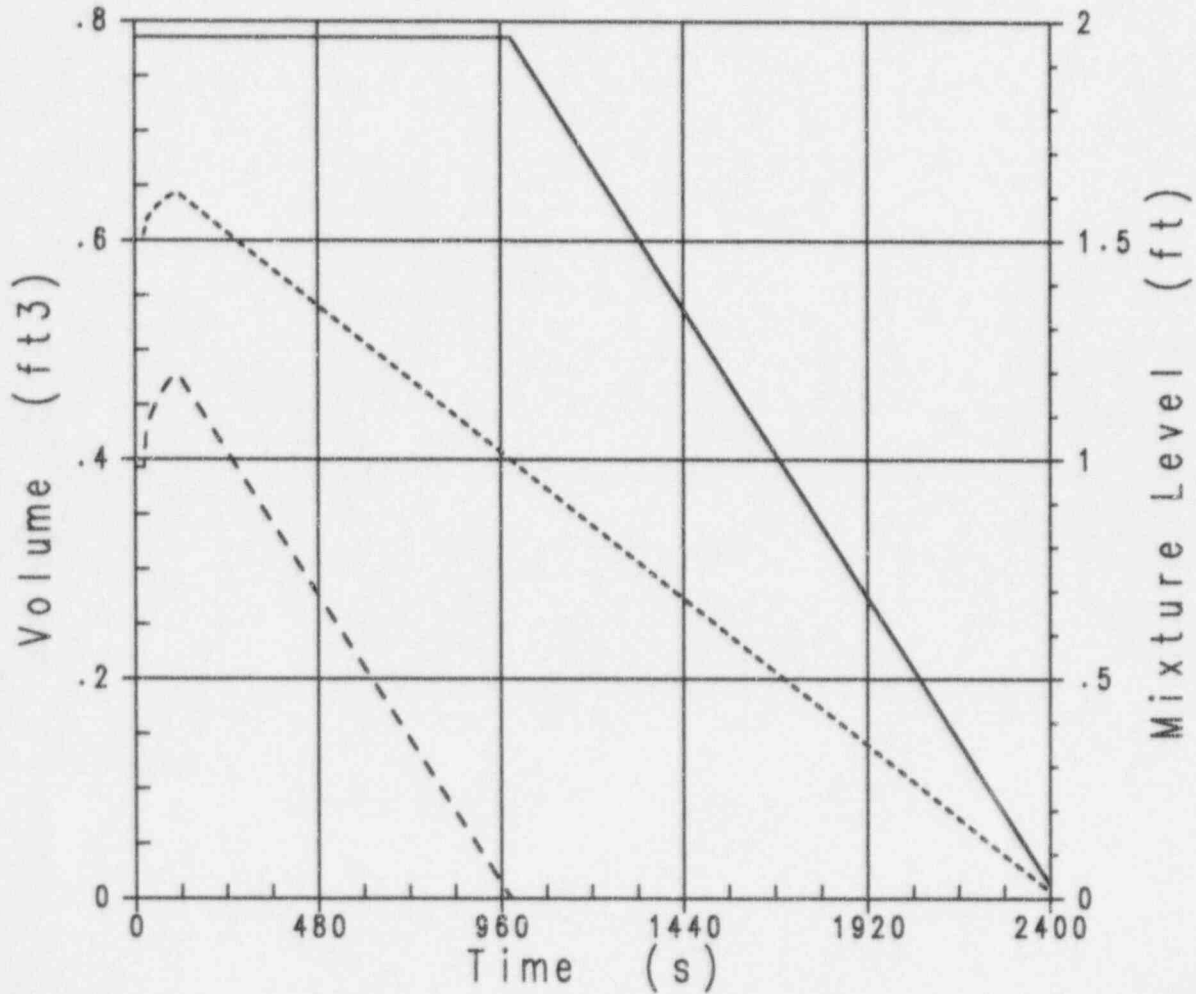


Figure 3.8-11 Two-Phase Constant-Pressure Boil-Gff Case: Stack Node Mixture Region Volumes with Stack Mixture Level

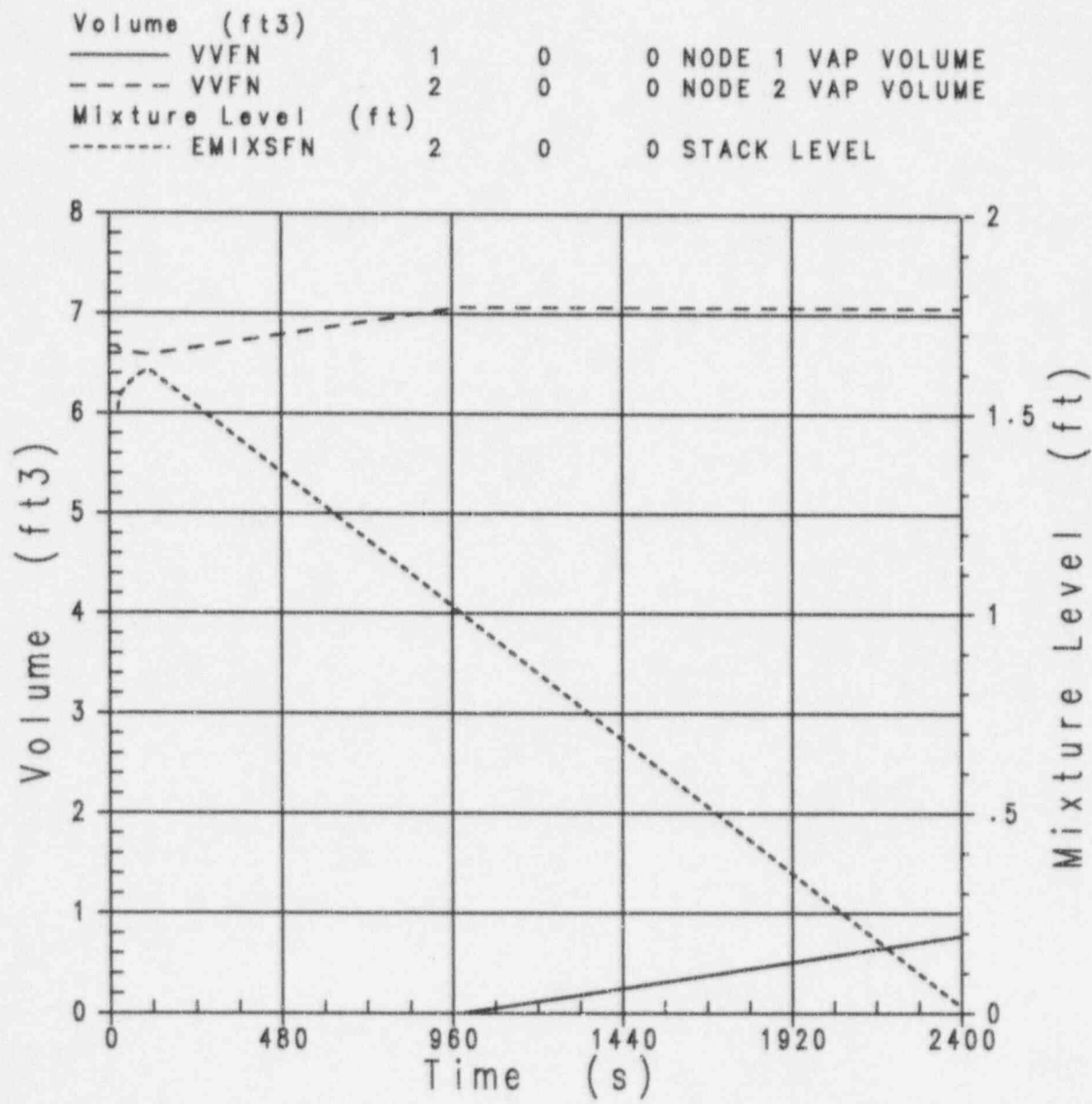


Figure 3.8-12 Two-Phase Constant-Pressure Boil-Off Case: Stack Node Vapor Region Volumes with Stack Mixture Level

Mixture Enthalpy (Btu/lbm)		Mixture Level (ft)	
—	SHMFN 1 0	0	NODE 1 MIX SPEC ENTH
- - - -	SHMFN 2 0	0	NODE 2 MIX SPEC ENTH
- - - - -	EMIXSFN 2 0	0	STACK LEVEL

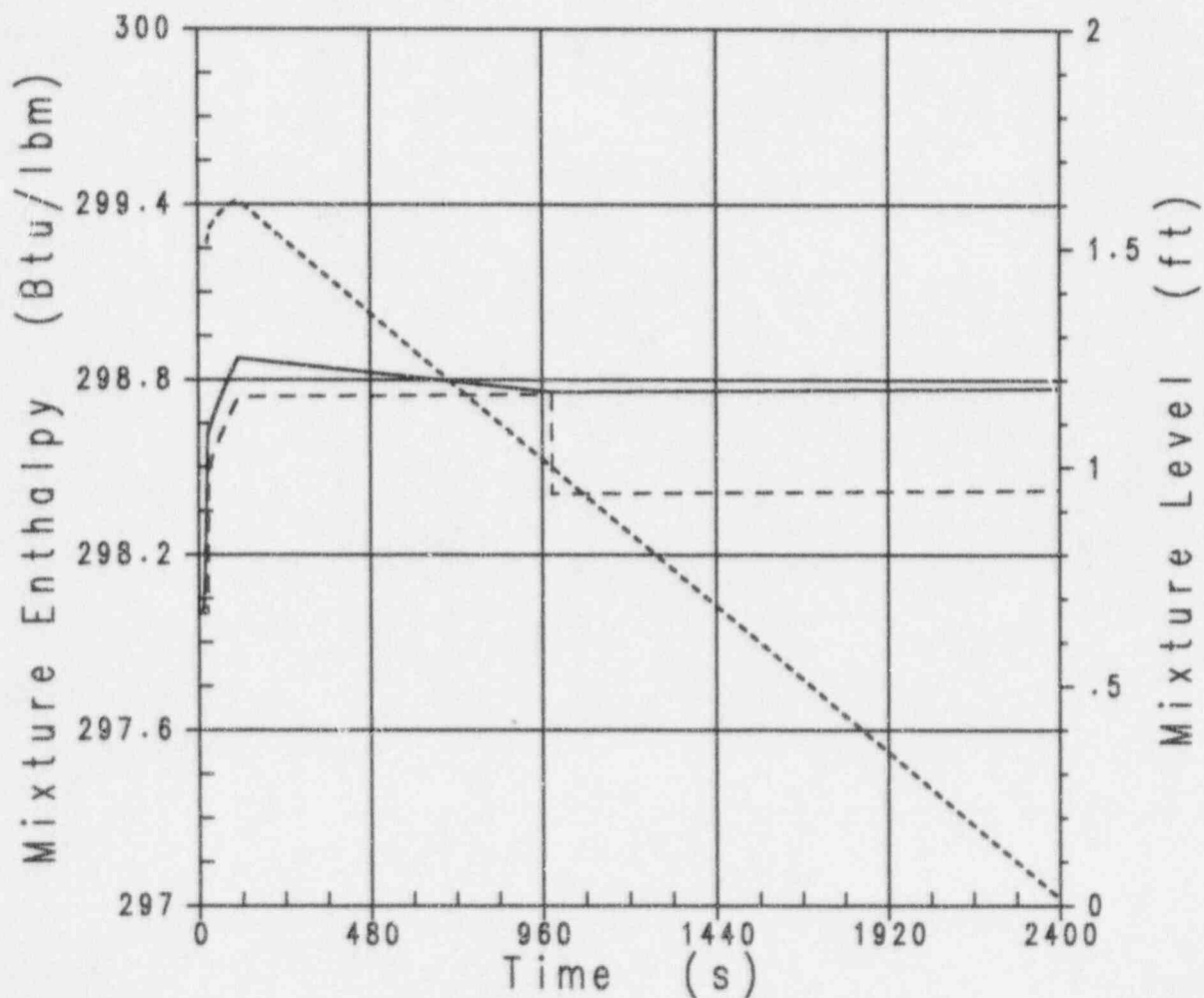


Figure 3.8-13 Two-Phase Constant-Pressure Boil-Off Case: Stack Node Mixture Region Specific Enthalpies with Stack Mixture Level

Enthalpy (Btu/lbm)				
————	SHVFN	1	0	C NODE 1 VAP SPEC ENTH
-----	SHVFN	2	0	0 NODE 2 VAP SPEC ENTH
Mixture Level (ft)				
-----	EMIXSFN	2	0	0 STACK LEVEL

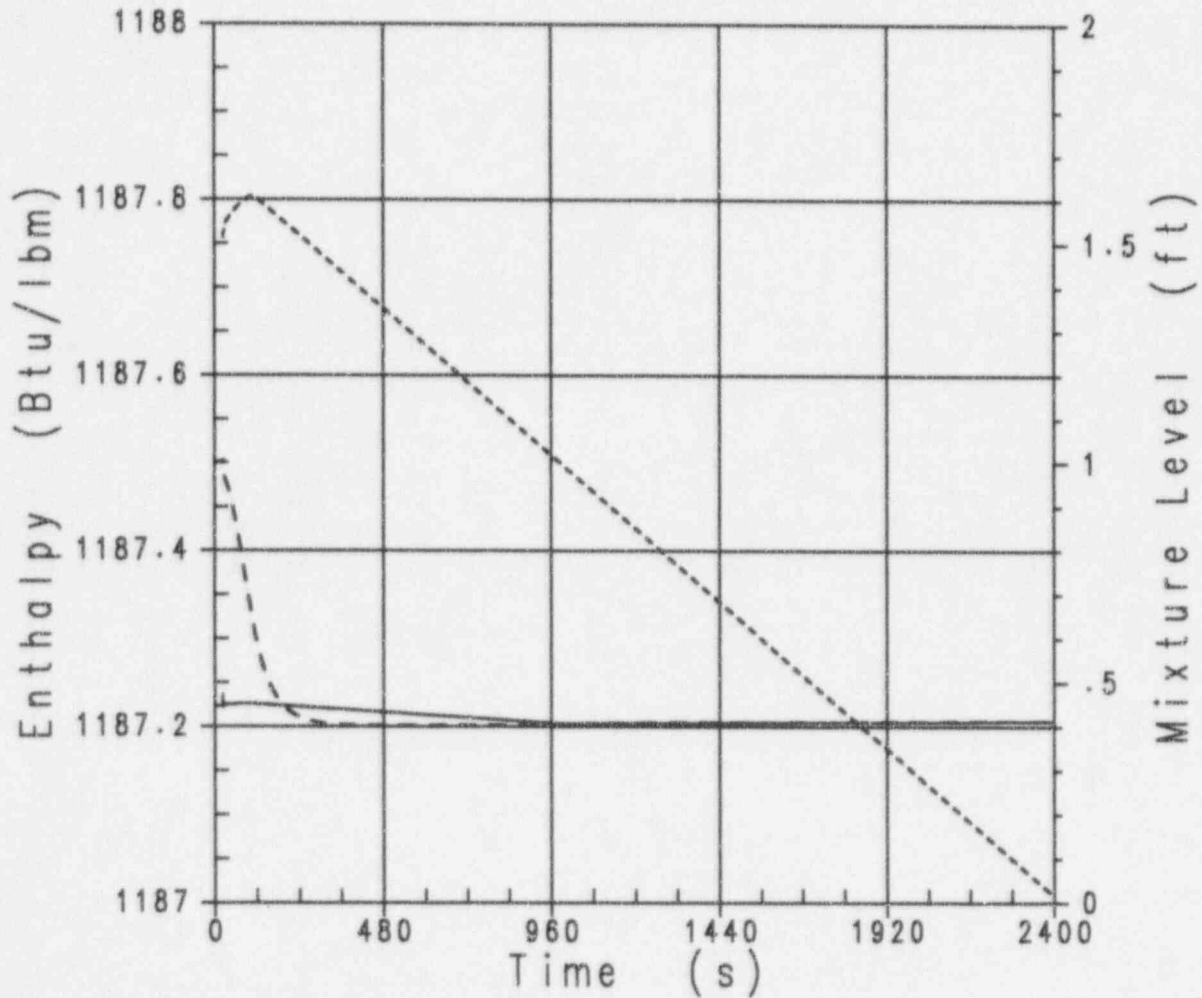


Figure 3.8-14 Two-Phase Constant-Pressure Boil-Off Case: Stack Node Vapor Region Specific Enthalpies with Stack Mixture Level

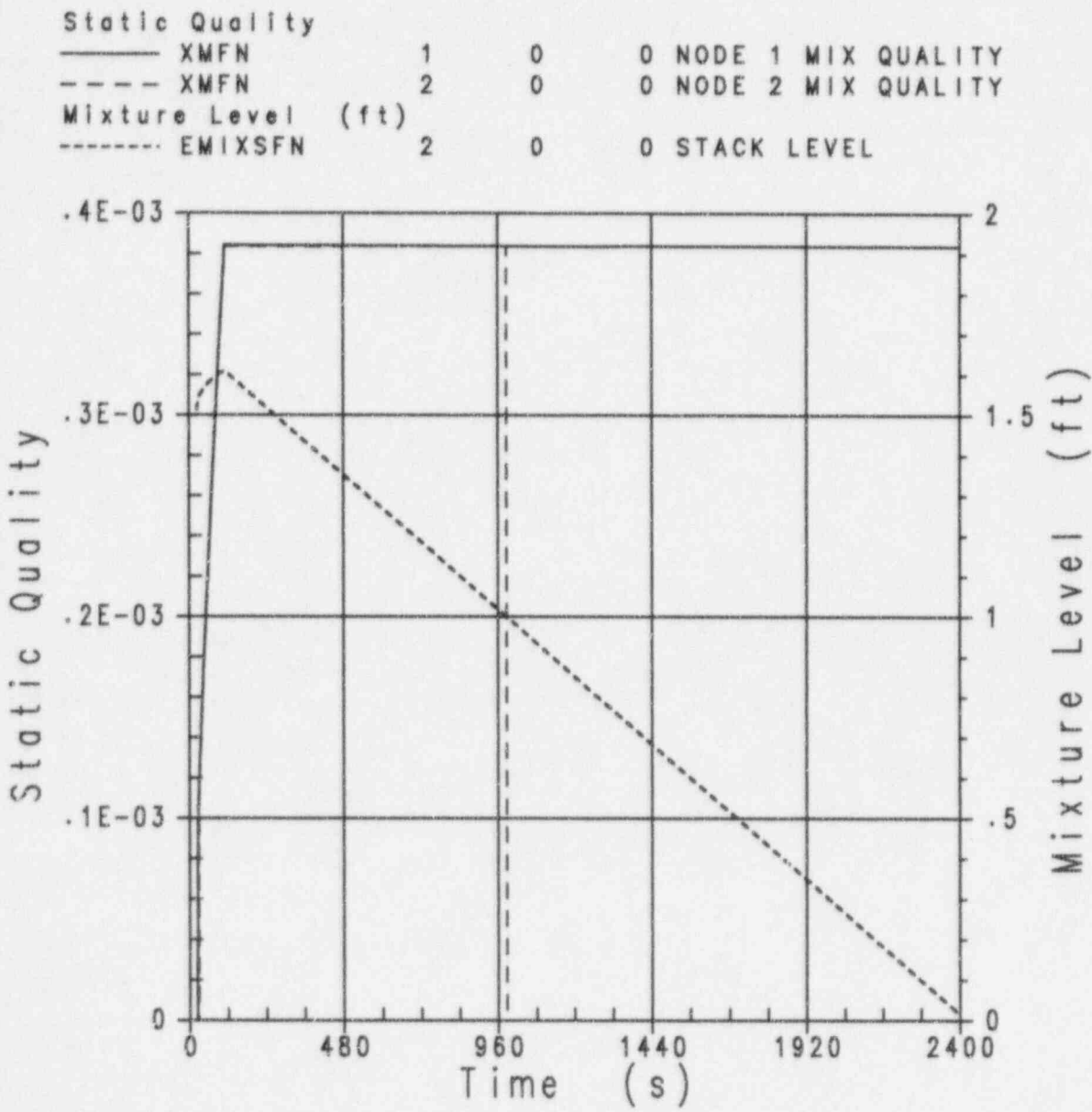


Figure 3.8-15 Two-Phase Constant-Pressure Boil-Off Case: Stack Node Mixture Region Qualities with Stack Mixture Level

Thermodynamic Quality				
————	XVFN	1	0	0 NODE 1 VAP QUALITY
-----	XVFN	2	0	0 NODE 2 VAP QUALITY
Mixture Level (ft)				
-----	EMIXSFN	2	0	0 STACK LEVEL

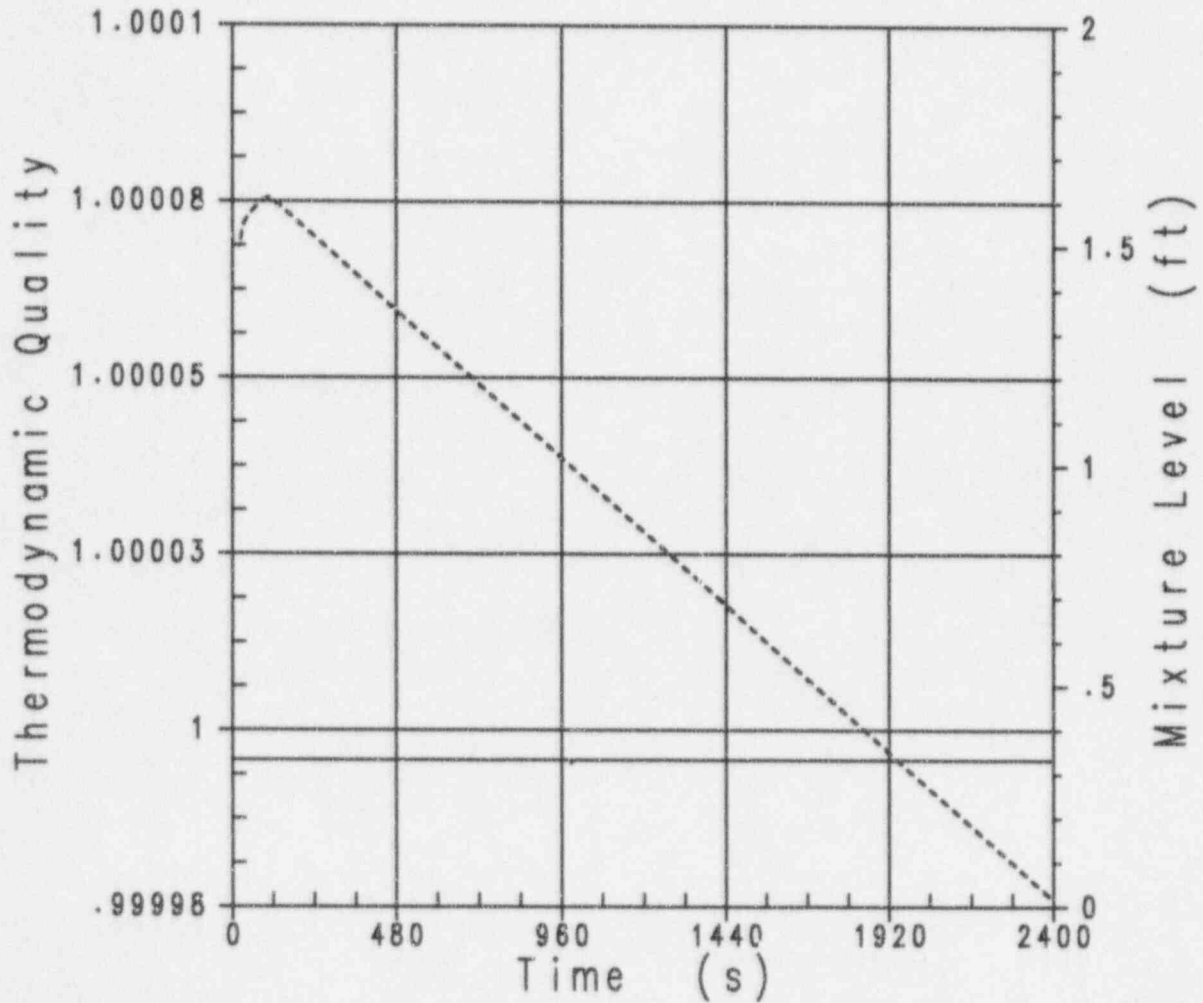


Figure 3.8-16 Two-Phase Constant-Pressure Boil-Off Case: Stack Node Vapor Region Qualities with Stack Mixture Level

Mass Flow Rate (lbm/s)				
—— WFFL	1	0	0	LINK 1 LIQ FLOW
Mixture Level (ft)				
----- EMIXSFN	2	0	0	STACK LEVEL

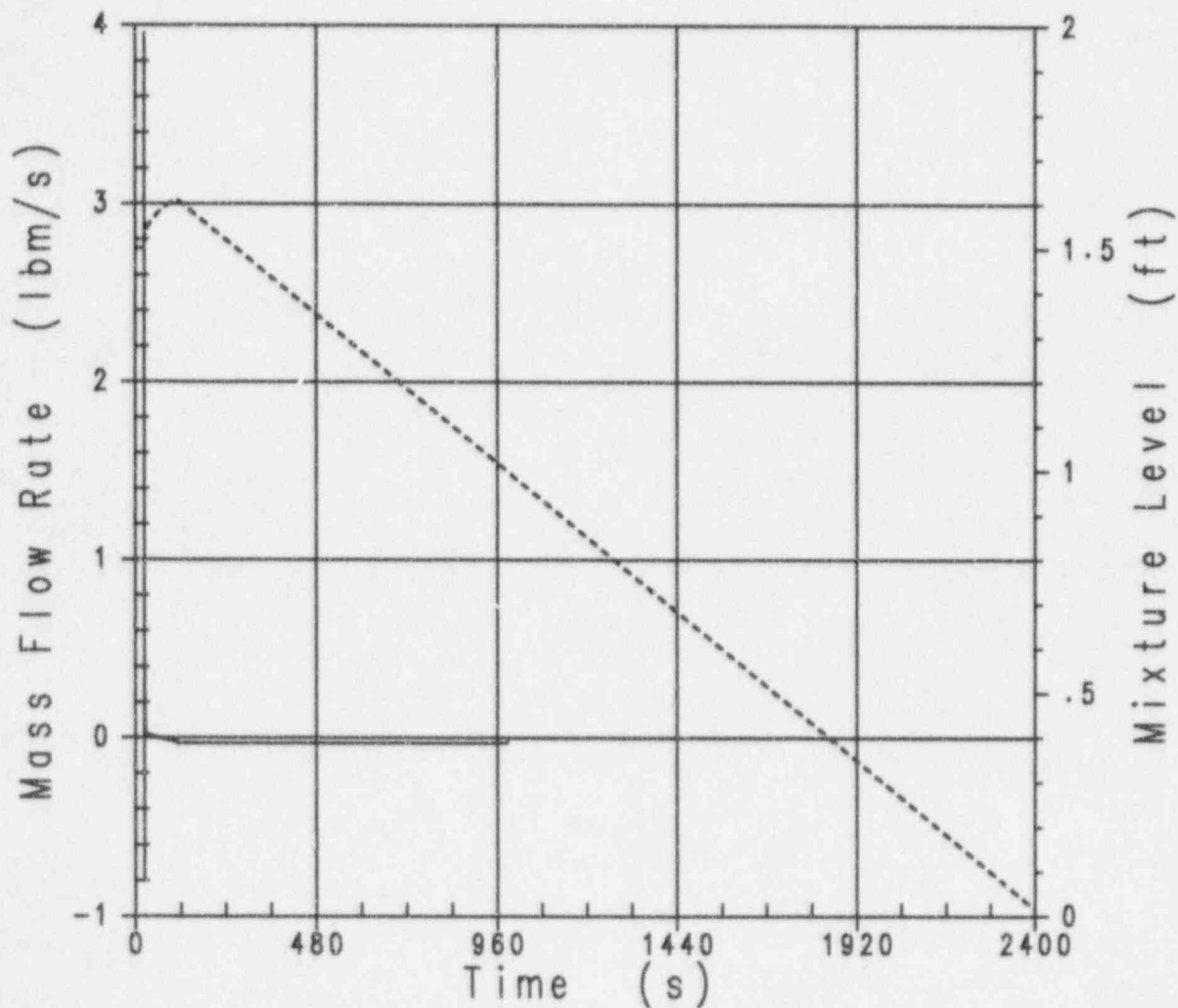


Figure 3.8-17 Two-Phase Constant-Pressure Boil-Off Case: Stack Flowlink Liquid Mass Flow Rate with Stack Mixture Level

Mass Flow Rate (lbm/s)			
—— WFFL	1	0	0 LINK 1 LIQ FLOW
Mixture Level (ft)			
----- EMIXSFN	2	0	0 STACK LEVEL

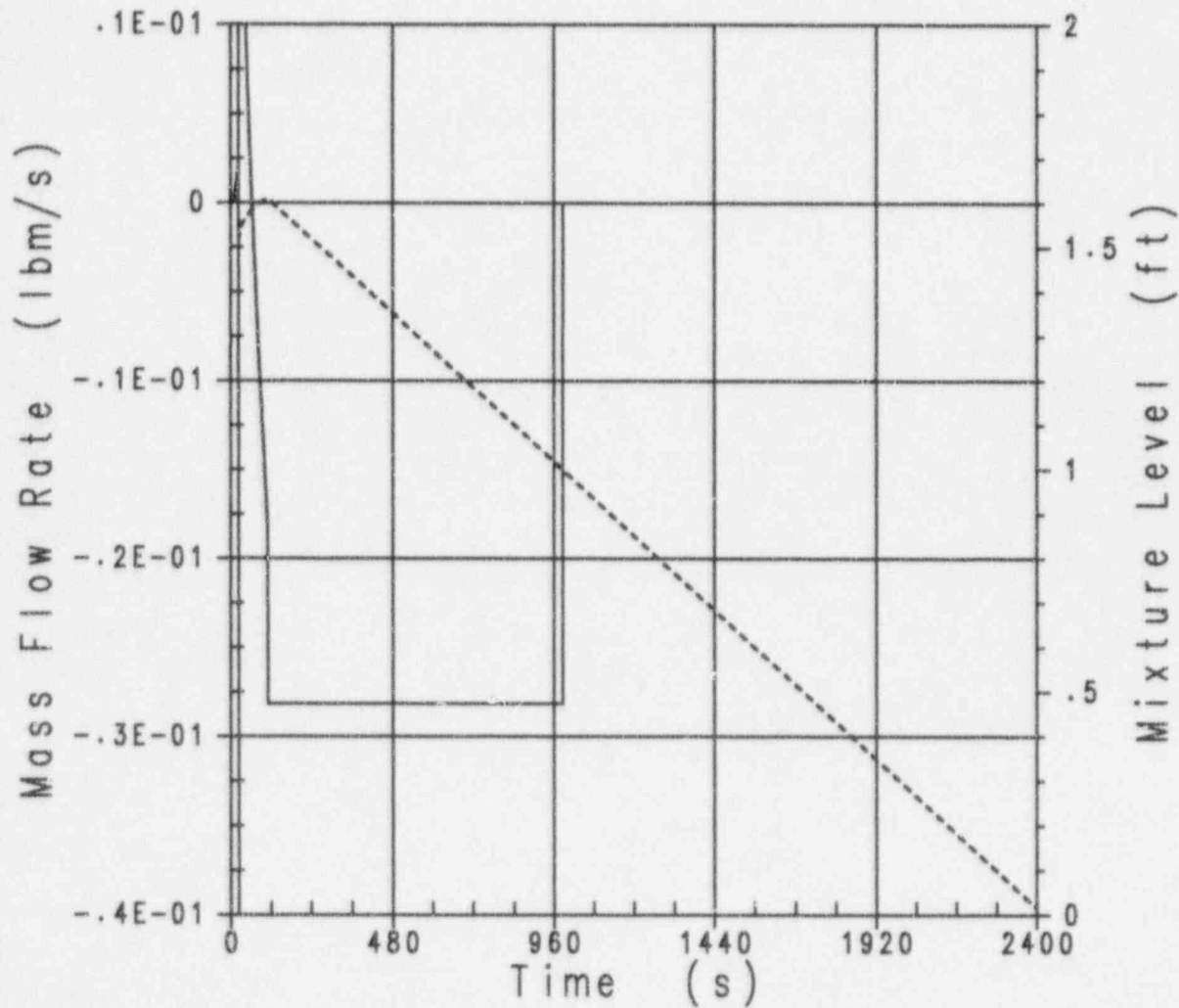


Figure 3.8-18 Two-Phase Constant-Pressure Boil-Off Case: Stack Flowlink Liquid Mass Flow Rate with Stack Mixture Level (with Expanded y-axis Scale)

Mass Flow Rate (lbm/s)				
—— WGFL	1	0	0	LINK 1 GAS FLOW
Mixture Level (ft)				
----- EMIXSFN	2	0	0	STACK LEVEL

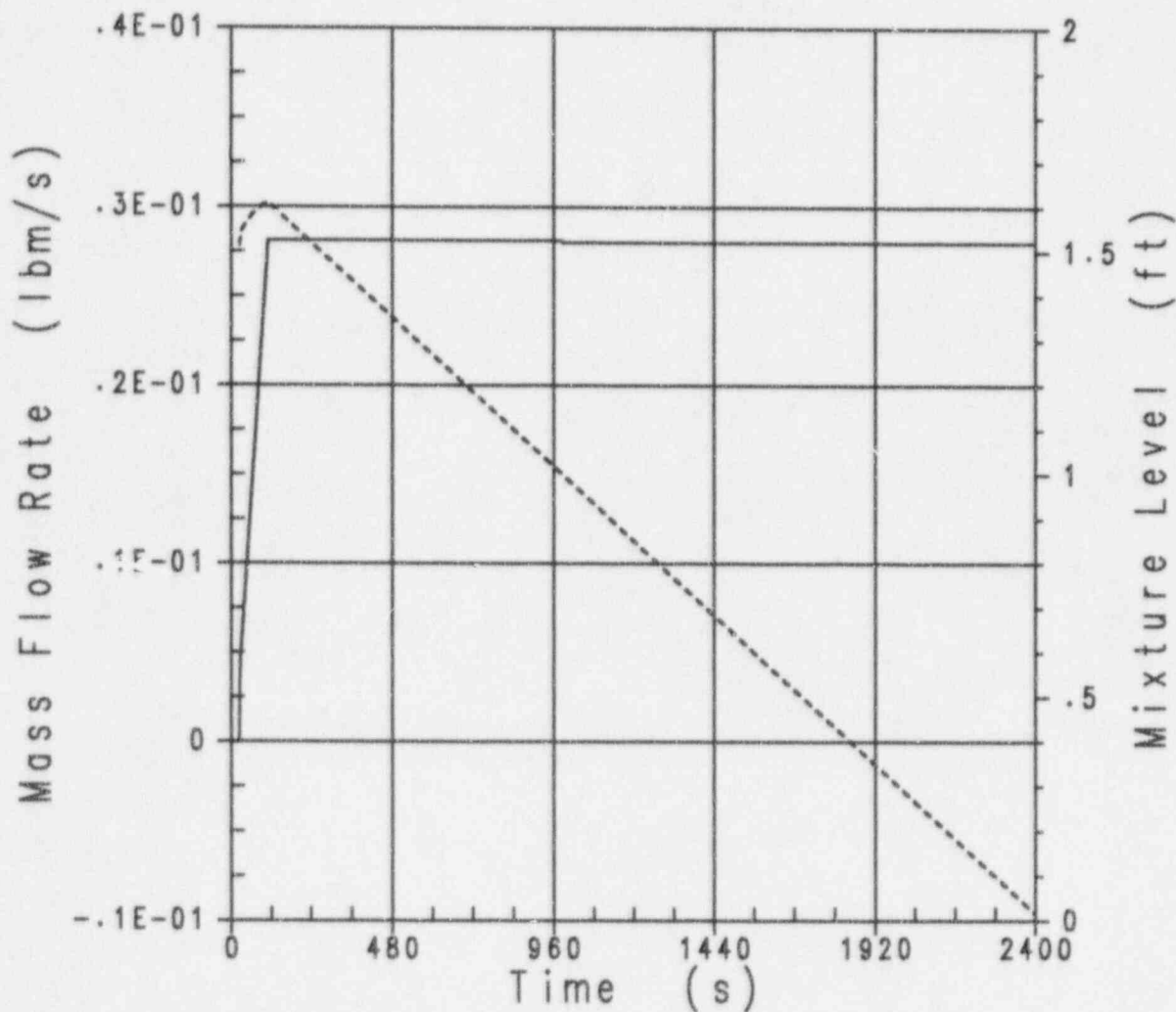


Figure 3.8-19 Two-Phase Constant-Pressure Boil-Off Case: Stack Flowlink Vapor Mass Flow Rate with Stack Mixture Level

Pressure (psia)					
————	PFN	1	0	0	NODE 1 PRESSURE
-----	PFN	2	0	0	NODE 2 PRESSURE
Mixture Level (ft)					
-----	EMIXSFN	2	0	0	STACK LEVEL

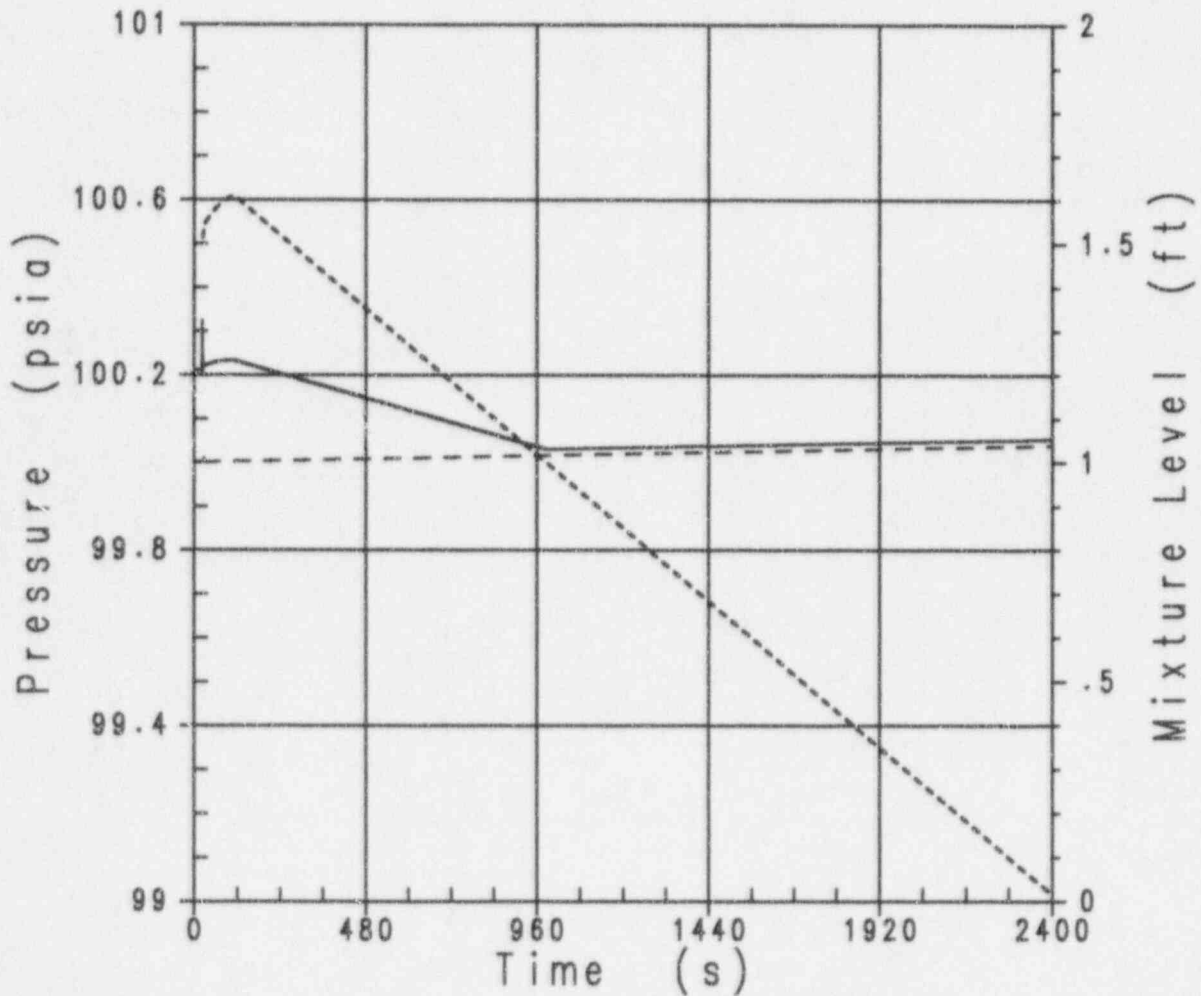


Figure 3.8-20 Two-Phase Constant-Pressure Boil-Off Case: Stack Node Pressures with Stack Node Pressures with Stack Mixture Level